

DOCTORAL THESIS

Development of Sb_2Se_3 and Sb_2S_3 Thin Film Solar Cells by Close-Spaced Sublimation

Robert Krautmann

TALLINN UNIVERSITY OF TECHNOLOGY
DOCTORAL THESIS
41/2023

**Development of Sb_2Se_3 and Sb_2S_3 Thin
Film Solar Cells by Close-Spaced
Sublimation**

ROBERT KRAUTMANN



TALLINN UNIVERSITY OF TECHNOLOGY
School of Engineering
Department of Materials and Environmental Technology

This dissertation was accepted for the defence of the degree 07/07/2023

Supervisor: Dr. Nicolae Spalatu
School of Engineering
Tallinn University of Technology
Tallinn, Estonia

Co-supervisor: Prof. Dr. Ilona Oja Acik
School of Engineering
Tallinn University of Technology
Tallinn, Estonia

Opponents: Dr. Jon Major
School of Physical Sciences
Department of Physics
University of Liverpool
Liverpool, UK

Prof. Dr. Marco Kirm
Institute of Physics
Department of Materials Science
University of Tartu
Tartu, Estonia

Defence of the thesis: 03/10/2023, Tallinn

Declaration:

Hereby I declare that this doctoral thesis, my original investigation and achievement, submitted for the doctoral degree at Tallinn University of Technology has not been submitted for doctoral or equivalent academic degree.

Robert Krautmann

.....

signature



European Union
European Regional
Development Fund



Investing
in your future

Copyright: Robert Krautmann, 2023
ISSN 2585-6898 (publication)
ISBN 978-9916-80-037-9 (publication)
ISSN 2585-6901 (PDF)
ISBN 978-9916-80-038-6 (PDF)
Printed by Koopia Niini & Rauam

TALLINNA TEHNIKAÜLIKOOL
DOKTORITÖÖ
41/2023

**Sb₂Se₃ ja Sb₂S₃ õhukesekileliste
päikesepatareide arendamine
lähidistants-sublimatsiooni meetodil**

ROBERT KRAUTMANN



Contents

Contents	5
List of publications	7
Author's contribution to the publications	8
Introduction	9
Abbreviations	11
1 Literature review	13
1.1 Present status of solar photovoltaics (PV)	13
1.2 Sb-chalcogenides as promising absorber materials for thin film solar cells	15
1.2.1 Physical vapor deposition (PVD) methods for fabricating Sb_2Se_3 and Sb_2S_3 thin films	19
1.2.2 Electron transport layers (ETLs)	22
1.2.3 State-of-the-art of Sb_2Se_3 , Sb_2S_3 , and $\text{Sb}_2(\text{S},\text{Se})_3$ solar cells	23
1.3 Performance limiting factors in Sb_2Se_3 and Sb_2S_3 PV devices	26
1.3.1 Controlling microstructure quality and grain orientation in Sb_2Se_3 and Sb_2S_3 thin films	26
1.3.2 Defect properties in Sb_2Se_3 and Sb_2S_3	28
Summary of the literature review and the aims of the study	39
2 Experimental	41
2.1 Fabrication of Sb_2Se_3 and Sb_2S_3 PV devices	41
2.2 Sb_2Se_3 and Sb_2S_3 thin film characterization	43
2.3 Sb_2Se_3 and Sb_2S_3 PV device characterization	43
3 Results and discussion	45
3.1 Developing growth strategy to fabricate Sb_2Se_3 thin films solar cells by CSS	45
3.1.1 The effect of CSS substrate temperature on Sb_2Se_3 film microstructure and grain orientation	45
3.1.2 The effect of Sb_2Se_3 film microstructure and grain orientation on the Sb_2Se_3 device performance	47
3.1.3 The effect of CBD-CdS and TiO_2 ETLs on the Sb_2Se_3 film morphology and grain orientation	49
3.1.4 Analysis of grain orientation in Sb_2Se_3 thin films	52
3.1.5 The effect of ETL and seed screening on the Sb_2Se_3 device performance	54
3.1.6 Analysis of recombination mechanisms in the Sb_2Se_3 devices	55
3.1.7 Analysis of free carrier and defect densities in Sb_2Se_3 PV devices	57

3.2 Developing growth strategy for depositing Sb ₂ S ₃ thin films by CSS	61
3.2.1 The effect of CSS substrate temperature on Sb ₂ S ₃ film morphology and grain orientation	61
3.2.2 The effect of Sb ₂ S ₃ film microstructure and grain orientation on the Sb ₂ S ₃ PV device performance.....	63
3.2.3 Recombination pathways and heterojunction band alignment in CdS/Sb ₂ S ₃ devices.....	65
Conclusions	69
Acknowledgements.....	71
Abstract	72
Kokkuvõte.....	75
References.....	78
Appendix 1	91
Appendix 2	109
Appendix 3	119
Curriculum vitae	130
Elulookirjeldus.....	133

List of publications

The list of author's publications, on the basis of which the thesis has been prepared:

- I N. Spalatu, **R. Krautmann**, A. Katerski, E. Kärber, R. Josepson, J. Hiie, I. Oja Acik, M. Krunks, "Screening and optimization of processing temperature for Sb_2Se_3 thin film growth protocol: Interrelation between grain structure, interface intermixing and solar cell performance", *Solar Energy Materials and Solar Cells*, vol. 225, 2021, DOI: 10.1016/j.solmat.2021.111045
- II **R. Krautmann**, N. Spalatu, R. Gunder, D. Abou-Ras, T. Unold, S. Schorr, M. Krunks, I. Oja Acik, "Analysis of grain orientation and defects in Sb_2Se_3 solar cells fabricated by close-spaced sublimation", *Solar Energy*, vol. 225, pp. 494–500, 2021, DOI: 10.1016/j.solener.2021.07.022.
- III **R. Krautmann**, N. Spalatu, R. Josepson, R. Nedzinskas, R. Kondrotas, R. Gržibovskis, A. Vembris, M. Krunks, I. Oja Acik, "Low processing temperatures explored in Sb_2S_3 solar cells by close-spaced sublimation and analysis of bulk and interface related defects", *Solar Energy Materials and Solar Cells*, vol. 251, 2023, DOI: 10.1016/j.solmat.2022.112139.

Author's contribution to the publications

Contribution to the papers in this thesis are:

- I Deposition of Sb_2Se_3 and CdS thin films by close-spaced sublimation (CSS); deposition of TiO_2 thin films by ultrasonic spray pyrolysis (USP) and CdS thin films by chemical bath deposition (CBD), post-deposition treatment of TiO_2 and CdS thin films; material characterization by X-ray diffraction (XRD), Van der Pauw, and hot probe analysis methods; device characterization by I–V curves and external quantum efficiency (EQE) measurement; data analysis and visualization; minor role in writing.
- II Deposition of Sb_2Se_3 thin films by CSS; material characterization by XRD, device characterization by I–V curves, EQE, CV profiling, and temperature-dependent admittance spectroscopy (TAS); data analysis and visualization; major role in writing.
- III Deposition of Sb_2S_3 and CdS thin films by CSS; material characterization by XRD, device characterization by I–V curves, EQE, and TAS; data analysis and visualization; major role in writing.

Introduction

Tackling climate change requires complete decarbonization of electricity generation, industries, transport, and buildings. Net zero emissions (NZE) can only be achieved by substantially increasing capacities of renewable technologies and through diversification of energy production and storage. Solar power produces electricity from the sunlight, with the Sun providing an abundant and infinite source of energy. Solar photovoltaics (PV) already provides one of the cheapest sources of electricity [1], [2] and hence will be one of the integral technologies for global energy transition to carbon-free electricity production. International Energy Agency projects that the total installed capacity of solar PV should reach 5 TW by 2030 to follow the NZE by 2050 scenario [3], [4]. The European Union's Solar Energy Strategy plans to bring online almost 0.6 TW of solar PV by 2030 [5]. The increasing demand for solar PV deployment has led to extensive research and development of next-generation PV technologies. In contrast to the incumbent PV technologies such as crystalline silicon (c-Si), CdTe, and Cu(In,Ga)(S,Se)₂ (CIGSSe), the next-generation PV technologies offer several advantages. These novel technologies not only deliver comparable power conversion efficiencies (PCEs) and extended product lifetimes, but they also possess the transformative ability to revolutionize the solar PV industry. With the potential to significantly reduce manufacturing costs, establish sustainable product life cycles, and unlock novel applications beyond traditional c-Si modules, such as multi-junction tandem solar cells, solar windows, internet-of-things (IoT) devices, and building-integrated PV (BIPV) [5], [6].

This doctoral thesis focuses on the development of thin film PV technology based on an emerging class of highly promising inorganic antimony chalcogenide [Sb₂X₃ (X = S, Se, or S_xSe_{1-x})] PV absorbers. Over the last decade, Sb-chalcogenides have been studied intensively due to their fascinating optoelectronic properties, including simple binary structure, low toxicity, earth-abundant constituents, and low processing temperatures. While conventional thin film PV absorbers CdTe and CIGSSe display three-dimensional (3D) grain growth, Sb-chalcogenides exhibit a unique quasi-one-dimensional (Q-1D) crystal growth, which bring about strongly anisotropic electrical properties [7]. Adoption of novel growth strategies and improvements to device architecture have enabled Sb-chalcogenide PV devices to reach PCEs of 8–11% [8]–[13]. Despite exceeding >10% efficiency, thin film solar cells based on CdTe, CIGSSe, Cu₂ZnSn(S,Se)₄ (CZTSSe), and perovskite absorbers still outperform Sb₂X₃ PV devices. Hence, performance limiting factors related to unfavorable grain orientation and intensive non-radiative recombination still must be resolved to ramp up the performance.

Physical vapor deposition (PVD) methods, such as vapor transport deposition (VTD) and close-spaced sublimation (CSS), offer a facile and fast deposition route for Sb₂X₃ absorber materials. Optimized grain microstructure and orientation control of physically deposited Q-1D Sb₂X₃ films have been key aspects to achieving high-performance solar cells. Sb-chalcogenides possess orthorhombic crystal structure, where [Sb₄X₆]_n ribbons stack along the c-axis, or the [001] crystal direction. Consequently, carrier transport along the covalently bonded [Sb₄X₆]_n ribbons is significantly better than carrier hopping between the ribbons. The technological challenge is to develop a deposition strategy, which allows the growth of Sb₂X₃ films with compact and large grain morphology as well as quasi-vertical orientation (crystal orientations [hkl], where l ≠ 0). Various growth strategies, which include optimization of substrate temperature, seed screening, use of different ETLs, and post-deposition treatment, have been demonstrated to promote

Sb₂X₃ film growth along the [001] direction [14]–[20]. Changes to the grain orientation in Sb₂X₃ films are usually determined using texture coefficient (TC) analysis, although which has been argued to not be best suited for highly anisotropic polycrystalline films due to potential overestimation of the actual distribution of grain orientations [21].

A large open-circuit voltage (V_{oc}) deficit is one of the biggest bottlenecks to why Sb₂Se₃ devices are still far from the theoretical efficiency limit [22]. V_{oc} losses can be attributed to bulk defects, which lie deep in the band gap and cause charge trapping and consequent recombination, and interface defects, which arise from unfavorable band alignment, dangling bonds, or lattice mismatch at the heterojunction interface [6], [23]. Comprehensive understanding of defect structure is required for refining processing steps tackling the recombination processes. Theoretical studies have thus far predicted large concentrations of deep defects, such as Sb_{Se} and Se_{Sb} antisite defects in Sb₂Se₃ and V_{Sb} and V_S vacancies in Sb₂S₃, which could be lying deep in the bandgap. Besides deep level transient spectroscopy (DLTS), photoluminescence (PL), and temperature-dependent conductivity measurements, there are only few studies in the literature characterizing deep defects in Sb₂Se₃ and Sb₂S₃ devices by temperature-dependent admittance spectroscopy (TAS). Comparison of these studies shows significant discrepancies between the reported activation energies and the assignments to certain types of defects. Further information is needed to elucidate the defect chemistry of Sb₂Se₃ and Sb₂S₃.

In this doctoral thesis, we developed CSS deposition strategies, which entailed optimization of processing variables such as substrate temperature, seed screening, and selection of suitable optimal ETL, and which enabled growth of high-quality Sb₂Se₃ and Sb₂S₃ thin films. We demonstrated pole figures and electron backscatter diffraction (EBSD) to improve accuracy of grain orientation analysis for Sb-chalcogenide films. We determined thermal activation energies of potential deep defects in both Sb₂Se₃ and Sb₂S₃ devices using TAS. By developing the comprehensive growth approach improving knowledge of performance-limiting defects in Sb₂Se₃ and Sb₂S₃ absorbers, this work helped to lay the groundwork for future development of Sb₂(S,Se)₃ solar cells by CSS.

The doctoral thesis is composed of three main chapters. Chapter 1 begins with an overview of the present and emerging solar PV technologies, which is followed by an introduction to the attractive properties of Sb-chalcogenides and current challenges limiting the performance of Sb₂Se₃ and Sb₂S₃ PV devices. Chapter 2 covers the experimental procedures, which were employed in the work to fabricate and characterize Sb₂Se₃ and Sb₂S₃ thin films absorbers and completed PV devices. Chapter 3 is divided into four sections, which are all based on results and discussion obtained originally during the development of Sb₂Se₃ and Sb₂S₃ PV devices. The first section focuses on the development of CSS growth strategy for Sb₂Se₃ thin films. The second section focuses on the device characterization of Sb₂Se₃ PV devices to reveal potential deep defects in Sb₂Se₃ as well as other recombination processes. The third section focuses on the development of CSS growth strategy for Sb₂S₃ thin films. The fourth section focuses on the device characterization of Sb₂Se₃ PV devices to reveal potential deep defects in Sb₂Se₃ as well as other recombination processes. The thesis concludes with a summary highlighting the main goals achieved during the doctoral work.

Abbreviations

NZE	Net zero emissions
PV	Photovoltaics
c-Si	Crystalline silicon
mc-Si	Multicrystalline silicon
a-Si:H	Amorphous silicon
Sb ₂ Se ₃	Antimony selenide
Sb ₂ S ₃	Antimony sulfide
Sb ₂ (S,Se) ₃	Antimony sulfoselenide
Sb ₂ X ₃	Antimony chalcogenide – Sb ₂ Se ₃ , Sb ₂ S ₃ , Sb ₂ (S,Se) ₃
CdTe	Cadmium telluride
CIGSSe	Copper indium gallium sulfoselenide – Cu(In,Ga)(S,Se) ₂
CZTSSe	Kesterite – Cu ₂ ZnSn(S,Se) ₄
GaAs	Gallium arsenide
InP	Indium phosphide
GaInP	Gallium indium phosphide
AlN	Aluminium nitride
E _g	Bandgap energy
α	Photoabsorption coefficient
vdW	Van der Waals
CSS	Close-spaced sublimation
RTE	Rapid thermal evaporation
VTD	Vapor transport deposition
IVD	Injection vapor deposition
TE	Thermal evaporation
ALD	Atomic layer deposition
CBD	Chemical bath deposition
HT	Hydrothermal method
TCO	Transparent conductive oxide
FTO	Fluorine-doped tin oxide
ITO	Indium-doped tin oxide
AZO	Aluminium-doped zinc oxide
ETL	Electron transport layer
HTM	Hole transport material
V _{oc}	Open-circuit voltage
J _{sc}	Short-circuit density
FF	Fill factor
PCE	Power conversion efficiency
R _s	Series resistance
R _{SH}	Shunt resistance
E _A	Activation energy

N_{cv}	Carrier density
C	Capacitance
q	Elementary charge
k_B	Boltzmann constant
T	Temperature
AC	Alternating current
TC	Texture coefficient
ΔG	Gibbs free energy

1 Literature review

1.1 Present status of solar photovoltaics (PV)

Today's PV market is dominated by crystalline silicon (c-Si) that boasts a 95% market share. Substantial efficiency growth from 15% to 20% for an average commercial c-Si module over the last decade, declined manufacturing costs and increased production volumes have driven c-Si module costs down significantly, with wholesale module prices having dropped to US\$ 0.17–0.25 W⁻¹ in 2021 [24], [25]. Power conversion efficiency (PCE) of a record c-Si solar cell is 26.8%, which still leaves room for further improvement [26], since the detailed balance limit of efficiency for a single-junction solar cell with bandgap energy of 1.1 eV is 32% [27]. To compete with c-Si for a larger market share, any PV technology must demonstrate better pricing or efficiency while maintaining a similar average lifetime [24], [28]. Figure 1 displays the highest PCEs achieved by both older generation and emerging solar PV technologies, plotted against the bandgap energy (E_g) of the respective PV absorbers. The green curve represents the maximum theoretical efficiency according to the Shockley-Queisser (S-Q) detailed balance limit, a fundamental concept in the field of PV research [27].

Thin film PV – CdTe, CIGSSe, and a-Si – and III-V group PV currently make up the remaining 5% of global market share. Cadmium telluride (CdTe) and copper indium gallium sulfoselenide (CIGSSe) are widely studied chalcogenide solar cells, which have achieved efficiencies 22.1% and 23.4%, respectively [26]. Of these two, CdTe has recently shown greater promise with module efficiencies having reached 18.6% for a module price of US\$ 0.28 W⁻¹ [25]. However, further market uptake of CdTe PV modules has been constrained by scarcity of tellurium (Te) and negative perception of cadmium [29]. Cadmium (Cd), in its elemental form, is carcinogenic. On the other hand, CdTe is a chemically robust compound, which has been found to be 100 times less toxic than Cd [29]. CdTe PV modules are also exempt from the EU ban on Cd-based electronic equipment [30].

Champion CIGSSe PV modules have demonstrated PCE of 19.8% [26], while commercially available modules show efficiencies of 12–16% [25]. Although CIGSSe modules currently have larger prices, their development today is focused more on flexible PV applications [25], [31]. Large-scale production of CIGSSe modules could be limited by availability and high price of In and Ga [28]. Amorphous silicon (a-Si) solar cell has reached PCE of 10.2% but has not shown any progress over the last decade [26], [28]. Gallium arsenide (GaAs), gallium indium phosphide (GaInP), and indium phosphide (InP) are III-V materials. GaAs has recorded PCE of 29.1%, the highest ever produced for a single-junction PV device [26]. GaInP and InP solar cell have achieved PCEs of 22.0 and 24.2%, respectively [28]. Commercially available triple-junction III-V modules, which are based on GaAlAs, GaInP, and InGaAs, have shown efficiencies 25–32%, but significantly higher costs – orders of magnitude greater than that of c-Si – have limited III-V modules to niche markets, such as aerospace applications [25], [26], [28].

Emerging PV technologies include kesterite, perovskite, organic, quantum dot and dye-sensitized solar cells. Kesterite materials CZTS (Cu₂ZnSnS₄) and CZTSSe (Cu₂ZnSnS_{4-x}Se_x) emerged as alternatives to CIGSSe, which can be processed by following similar strategies, but where rare elements Ga and In are substituted for more readily available Zn and Sn [28], [32]. Record PCEs of CZTS and CZTSSe solar cells are 11.0% and 13.0%, respectively [26]. Kesterite PV devices are currently hampered by bulk defects and

unfavorable heterojunction band alignment, which severely limit the open-circuit voltage (V_{oc}) [28], [32], [33]. Solar cells based on metal halide perovskites ABX_3 have caused huge excitement among the PV community, having reached efficiencies of >20% already within a decade of research [33]. Champion Pb-based halide perovskite solar cell and module have demonstrated PCEs of 25.7% [34] and 22.7% [35], respectively. More importantly, a perovskite/Si tandem solar cell has reached a remarkable PCE of 32.5%, which rivals the performance of more expensive III-V multijunction solar cells [36].

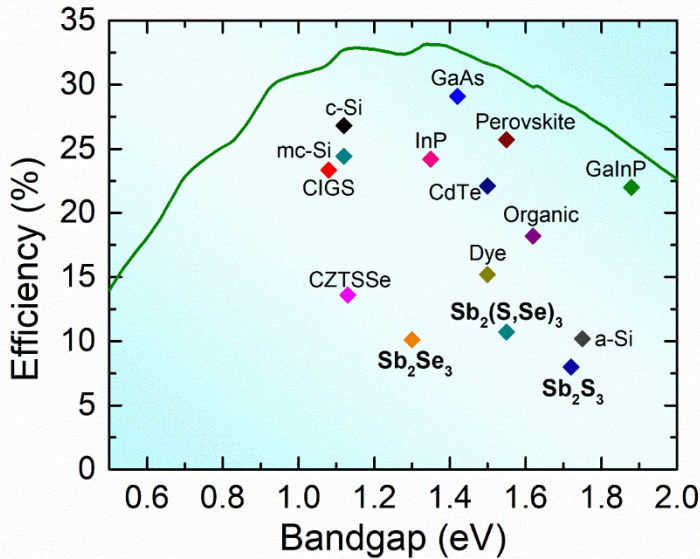


Figure 1. The highest PCEs of various solar PV technologies, plotted against the bandgap energy (E_g) of the respective PV absorbers, with the green curve depicting the maximum theoretical efficiency according to the Shockley-Queisser detailed balance limit [27].

Unusually good defect tolerance, excellent band alignment with various inorganic and organic electron and hole transport layers, and low-cost processing have been the key factors behind the fast progress of halide perovskites solar cells [28], [33], [37]. Despite that, several issues still hinder their commercialization. With the degradation rates still largely unknown, chemical stability of perovskite solar cells remains as the main issue [25], [38]. Toxicity of lead (Pb) in halide perovskites solar cells poses environmental hazards [39]. Organic photovoltaics (OPV), which are based on bulk heterojunction between donor-acceptor-polymers, have progressed efficiencies above 18% [40], [41]. Dye-sensitized solar cell (DSC), which employs a light-harvesting organic photosensitizer on a mesoporous nanocrystalline semiconductor film and a redox electrolyte, has produced a PCE of 15.2% [42]. Quantum dot solar cell (QDSC) has also thrived fast, having reached an impressive PCE of 18.2% in ten years of research [36]. QDSCs have bandgap energies that can be tuned by the colloidal nanoparticle size, thus providing a facile processing route for fabricating multi-junction solar cell.

Significantly advancing over the past decade, Sb_2Se_3 , Sb_2S_3 , and $Sb_2(S,Se)_3$ thin film solar cells demonstrated remarkable progress, achieving impressive power conversion efficiencies (PCEs) of 10.1%, 8.0%, and 10.7%, respectively [9], [10], [13]. The excellent optoelectronic properties and physicochemical stability of Sb_2X_3 , combined with its

processability, enable seamless integration into various PV device architectures, further enhancing its appeal for a diverse range of cutting-edge photovoltaic (PV) applications. These applications include tandem solar cells, internet-of-things (IoT) devices, flexible solar cells, and building-integrated PV (BIPV) [5], [6]. Additionally, the distinctive Q–1D properties of Sb_2X_3 offer opportunities to tailor its electrical characteristics, enabling higher charge carrier mobilities and increased defect tolerance. Moreover, the sustainability factor of Sb_2X_3 makes it an environmentally friendly choice, perfectly aligning with the growing global focus on sustainable renewable energy technologies. Altogether, these exceptional features position Sb_2X_3 as a highly compelling candidate for the next generation of PV technologies.

1.2 Sb-chalcogenides as promising absorber materials for thin film solar cells

Excellent optoelectronic properties

Antimony selenide (Sb_2Se_3) and antimony sulfide (Sb_2S_3) are inorganic semiconductor materials that belong to a family of V-VI group binary metal-chalcogenides (e.g., Bi_2S_3 , Bi_2Se_3 , Bi_2Te_3 , Sb_2Te_3) [43]. High light absorption coefficient ($\alpha > 10^4 \text{ cm}^{-1}$) [44], [45] and suitable bandgap energy (E_g) are excellent optoelectronic properties, which have made Sb_2Se_3 and Sb_2S_3 attractive for PV applications. Sb_2Se_3 exhibits E_g of 1.1–1.3 eV [12] and is reported having p-type conductivity [12], [44], [46], although n-type conductivity related to extrinsic impurities has also been reported [47]. Sb_2S_3 has a wider E_g of 1.7–1.8 eV [48]. Experimentally determined bandgaps of Sb_2Se_3 and Sb_2S_3 are presented in Fig. 2.

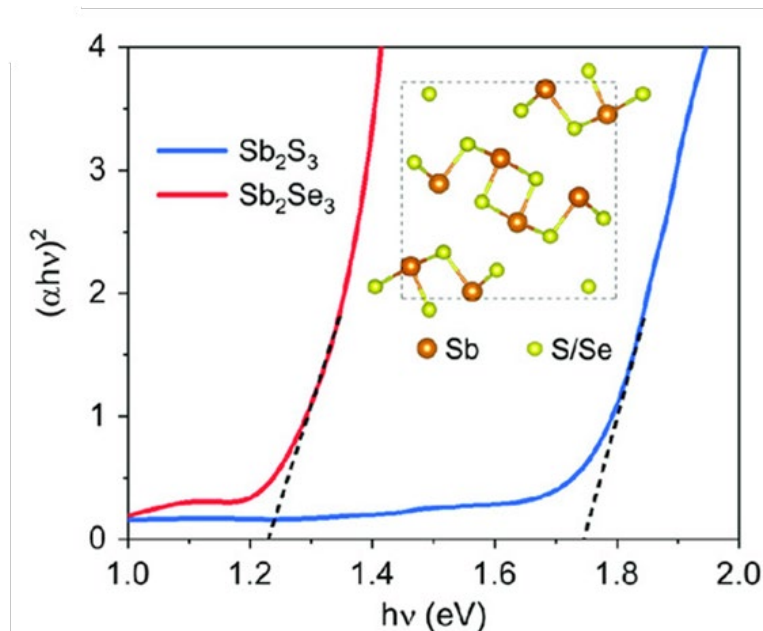


Figure 2. Tauc plot for bandgap calculation of the as-synthesized Sb_2Se_3 and Sb_2S_3 films. Adapted with permission [49]. Copyright 2020 Wiley-VCH.

Low electrical conductivity suggests that Sb_2S_3 are intrinsic, although n-type conductivity has been reported for chemically processed Sb_2S_3 [45]. Since sulfur (S) and selenium (Se) have comparable ionic radii (170 and 190 pm, respectively), electronegativities, and valency, both Sb_2Se_3 and Sb_2S_3 crystallize into the same orthorhombic crystal phase and can hence form $\text{Sb}_2(\text{S,Se})_3$ solid solutions [6]. Changing the atomic ratio of S/Se allows tailoring the E_g of the $\text{Sb}_2(\text{S}_{1-x}\text{Se}_x)_3$ between the range of 1.1–1.8 eV [50]. The optimum E_g range of a single-junction solar cell is 1.3–1.6 eV, as predicted by the Shockley-Queisser (S-Q) detailed-balance model [27]. The maximum theoretical efficiency of 33.7% for a single junction solar cell is achievable with E_g of 1.34 eV [6].

Simple inorganic compounds

Simple binary composition and a single crystal phase are notable advantages that facilitate physical and chemical processing of Sb_2X_3 films [6]. Sb_2X_3 crystallize into orthorhombic crystal structure with Pbnm space group symmetry; there are no stable competing phases [6], [22]. The lattice constants of Sb_2Se_3 are $a = 11.633 \text{ \AA}$, $b = 11.780 \text{ \AA}$, and $c = 3.985 \text{ \AA}$ [43]; the respective values for Sb_2S_3 are $a = 11.229 \text{ \AA}$, $b = 11.311 \text{ \AA}$, $c = 3.836 \text{ \AA}$ [48]. Both Sb_2Se_3 and Sb_2S_3 have low melting points of $612 \text{ }^\circ\text{C}$ [51] and $546 \text{ }^\circ\text{C}$ [20], respectively. Fig. 3a and b display temperature-dependent saturated vapor pressures calculated for Sb, Se, and Sb_2Se_3 and Sb, S, and Sb_2S_3 , respectively, which in both cases indicate high saturated vapor pressures for Sb_2Se_3 and Sb_2S_3 compounds ($>10^3 \text{ Pa}$ at $450 \text{ }^\circ\text{C}$) [20], [51]. Such physical properties are perfectly suitable for depositing thin film using vacuum-based physical vapor deposition (PVD) methods, which have been previously established for fabricating CdTe thin film solar cells [29].

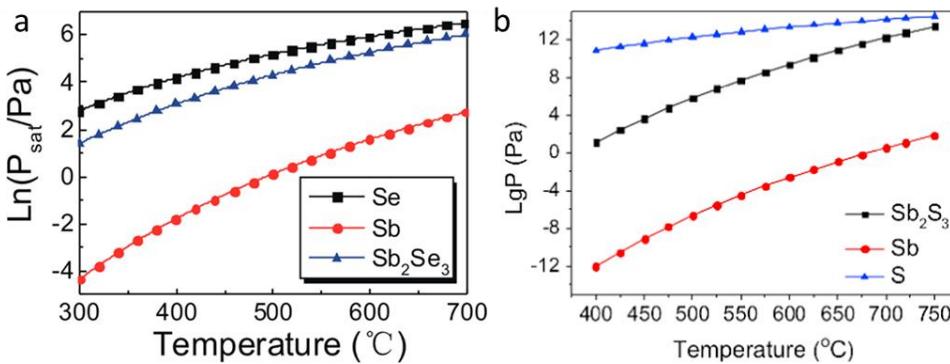


Figure 3. (a) Temperature-dependent saturated vapor pressure of Sb, Se, and Sb_2Se_3 in the temperature range from 300 to 700 $^\circ\text{C}$. Adapted with permission [51]. Copyright 2014, American Chemical Society. (b) Temperature-dependent saturated vapor pressures of Sb, S, and Sb_2S_3 in the temperature range from 400 to 750 $^\circ\text{C}$. Adapted with permission [20]. Copyright 2016, Elsevier.

Regarding the sustainability of Sb-chalcogenide PV, it should be noted that Sb_2Se_3 and Sb_2S_3 are composed of relatively abundant elements, have low toxicity, and exhibit excellent physicochemical stability [52], [53]. Antimony (Sb) is primarily obtained from stibnite, a naturally occurring mineral with the chemical formula Sb_2S_3 . Similarly, selenium (Se) is found in metal sulfide ores and can replace sulfur (S) in these ores. Sb_2Se_3 and Sb_2S_3 are not classified as highly toxic materials by American, European Union, or Chinese regulation authorities, and not listed in the lethal dose LD50 or lethal concentration LCt50 data [52]. Chemical elements Sb, Se, and S are relatively abundant in the Earth's crust with abundances of 0.2, 0.05, and 520 ppm, respectively [6]. According

to the U.S. Geological Survey's data on global mineral commodities, the current prices for Sb, Se, and S minerals are 13.6 € kg⁻¹, 19.4 € kg⁻¹, and 0.15 € kg⁻¹, respectively [54].

The unique feature that distinguishes Sb₂X₃ from the traditional photovoltaic absorbers is the Q-1D film growth and highly anisotropic properties resulting from the orthorhombic crystal structure [6], [45], [55]. Sb₂X₃ crystals are composed of [Sb₄X₆]_n atomic chains, as shown in Fig. 4a, which form Q-1D ribbons that stack along [001] crystal direction, or c-axis, according to the Pbnm space group symmetry [48], [52]. While adjacent ribbons are bound by weak van der Waals' (vdW) forces in the [100] and [010] crystal direction, strong covalent bonding Sb-X chains occurs within ribbons in the [001] direction [43]. Direction-dependent bonding gives rise to highly anisotropic properties, with direct implications to carrier transport across the PV absorber layer. Notably, carrier transport is significantly better along the covalently bonded [Sb₄X₆]_n ribbons than between them, as depicted in Fig. 4 [44], [56]. As a result, various strategies have been explored, also present in this doctoral thesis, which are designed to enhance the Sb₂X₃ film growth along the [001] direction. These efforts will be further discussed in Section 1.3.1.

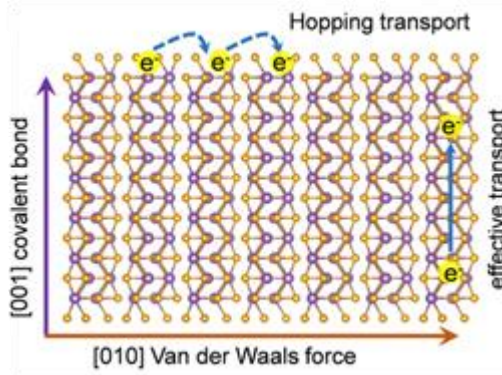


Figure 4. Anisotropic carrier transport along [010] and [001] directions. Reproduced with permission [53]. Copyright 2022, Wiley-VCH

Another positive feature of asymmetric coordination concerns greater defect tolerance of Sb₂X₃ to grain boundary (GB) recombination. While GBs are potent recombination centres in three-dimensional (3D) absorber materials, such as CdTe, CIGSSe, and CZTSSe, the absence of disruptions and dangling bonds between the ribbons in Q1D Sb₂X₃ renders the GBs benign, as can be seen in Fig. 5 [46], [55].

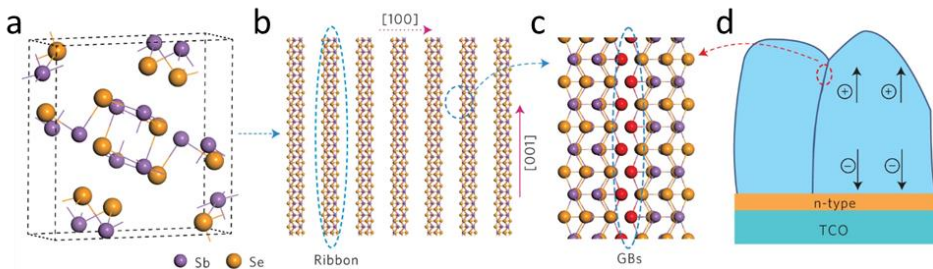


Figure 5. (a) Schematic of a unit cell of a Sb₂Se₃ crystal composed of [Sb₄X₆]_n ribbons, (b) ribbons stacked along the [001] crystal direction, (c) schematic highlighting saturated bonds and absence of dangling bonds, (d) grain boundaries of vertical Sb₂Se₃ grains do not lead to recombination. Modified with permission [46]. Copyright 2015, Springer Nature.

It has been demonstrated that crystal planes of (010), (110), (120) of Sb_2Se_3 , which extend parallel with the [001] direction, have lowest surface energies and hence require no breaking of Sb-Se bonds inside the ribbons [46]. Furthermore, Sb_2Se_3 has been reported to possess a self-healing property, according to which structural relaxation of atoms at the GBs can eliminate the deep defect states generated by dangling bonds on the surface of (100) and (010) crystal planes [6], [57].

Flexible device architectures

To date, a wide range of physical and chemical deposition methods have been utilized for the fabrication of Sb_2Se_3 and Sb_2S_3 thin films. In this respect, several device architectures have been investigated to fully harness the unique properties of Sb_2X_3 materials.

The sensitized-type solar cell (SSC) device architecture, as shown in Fig. 6a, has been adapted from the organic DSC structure and is primarily deployed with the Sb_2S_3 absorber. The device is fabricated on a glass substrate coated with a transparent conductive oxide (TCO). Fluorine-doped tin oxide (FTO) and indium-doped tin oxide (ITO) are two of the more commonly used TCOs, which have large bandgap energies ($E_g \sim 3-4$ eV), high optical transmittance (>80%) and low sheet resistance (<15 Ω /sq). Subsequently, a compact titanium dioxide (TiO_2) film is deposited on the TCO and covered with a mesoporous TiO_2 (mp- TiO_2) scaffold. This is followed by the deposition of an extremely thin absorber (ETA) of Sb_2X_3 , often with a chemical bath deposition (CBD) method. On top of the Sb_2S_3 absorber, a hole transport material (HTM), or a hole transport layer (HTL), is deposited, followed by a conductive metal film acting as the back electrode. HTMs are typically made from organic p-type semiconductor materials. The most commonly used HTMs include poly(3-hexylthiophene-2,5-diyl) (P3HT) and spiro-OMeTAD. Back electrodes are typically composed of non-transparent thin films of metal, such as gold (Au), silver (Ag), or platinum (Pt), which have excellent electrical conductivity. When exposed to sunlight, electron-hole pairs are generated within the absorber layer. The resulting electrons are then extracted across the mp- TiO_2 scaffold to the front electrode, while the holes are transported through the HTM to the back electrode. The final structure is TCO/ TiO_2 /mp- TiO_2 / Sb_2X_3 /HTM/metal [7], [58].

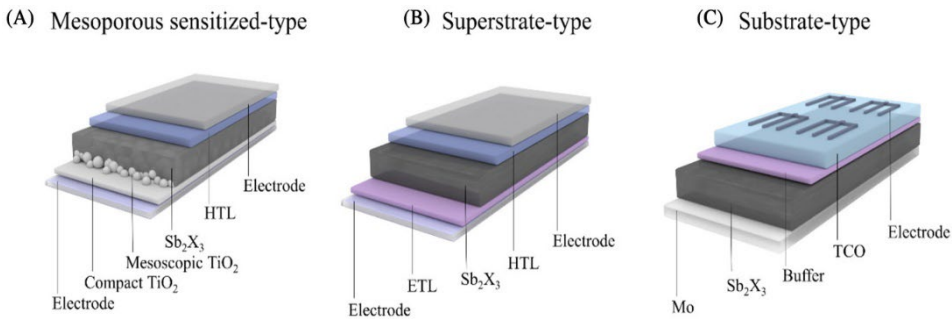


Figure 6. Device configurations for sensitized, superstrate and substrate solar cells. Sb_2X_3 is the common chemical formula for Sb_2S_3 , Sb_2Se_3 , $Sb_2(S,Se)_3$. Reproduced with permission [23]. Copyright 2021, Wiley-VCH.

Both the superstrate-type device and the SSC have their layers stacked on a TCO/glass substrate, as depicted in Fig. 6b and 6c, respectively, and they need to be inverted when exposed to sunlight to function properly. However, superstrate-type devices differ from SSCs in that they use planar thin films. An electron transport layer (ETL), also known as a

heterojunction (HTJ) partner layer or buffer layer, is deposited first on the TCO. Generally, ETLs exhibit n-type conductivity and participate in the formation of a pn-junction at the heterojunction interface between the ETL and the Sb_2X_3 absorber. If the ETL layer has a carrier density that is several orders of magnitude higher than that of the adjacent absorber, the pn-junction can extend further into the absorber. Inorganic wide bandgap n-type semiconductor materials, such as titanium dioxide (TiO_2), cadmium sulfide (CdS), and zinc oxide (ZnO), are typical ETLs for Sb_2Se_3 and Sb_2S_3 [17], [20], [59], [60]. After the ETL, Sb_2Se_3 and Sb_2S_3 absorber films are deposited, sometimes followed by the HTM. Finally, metal contacts are added to complete the device structure, which is TCO/ETL/ Sb_2X_3 /HTM/metal. Substrate-type devices differ from both SSCs and superstrate devices in their structure and deposition sequence. In these devices, the entire structure is stacked on a non-transparent molybdenum (Mo) film, which serves as the back electrode. The deposition sequence is reversed compared to that of SSCs and superstrate devices. In substrate devices, the structure is Mo/ Sb_2X_3 /ETL/TCO, with the Sb_2X_3 absorber layer deposited directly onto the Mo substrate. This is followed by the ETL layer and then the transparent conductive oxide (TCO) layer. The front electrode in substrate solar cells is typically made of aluminium-doped zinc oxide (AZO).

1.2.1 Physical vapor deposition (PVD) methods for fabricating Sb_2Se_3 and Sb_2S_3 thin films

Vapor transport deposition (VTD)

Vapor transport deposition (VTD) is a rapid and low-cost thin film deposition method, which has commercial application in fabricating CdTe solar modules [11]. Vapor transport deposition (VTD) allows independent control of the source and substrate temperature. In addition, distance between the source and substrate and partial pressure of ambient gases can be tuned for optimal film growth [52]. Thin film deposition is assisted by an inert carrier gas, like N_2 , Ar, or He, which facilitates vapor flux transport to the substrate surface, but also reduces the kinetic energy of vapor particles. [11]. VTD deposition is usually conducted in a horizontal quartz tube with two independent heating zones, as depicted in Fig. 7 [11]. The source powder is placed in a graphite crucible, while the substrate is placed on a slanted substrate at >10 cm from the source [11], [18].

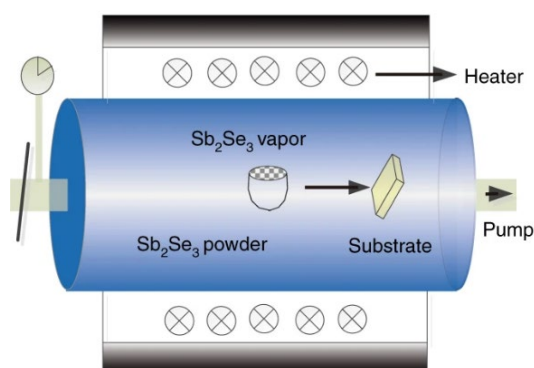


Figure 7. Schematic of a VTD system. Reproduced with permission [11]. Copyright 2018, Springer Nature.

Tang's group demonstrated that the VTD-fabricated Sb_2Se_3 films had higher film crystallinity, longer carrier lifetimes and lower density of bulk and interfacial defects as compared with Sb_2S_3 films deposited by rapid thermal evaporation (RTE); it was concluded that longer deposition and larger space between the source and substrate in the VTD process improved even mixing of vapor particles [11], [53]. Zeng et al. studied the deposition of Sb_2S_3 films with RTE and VTD and found that longer deposition time and larger distance between the source and substrate facilitate Sb_2S_3 film growth with enhanced texture of (hk1) planes [61]. Highest PCEs of achieved by VTD-fabricated Sb_2Se_3 and Sb_2S_3 solar cells are 7.6% [11] and 3.5% [20], respectively.

Close-spaced sublimation (CSS)

Close-spaced sublimation (CSS) is a thin film deposition method known for its higher growth rates ($1.0\text{--}1.5\ \mu\text{m}\ \text{min}^{-1}$) compared to VTD [45], [52]. In the context of this doctoral work, a description of a custom-made CSS reactor is provided, as depicted in Fig. 8. The reactor is a cylindrical structure with stainless metal cladding on the sides and enclosed by graphite plates at both ends. The source powder and substrate are confined between the two graphite plates, positioned approximately 3–11 mm apart. The source material is placed in the cylindrical quartz crucible, with the walls of the quartz crucible extending up to the substrate, thereby providing an enclosed deposition environment.

The substrate, fixed on the edges of the crucible walls and supported by the upper graphite plate from the back, faces down towards the source. Independent temperature control is achieved through two sets of heaters and embedded thermocouples within the graphite plates [12]. The heat, radiated by tungsten coils or lamp heaters, is transferred by the graphite plates to the source and substrate. The high vacuum maintained within the reaction chamber ($10^{-4}\text{--}10^{-6}$ Torr) ensures the sublimation process (solid to gas phase transition) occurs at source temperatures below the melting point of the source material.

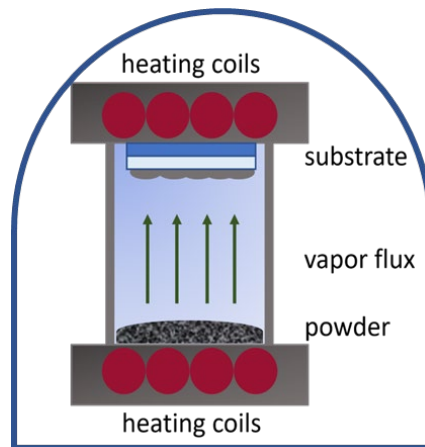


Figure 8. Schematic of a CSS system. Source and substrate temperatures are independently controlled using two sets of heating elements and thermocouples.

Thin film deposition is driven by the temperature gradient, where the vapor flux travels and condenses on the substrate as a solid film. The substrate is held at a lower temperature, sufficient for crystallization to occur. The heated crucible walls play a role in maintaining isothermal conditions within the confined space, ensuring uniform and congruent deposition of Sb_2Se_3 and Sb_2S_3 thin films. CSS deposition can also be conducted

in an inert gas environment, such as N_2 or Ar. For example, Major et al. deposited Sb_2Se_3 films under 10 Torr of nitrogen [47]. Record PCEs achieved by CSS-fabricated Sb_2Se_3 and Sb_2S_3 are 9.3% [62] and 4.5% [63], respectively. The 4.5%-efficient Sb_2S_3 device was attained through co-sublimation of a solid mixture comprising of Sb_2S_3 and Se [64]. The comparable vapor pressures of Sb_2Se_3 and Sb_2S_3 make CSS suitable for co-sublimation and deposition of $Sb_2(S,Se)_3$ thin film solar cells [50].

Rapid thermal evaporation (RTE)

Tang's group developed a rapid thermal evaporation (RTE) technique, which is an advancement from simple thermal evaporation. RTE was developed because thermal evaporation (TE) deposition rates were low (up to $0.1 \mu m \text{ min}^{-1}$) and resulted in Sb_2Se_3 film growth with increased presence of [hk0] grain orientations [53]. The deposition process is similar to the CSS; the distance between the source and substrate is around 1 cm and the growth rates reach $1 \mu m \text{ min}^{-1}$ [46]. RTE differs from CSS in the fact that the source powder first melts and then evaporates from the liquid phase [46]. The schematic of a RTE setup is given in Fig. 9 [65].

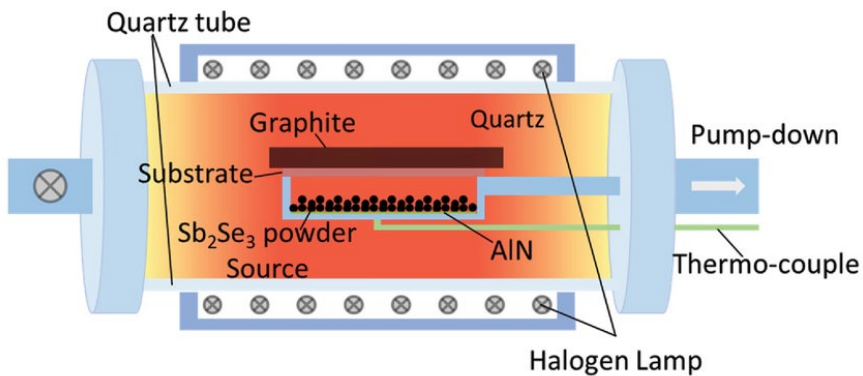


Figure 9. Schematic of an RTE setup, where halogen lamps provide heat to the source and substrate. Reproduced with permission [65]. Copyright 2019, Wiley-VCH.

Source powder is placed on a support made of aluminium nitride (AlN), the substrate is placed above the source, with the substrate facing down. Graphite is used as heat sink, which covers the backside of the substrate [65]. Infrared radiation from halogen lamps provides heat, resulting in high temperature ramp rates ($10 \text{ }^\circ\text{C s}^{-1}$) [65]. Highest efficiencies of RTE-fabricated Sb_2Se_3 and Sb_2S_3 solar cells are 7.6% [65] and 4.5% [20], respectively.

Chemical methods

In addition to PVD methods, numerous chemical methods have been used to successfully fabricate Sb_2X_3 thin film solar cells, especially Sb_2S_3 and $Sb_2(S,Se)_3$ devices. These include chemical bath deposition (CBD), spin coating, hydrothermal (HT) method, atomic layer deposition (ALD), and chemical spray pyrolysis (CSP). CBD is the most widely used method for producing Sb_2S_3 thin films, which offers inexpensive fabrication and simple process control [66]. The record planar and sensitized Sb_2S_3 solar cells, which have achieved PCEs of 8.0% and 7.5%, respectively, have been obtained using CBD [6], [8], [9]. The main limitations of CBD-deposited films are concerned with the presence of secondary phases and weak presence of (hk1) planes [6]. Spin coating is another rapid and low-cost

deposition method, with which Sb_2Se_3 and Sb_2S_3 solar cells have produced efficiencies of 7.1% and 5.4%, respectively [67], [68], but which often lacks uniform coverage and requires annealing step for crystallization [66]. The HT method is similar to CBD, but is carried out in an autoclave, which allows elevated pressures, higher temperatures and inert atmospheres [66]. The HT-deposited $\text{Sb}_2(\text{S,Se})_3$ solar cell has produced the highest PCE of 10.7% [13]. ALD offers greater phase purity and better uniformity of Sb_2X_3 thin films than previously mentioned methods but lacks compatibility for large-scale manufacturing and requires ultrahigh vacuum [6]. CSP is a wet chemical method suitable for large scale manufacturing. Ultrasonic spray pyrolysis (USP), which is a subclass of CSP, is deployed within our research group for fabricating Sb_2S_3 and TiO_2 films. Our group has reported USP-deposited Sb_2S_3 solar cell with PCE of 5.5% [69].

1.2.2 Electron transport layers (ETLs)

Titanium dioxide (TiO_2)

Titanium dioxide (TiO_2) is a IV-VI group semiconductor, which has been widely investigated in PV devices and photocatalytic applications [70], [71]. With a wide E_g of 3.0–3.2 eV, TiO_2 ensures high optical transmittance in the visible and near-infrared (NIR) wavelength region and photosensitivity in the ultraviolet (UV) wavelength region [70]. In addition, TiO_2 demonstrates n-type conductivity attributed to the presence of donor-type oxygen vacancies [72]. Both anatase and rutile are the prevalent crystal phases of TiO_2 [73].

TiO_2 thin films can be synthesized using various techniques, including solution-based methods such as sol-gel, spray pyrolysis, and spin coating, as well as vacuum-based methods like sputtering, pulsed laser deposition (PLD), chemical vapor deposition (CVD), and atomic layer deposition (ALD) [74]. These different techniques allow the production of TiO_2 in different forms, such as planar, mesoporous, nanoparticle structures. TiO_2 finds particularly extensive use as the ETL in DSCs and PSCs. Notably, mesoporous TiO_2 (mp- TiO_2), deposited on a metal oxide blocking layer, serves as a scaffold, providing a highly porous structure of interconnected nanoparticles that facilitates efficient separation of photocarriers [75]. Although TiO_2 ETLs have demonstrated high electron injection rates and proper energy band alignment in PSCs, but their relatively low electron mobility of $0.1\text{--}1.0\text{ cm}^2\text{ V}^{-1}\text{ s}^{-1}$ contributes to recombination rates, prompting research groups to explore viable alternatives [70].

One of the disadvantages about using TiO_2 layers relates to their poor bonding and consequently bad adhesion with Sb_2Se_3 and Sb_2S_3 at the interface. Since Sb-S and Sb-Se bonds have low polarity, it renders Sb_2Se_3 and Sb_2S_3 hydrophobic. The surface of the TiO_2 layer, however, has a hydrophilic nature, which could obstruct efficient wetting of Sb_2Se_3 and Sb_2S_3 onto the TiO_2 surface. Furthermore, dangling bonds, which result from poor bonding, are potent recombination sites, and therefore increase interface recombination [6].

Cadmium sulfide (CdS)

Cadmium sulfide (CdS) is a semiconductor belonging to the II-VI group. It finds extensive use as a ETL in CdTe, CIGSSe, and CZTSSe thin film solar cells. It has a relatively narrow E_g of 2.4 eV and exhibits intrinsic n-type conductivity due to the presence of sulfur vacancies [76]. Its high electron affinity and mobility have also made CdS thin films a popular choice as an ETL also in Sb_2Se_3 and Sb_2S_3 solar cells. CdS has two main crystal phases: cubic zinc

blende and hexagonal wurtzite. The most common fabrication method is the chemical bath deposition (CBD) technique. Other reported methods include RF-magnetron sputtering, thermal evaporation (TE), and CSS [11], [76]–[78].

To enhance the conductivity of CdS films, some groups utilize a post-deposition treatment with cadmium chloride (CdCl₂). This treatment introduces chlorine (Cl) dopants, which create shallow donor levels in the bandgap, improving the film conductivity [79], [80]. However, CdS has certain drawbacks, including parasitic absorption and the toxicity of cadmium. The narrow bandgap of CdS causes parasitic absorption of blue light, which hinders charge excitation within the absorber. This issue can be mitigated by using thinner CdS films (<80 nm) [76]. Exposure to ultraviolet (UV) light can trigger a photocorrosion process in CdS, leading to the release of highly toxic Cd²⁺ ions [74].

Chemical intermixing between CdS and Sb₂Se₃ has been reported in devices with superstrate architecture. Higher processing temperatures could induce Cd outdiffusion from CdS and cause chemical intermixing with Se from Sb₂Se₃ at the interface. Hutter et al. reported about the formation of a CdSe interface layer, which has a wider bandgap than CdS and may act as a barrier to electron transport [59].

Heterojunction band alignment

Proper heterojunction band alignment plays a crucial role in facilitating effective carrier transport within the PV device. It remains unclear which ETL offers better alignment with the Sb₂Se₃ and Sb₂S₃ absorbers. Heterojunction band alignment refers to the alignment of energy levels, specifically the valence band maximum (VBM) and conduction band maximum (CBM), between the ETLs and absorber layers. These energy levels are referenced to the vacuum level. Band offset, on the other hand, represents the energy difference between the respective VBM or CBM levels. A positive conduction band offset (CBO) creates a spike, which acts as an electrostatic barrier, hindering electron transport into the ETL layer [47], [77]. Ideally, a small negative offset ($\Delta\text{CBO} < 0$) is desirable. However, excessively negative offsets cause the CBM of the ETL and the VBM of the absorber to come too close, leading to electron-hole recombination through interface defect states. Shiel et al. [77] demonstrated that TiO₂ exhibits a large positive conduction band offset ($\Delta\text{CBO} > 0$) with Sb₂Se₃, creating a barrier to electron flow. On the other hand, CdS shows excellent alignment between the CBM levels of CdS and Sb₂Se₃ thin films, making it a more favorable choice as an ETL candidate.

1.2.3 State-of-the-art of Sb₂Se₃, Sb₂S₃, and Sb₂(S,Se)₃ solar cells

Different device architectures are not the only parameter that distinguishes Sb₂X₃ solar cells. The deposition method used to fabricate the Sb₂X₃ absorber is another significant factor. This doctoral work primarily focuses on the physical processing of Sb₂Se₃ and Sb₂S₃ thin films, and the following section highlights the major milestones of the physically processed PV devices. However, it is worth noting that in the case of Sb₂S₃ and Sb₂(S,Se)₃, the chemically processed PV devices have progressed further.

Sb₂Se₃ solar cells

In 2009, the first Sb₂Se₃ PV device was produced, demonstrating a PCE of 0.66% [81]. In 2013, Choi et al. reported a 3.2%-efficient Sb₂Se₃ solar cell that utilized spin-coated Sb₂Se₃ as a light sensitizer on mp-TiO₂, mimicking the configuration of DSCs [82]. Since then, substantial progress has been achieved in enhancing the efficiency of both superstrate and substrate Sb₂Se₃ solar cells, particularly in relation to the deposition of Sb₂Se₃ absorbers using PVD methods. In 2015, Zhou et al. demonstrated a CdS/Sb₂Se₃

solar cell with a PCE of 5.6% [46]. In 2017, Wang et al. achieved a 6%-efficient solar cell with a superstrate ZnO/Sb₂Se₃ device [17]. In the same year, Chen et al. employed a colloidal PbS film as an HTM on the Sb₂Se₃ absorber, attaining a PCE of 6.5% with a CdS/Sb₂Se₃/PbS superstrate structure [83]. In all three previous studies, the Sb₂Se₃ film was deposited by RTE, which exhibits a growth rate comparable to the CSS method.

In 2018, Hutter et al. reported a 6.6%-efficient superstrate TiO₂/Sb₂Se₃/PCDTBT solar cell, with Sb₂Se₃ deposited by CSS [59]. In the same year, Tang's group achieved a champion solar cell with a superstrate CdS/Sb₂Se₃ configuration, exhibiting a PCE of 7.6% [11]. In 2019, Mai's group achieved a PCE of 9.2% with a device structure of ZnO:Al/ZnO/CdS/TiO₂/Sb₂Se₃/MoSe₂/Mo in substrate configuration, which incorporated nanostructured Sb₂Se₃ arrays deposited by CSS [12]. It is noteworthy that previous solar cells predominantly exhibited Sb₂Se₃ grains growing along the [211] and [221] directions [11], [17], [46], [59], [78]. In contrast, Li et al. were first to demonstrate Sb₂Se₃ ribbons that were aligned along the [001] direction, parallel with the c-axis [12]. In the same year, Major's group achieved a PCE of 5.5% for a TiO₂/Sb₂Se₃ superstrate configuration, utilizing CSS for the growth of Sb₂Se₃. In 2020, Major's group achieved an efficiency of 7.3% using a CSS-deposited n-type Sb₂Se₃ in a superstrate FTO/TiO₂/Sb₂Se₃/Au solar cell [47]. In 2022, Mai's group reported record efficiency of 10.1% with a substrate glass/Mo/MoSe₂/Sb₂Se₃/CdS/i-ZnO/AZO/Au device, employing a novel injection vapor deposition (IVD) approach for Sb₂Se₃ fabrication [10]. In 2023, Shangwei Dong et al. applied the RTE approach on Sb₂Se₃ and obtained PCE of 7.6% with a superstrate ITO/CdS/Sb₂Se₃/Au device [84].

Sb₂S₃ solar cells

The first Sb₂S₃ solar cell was reported by Savadogo et al. in 1994. The device had an n-type Sb₂S₃ absorber layer deposited onto a p-Si substrate using chemical bath deposition (CBD) and achieved an impressive PCE of 5.2% under 1 sun intensity [6], [85]. Despite its apparent potential, intensive research into Sb₂S₃ solar cells did not take off until more than a decade later, when a Sb₂S₃-sensitized solar cell demonstrating 3.4% efficiency was reported in 2009 [86]. In the following years, improved treatment strategies and introduction of organic HTM layers led to efficiencies 5.1% [87] and 6.3% [88]. In 2015, Seok's group introduced thioacetamide (TA) post-deposition treatment and fabricated a champion Sb₂S₃-sensitized device with PCE of 7.5% [8]. All these reported studies employed Sb₂S₃ absorbers, which were synthesized by chemical bath deposition (CBD) method.

Planar Sb₂S₃ solar cells have almost exclusively been fabricated in superstrate configuration with both chemical and physical deposition methods. Kim et al. employed atomic layer deposition (ALD) in 2014 to fabricate Sb₂S₃ solar cells, achieving 5.8% efficiency with a planar superstrate FTO/TiO₂/Sb₂S₃/P3HT/PEDOT:PSS/Au device [89]. In 2019, Han et al. reported PCE of 7.1% for a planar FTO/TiO₂/Sb₂S₃/SbCl₃/Spiro-OMeTad/Au solar cell that employed a solution-processed Sb₂S₃ with SbCl₃ post-deposition treatment [90]. The same year, our group presented a superstrate ITO/TiO₂/Sb₂S₃/P3HT/Au solar cell with PCE of 5.5%, using ultrasonic spray pyrolysis (USP) to deposit Sb₂S₃ ETA film [91]. In 2021, Ning et al. applied hydrothermal method to deposit Sb₂S₃ and achieved PCE of 6.5% with an FTO/TiO₂/K:CdS/Sb₂S₃/Spiro-OMeTAD/Au device [92]. In 2022, Chen's group demonstrated record PCE of 8.0% for Sb₂S₃ solar cells with a planar FTO/CdS/Sb₂S₃/Spiro-OMeTad/Au device, where a Sb₂S₃ absorber was CBD-deposited with a novel precursor containing multi-sulfur sources [9]. It is worth noting that chemically processed planar Sb₂S₃ solar cells have adopted the n-i-p junction, which is similar to SSCs

and requires the use of a hole-transporting material (HTM). Absorber layers of chemically deposited Sb_2S_3 solar cells are typically much thinner than those of vacuum processed Sb_2S_3 solar cells. More recently, improvements to Sb_2S_3 solar cells, fabricated with vacuum processed methods, have been reported. Zeng et al. in 2020 used vapor transport deposition (VTD) to deposit Sb_2S_3 and achieved a superstrate ITO/CdS/ Sb_2S_3 /Au solar cell with PCE of 4.7% [61]. In 2021, Chen's group attained PCE of 6.2% with FTO/CdS/ Sb_2S_3 /Spiro-OMeTAD/Au solar cell, for which Sb_2S_3 was deposited by thermal evaporation (TE) from a Sb_2S_3 and an additional S powder sources [93]. In 2022, Deng et al. demonstrated an FTO/ TiO_2 / Sb_2S_3 / Sb_2Se_3 /Au structure with 5.8% efficiency, where both Sb_2S_3 and Sb_2Se_3 films were deposited by rapid thermal evaporation (RTE) and a 60-nm thick Sb_2Se_3 film acted as an HTM [94]. The same year, Xie et al. employed a Sb_2S_3 absorber, which was deposited by close-spaced sublimation (CSS) and achieved 4.5% efficiency with an FTO/CdS/ Sb_2S_3 /Au device [64]. Thus far, substrate Sb_2S_3 devices fabricated using sputtering and RTE methods have achieved efficiencies of less than 2.5% [95], [96].

$\text{Sb}_2(\text{S},\text{Se})_3$ solar cells

In 2014, Chan Choi et al. produced a $\text{Sb}_2(\text{S},\text{Se})_3$ -sensitized solar cell with a PCE of 6.6%, in which Sb_2Se_3 and Sb_2S_3 films were sequentially deposited by spin coating and chemical bath deposition (CBD) onto a mesoporous TiO_2 (mp- TiO_2) electron transport layer (ETL) [97]. In 2017, Yang et al. developed a 5.8%-efficient superstrate device with $\text{Sb}_2(\text{Se}_{0.8}\text{S}_{0.2})_3$ absorber, which was fabricated by RTE from Sb_2Se_3 and S powder sources [98]. In 2018, Wang et al. presented a superstrate FTO/CdS/ $\text{Sb}_2(\text{S},\text{Se})_3$ /Spiro-OMeTAD/Au solar cell with PCE of 6.1%, where a $\text{Sb}_2(\text{S},\text{Se})_3$ absorber was realized by depositing Sb_2Se_3 with hydrothermal (HT) and following post-selenization treatment [99]. In the same year, another superstrate device achieved PCE of 6.2% with FTO/CdS/ $\text{Sb}_2(\text{S},\text{Se})_3$ /C-Ag stack; Sanchez et al. employed a $\text{Sb}_2\text{S}_{0.7}\text{Se}_{2.3}$ absorber, which was obtained by thermal evaporation of chemically synthesized Sb-S-Se precipitates and SbCl_3 [100]. In 2020, Chen's group achieved PCE of 10.0% for a superstrate device with FTO/ TiO_2 /CdS/ $\text{Sb}_2(\text{S},\text{Se})_3$ /Spiro-OMeTAD/Au configuration; $\text{Sb}_2(\text{S},\text{Se})_3$ absorber was synthesized by HT and thermally annealed in N_2 environment [101]. Soon after, they demonstrated how adding ethylenediaminetetraacetic acid (EDTA) to the HT synthesis further improved PCE to 10.5% [102].

In 2021, Chen's group fabricated record $\text{Sb}_2(\text{S},\text{Se})_3$ solar cell with 10.7% efficiency, where the $\text{Sb}_2(\text{S},\text{Se})_3$ absorber was subjected to alkali treatment. Post-deposition treatment by NaF changed the S/Sb grading, which improved the heterojunction band alignment and device parameters [13]. The same year, Li et al. reported a CSS-fabricated $\text{Sb}_2(\text{S},\text{Se})_3$ device with PCE of 2.8%, with $\text{Sb}_2(\text{S}_{0.25}\text{Se}_{0.75})_3$ absorber having optimal S/Se ratio [103]. The record $\text{Sb}_2(\text{S},\text{Se})_3$ solar cell. This year, a VTD-fabricated $\text{Sb}_2(\text{S},\text{Se})_3$ solar cell demonstrated PCE of 7.1%; Pan et al. deposited $\text{Sb}_2(\text{S},\text{Se})_3$ using a solid mixture Sb_2Se_3 and Sb_2S_3 with 3:1 mole ratio [104]. Table 1 summarizes the record solar cell efficiencies reported to date for Sb_2Se_3 , Sb_2S_3 , and $\text{Sb}_2(\text{S},\text{Se})_3$ solar cells fabricated using physical and chemical deposition methods. Physical deposition methods have yielded higher efficiencies for Sb_2Se_3 solar cells, while chemical methods have demonstrated superior performance for Sb_2S_3 and $\text{Sb}_2(\text{S},\text{Se})_3$ solar cells.

Table 1. Record solar cell efficiencies reported for Sb_2Se_3 , Sb_2S_3 , and $Sb_2(S,Se)_3$ solar cells fabricated with physical and chemical methods. CSS-deposited solar cells were included for comparison.

Absorber	Configuration	Method	Device structure	PCE (%)	Ref
Sb_2Se_3	Substrate	IVD	Mo/MoSe ₂ /Sb ₂ Se ₃ /CdS/i-ZnO/AZO/Au	10.1	[10]
		CSS	Mo/MoSe ₂ /Sb ₂ Se ₃ /TiO ₂ /CdS/ZnO/ZnO:Al	9.2	[12]
	Superstrate	VTD	ITO/CdS/Sb ₂ Se ₃ /Au	7.6	[11]
		CSS	FTO/TiO ₂ /Sb ₂ Se ₃ /Au	7.3	[47]
Sb_2S_3	Sensitized	CBD	FTO/mp-TiO ₂ /Sb ₂ S ₃ /PCPDTBT/Au	7.5	[8]
	Superstrate	CBD	FTO/CdS/Sb ₂ S ₃ /Spiro-OMeTad/Au	8.0	[9]
		TE	FTO/CdS/Sb ₂ S ₃ /Spiro-OMeTAD/Au	6.2	[93]
		CSS	FTO/CdS /Se:Sb ₂ S ₃ /Au	4.5	[64]
$Sb_2(S,Se)_3$	Superstrate	HT	FTO/Zn(O,S)/CdS/Sb ₂ (S,Se) ₃ /Spiro-OMeTAD/Au	10.7	[13]
		VTD	ITO/CdS/Sb ₂ (S,Se) ₃ /Au	7.1	[104]
		CSS	FTO/CdS/Sb ₂ (S,Se) ₃ /Au	2.7	[103]

1.3 Performance limiting factors in Sb_2Se_3 and Sb_2S_3 PV devices

1.3.1 Controlling microstructure quality and grain orientation in Sb_2Se_3 and Sb_2S_3 thin films

Developing high-quality microstructures with enhanced grain orientation along the [001] direction has emerged as a crucial strategy for achieving efficient PV devices using Sb_2Se_3 and Sb_2S_3 . Despite the Q-1D ribbon-like growth of Sb_2Se_3 and Sb_2S_3 compounds, the optimal microstructures of Sb_2Se_3 and Sb_2S_3 closely resemble the grain structures found in 3D PV absorbers such as CdTe and CIGSSe. State-of-the-art Sb_2Se_3 and Sb_2S_3 devices have been successfully achieved by incorporating absorbers with compact and large grain morphologies [9]–[11], [47], [93], except for a notable 9.2%-efficient substrate solar cell that utilized a nanorod array structured absorber [12]. The presence of large columnar grains without lateral grain boundaries is advantageous because it facilitates vertical carrier transport [59]. To improve grain orientation in the [001] direction, several

strategies have been adopted, including optimizing processing temperatures, substrate selection, seed screening, and post-deposition treatments [14]–[20]. While achieving a fully columnar structure with a single preferred grain orientation along the [001] direction is technologically challenging for polycrystalline films with an orthorhombic crystal structure, notable advancements have been made in enhancing growth of compact films with large and quasi-vertically oriented grains.

In the case of Sb_2S_3 thin films deposited by PVD methods, improved crystallinity and columnar grain growth have been demonstrated with source (or evaporation) temperatures in the range of 460–540 °C and substrate temperatures in the range of 390–450 °C. These conditions have also shown the presence of [hk1] grain orientations [11], [12], [47], [59], [84]. These [hk1] orientations refer to tilted grains that have a small angle with respect to the [001] direction, as depicted in Fig. 10, [18], [65], [105], [106]. Due to the lower melting point of Sb_2S_3 , the deposition process can be carried out at lower processing temperatures. For optimal Sb_2S_3 thin films, source temperatures in the range of 450–540 °C and substrate temperatures in the range of 370–450 °C have been employed [18], [61], [64].

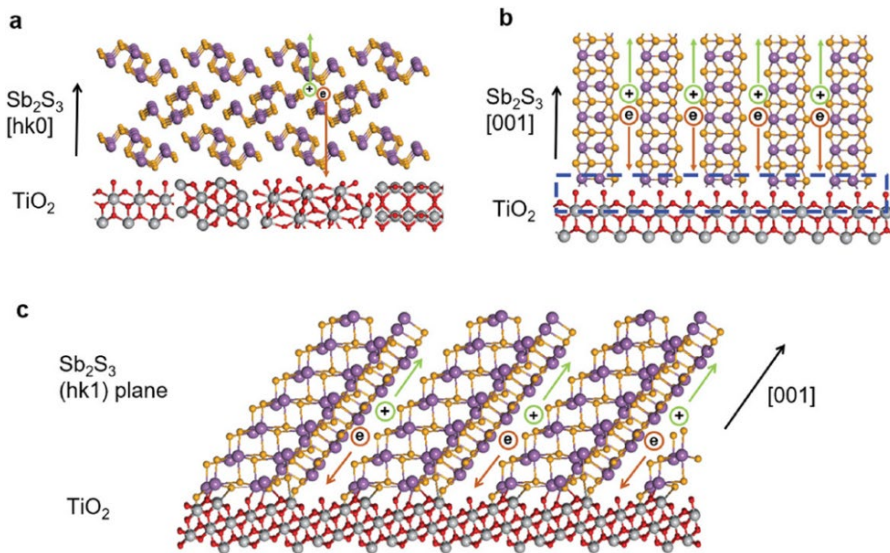


Figure 10. Crystal structures of $[\text{Sb}_4\text{S}_6]_n$ ribbons schematically stacked on TiO_2 . (a) [hk0]-oriented Sb_2S_3 ribbons lie on the nanocrystalline TiO_2 ETL leading to hopping carrier transport. (b) [001]-oriented Sb_2S_3 ribbons stand vertically on crystalline TiO_2 with mismatched lattices. (c) [hk1] orientation Sb_2S_3 ribbons chemically bond with crystalline [101]-oriented TiO_2 surface. Modified with permission [105]. Copyright 2019, Wiley-VCH.

As for the substrate selection, Pattini et al. studied Sb_2Se_3 film growth on different substrates, with FTO found optimal substrate for enhancing [001] grain orientation, while Mo substrate caused lateral growth of Sb_2Se_3 grains [17]. Wang et al. demonstrated that a ZnO ETL improves the Sb_2Se_3 film growth and enhances [221] grain orientation [17]. Similarly, Sb_2S_3 films grown on a CdS ETL displayed compact morphology with enhanced [hk1] grain orientation. This was attributed to CdS supplying dangling bonds of Cd^{2+} and S^{2-} , which form covalent bonds with S^{2-} and Sb^{3+} atoms, respectively, thereby facilitating $[\text{Sb}_4\text{Se}_6]_n$ ribbon growth in the [001] direction [107]. Controlling grain orientation in the Sb_2Se_3 films grown on the TiO_2 ETL was considered more difficult than on the ZnO or CdS

due to the larger bond energy of Ti–O (662 kJ mol^{-1}) as compared to Zn–O (284 kJ mol^{-1}) and Cd–S (196 kJ mol^{-1}). Consequently, Sb^{3+} and Se^{2-} atoms do not bond with O^{2-} and Ti^{4+} atoms TiO_2 substrate easily, causing lateral growth of $[\text{Sb}_4\text{Se}_6]_n$ ribbons [65]. This obstacle has been overcome by seed screening strategy.

The objective of a seed layer, which is of the same composition as the main film, is to produce high nucleation density on the substrate for the second stage of the film growth [59], [106]. Additionally, it ensures good coverage of the absorber film on the ETL, preventing shunting pathways between the n-type ETL and the back contact [47], [59]. Although the seed layer incorporates nucleation seeds with both [hk1] and [hk0] orientations, high substrate temperatures lead to the re-evaporation of [hk0]-oriented seeds. These seeds have weak van der Waals (vdW) interactions with the underlying substrate. In contrast, the [hk1]-oriented seeds remain intact due to stronger covalent bonding [65].

Selenization has been employed as a post-deposition treatment to improve the grain structure and orientation. Li et al. selenized the Mo substrate prior to the Sb_2Se_3 film deposition, achieving nanorod array structure with strong texture in the [001] direction [12]. Kumar et al. reported that post-selenization of thermally evaporated Sb_2Se_3 thin films improves the absorber quality by increasing compactness and grain size with enhancement of [hk1] orientations. Zhang et al. demonstrated a two-step post-annealing process, which consolidates the [hk1] grain orientations in the Sb_2S_3 films [108].

Various strategies have been employed to control the grain orientation and microstructure of Sb_2Se_3 and Sb_2S_3 films, as demonstrated earlier. To optimize the CSS deposition process and attain compact Sb_2Se_3 and Sb_2S_3 films with enlarged grain morphology and improved grain orientation along the [001] direction, a systematic investigation of these strategies will be required.

1.3.2 Defect properties in Sb_2Se_3 and Sb_2S_3

High open-circuit voltage (V_{oc}) deficit, which is defined as $E_g/q - V_{\text{oc}}$, represents a significant barrier for Sb_2X_3 PV devices to achieve their theoretical efficiency values [22]. Fig. 11 shows the V_{oc} values of state-of-the-art planar Sb_2Se_3 , Sb_2S_3 , and $\text{Sb}_2(\text{S,Se})_3$ devices, ranging from 0.7–0.9 V [23]. These values fall far short of the potential V_{oc} values estimated by the S-Q limit [22], [23]. The substantial V_{oc} deficit is primarily attributed to the high concentration of intrinsic defects, which contribute to carrier recombination and consequently degrade the device performance.

Intrinsic point defects in semiconductor materials arise from vacancies (missing atoms in the crystal lattice), interstitials (atoms located between lattice sites), and antisites (when a cation replaces an anion, or vice versa) in the crystal lattice, with defects introducing electronic states within the bandgap. The initial expectation was that both Sb_2Se_3 and Sb_2S_3 would exhibit six distinct types of intrinsic point defects. For Sb_2Se_3 , these defects would include two vacancies (cation vacancy, V_{Sb} , and anion vacancy, V_{Se}), two interstitials (antimony interstitial, Sb_i , and selenium interstitial, Se_i), and two antisites (cation-replace-anion antisite, Sb_{Se} , and anion-replace-cation antisite, Se_{Sb}) [109]. Similarly, for Sb_2S_3 , the defects would be V_{Sb} , V_{S} , Sb_i , S_i , Sb_s , S_{Sb} . However, theoretical investigations revealed the complexity of the defect chemistry in these compounds.

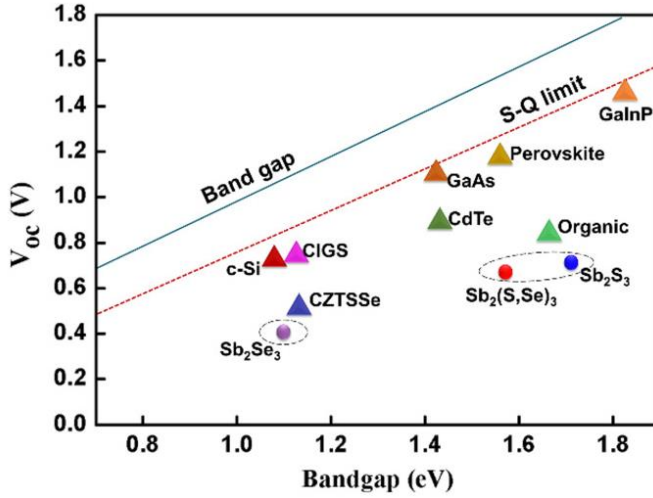


Figure 11. V_{oc} values of state-of-the-art solar cells based on different PV absorbers with the calculated theoretical Shockley-Queisser (S-Q) V_{oc} limit depicted as a red dotted line. Reproduced with permission [23]. Copyright 2021, Wiley-VCH.

Fig. 12a illustrates the stacking of $[Sb_4X_6]_n$ ribbons, with each $[Sb_4X_6]_n$ consisting of two trigonal SbX_3 and two square SbX_5 pyramids, as shown in Fig. 12b [48]. The square pyramidal coordination is induced by the presence of $Sb\ s^2$ lone pair, which occupies the space between the ribbons [55], [110], [111]. The asymmetric coordination of Sb, Se, and S atoms leads to non-equivalent atomic sites for Sb, Se, and S atoms within the $[Sb_4X_6]_n$ ribbons, exposing them to different bonding environments and producing multiple defect energy levels for the same type of defect [48], [109], [112].

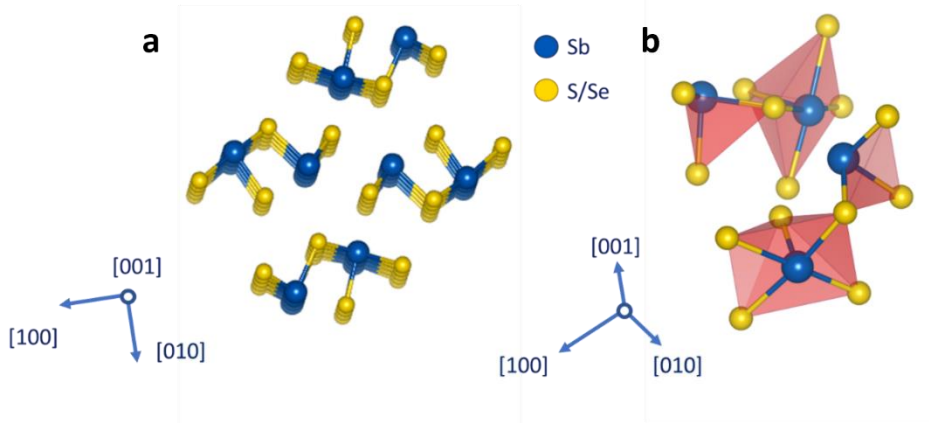


Figure 12. (a) Top-down view showing the stacking of $[Sb_4X_6]_n$ ribbons. (b) $[Sb_4X_6]_n$ atomic chains are composed of two trigonal SbX_3 and two square SbX_5 pyramids resulting in non-equivalent atomic sites for Sb, Se, and S atoms.

Specifically, there are two non-equivalent sites for Sb (Sb1, Sb2), where Sb atoms are bonded to either three Se (or S) atoms or five Se (or S) atoms. Additionally, there are three non-equivalent sites for Se (or S) atoms (Se1, Se2, Se3, or S1, S2, S3), with Se (or S) atoms forming either three or two covalent bonds with Sb atoms [112]–[114].

Consequently, the properties of defects related to specific atomic sites can be very different, which contrasts with the defect properties observed in 3D materials like CdTe, where all cation and anion sites are considered equivalent [109], [112]. Furthermore, the presence of weak vdW interactions between the Q-1D ribbons creates ample space, thereby facilitating the formation of unconventional antisite defects [112].

Both low conductivities of 10^{-6} – 10^{-8} S cm⁻¹ and high defect densities of 10^{14} – 10^{15} cm⁻³ reported in the Sb₂Se₃ and Sb₂S₃ indicate extensive defect compensation of free carrier densities [11], [44], [93], [115], [116]. This presents a challenge to analyzing properties, such as carrier density and mobility [109]. So far, Sb₂Se₃ absorber has been predominantly exhibited p-type conductivity [44], [117], [118]. However, it should be noted that n-type Sb₂Se₃ absorbers have also been reported, attributed to the unintended presence of extrinsic chlorine (Cl) impurities [47]. In the case of Sb₂S₃, n-type conductivity is predominantly reported in chemically processed Sb₂S₃ [116], while p-type conductivity has been claimed in physically evaporated Sb₂S₃ films [6], [119]. The conductivity type determines the majority carrier type, which is essential for defect analysis. The defect energy levels, particularly thermal activation energies, identified through defect analysis methods, are referenced relative to either the VBM or the CBM.

Theoretical investigations of defect chemistry in Sb₂Se₃ and Sb₂S₃

Defect formation in thin films can be influenced by the deposition method and processing conditions, resulting in Sb- or Se-(S-rich) compositions in the final films. Theoretical investigations, such as first-principles calculations and density functional theory (DFT) studies, report defect formation energies and identify dominant defects in both Sb-rich and Se-(or S-) rich conditions. The formation energy refers to the Gibbs free energy required for defect formation [109]. Defects can begin to have significant concentrations when their formation energies are below 1.5 eV [22]. A lower energy value corresponds to a higher expected concentration of the specific defect type. Dominant defects are typically those with the lowest formation energies and contribute to the electrical compensation of oppositely charged defects, thereby determining the position of the Fermi level and conductivity type.

In terms of Se-rich Sb₂Se₃, several studies have reported an unusually low formation energy for Se_{Sb} antisite defects, indicating their expected presence in high concentration of 10^{14} cm⁻³ [112]. While the anion-replace-cation antisite defect would typically act as a donor defect, the Se_{Sb} antisite defect in Sb₂Se₃ is known to behave as an acceptor defect, which could account for the p-type character [109]. Additionally, Huang et al. claimed that the low symmetry of Q-1D Sb₂Se₃ facilitates the formation of 2Se_{Sb} (2Se_{Sb1} and 2Se_{Sb2}) complex antisite defects, where two Se anions replace one Sb cation [112]. As depicted in Fig. 13, these defects exhibit low formation energies and are likely to occur in high concentrations, thereby contributing to the p-type conductivity [112].

Scanlon et al. proposed that the Se_{Sb} antisite defect has an amphoteric nature and is positioned deep within the bandgap, serving as a recombination center for both holes and electrons. Compensation for the Se_{Sb} antisite defect occurs through a V_{Sb} vacancy, which acts as a deep acceptor with defect energy levels that are more than $k_B T$ (25 meV) away from the valence band maximum (VBM) [22]. Liu et al. also revealed that the V_{Sb} vacancy acts as an acceptor, with a defect energy level located 0.15 eV above the VBM.

However, the formation enthalpy taking negative values as the Fermi level approaches the conduction band minimum (CBM) makes the V_{Sb} defect an unlikely candidate for being responsible for the p-type behavior observed in Sb_2Se_3 [120]. In Sb-rich conditions, the formation energies of Se_{Sb} acceptor defects show a significant increase, while the formation energies of donor defects, such as Sb_{Se} and V_{Se} , decrease [22], [109]. It has been revealed by Liu et al. that the V_{Se} vacancy defects largely remain unionized, with defect levels positioned deep within the bandgap [120]. This limits their contribution to the n-type conductivity. Similarly, the Sb_{Se} defects exhibit defect energy levels deep in the bandgap, acting as recombination centres for both holes and electrons. Consequently, achieving intrinsic n-type Sb_2Se_3 is challenging due to these deep trap states, which cause the Fermi level to be pinned in the middle of the bandgap [109].

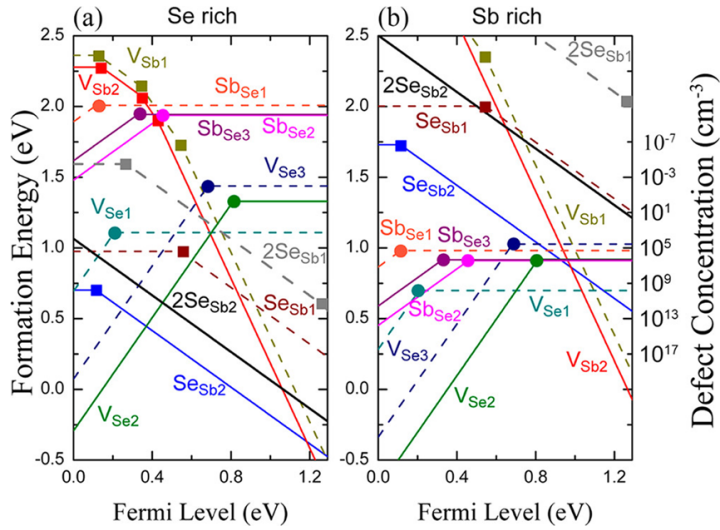


Figure 13. Calculated formation energies and equilibrium concentrations of different defects as functions of the Fermi level in Sb_2Se_3 , under the (a) Se-rich and (b) Sb-rich conditions. Adapted with permission [112]. Copyright 2019, American Chemical Society.

Regarding the defect chemistry of Sb_2S_3 in S-rich conditions, similar to Se_{Sb} in Sb_2Se_3 , S_{Sb} antisite defects are reported to have low formation energies and act as unconventional acceptor defects, contributing to weak p-type conductivity. The V_S , Sb_i , and S_{Sb} are dominant defects with low formation energies under S-rich conditions [121]. Additionally, according to Cai et al., under Sb-rich conditions, there is a competition between V_S vacancies acting as donor defects and Sb_S and V_{Sb} acting as acceptors, as shown in Fig. 14 [113].

This competition results in the Fermi level being pinned slightly closer to the conduction band minimum (CBM), leading to weak n-type conductivity. In contrast, Zhao et al. reveals that both V_{Sb} and V_S are dominant defects in both Sb- and S-rich conditions, with Sb_S and S_{Sb} antisites exhibiting higher formation energies [114].

The reduced presence of antisite defects is attributed to the larger size difference between Sb and S atoms compared to Sb and Se atoms, which affects both the formation energy and activation energy. Zhao et al. further claims that all defects, except for V_S , introduce deep defects [114]. Zhang et al. also reports low formation energies for V_S in both S- and Sb-rich conditions but considers it a deep defect [121]. Overall, the dominant defects (V_S , V_{Sb} , S_{Sb} , and Sb_S) in both S- and Sb-rich conditions exhibit relatively deep defect energy levels within the bandgap [113], [114].

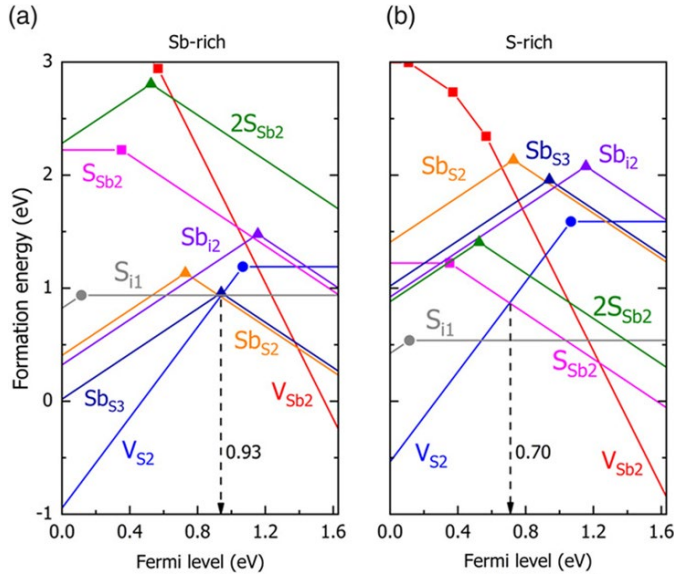


Figure 14. Calculated formation energies of intrinsic point defects in Sb_2S_3 as functions of the Fermi level under the (a) Sb-rich and (b) S-rich conditions. Adapted with permission [113]. Copyright 2019, Wiley-VCH.

Experimental techniques for investigating defects in Sb_2Se_3 and Sb_2S_3

Experimental techniques, such as deep-level transient spectroscopy (DLTS), temperature-dependent admittance spectroscopy (TAS), photoluminescence (PL), and temperature-dependent conductivity measurements, play a crucial role in validating the defect levels proposed by theoretical studies. By employing these experimental methods, researchers can complement the theoretical findings and identify the defects that contribute most significantly to the non-radiative recombination within solar cells. However, it is important to acknowledge that differences in device configurations, deposition methods, and approximations in defect analysis can introduce variations in the energies of defect levels. Nonetheless, the ultimate objective is to enhance our understanding of these underlying defects, which in turn facilitates the development of strategies to mitigate and passivate these defects. Subsequently, a brief description of the defect analysis methods is provided.

Temperature-dependent admittance spectroscopy (TAS)

Temperature-dependent admittance spectroscopy (TAS) entails capacitance response from the free carriers, bulk and possibly interface defects [12]. TAS measurements are generally conducted using an equivalent circuit model that includes a capacitor C , which is a function of angular frequency ω and temperature T , a series resistor R_s and a resistor R in parallel, as depicted in Fig. 15a [122], [123]. While admittance measurements are

analyzed using depletion approximation, where majority carriers follow small alternating current (AC) voltage bias and contribute to depletion capacitance C_d , it does not hold true for thin-film solar cells, which have reasonable concentrations of deep defect states in the band gap [124], [125]. When band bending in the space charge region (SCR) results from a small voltage perturbation, deep defects can be detected if the defect state crosses the Fermi level, as depicted in Fig. 15b [124].

This causes defect states to trap charge and modify the space charge density, thereby contributing to the overall capacitance response [124]. Trap states undergo charge capture and emission until the applied ω of ac bias exceeds the emission rate of the defect state. This marks the relaxation frequency ω_0 , using which the activation energy of a potential defect state can be determined using the following Eq. 1:

$$\begin{aligned}\omega_0(T) &= 2e_t(T) = 2N_{c,v}v_{th}\sigma_{n,p} \exp(-E_A/k_B T) \\ &= 2\xi_0 T^2 \exp(-E_A/k_B T)\end{aligned}\quad (1)$$

where e_t is trap emission rate, $N_{c,v}$ is the effective density of states of a conduction and a valence band, v_{th} is thermal velocity of minority carriers, $\sigma_{n,p}$ is capture cross-section of electron and hole, E_A is activation energy of a defect state with respect to a valence band edge, k_B is Boltzmann constant, and ξ_0 is thermal emission prefactor, which comprises all temperature-independent parameters.

Voltage-dependent TAS can be carried out to distinguish between bulk and interface defects. Different AC voltage bias changes the magnitude of band bending across the SCR. In the case of an interface state, which depends on a quasi-Fermi level crossing the defect level, its relaxation frequency ω_0 will change. This is not the case for a bulk deep defect, which is traditionally assumed to have a homogeneous distribution across the width of the absorber.

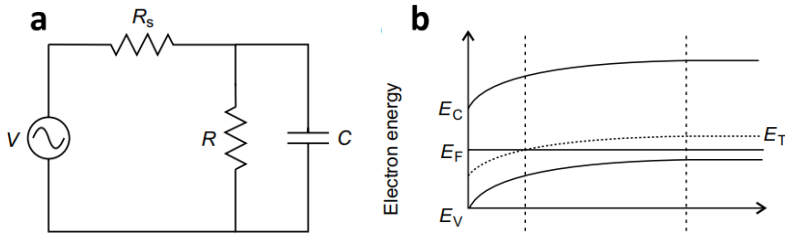


Figure 15. (a) Equivalent circuit model used in admittance measurements. (b) Band bending causes Fermi level E_F to cross with deep trap state E_T . Reproduced with permission [124]. Copyright 2016, Wiley-VCH.

Photoluminescence (PL) spectroscopy

Photoluminescence (PL) spectroscopy is a sensitive, non-destructive technique to study shallow and deep defects in thin-film PV absorber materials. PL is optical radiation that is emitted by the semiconductor material, which results from radiative recombination by photoexcited electron-hole pair [126]. When a monochromatic light source irradiates the surface of the absorber material, strongly localized absorption of light causes the formation of electron-hole pairs, provided that the incident photon energy is greater than the bandgap energy of the absorber material. Electrons excited to the conduction band are at a non-equilibrium state and will return to an equilibrium state in the valence band. In case electron has gained excess energy with respect to bandgap energy, it gives off excess energy to phonon interactions with the crystal lattice and moves to the conduction band edge.

Once the electron falls back to the valence band, it recombines with a hole, resulting in the emission of a photon with energy, which is the energy difference between the two energy states.

There are numerous recombination mechanisms that lead to radiative recombination. In addition to band-to-band transition, excitonic, donor-acceptor pair (DAP), band-to-acceptor, donor-to-band emissions can be distinguished, as depicted in Fig. 16 [127]. DAP transitions can involve shallow acceptors that cannot be detected by TAS [128].

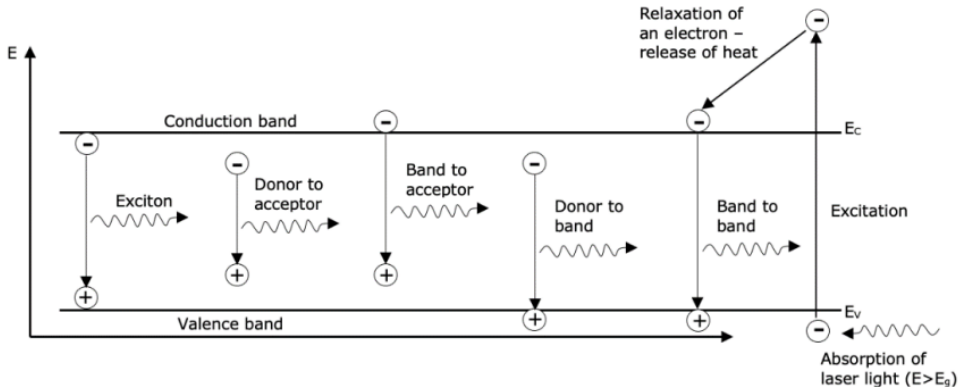


Figure 16. Typical radiative transitions, which can be observed in photoluminescence spectroscopy. Modified with permission [127]. Copyright 2022, TalTech press.

Deep level transient spectroscopy (DLTS)

Deep level transient spectroscopy (DLTS) is a powerful technique to study deep level energy levels and their respective emission rates and densities in thin-film solar cells [11], [129]. Most reports that have investigated deep defects levels in Sb-chalcogenides have adopted DLTS approach with minority carrier injection (inj-DLTS). DLTS differs from admittance in the fact that the device is held at a constant reverse bias during the measurement. In standard DLTS mode, the reverse bias is reduced to allow the traps to refill with majority carriers in thermal equilibrium [129]. Inj-DLTS mode involves a forward bias filling pulse, as depicted in Fig. 17a, which is applied on the diode to inject carriers into the depletion region [129].

Capturing a carrier changes the charge on the defect state, inducing change in the transient junction capacitance. When the filling pulse is relaxed, the carriers will be emitted, as shown in Fig. 17b, resulting in a DLTS signal [130]. Forward bias allows detection of both electrons and holes. For p-type absorbers, donor defects produce negative peaks in the DLTS spectra, while acceptors produce positive peaks [11], [109], [130]. The capture rate of defect states is affected by varying the current in the forward bias pulse [129]. Under forward-bias filling pulse, both electron and acceptors can be detected [11], [129], [130].

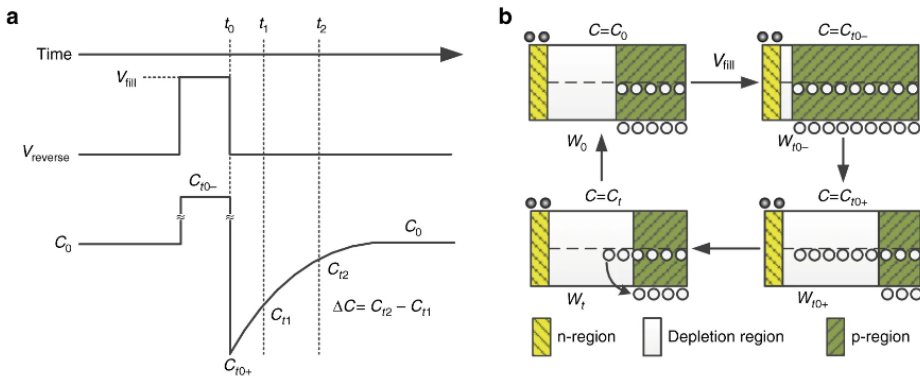


Figure 17. (a) Schematic of mechanisms during DLTS measurement, (b) Diagram showing the capture and emission of holes during the DLTS measurement. Reproduced and modified with permission [11]. Copyright 2018, Springer Nature.

Experimental reports of defects in Sb_2Se_3 thin films and crystals

Wen et al. conducted a DLTS analysis on RTE- and VTD-fabricated Sb_2Se_3 devices and revealed deep defect energy levels, which matched well with defect levels predicted by Savory et al. in a theoretical DFT study [22]. Two hole traps at energy levels of 0.48–0.49 eV and 0.71–0.74 eV above VBM and one electron trap at 0.60–0.61 eV below CBM were detected in both RTE- and VTD-processed Sb_2Se_3 films. The first two energy levels were assigned to acceptor defects V_{Sb} and Se_{Sb} , the electron trap was attributed to a donor defect Sb_{Se} [11]. Furthermore, defect densities in the order of 10^{14} cm^{-1} were measured in VTD- Sb_2Se_3 films, which is one order of magnitude smaller than in RTE- Sb_2Se_3 films [11]. Hobson et al. conducted a standard DLTS analysis on n-type bulk Sb_2Se_3 crystals and Sb_2Se_3 thin film solar cells. Notably, three activation energy levels of 0.35–0.37 eV, 0.45–0.46 eV and 0.69 eV below CBM were found in both sample types. Although these defect levels were not identified, the identification of common deep level defects suggests there is minimal impact from the grain boundaries on the defect composition; the Sb_2Se_3 thin films act as if they are single crystals [131]. Ma et al. performed DLTS analysis on Sb_2Se_3 devices fabricated using spin-coating technique. DLTS spectra of the best 5.23%-efficient device showed three energy levels of 0.48 eV, 0.710eV, and 0.63 eV [132]. The first two were hole trap energies, which were assigned to the V_{Sb} and Se_{Sb} according to Savory et al. DFT study [22]. The third energy level was an electron trap, which was assigned to the Sb_{Se} defect. Recently, Duan et al. employed DLTS on the Sb_2Se_3 devices fabricated by injection vapor deposition (IVD), CSS, and thermal co-evaporation (CoE). All three devices showed an activation energy at 0.54–0.57 eV below the CBM [10], which was attributed to a Se_{Sb2} defect. Stolaroff reported a DFT study, which predicted Se_{Sb2} defect to have energy level at 0.60 eV below CBM [133]. The same study was used to assign defect energy level of 0.53 above VBM to a Se_{Sb1} defect, which was detected only in the co-evaporated Sb_2Se_3 [10].

Liu et al. studied Sb_2Se_3 devices with temperature-dependent conductivity measurement. Thermally evaporated Sb_2Se_3 film, which had had been subjected to in situ selenization, revealed an activation energy of 0.107 eV. Theoretical calculations presented in the study attribute this energy to a shallow acceptor defect Se_{Sb} [120]. Chen et al. employed TAS and temperature-dependent conductivity measurements and detected activation energy levels of 0.10 eV and 0.11 eV, respectively [44]. Both energy levels were assumed to originate from the same point defect, which shows a defect

density above 10^{15} cm^{-3} . According to the first-principles calculations study conducted by Huang et al, such defect level could well correspond to the Se_{Sb} acceptor defect, which was predicted to have low formation energy and hence contribute to the intrinsic p-type conductivity of Sb_2Se_3 [112]. Hu et al. has conducted several TAS studies on Sb_2Se_3 solar cells, reporting three activation energy levels of 0.30–0.40 eV, 0.20–0.60 eV, and 0.50–0.60 eV above VBM [134]–[136]. Only the highest activation energy level was attributed to an interface defect. Tang et al. performed TAS analysis on sputtered Sb_2Se_3 films, which had been selenized at 420 °C and 380 °C, revealed two activation energy levels of 0.46 eV and 0.50 eV above VBM, respectively [137]. According to the first-principles calculations study reported by Liu et al. [120], the respective activation energies were assigned to donor defect V_{Se} and Sb_{Se} [137].

Grossberg et al. analyzed Sb_2Se_3 polycrystals with PL and detected three PL bands positioned at 0.94 eV (PL3), 1.10 eV (PL2), and 1.24 eV (PL1). Thermal activation energies of 0.09 eV, 0.07 eV, and 0.03 eV were derived for the respective PL bands. While PL1 and PL3 bands were attributed to donor-acceptor pair (DAP) recombination, PL2 band was assumed to be related to grain boundaries [138]. Furthermore, PL1 band could have arisen from a distant DAP, with shallow acceptor Se_{Sb} being involved [44], [112], [138]. PL3 band alluded to a deep donor-deep acceptor (DD-DA) pair recombination. A comprehensive list including all the reported Sb_2Se_3 defects is provided in Table 2.

Experimental reports of defects in Sb_2S_3 thin films and crystals

Unlike Sb_2Se_3 films and devices, which have been extensively studied for defect analysis, there is a noticeable scarcity of studies regarding defect characterization in Sb_2S_3 . This disparity can be attributed to the lower conductivity of Sb_2S_3 , leading to even higher deep defect densities compared to Sb_2Se_3 . Nonetheless, there have been attempts with DLTS and TAS to elucidate the defect composition of Sb_2S_3 . Lian et al. conducted optical DLTS (O-DLTS) analysis on thermally evaporated Sb-rich and Se-rich Sb_2S_3 films [93]. Both Sb-rich and Se-rich Sb_2S_3 films were considered n-type without further elaboration. Three electron traps were detected in Sb-rich Sb_2S_3 at energy levels of 0.31 eV, 0.60 eV, and 0.69 eV below the CBM, and were assigned to Sb_i , V_s , and Sb_s defects. Se-rich Sb_2S_3 films showed two hole traps with energies of 0.64 eV and 0.71 eV above the VBM, which were attributed to V_{Sb} and S_{Sb} defects [93]. Zhang et al. performed DLTS on Sb_2S_3 films grown onto TiO_2 ETL via seed screening. In total, four negative DLTS peaks were ascribed to hole traps with energies of 0.32 eV, 0.47 eV, 0.58 eV, and 0.78 eV above VBM; the lowest activation energy was assigned to the V_{Sb} defect, while the remaining three were attributed to Sb_s antisite defects at different atomic sites [106]. Wang et al. reported DLTS analysis on VTD-fabricated Sb_2S_3 films, which were subjected to Sb_2Se_3 post-treatment. An electron trap energy of 0.74 eV below CBM was detected in an untreated Sb_2S_3 ; the defect energy level was ascribed to the V_s defect [139]. More recently, DLTS analysis was performed on n-type Sb_2S_3 solar cells deposited with hydrothermal method. Wu et al. revealed two hole traps with energies of 0.58 eV and 0.70 eV above VBM, which were assigned to V_{Sb} and S_{Sb} defects, respectively [140]. Qin et al. performed TAS analysis on VTD-fabricated Sb_2S_3 devices, deposited at different working pressures. Different samples with low efficiencies of 0.67–0.86% showed a potential defect signature between the energy range of 0.10–0.15 eV above VBM [141].

Table 2. Overview of experimentally determined defects in Sb_2Se_3 thin films and crystals.

Analysis method	Defect type	Activation energy (eV)	Assignment	Defect density (cm^{-3})	PCE (%)	Ref.
DLTS	Hole trap	0.48–0.49	V_{Sb}	1.2×10^{15}	7.60	[11]
	Hole trap	0.71–0.74	Se_{Sb}	1.1×10^{14}		
	Electron trap	0.60–0.61	Sb_{Se}	2.6×10^{14}		
DLTS	Hole trap	0.48	V_{Sb}	6.1×10^{14}	5.23	[132]
	Hole trap	0.71	Se_{Sb}	1.0×10^{15}		
	Electron trap	0.63	Sb_{Se}	3.6×10^{15}		
DLTS	Electron trap	0.38	-	$(1.0-1.1) \times 10^{14}$	5.60	[131]
	Electron trap	0.46	-	$(4.2-8.7) \times 10^{14}$		
	Electron trap	0.69	-	$(1.2-2.6) \times 10^{15}$		
DLTS	Electron trap	0.21	-	2.7×10^{14}	10.12	[62]
	Hole trap	0.53	Se_{Sb_2}	3.5×10^{14}	3.96	
	Electron trap	0.54–0.57	Se_{Sb_1}	8.0×10^{14}	10.12	
	Electron trap	0.59	-	4.3×10^{14}	9.31	
Conductivity	Acceptor	0.11	Se_{Sb}	-	5.46	[120]
Conductivity	Acceptor	0.11	Se_{Sb}	-	-	[44]
TAS	Acceptor	0.10	Se_{Sb}	1.3×10^{15}	-	
TAS	Acceptor	0.46	V_{Se}	9.3×10^{15}	6.06	[137]
	Acceptor	0.50	Sb_{Se}	2.1×10^{16}	2.26	
TAS	Acceptor	0.18	V_{Sb}	8.6×10^{15}	6.15	[142]
	Acceptor	0.53	Sb_i	4.2×10^{16}		
	Acceptor	0.57	Se_{Sb}	2.5×10^{16}		
PL	DAP	0.03	V_{Sb}	-	-	[138]
	-	0.07	-	-	-	
	DD-DA	0.09	-	-	-	

There are only a few PL studies reported on Sb_2S_3 films. Medina-Montes et al. reported room-temperature PL measurement on Sb_2S_3 , which revealed four PL bands positioned at 2.38 eV, 2.57 eV, 2.85 eV, and 3.43 eV, but did not elaborate on the potential origin of the PL bands [143]. Uslu et al. studied $Sb_2(Se_{1-x}S_x)$ solid solutions with PL and reported a single PL band of 1.73 eV for an amorphous Sb_2S_3 crystal, without providing any further analysis [144]. The lack of PL studies suggests the presence of significant non-radiative recombination not only in Sb_2Se_3 and Sb_2S_3 thin films but also in their crystals. A comprehensive list including all the reported Sb_2S_3 defects is provided in Table 3.

Table 3. Overview of experimentally determined defects in Sb_2Se_3 thin films and crystals.

Analysis method	Defect type	Activation energy (eV)	Assignment	Defect density (cm^{-3})	PCE (%)	Ref.
DLTS	Electron trap	0.31	Sb_i	$(3.75-5.63) \times 10^{14}$	6.20	[93]
		0.60	V_s	$(1.57-3.31) \times 10^{15}$		
	Electron trap	0.69	Sb_s	$(1.38-2.01) \times 10^{15}$	5.00	
		0.64	V_{Sb}	$(0.45-1.58) \times 10^{15}$		
	Electron trap	0.71	S_{Sb}	$(6.71-8.57) \times 10^{14}$		
	Hole trap					
DLTS	Hole trap	0.32	V_{Sb}	1.15×10^{14}	4.80	[106]
	Hole trap	0.47	Sb_{S1}	1.55×10^{14}		
	Hole trap	0.58	Sb_{S2}	4.37×10^{14}		
	Hole trap	0.78	Sb_{S3}	5.59×10^{14}		
DLTS	Electron trap	0.74	V_s	$5.52E+14$	2.70	[139]
DLTS	Hole trap	0.58	V_{Sb}		6.27	[140]
	Hole trap	0.70	S_{Sb}		6.82	
TAS	Acceptor	0.10–0.15	-	$(0.78-2.73) \times 10^{14}$	0.86	[141]

Future outlook for mitigating defects and enhancing conductivity in Sb_2Se_3 and Sb_2S_3 thin films

Theoretical and experimental findings have revealed a substantial presence of defects in both Sb_2Se_3 and Sb_2S_3 thin films. Consequently, the low conductivities observed in Sb_2Se_3 and Sb_2S_3 thin films, as well as the low V_{OC} values in their corresponding PV devices, can be attributed to defect compensation and non-radiative recombination through deep defect states. While deep defects are known to impede significant p- or n-type doping, implementing appropriate doping and defect passivation strategies can still enhance the free carrier density and mitigate the formation of deep defects by forming defect complexes between intrinsic defects and dopants, thereby lowering their energy levels.

Several extrinsic dopants have been proposed, with tin (Sn) and lead (Pb) identified as effective p-type dopants [145], [146], and copper (Cu), tellurium (Te), and chlorine (Cl) as effective n-type dopants for Sb_2Se_3 thin films [47], [147], [148]. Similarly, carbon (C), cesium (Cs), titanium (Ti), zinc (Zn), and copper (Cu) have enhanced the conductivities of n-type Sb_2S_3 thin films by passivating deep V_{Sb} defects [6]. Additionally, post-deposition annealing in selenium (Se) and oxygen (O_2) atmospheres has exhibited an increase in p-type conductivity in Sb_2Se_3 thin films, attributed to the passivation of deep V_{Se} and Sb_{Se} defects [109]. Therefore, should an optimal doping concentration or suitable conditions for post-deposition treatment be identified, it has the potential to significantly advance the performance of Sb_2Se_3 and Sb_2S_3 devices.

The comparison of defect studies revealed significant discrepancies between the reported activation energies and the assignment of specific types of defects. These inconsistencies underscore the complexity of the defect chemistry in Sb_2Se_3 and Sb_2S_3 and the challenges associated with accurately identifying and characterizing the defect states. Further research efforts are necessary to gain a comprehensive understanding of the defect structure of Sb_2Se_3 and Sb_2S_3 , which will be instrumental in the development of effective defect passivation strategies.

Summary of the literature review and the aims of the study

The literature review can be summarized as follows:

1. Sb-chalcogenides Sb_2X_3 [$X = S, Se, S_xSe_{1-x}$] are IV-V group compounds, which have emerged as highly promising absorber materials for next-generation PV applications. This is primarily attributed to their excellent optoelectronic properties, which include appropriate bandgap energies in the range of 1.1–1.8 eV and high photoabsorption coefficient exceeding 10^4 cm^{-1} .
2. Both Sb_2Se_3 and Sb_2S_3 have a single orthorhombic crystal phase and a simple binary composition, comprising abundant chemical elements, which ensures sustainable supply of the materials and contributes to their economic viability. Additionally, these compounds exhibit low toxicity, enhancing their desirability in terms of environmental impact and human health considerations. Additionally, low melting points and high saturated vapor pressures of Sb_2Se_3 and Sb_2S_3 compounds facilitate the processing of Sb_2Se_3 and Sb_2S_3 thin films using rapid and low-cost physical vapor deposition (PVD) methods, such as VTD, CSS, and RTE.
3. Orthorhombic crystal structure induces Q–1D crystal growth and highly anisotropic properties in the Sb_2X_3 films. The Q–1D ribbons are composed of $[Sb_4X_6]_n$ atomic chains, which stack along the [001] crystal direction. While strong covalent Sb–X bonds hold ribbons together, there are only weak vdW forces between the ribbons. Consequently, carrier transport depends strongly on the grain orientation, with the most efficient transport occurring along the [001] direction. Weak interactions between the ribbons also result in benign grain boundaries, which lead to extensive recombination in the conventional 3D photovoltaic absorber materials.
4. The performance of Sb_2Se_3 and Sb_2S_3 PV devices is significantly influenced by the orientation of Sb_2Se_3 and Sb_2S_3 films. To address this challenge, several strategies have been employed to control the grain orientation and microstructure of Sb_2Se_3 and Sb_2S_3 . These strategies encompass optimizing the processing conditions, seed screening, selecting suitable ETL layer, and implementing post-deposition treatments. Systematic investigation into these strategies is required for the CSS deposition process to achieve compact Sb_2Se_3 and Sb_2S_3 films with optimal grain orientation.
5. High open-circuit voltage (V_{oc}) deficit Sb_2Se_3 and Sb_2S_3 solar cells is a significant hurdle in attaining theoretical efficiency values. The V_{oc} losses can be partly attributed to the presence of deep defects within the Sb_2Se_3 and Sb_2S_3 , as predicted by theoretical investigations. Asymmetric coordination of Sb and X atoms in the $[Sb_4X_6]_n$ units complicates the defect structures of Sb_2Se_3 and Sb_2S_3 , giving rise to multiple defect levels for the same type of defects. Notably, defects with energy levels located deep within the bandgap are expected to dominate and occur in high concentrations due to their low formation energies.
6. Experimental characterization of even the best-reported Sb_2Se_3 and Sb_2S_3 solar cells has provided evidence of high deep defect densities of 10^{14} – 10^{15} and low carrier densities of 10^{13} – 10^{14} cm^{-3} . Various defect characterization methods, including temperature-dependent conductivity, DLTS, TAS, and PL, have been employed to investigate the defects in Sb_2Se_3 and Sb_2S_3 . Comparison of these studies reveals significant discrepancies between the reported activation energies and the assignment of specific types of defects. These inconsistencies highlight the complexity of the defect chemistry in Sb_2Se_3 and Sb_2S_3 and the challenges

associated with accurately identifying and characterizing the defect states. Further research efforts are necessary to gain a comprehensive understanding of the defect structure of Sb_2Se_3 and Sb_2S_3 .

Based on the literature review and the mentioned technological challenges, the hypotheses of this thesis are as follows:

1. Optimization of grain morphology and orientation will allow for the fabrication of high quality Sb_2Se_3 and Sb_2S_3 absorber thin films, which improve the carrier transport and collection, and lead to efficient solar cell device.
2. Characterizing defects and recombination pathways in Sb_2Se_3 and Sb_2S_3 thin films and PV devices provides valuable insight into the defect chemistry of the respective thin films and enables for the development and optimization of doping and defect passivation strategies, which are important steps for improving the future device performance.

Based on the literature review, this thesis has the following aims:

1. To establish an effective growth strategy for the CSS deposition of Sb_2Se_3 and Sb_2S_3 thin films, which involves optimizing the processing conditions, seed screening, and identifying suitable electron transport layer.
2. To systematically investigate the influence of CSS substrate temperature on the microstructure and grain orientation of Sb_2Se_3 and Sb_2S_3 thin films and the performance of PV devices utilizing the respective Sb_2Se_3 and Sb_2S_3 absorbers.
3. To conduct a detailed analysis of crystal orientations in Sb_2Se_3 thin films through measurement of pole figures by XRD and the generation of orientation distribution maps using EBSD to refine the understanding of determining grain orientation in both the Sb_2Se_3 and Sb_2S_3 thin films.
4. To improve the knowledge of defect chemistry of Sb_2Se_3 and Sb_2S_3 using TAS analysis.
5. To investigate prevalent recombination mechanisms in Sb_2Se_3 and Sb_2S_3 PV devices.

2 Experimental

This chapter provides a summary of the fabrication steps of Sb_2Se_3 and Sb_2S_3 thin film solar cells, as well as the experimental analysis methods utilized in articles I–III.

2.1 Fabrication of Sb_2Se_3 and Sb_2S_3 PV devices

Glass/FTO substrate

Fluorine-doped tin oxide (FTO) coated glass substrates make the bottom layer in the superstrate device architecture. Purchased from Sigma-Aldrich, a 200 nm-thick FTO has a sheet resistance of $<20 \Omega \text{ sq}^{-1}$. Substrates are subject to a standardized preparation procedure. Glass/FTO substrates are first cut into dimensions of 25 x 25 x 2 mm. Substrates are then placed into a degreasing solution for 2–3 hours. Degreasing solution contains 10 g of potassium dichromate ($\text{K}_2\text{Cr}_2\text{O}_7$), 100 mL of concentrated sulfuric acid (H_2SO_4), and 10 mL of deionized water [149]. After that, the substrates are rinsed, boiled in distilled water, and dried with a dryer.

TiO₂ thin film deposition by ultrasonic spray pyrolysis (USP)

In Article I and II, TiO_2 films with 100–200 nm thickness were deposited onto FTO by USP at 350 °C using a precursor solution of 0.1 M titanium (IV) isopropoxide (TTIP) and 0.4 M acetylacetone (AcacH) dissolved in ethanol [91]. Post-deposition treatment of TiO_2 films involved two 30-minute annealing steps: first under vacuum at 120 °C and then in air at 450 °C.

CdS thin film deposition by close-spaced sublimation (CSS)

In article I and III, CdS thin films with 80–100 nm thickness were deposited onto FTO by CSS at source and substrate temperatures of 650 °C and 350 °C, respectively. A commercially available CdS powder (Sigma-Aldrich) was used with 5N (99.999%) purity. CSS reactor was under high vacuum of 10^{-6} Torr.

CdS thin film deposition by chemical bath deposition (CBD)

In Article I, CdS ETL films with 80–100 nm thickness were deposited onto FTO by chemical bath deposition (CBD). A water solution containing 1 mM CdSO_4 , 10 mM thiourea (TU), 0.2 M NH_4OH , 30 mM $(\text{NH}_4)_2\text{SO}_4$, and 0.1 μM of NH_4Cl was used in the chemical bath [150], [151]. Film deposition was carried out at solution temperature of 85 °C and stirring speed of 500 rpm. Post-deposition treatment involved thermal annealing at 120 °C under vacuum for 1 h.

Sb₂Se₃ and Sb₂S₃ thin film deposition by CSS

Sb_2Se_3 and Sb_2S_3 thin films were deposited using independent CSS systems (see Fig. 8 in the literature overview) employing source powders of Sb_2Se_3 and Sb_2S_3 purchased from Sigma-Aldrich with a purity of 99.999% (5N). The experimental details of Sb_2Se_3 and Sb_2S_3 film deposition in articles I and II are summarized in Table 4. A seed layer comprised of an amorphous Sb_2Se_3 film, with <100 nm thickness, which was deposited at CSS substrate temperature of 300 °C prior to the main layer deposition.

Back contact deposition by thermal evaporation

Back contacts were deposited from Au (Alfa Aesar) by thermal evaporation (TE) to complete Sb_2S_3 and Sb_2Se_3 solar cells. A mica mask was placed on the surface of the absorber to obtain contacts with 25 mm^2 area. The TE system was under a high vacuum of 10^{-6} Torr. The PV device stacks obtained after adding the back contact are presented in Fig. 18.

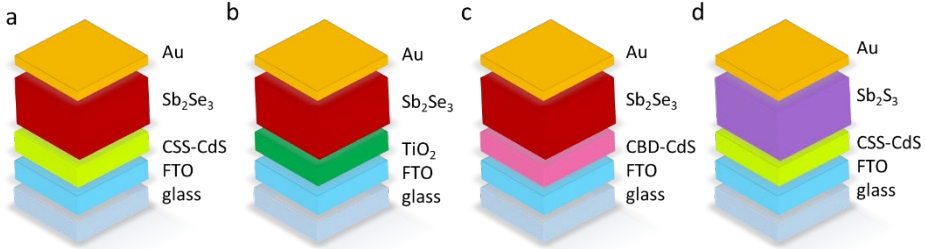


Figure 18. Device stacks used in the studies: (a) FTO/CSS-CdS/ Sb_2Se_3 /Au, (b) FTO/ TiO_2 / Sb_2Se_3 /Au, (c) FTO/CBD-CdS/ Sb_2Se_3 /Au (from articles I and II), and (d) FTO/(CSS-)CdS/ Sb_2S_3 /Au (from article III).

Table 4. Experimental details of Sb_2Se_3 and Sb_2S_3 thin film deposition by CSS. The table outlines the substrate, inclusion of seed layer, CSS source and substrate temperatures, and the final PV device stack.

Article	Substrate	Source powder	Seed layer	Absorber deposition parameters			Solar cell stack
				Vacuum level, Torr	T_{source} , °C	T_{sub} , °C	
I	glass/FTO/CSS-CdS	Sb_2Se_3 99.999 % purity (5N) Sigma-Aldrich	+	10^{-6}	490	300–450	glass/FTO/CSS-CdS/ Sb_2Se_3 /Au
	glass/FTO/ TiO_2						glass/FTO/ TiO_2 / Sb_2Se_3 /Au
	glass/FTO/CBD-CdS						glass/FTO/CBD-CdS/ Sb_2Se_3 /Au
II	glass/FTO/ TiO_2		+		490	450	glass/FTO/ TiO_2 / Sb_2Se_3 /Au
III	glass/FTO/CSS-CdS	Sb_2S_3 99.999 % purity (5N) Sigma-Aldrich	-		450	260–400	glass/FTO/CSS-CdS/ Sb_2S_3 /Au

2.2 Sb₂Se₃ and Sb₂S₃ thin film characterization

Morphology of Sb₂S₃ and Sb₂Se₃ thin films (Article I–III) were analyzed by Zeiss EVO-MA15 scanning electron microscope (SEM) equipped with a Zeiss HR FESEM Ultra 55 system. Crystal structure was characterized by measuring X-ray diffraction (XRD) patterns of glass/FTO/CdS/Sb₂S₃ (Article III), glass/FTO/CdS/Sb₂Se₃ (Article I), and glass/FTO/TiO₂/Sb₂Se₃ (Articles I and II) stacks using a Rigaku Ultima IV diffractometer with Cu K α radiation ($\lambda = 1.54 \text{ \AA}$, 40 kV, 40 mA). XRD patterns were analyzed with a Rigaku PDXL2 software, with peaks indexed according to powder diffraction file (PDF) data issued by the Joint Committee on Powder Diffraction Standards (JCPDS).

Texture analysis was performed on glass/FTO/TiO₂/Sb₂Se₃ stacks (Article II) by PANalytical MRD X-ray diffractometer equipped with Eulerian cradle employing two-axis scans along ϕ and χ in increments of 5° each. The intensity distribution was recorded along full circles ($\phi = 0^\circ$ to 360°) and at sample tilts χ ranging between 0° and 85°. Texture analysis was carried out by René Schwiddessen at Helmholtz-Zentrum Berlin for Materials and Energy. Additionally, electron backscatter diffraction (EBSD) orientation maps were acquired for a glass/FTO/TiO₂/Sb₂Se₃ stack (Article II) using a Zeiss UltraPlus SEM equipped with an Oxford Instruments Symmetry EBSD detector. The measurements were conducted at a beam energy of 20 keV and a beam current of about 6nA, by use of the acquisition and evaluation software AZtec. Dr. Daniel Abou-Ras from Helmholtz-Zentrum Berlin for Materials and Energy carried out the EBSD mapping on the Sb₂Se₃ film.

Low-temperature photoluminescence (PL) measurements from glass/FTO/CdS/Sb₂S₃ stacks were conducted using a diode-pumped Nd:YAG solid state laser with wavelength of 266 nm, pulse width of 0.6 ns, and repetition rate of 19 kHz. The maximum average power was approximately 3 mW, maximum peak power density was approximately 276.5 kW cm⁻². PL signal was detected using a 0.5 m focal length Andor SR-500i monochromator and thermoelectrically cooled InGaAs detector IGA-030-TE2-H of Electro-Optical Systems Inc that is equipped with a Hamamatsu R632 photomultiplier tube. The low-temperature PL measurements and analysis were carried out by Ramunas Nedzinskas and Rokas Kondrotas from the Lithuanian State Research Institute Center for Physical Sciences and Technology.

Ionization energies of CdS and Sb₂S₃ thin films, presented in Article III, were determined with photoelectron emission spectroscopy (PES), by using an ENERGETIQ Laser Driven Light Source (LDLS EQ-99) white light source, a Spectral Products DK240 1/4 m monochromator and a Keithley 617 electrometer. The PES measurements and analysis were conducted by Raitis Gržibovskis and Aivars Vembris from the University of Latvia.

2.3 Sb₂Se₃ and Sb₂S₃ PV device characterization

I–V curves of Sb₂Se₃ and Sb₂S₃ devices were measured in ambient air at room temperature using an AUTOLAB PGSTAT 30 combined with an Oriel class A solar simulator 91159A (100 mW cm⁻², AM1.5) (Article I and II) and a Wavelabs LS-2 LED solar simulator (100 mW cm⁻², AM1.5). Temperature-dependent I–V (I–V–T) curves in articles I and III were measured with a KEITHLEY 2400 SourceMeter under 100 mW cm⁻² illumination, with Sb₂S₃ and Sb₂Se₃ devices mounted on a Janis closed-cycle He cryostat. External quantum efficiency (EQE) spectra were measured for Sb₂S₃ and Sb₂Se₃ devices (Articles I–III) with a monochromatized light source (Newport 300 W Xenon lamp, Newport Cornerstone 260 monochromator), a Merlin digital lock-in detector and a factory-calibrated Si reference detector.

Capacitance-voltage (CV) profiling and TAS measurements were carried out at two different locations. CV profiles and $C-f-T$ curves were measured for the best Sb_2Se_3 (Article I) and Sb_2S_3 devices (Article III) using a Wayne Kerr 6500B impedance meter. Capacitance was derived and calculated from recorded impedance Z and phase angle θ values. CV profiles were obtained at room temperature from DC voltage scans in the range of -0.3 V to $+0.2$ V. Admittance measurements were measured at 0 V bias and in the temperature range of 20–320 K ($\Delta T = 10$ K). Abovementioned $J-V-T$, CV, and $C-f-T$ measurements were carried out by Dr. Raavo Josepson at Tallinn University of Technology. Analysis on the measurements, which are presented in Article I, were performed by Dr. Erki Kärber from Tallinn University of Technology. CV profiling and admittance measurements presented in Publication II were performed with a HP 4284 LCR meter. CV profiles were obtained at room temperature with frequencies ranging from 0.5 kHz to 20 kHz; DC bias was scanned from -0.3 V to 0 V. Admittance measurements were performed in a R-X (resistance–reactance) mode at 0 V bias and 30 mV AC voltage; temperature was varied from 80 K to 320 K in the frequency range of 100 kHz to 1 MHz. The capacitance measurements, which are presented in Publication II, were conducted at Helmholtz-Zentrum Berlin for Materials and Energy.

3 Results and discussion

This section highlights the key findings obtained in Publications I–III. Section 3.1 focuses on the fabrication and characterization of Sb_2Se_3 thin film solar cells, while Section 3.2 delves into the fabrication and characterization of Sb_2S_3 thin film solar cells.

3.1 Developing growth strategy to fabricate Sb_2Se_3 thin films solar cells by CSS

3.1.1 The effect of CSS substrate temperature on Sb_2Se_3 film microstructure and grain orientation

Given the previous knowledge within our research group on CdTe thin film processing, the CSS processing conditions were adapted to deposit Sb_2Se_3 films. Implementing the right growth strategy necessitates the optimization of processing parameters, such as source temperature, substrate temperature, and deposition time. Initial trials showed that a source temperature of 450 °C is sufficient for inducing sublimation and consequent vapor flux for thin film deposition with growth rate at around $1 \mu\text{ min}^{-1}$. This doctoral study focused on determining the optimal substrate temperature for high-performance Sb_2Se_3 thin films. While source temperature was held constant at 490 °C, substrate temperatures were varied in the range of 300–450 °C. To optimize the substrate temperature, Sb_2Se_3 films were deposited on CdS/FTO/glass substrates. CSS-deposited CdS was selected as the ETL since its processing has been previously established for CdTe thin film solar cells.

Figure 19 displays top-down and cross-sectional SEM images, which reveal a strong impact of the substrate temperature on the grain structure of Sb_2Se_3 films. Fig. 19a shows that Sb_2Se_3 films deposited at 300 °C (Sb_2Se_3 -300 °C) exhibit highly dispersed and porous ribbon-like structures. Deposition at 350 °C leads to denser absorber films (Sb_2Se_3 -350 °C) with larger grain size and more homogeneous distribution, as seen in Fig. 19b. Increase of substrate temperature to 400 °C further enlarges the grain size, as seen in Fig. 19c, also making absorber films (Sb_2Se_3 -400 °C) more compact at the interface between Sb_2Se_3 and CdS; the faceted grains with sharp edges increase the surface roughness and give rise to open column boundaries near the rear surface. As shown in Fig. 19d, substrate temperature of 450 °C results in films (Sb_2Se_3 -450 °C) with largest grains, which are columnar, closely packed, and with smooth crystal facets.

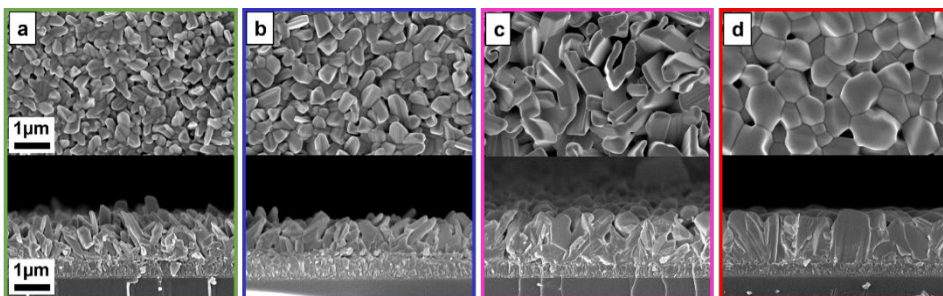


Figure 19. Top-down and cross-sectional SEM images of Sb_2Se_3 films deposited by CSS onto CdS/FTO/glass substrates at substrate temperatures of (a) 300 °C, (b) 350 °C, (c) 400 °C, and (d) 450 °C.

Figure 20a shows XRD patterns of CSS-processed Sb_2Se_3 absorber layers deposited at substrate temperatures in the range of 300–450 °C onto CdS/FTO/glass substrates. Strong reflections at 2θ values of 28.2°, 31.2°, 32.2° can be indexed to (211), (221), (301) crystal planes, which are characteristic of an orthorhombic Sb_2Se_3 crystal structure with Pbnm space group symmetry (JCPDS Card No. 15–0861). Reflections of (020) and (120) peaks show low intensity. No secondary phases can be found.

Texture coefficient (TC) analysis is a common method for evaluating texture in the Q–1D Sb_2Se_3 films. By definition, a texture coefficient (TC) value larger than 1 indicates a preferred orientation of a hkl reflection when compared to the random distribution of grains in a powder [152]. The TC values are calculated by Equation (2):

$$TC(hkl) = \frac{I(hkl)}{I_0(hkl)} \times \left[\frac{1}{N} \sum_{i=0}^N \frac{I(h_i k_i l_i)}{I_0(h_i k_i l_i)} \right]^{-1} \quad (2)$$

where $I(hkl)$ represents the experimentally obtained intensity for a given reflection with hkl indices, $I_0(hkl)$ corresponds to the reference intensity for the corresponding reflection acquired from the JCPDS Card No. 15–0861, and N denotes the number of reflections considered in the calculations [152].

In Fig. 20b, it can be observed that the TC values of (hk0) planes remain unchanged regardless of the substrate temperature. However, a significant increase in the TC values of (hk1) planes is evident at substrate temperatures of 400 °C and 450 °C. This observation suggests that the higher substrate temperature facilitated the growth of Sb_2Se_3 grains more prominently along the [001] crystal direction.

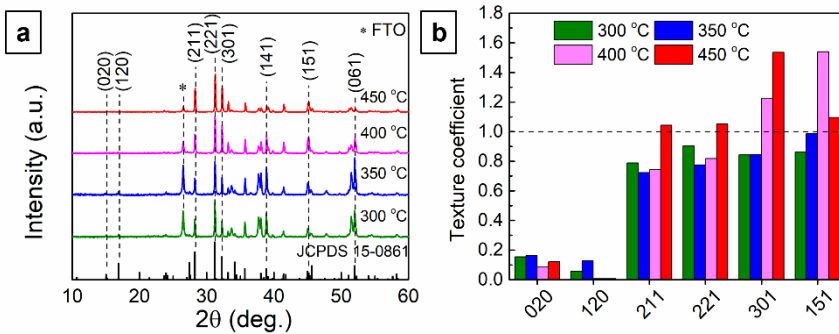


Figure 20. (a) XRD patterns of Sb_2Se_3 absorber films deposited by CSS at substrate temperatures of 300–450 °C onto CdS/FTO/glass substrates. (b) Texture coefficient (TC) values calculated for prominent (hk0) and (hk1) crystal planes in Sb_2Se_3 films.

As observed, a higher substrate temperature resulted in an increased texture along the [001] direction, as deduced from the texture coefficient (TC) analysis of X-ray diffraction (XRD) patterns, and facilitated the growth of larger columnar grains, as evidenced by scanning electron microscopy (SEM) images. These complementary phenomena can be explained by considering the nucleation density and grain coalescence rate, which are strongly influenced by the temperature gradient between the source and substrate, as well as the supersaturation of the vapor phase in the CSS reactor.

Lower substrate temperatures result in higher source-substrate temperature gradients, leading to a greater degree of supersaturation near the substrate surface, thereby promoting a higher nucleation density. Additionally, as adatom mobility and surface diffusion are proportional to the substrate temperature, substrate temperatures of 300 °C and 350 °C yielded more porous films comprising dispersed grains of different sizes. Conversely, a higher substrate temperature of 400 °C reduced the degree of supersaturation on the substrate surface, resulting in fewer nucleation sites. The increased adatom mobility and surface diffusion promoted the local epitaxial growth of small grain islands at these nucleation sites. Grain coarsening occurred at the grain boundaries (GBs), during which neighboring grains with large surface-to-volume ratios coalesced into larger grains. At a substrate temperature of 450 °C, these growth phenomena were even more pronounced, leading to complete coalescence of relatively large islands due to the high rate of material transfer between islands. Atom migration from the GBs likely occurred not only during coalescence but also throughout the film-thickening process.

The final grain orientation is determined by the grain coarsening and GB movement, which reduce the total free energy of the system. This essentially promotes the growth of GBs along the vertical (100) and (010) planes, known to possess the lowest surface energy, thereby facilitating grain growth along the [001] direction. Ultimately, employing a substrate temperature of 450 °C resulted in closely packed Sb₂Se₃ films with large columnar grains and the stronger presence of (211) and (221) planes, signifying an improvement in texture along the [001] direction.

3.1.2 The effect of Sb₂Se₃ film microstructure and grain orientation on the Sb₂Se₃ device performance

At the time of this study, several groups had reported improved efficiencies attributed to enhanced texture in the [001] direction [11], [12], [17], [46], [59]. While the Sb₂Se₃ device with substrate configuration utilized nanostructured Sb₂Se₃ arrays, achieving 9.2% efficiency [12], superstrate devices had achieved higher performance by employing Sb₂Se₃ films with compact and large grain morphologies [11], [59]. In our investigation, we fabricated a series of glass/FTO/CdS/Sb₂Se₃/Au devices using Sb₂Se₃ films deposited at various substrate temperatures to examine the influence of the Sb₂Se₃ film microstructure and grain orientation on the device properties.

Figure 21a illustrates the J-V curves of Sb₂Se₃ solar cells, with Sb₂Se₃ absorbers deposited at various substrate temperatures ranging from 300 °C to 450 °C. It is evident that the Sb₂Se₃-300 °C and Sb₂Se₃-350 °C devices exhibited negligible performance. The low photocurrent can be attributed to the low-quality of the Sb₂Se₃ absorber, characterized by a high density of voids that increase shunting pathways across the junction, as observed in Figure 21a and 21b.

In contrast, the Sb₂Se₃-400 °C devices showed a clear improvement, resulting in substantially higher J_{sc} values of 16.5 ± 0.4 mA cm⁻² and the highest PCE of 1.6%. Finally, the Sb₂Se₃-450 °C solar cell achieved the highest PCE of 2.8%, demonstrating increases in J_{sc} to 19.5 ± 0.5 mA cm⁻², V_{oc} to 380 ± 10 mV, and FF to 38 ± 3%. The EQE spectra of the four devices, presented in Figure 21b, validate the observations derived from the J-V curves. The Sb₂Se₃-450 °C solar cell exhibited the highest spectral response in the wavelength range of 300–1050 nm. This can be attributed, once again, to the superior quality of the Sb₂Se₃-450 °C absorber, characterized by a compact grain morphology with large columnar grains that facilitate efficient charge collection.

However, even for the best-performing device, the EQE response is relatively modest, exhibiting steep declines at both shorter and longer wavelengths. Losses at shorter wavelengths are known to result from parasitic absorption by the CdS ETL layer [51], [78]. The low EQE at longer wavelengths could be attributed to back surface recombination and the short diffusion lengths of electrons. Previous reports have indicated intragrain carrier diffusion lengths of electrons in the range of 0.3–0.6 μm [44], which are at least two times shorter than the absorber layer thicknesses ($\sim 1.5 \mu\text{m}$) obtained for the deposited Sb_2Se_3 absorbers.

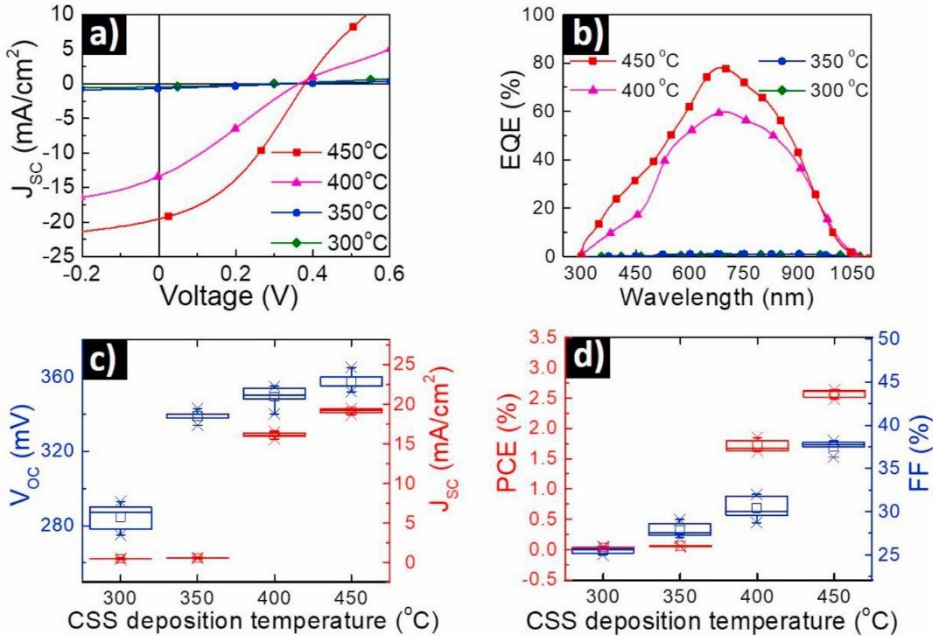


Figure 21. (a) J-V curves of the glass/FTO/CdS/ Sb_2Se_3 /Au solar cells using Sb_2Se_3 films deposited at substrate temperatures ranging from 300 °C to 450 °C, (b) EQE spectra of the corresponding devices, (c) and (d) evolution of the PV parameters with the CSS substrate temperature. Each deposition temperature was evaluated using five cells, and the average values of the PV parameters are reported.

The impact of CSS substrate temperature on the grain morphology of Sb_2Se_3 thin films and consequent CdS/ Sb_2Se_3 device performance has also been investigated by several other groups. Guo et al. found that the optimal substrate temperature should be below 300 °C to prevent grain growth along [hk0] crystal directions [153]. Therein it was shown that [211]-preferred orientation leads to the minimum series resistance, enhanced light absorbance, and 4.2% efficient CdS/ Sb_2Se_3 solar cells. In another study, the same group reported use of sputtered oxygenated CdS ETL as an effective approach to improve the grain growth of Sb_2Se_3 absorber and performance of CdS:O/ Sb_2Se_3 solar cells [154]. The last approach included oxygen plasma treatment and deposition of a monoatomic Al_2O_3 layer at the CdS– Sb_2Se_3 interface [155]. The introduction of oxygen was considered beneficial for preventing the Cd diffusion and formation of detrimental Cd interstitials. In contrast with these studies Wen et al. demonstrated 7.6% efficient CdS/ Sb_2Se_3 solar cells (the highest reported efficiency for such configuration) with the necessity of high deposition VTD temperature ($\geq 400 \text{ }^\circ\text{C}$) to obtain dense and dense Sb_2Se_3 absorber films

with increased texture for (221) planes [11]. Therein it was claimed that diffusion of Cd into absorber reduces the interface defects and recombination at the heterojunction interface, both beneficial for device performance. At the same time, a common particularity for all these studies is that the CdS ETL layer, deposited by CBD or sputtering always undergoes air, CdCl₂, and/or oxygen treatments which might be crucial for the final device efficiency. In terms of CSS processing temperature, our results seem to support the findings by Wen et al. [11], rather than the results reported by Guo et al. [153], as the 450 °C was the only deposition temperature enabling deposition of compact Sb₂Se₃ absorber layers with large columnar grains and enhanced texture for (hk1) planes.

Despite finding the optimal substrate temperature, the resulting device PCE of 2.8% was still modest compared with record superstrate CdS/Sb₂Se₃ devices. Aside from tuning the CSS processing conditions, recent studies had reported about the role of the substrate on the Sb₂Se₃ film [156], [157]. Ultimately, the ETL layer significantly affects not only the Sb₂Se₃ film growth and grain orientation, but also atomic intermixing and heterojunction band alignment at the interface, which all impact the device performance. Therefore, our next strategy involved employing CBD-CdS and spray deposited TiO₂ ETLs to investigate their effect on the Sb₂Se₃ film structure and grain orientation as well as chemical intermixing.

3.1.3 The effect of CBD-CdS and TiO₂ ETLs on the Sb₂Se₃ film morphology and grain orientation

In the previous section, we demonstrated that substrate temperature of 450 °C was optimal, enabling fabrication of Sb₂Se₃ films with columnar sintered grains and enhanced preference for (hk1) crystal planes. Furthermore, such grain structure yielded the highest solar cell performance, demonstrating that compact Sb₂Se₃ film structure with large columnar grains is essential for efficient Sb₂Se₃ devices in superstrate configuration. For the next step, however, it was unclear whether using the CSS processing temperature of 450 °C, optimized for the CSS-deposited CdS ETL layer (CSS-CdS), would reproduce desired microstructures also for Sb₂Se₃ films deposited on CBD-CdS and TiO₂ ETLs, wherein both are deposited with an approximate thickness of 100 nm. CBD-CdS was selected since CBD has been the common fabrication method for CdS films in the Sb₂Se₃ devices. It also allowed to investigate the intermixing phenomenon at the Sb₂Se₃–CdS interface, previously reported by Phillips et al. [78], by comparing CBD-CdS ETL processed at lower temperatures (<100 °C) and CSS-CdS processed at higher temperatures (>300 °C). While CSS-CdS did not have undergo any post-deposition treatment, CBD-CdS and TiO₂ films were subjected to following post-annealing treatments. TiO₂ films went through a standard annealing procedure; they were annealed in air at 450 °C for 30 min to provide better crystallinity [158]–[160]. CBD-CdS films were also subject to a common annealing procedure, which involved air annealing at 120 °C for 1 h, to purge layer surface from any secondary phases [151], [161]. Furthermore, we implemented a seed screening strategy. This involved a deposition of a <100 nm thick amorphous Sb₂Se₃ film, which was deposited by CSS at 300 °C prior to the deposition of the main Sb₂Se₃ absorber layer. The optimal deposition temperature of 300 °C was selected for the seed film after scanning through the temperature range of 250–350 °C.

Figure 22 presents top-down and cross-sectional SEM images of Sb₂Se₃ films deposited with and without a seed layer on CBD-CdS/FTO/glass and TiO₂/FTO/glass substrates at a substrate temperature of 450 °C. In the absence of a seed layer, the Sb₂Se₃ film deposited on CBD-CdS, as depicted in Fig. 22a, exhibits a morphology comparable to Sb₂Se₃ films

deposited at 350 °C on CSS-CdS films. The microstructure is characterized by narrow inclined Sb_2Se_3 grains that are highly dispersed, with a high density of microvoids present between them. However, the inclusion of a seed layer, as seen in Fig. 22b, significantly improves the microstructure, resulting in a more compact morphology. Nevertheless, the Sb_2Se_3 grains in this case tend to grow more parallel to the substrate. Notably, the microstructure and morphology undergo drastic changes when the TiO_2 ETL layer is employed. The Sb_2Se_3 film deposited with a seed layer on TiO_2 , as shown in Fig. 22d, exhibits a more compact structure compared to the film without a seed layer, as presented in Fig. 22c. The seed layer appears to provide a foundation for the growth of columnar grains and increased compactness, with the grains displaying a more upright orientation.

Fig. 23a displays XRD patterns of Sb_2Se_3 absorber layers deposited at substrate temperature of 450 °C with and without seed layer onto glass/FTO/CBD-CdS and glass/FTO/ TiO_2 substrates. XRD patterns are characteristic of orthorhombic Sb_2Se_3 (Pbnm space group symmetry; JCPDS 15–0861). No secondary phases were detected.

Figure 23b shows TC values calculated for the dominant crystal planes in Sb_2Se_3 , which reveal lower TC values for (hk0) planes than for (hk1) planes. Sb_2Se_3 films with seed layers (denoted with a suffix of '+ SL') show higher TC values for (hk1) planes than Sb_2Se_3 films without seed layers.

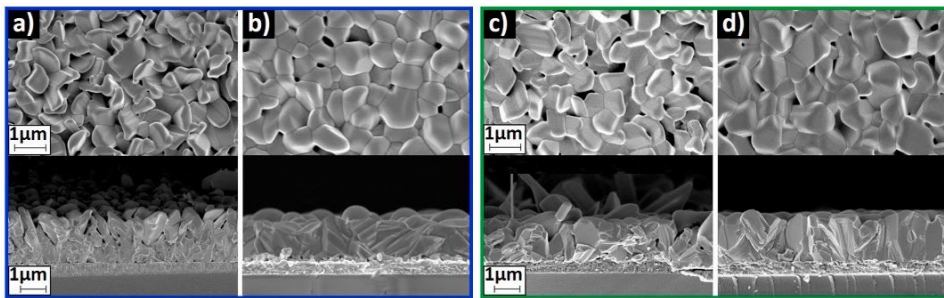


Figure 22. Top-down and cross-sectional SEM images of Sb_2Se_3 absorber films deposited at 450 °C onto CBD-CdS ETL (a) without and (b) with a seed film and onto TiO_2 ETL (c) without and (d) with a seed film. Seed film was deposited by CSS at 300 °C before the main Sb_2Se_3 layer deposition.

This could imply more Sb_2Se_3 crystals are orienting along the c-axis direction, which facilitates effective charge transport. Most notably, the Sb_2Se_3 + SL film deposited on the TiO_2 shows a large TC value above 1.2, while the corresponding value for Sb_2Se_3 without seed layer remains low. TC value of (002) plane is also higher for Sb_2Se_3 + SL grown on the CBD-CdS as compared to the Sb_2Se_3 film without seed. Given that the (002) crystal plane refers to vertical Sb_2Se_3 crystals, TC values suggest the Sb_2Se_3 + SL on the TiO_2 could exhibit a preferred grain orientation in the [001] direction.

We have shown that the seed layer significantly influences the subsequent growth of the absorber material, leading to larger and more compact grain morphologies. Furthermore, our findings provide a comprehensive explanation for the observed seed screening phenomenon. In our case, the Sb_2Se_3 seed film deposited by CSS onto TiO_2 at 300 °C had a nanorod grain structure, displaying similarity to the Sb_2Se_3 absorber film morphology deposited at 300 °C on the CSS-CdS, as was shown in Fig. 19a, but has a much lower thickness of 60–80 nm. At substrate temperature of 300 °C, there is a wide distribution of grain sizes and crystal orientations resulting from the high nucleation density at the substrate surface.

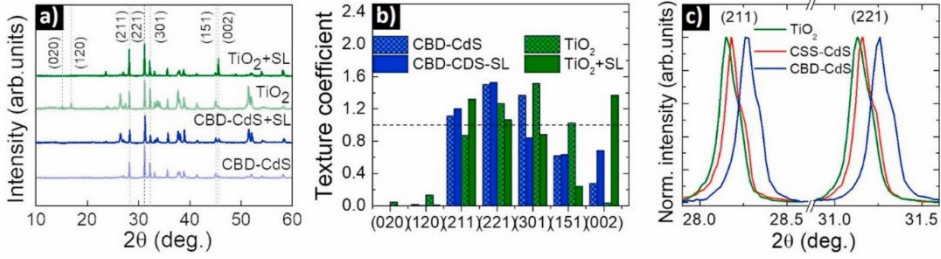
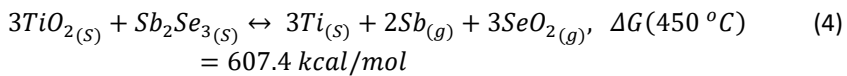
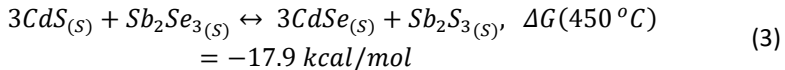


Figure 23. (a) XRD patterns of Sb_2Se_3 absorber films deposited at 450 °C onto CBD-CdS and TiO_2 ETLs without and with the seed film, b) Texture coefficient values for dominant crystal planes in Sb_2Se_3 films, c) XRD peaks (211) and (221) peaks of Sb_2Se_3 shifted to larger 2θ values when deposited on the CBD-CdS ETL.

During the subsequent CSS deposition of the absorber at 450 °C, the seeds aligned parallel to the substrate are easily re-evaporated, as they are bonded with the TiO_2 and CdS ETLs via weak vdW interactions. Only those vertically standing nanorods, that are bonded through the strong covalent bonds with the substrate and are stable enough to resist re-evaporation, continue to grow by the addition of material from the vapor and by the high adatom surface diffusion at 450 °C. Thus, large Sb_2Se_3 columnar sintered grains with low surface energies grow perpendicular with the TiO_2 substrate, leading to the formation of compact Sb_2Se_3 films with large grains and enhanced presence of (002) planes, as evidenced by Fig. 23b.

To investigate the possible intermixing effect between CdS and Sb_2Se_3 , we analyzed the diffraction patterns at a higher resolution. In the 28–32° range, as illustrated in Fig. 23c, we observed a noticeable shift towards higher 2θ values for the (211) and (221) main peaks in Sb_2Se_3 films deposited on the CdS ETLs, in comparison to Sb_2Se_3 films deposited on TiO_2 ETL. This phenomenon was particularly prominent in Sb_2Se_3 films deposited on the CBD-CdS ETL. A similar effect was previously seen for the (511) and (111) XRD peaks in the halide processed CdS/CdTe and CdS/SnS heterostructures deposited by CSS [149], [162]. Therein the phenomenon was explained by the intermixing at the CdS/CdTe interface with the formation of a $Cd_{1-x}S_x$ alloy and/or incorporation of chlorine impurity in the lattice of CdTe and SnS [162], [163]. Analogous to CdS/CdTe interface, we explain the displacement of the (211) and (221) XRD peak shown in Fig. 23c as being due to the interdiffusion of S from CdS into the Sb_2Se_3 absorber and Se from the absorber into the CBD-CdS buffer with the formation of $Cd_{1-x}Se_x/Sb_2Se_{3-y}$ alloy at the interface. It is important to note that the interdiffusion took place due to subsequent absorber deposition at 450 °C. To prove these assumptions, we analyzed the possible thermodynamic reactions in the CdS/ Sb_2Se_3 and TiO_2/Sb_2Se_3 systems using Equations 3 and 4.



The Gibbs free energy (ΔG) in Eq. 3 gives a negative value, which means the reaction is thermodynamically favored toward the formation of solid CdSe and Sb_2Se_3 . This implies full transformation to CdSe and Sb_2Se_3 depending on the kinetics and quantities of the starting compounds. According to the phase diagrams of Sb_2Se_3 -CdS and Sb_2Se_3 -CdSe

[164], there is high mutual solubility and probability for the formation of compounds like CdSb_2Se_4 . In contrast, the ΔG of the reaction between TiO_2 and Sb_2Se_3 , as shown in Eq. 4, is largely positive indicating the thermodynamically unfavorable reaction in this system.

Considering the Eq. 3, we claim that the intermixing occurs at the $\text{CdS}/\text{Sb}_2\text{Se}_3$ interface, converting this interface into a $\text{CdS}_{1-x}\text{Se}_x/\text{Sb}_2\text{Se}_{3-y}\text{S}_y$ solid alloy. At the optimized CSS substrate temperature of 450°C , the solubility of Se into CdS is higher than the solubility of S in Sb_2Se_3 [164], which favors the formation of CdSe to a higher extent at the interface. The ionic radius of sulfur (S^{2-} : 170 pm) is smaller than the ionic radius of the selenium (Se^{2-} : 190 pm) [165] causing contraction of the Sb_2Se_3 sublattices and hence cause shifting of the (211) and (221) peaks toward higher 2θ values. Interestingly, for Sb_2Se_3 films deposited on the CSS-CdS, a small shift of the (211) and (221) peaks was observed compared with the CBD-CdS based structure. Given that the CBD-CdS ETL films, which are solution processed at 85°C , exhibit smaller grains with higher surface energy [151], they are more prone to interdiffusion by mass transport through the gas phase, and consequently lead to a high degree of alloy formation at the interface during the CSS deposition at 450°C .

There is still no consensus regarding the impact of the chemical intermixing on the device performance. The intermixing has been shown to be beneficial for the device efficiency, relying on the classical analogy with the CdS/CdTe heterojunction [11]. On the other hand, it has been reported that the CdSe interface layer establishes a potential barrier that impedes charge transport [78]. To understand the impact of the intermixing effect on the device performance we further compared and analyzed the Sb_2Se_3 devices with CSS-CdS, CBD-CdS, and TiO_2 ETLs.

3.1.4 Analysis of grain orientation in Sb_2Se_3 thin films

Building upon the promising results obtained from the TC analysis, we aimed to further investigate the significant increase in texture observed for (002) planes in $\text{Sb}_2\text{Se}_3 + \text{SL}$ on TiO_2 . While TC analysis has been regarded as a reliable tool for evaluating preferred orientation in Sb_2Se_3 films [156], we learned that its applicability may be limited for measuring texture in polycrystalline films with highly anisotropic crystals, as the grain morphology could potentially contribute to an overestimation of the actual texture [21].

Therefore, to gain a clearer understanding of the grain orientation in our Sb_2Se_3 films, we conducted additional analyses using pole figure measurements by X-ray diffraction (XRD) and orientation distribution maps via electron backscatter diffraction (EBSD). These complementary techniques were employed alongside TC analysis to provide a more comprehensive insight into the grain orientation of Sb_2Se_3 thin films. Our study represented the first demonstration of pole figures for Sb_2Se_3 films grown on the TiO_2 ETL.

Figure 24 displays pole figures of the Sb_2Se_3 absorbers deposited with seed and without seed on the TiO_2 in 020 and 002 projections measured by XRD. Each pole figure is provided with an intensity scale, where the intensity correlates directly to the multiple of random distribution (MORD). Larger is the multiple of random distribution, stronger is the texture (strong texture translates into preferred orientation) [166]. It was noted that Sb_2Se_3 without seed layer showed stronger intensity for the 020 peak, while $\text{Sb}_2\text{Se}_3 + \text{SL}$ recorded significantly stronger intensity for the 002 peak. The MORD of 002 peak at $\chi = 0^\circ$ for Sb_2Se_3 without seed is around 0.5, while it increased by a factor of 5 for the $\text{Sb}_2\text{Se}_3 + \text{SL}$. These results are consistent with the findings from the TC analysis. While the pole figures confirmed the presence of enhanced texture in our Sb_2Se_3 films, the increase in intensity for the (002) plane was not significant enough to classify it as a strongly

preferred orientation. In a related study, Pattini et al. reported pole figures for Sb_2Se_3 films deposited on various substrates, including glass, Mo, CdS, FTO, and ZnO [156]. Among these substrates, the strongest texture along the [001] direction was observed in the Sb_2Se_3 films grown on FTO, as evidenced by the high pole intensity of the (061) peak [153]. Considering this, the presence of a strong pole intensity for the (002) peak in our Sb_2Se_3 films suggests that TiO_2 is a suitable electron transport layer (ETL) choice, facilitating grain growth along the [001] crystal direction.

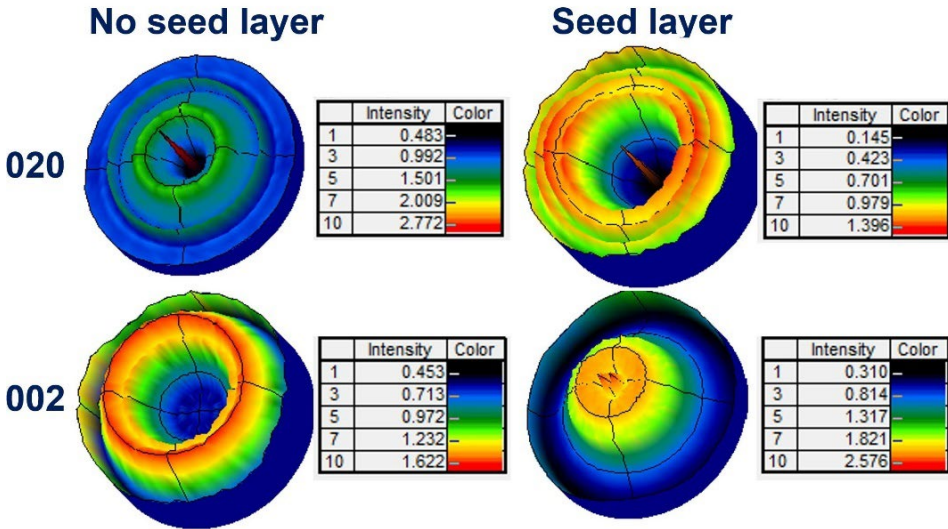


Figure 24. Pole figures in 020 and 002 projections derived from the XRD measurements of Sb_2Se_3 films grown without and with seed layer onto $\text{TiO}_2/\text{FTO}/\text{glass}$ substrates.

Texture measurements were also made on individual grains of Sb_2Se_3 + SL film via EBSD. The cross-sectional EBSD map shown in Fig. 25 illustrates that the Sb_2Se_3 layer does not exhibit any preferential growth direction. The average Sb_2Se_3 grain size was found to be around 300–400 nm. This means that not all grains start their growth from the seed layer up to the top and there is still room for improvement. This also relates to achieving favorable grain orientation. Although neither pole figures by XRD nor orientation distribution mapping by EBSD found proof for preferred orientation, clear increase of beneficial 002 peak in Sb_2Se_3 + SL was still detected, which could stem from the increased columnar growth. Hence, it can be argued that further enabling columnar growth would not only increase grain size but would also enhance texture along the [001] direction. As to the grain orientation, it is now clear the TC analysis does not provide enough evidence to claim for preferred orientation in the orthorhombic Sb_2Se_3 . Instead, careful texture analyses are required to draw strong conclusions on the preferred orientation.



Figure 25. EBSD map with orientation distribution of the Sb_2Se_3 + SL film (given by false colors, see legend) superimposed on the pattern-quality distribution of the FTO layer. The orientation distribution indicates no pronounced texture of the Sb_2Se_3 + SL layer.

3.1.5 The effect of ETL and seed screening on the Sb_2Se_3 device performance

Since the optimization of the CSS substrate temperature highlighted the importance of achieving a compact and large grain morphology, $\text{TiO}_2/\text{Sb}_2\text{Se}_3$ and CBD-CdS/ Sb_2Se_3 and thin film solar cells were fabricated using the seed screening approach. Figure 26a displays J–V curves of Sb_2Se_3 solar cells based on three different ETL/absorber heterojunctions: CSS-CdS/ Sb_2Se_3 , $\text{TiO}_2/\text{Sb}_2\text{Se}_3$, and CBD-CdS/ Sb_2Se_3 . The peak and average PV parameters of these devices are listed in Table 5. Among the different heterojunctions, the CBD-CdS/ Sb_2Se_3 solar cell exhibited the lowest performance, with a peak PCE of 2.1%, V_{oc} of 350 mV, J_{sc} of 15.6 mA cm^{-2} and FF of 38%. Compared with the CBD-CdS device, the CSS-CdS/ Sb_2Se_3 solar cell, discussed in Section 3.1.2, showed better performance with a higher V_{oc} , J_{sc} , and ultimately a PCE of 2.8%. Notably, the $\text{TiO}_2/\text{Sb}_2\text{Se}_3$ device outperformed the others, demonstrating the highest J_{sc} of 24.6 mA cm^{-2} , V_{oc} of 430 V, FF of 50%, and a PCE of 5.3%.

It is evident that the differences in the microstructure as well as grain orientation of the Sb_2Se_3 absorber films deposited on the three different ETLs with the seed layer reflected on the final device performance. Although PCE of 5.3% is a promising result for the $\text{TiO}_2/\text{Sb}_2\text{Se}_3$ device, the achieved efficiency is still lower than the efficiencies reported for the same device configuration [47], [59], [65]. The obtained V_{oc} of 430 mV and FF of 49% are comparable with the highest reported values of the record devices; the main limitation comes from the low J_{sc} values. EQE curves of the devices, as depicted in Fig. 26b, validate the results obtained from the J–V curves. The TiO_2 device showed the highest spectral response in the wavelength region from 350 to 1100 nm, which highlights a significantly better carrier collection efficiency in the short wavelength region. The CBD-CdS device, which showed lowest J_{sc} and PCE values, also demonstrated lowest spectral response in the visible light region of 400–700 nm. Compared with the CBD-CdS solar cell, the CSS-CdS solar cell showed a higher spectral response in the short wavelength region, but its spectral response showed an abrupt decrease from 700 to 1050 nm. Low spectral response at short and long wavelengths is related to the parasitic absorption of the CdS layer but also indicates to the high recombination currents near the ETL/absorber interface and short diffusion lengths of the minority carriers in the bulk of the absorber [128]. Phillips et al. encountered an identical drop of spectral response from 700 to 1050 nm in the device with a CSS-deposited CdS, attributing this loss to the formation of an interface CdSe layer, which has a positive CBO offset with the Sb_2Se_3 and therefore impedes charge transport [78].

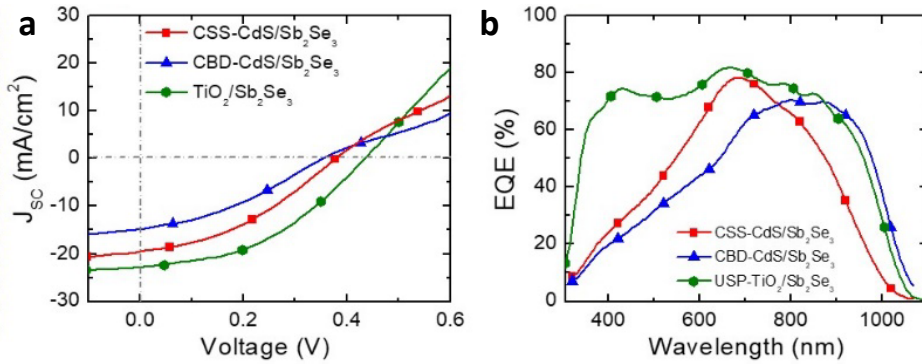


Figure 26. a) J - V curves of CSS-CdS/Sb₂Se₃, TiO₂/Sb₂Se₃, and CBD-CdS/Sb₂Se₃ solar cells and b) EQE curves of these devices.

Table 5. Peak and average PV parameters of CSS-CdS/Sb₂Se₃, TiO₂/Sb₂Se₃, and CBD-CdS/Sb₂Se₃ solar cells. Average values include standard deviation.

Device	Peak (P) Average (A)	V _{oc} [mV]	J _{sc} [mAcm ⁻²]	FF [%]	Eff [%]
CSS-CdS/Sb ₂ Se ₃	P	380	19.5	38	2.8
	A	360 ± 10	17.6 ± 0.8	36 ± 3	2.5 ± 0.9
TiO ₂ /Sb ₂ Se ₃	P	430	24.6	50	5.3
	A	410 ± 10	23.9 ± 0.5	49 ± 2	4.9 ± 1.2
CBD-CdS/Sb ₂ Se ₃	P	350	15.6	38	2.1
	A	320 ± 15	14.2 ± 1.1	37 ± 3	1.8 ± 1.5

Herein it is worth noting that the current champion Sb₂Se₃ solar cells in both superstrate and substrate device configuration have employed the CBD-CdS ETL layer [10], [11]. Both studies report the post-deposition treatment with CdCl₂ on the CBD-CdS, followed by air annealing at 400 °C, which has been previously established for CdTe PV technology [151]. Moreover, it has been shown that CdS/Sb₂Se₃ heterojunction band alignment is superior to TiO₂/Sb₂Se₃, being optimal for electron transfer [47]. Although our group has previously successfully demonstrated the positive effect of CdCl₂ treatment on the CdTe solar cells, we have not been able to produce an efficient device using the CdCl₂ processing step for CdS ETL was the uncontrollability of the residual oxychlorides (as secondary phases results of the treatment), which had a great impact on the absorber morphology and ETL/absorber interface quality. The fact that only those few groups reported relatively highly efficient CdS/Sb₂Se₃ devices and while other groups have not yet succeeded with the same cell configuration indicates that the control of the intermixing effect remains a key issue for the CdS/Sb₂Se₃ device in superstrate configuration.

3.1.6 Analysis of recombination mechanisms in the Sb₂Se₃ devices

Figures 27a–c display the I - V - T curves, which were measured to identify the performance limiting factors in the Sb₂Se₃ devices. We first analyzed the V_{oc}- T dependence for all three devices (insets of Fig. 27a–c) that can be described by Equation 5:

$$V_{OC} = \frac{E_A}{q} - \frac{Ak_B T}{q} \ln \left(\frac{J_{00}}{J_L} \right) \quad (5)$$

where E_A is the activation energy of dominant recombination path in heterojunction, q is elementary charge, A is the ideality factor, k_B is the Boltzmann constant, T is temperature, J_{00} is the reverse saturation diode current prefactor and J_L is photocurrent density.

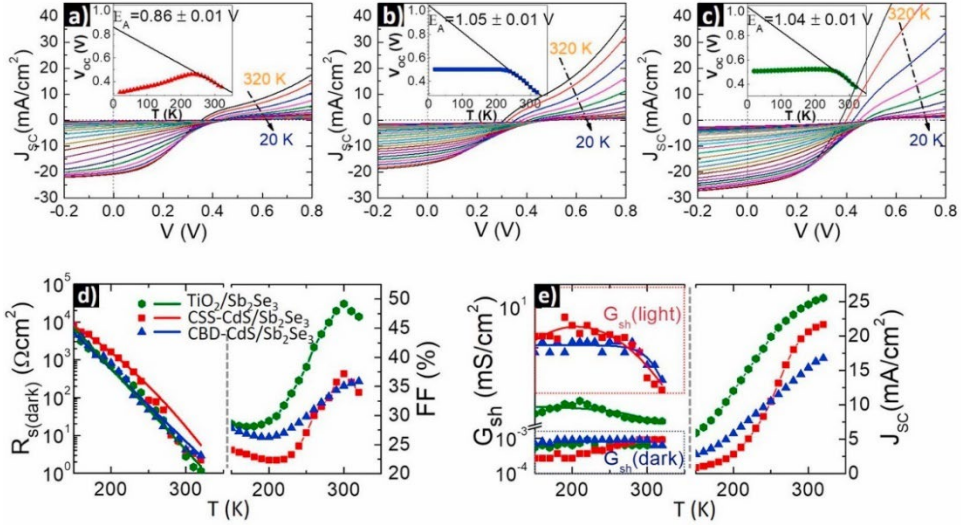


Figure 27. Temperature-dependent J - V curves of three solar cells: (a) CSS-CdS/Sb₂Se₃, (b) CBD-CdS/Sb₂Se₃, and (c) TiO₂/Sb₂Se₃. Insets display the V_{OC} temperature dependence together with the extrapolation to 0 K showing the activation energy (E_A) for the corresponding devices, (d) Temperature dependence of FF and series resistance (R_s) extracted from dark I - V - T measurements and (e) Temperature dependence of J_{SC} and shunt conductance (G_{sh}) extracted from the illuminated and dark I - V - T measurements.

For all three samples, the V_{OC} - T plot shows the usual initial increase at low temperature, which is expected as recombination is reduced at lower temperatures, decreasing the reverse dark saturation current. Below 240 K the V_{OC} starts to level off for the device with the CSS-CdS ETL, whereas a plateau was reached for the cells with the CBD-CdS and TiO₂ ETLs. A possible reason for such behavior in the CSS-CdS device is the carrier “freeze-out” effect that usually occurs in materials with deep defect levels and increasing blocking transport behavior at the interfaces (e.g., ETL/absorber or absorber/back contact); due to the low carrier density absorber, the device can no longer sustain high V_{OC} [167]–[169]. The carrier freeze-out effect is present in all three devices, nevertheless, the abrupt behavior of the V_{OC} - T below 240 K for the CSS-CdS based cell indicates that the effect is more drastic in this device. Extrapolation of the linear part of the V_{OC} - T plots to $T = 0$ K gave the activation energies of 0.86, 1.05 eV, and 1.04 eV for the solar cells with CSS-CdS, CBD-CdS, and TiO₂, respectively, as depicted in Fig. 27a–c insets. All these values are smaller than 1.17 eV, the E_g of Sb₂Se₃, indicating to the interface recombination being the predominant recombination mechanism limiting the V_{OC} in these devices.

The changes to FF and J_{SC} have the greatest impact on the reducing device efficiency with decreasing temperature, as depicted in Fig. 27d and e. Generally, in an ideal solar

cell, J_{SC} only changes a little with respect to temperature [128]. To identify the limiting factors for these two parameters, the temperature-dependence of the series resistance (R_s) and shunt conductance (G_{sh}) was analyzed, as seen in Fig. 27d and e. The analysis shows that the marked drop in the FF and J_{SC} is due to the significant increase of the R_s at low temperatures that distort the J–V curve and lower FF and J_{SC} values at low temperatures. The dark shunt conductance is very low ($G_{sh}(D) \sim 10^{-4} \text{ mS cm}^{-2}$) indicating no physical shunt or leakage problem across the cells, nevertheless, the light shunt conductance ($G_{sh}(L)$) is increased by four orders of magnitude under illumination, indicating that the FF is affected by the nonequilibrium phenomena. Such an effect may imply a voltage-dependent collection-efficiency problem under light [59] caused by a high recombination rate and resulting short minority carrier collection length. In this case, increasing the forward bias will reduce the depletion width and consequently the carrier collection, as the collection due to diffusion is minimal [170]. The latter effect results in a positive slope near 0 V or higher shunt conductance under illumination $G_{sh}(L)$.

3.1.7 Analysis of free carrier and defect densities in Sb_2Se_3 PV devices

The high resistivity of Sb_2Se_3 thin films presents challenges in determining the conductivity type and carrier density. Only a limited number of studies have reported measurements to determine the majority carrier. Some research groups have reported p-type conductivity with a low carrier density on the order of 10^{13} cm^{-3} [51], [117], [154], [155]. However, Hobson et al. [47] discovered n-type conductivity in Sb_2Se_3 films deposited using the CSS method, attributing it to chlorine impurities from the commercially purchased source material powder of Sb_2Se_3 .

To confirm chlorine as an n-type dopant, Hobson et al. deliberately doped Sb_2Se_3 crystals with MgCl_2 , which confirmed chlorine's role in introducing n-type conductivity [47]. It remains uncertain whether the chlorine impurities outdiffuse or persist in the material, and how this affects the conductivity type and carrier density in Sb_2Se_3 films.

These intriguing findings prompted us to analyze the conductivity type and carrier density of our CSS-deposited Sb_2Se_3 absorber films. The hot probe technique was employed to determine the conductivity type of the Sb_2Se_3 absorber films deposited on glass substrates. As a reference, a SnS thin film deposited using CSS on the same glass substrates was utilized, known to exhibit strong p-type conductivity [149]. Our analysis consistently revealed p-type conductivity in the Sb_2Se_3 absorber layers. Van der Pauw measurements demonstrated a high dark resistivity of $5 \times 10^6 \Omega\text{-cm}$, indicating significant self-compensation of native defects. Under illumination, the Sb_2Se_3 layers exhibited photoconductivity, with a dark-to-light resistance ratio of 30 and a resistivity of $\sim 10^5 \Omega\text{-cm}$. In comparison, untreated CdTe films displayed a semi-insulating character ($>10^{10} \Omega\text{-cm}$) and no photosensitivity [163]. This substantial difference may explain the superior performance of devices employing untreated Sb_2Se_3 absorber films compared to untreated CdTe films [171]. However, the resistivity of $\sim 10^6 \Omega\text{-cm}$ prevented us from conducting Hall measurements to determine the majority carrier and free carrier density of Sb_2Se_3 . Nevertheless, the carrier concentration of Sb_2Se_3 was estimated using the CV profiles of CSS- $\text{CdS}/\text{Sb}_2\text{Se}_3$, $\text{TiO}_2/\text{Sb}_2\text{Se}_3$, and CBD- $\text{CdS}/\text{Sb}_2\text{Se}_3$ PV devices. Considering the p-type conductivity indicated by the hot probe analysis, the CV profiles suggest hole carrier densities of approximately 10^{14} cm^{-3} .

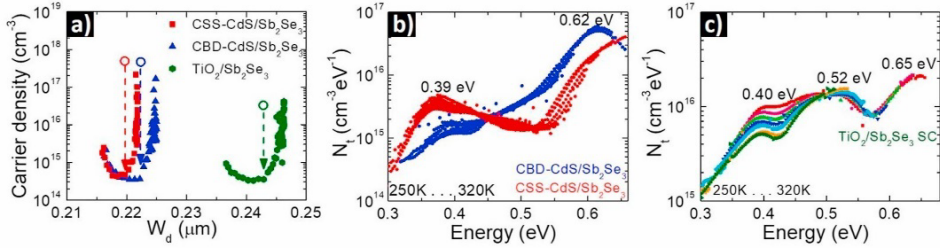


Figure 28. (a) Depth carrier density profile plotted against depletion width, determined from CV profiles. The circles denote the zero-voltage condition for three solar cell configurations: CSS-CdS/Sb₂Se₃, CBD-CdS/Sb₂Se₃, and USP-TiO₂/Sb₂Se₃; (b) and (c) Potential defect levels and densities in the Sb₂Se₃ films of the corresponding devices.

The measured carrier density in the absorber film was found to be three orders of magnitude lower than the recently reported value of 10¹⁷ cm⁻³ in the TiO₂/Sb₂Se₃ n-n isotype cell configuration [47], [59]. This discrepancy may explain the lower J_{sc} value of 24.6 mA cm⁻² observed in the TiO₂/Sb₂Se₃ n-p heterojunction devices developed in this study, compared to the 31.7 mA cm⁻² achieved in the TiO₂/Sb₂Se₃ n-n isotype device [47]. Additionally, the temperature-dependent evolution of the PV parameters for both the TiO₂/Sb₂Se₃ device and the devices with CdS ETLs indicated dominant interface recombination. The presence of a roll-over effect (photocurrent saturation at high forward bias) in the J-V curves of all three devices at low temperatures further indicated limitations to carrier transport, as shown in Figures 27a–c. This roll-over effect is typically observed in CdTe solar cells due to the Schottky barrier between CdTe and the metal back contact [128], [162]. However, the less pronounced roll-over effect in the TiO₂/Sb₂Se₃, compared to the devices employing CdS ETLs, suggests that the back contact barrier may not be the sole reason, and the ETL/absorber interface likely contributes significantly to this effect.

In the CdS-based devices, the roll-over effect occurs due to the interaction of two factors: (i) the formation of a Cd_{1-x}Se_x solid alloy at the interface, introducing an offset at the conduction band due to an intermediate layer, and (ii) the low hole concentration in the Sb₂Se₃ absorber and similar densities of the compensating recombination centers in the ETL and absorber. In contrast, the absence of intermixing in the TiO₂/Sb₂Se₃ device suggests that the deficiency in hole density in the absorber still contributes significantly to the roll-over effect at low temperatures. When the electron barrier at the ETL/absorber interface and is sufficiently large, the diode current is completely blocked, allowing only photocurrent to pass the barrier, resulting in a roll-over anomaly in the light J-V curve [55]. In this context, the carrier density in the ETL also plays a critical role.

Among the three ETLs used in this work, CSS-CdS exhibits the highest resistivity (>10¹⁰ Ω·cm), while CBD-CdS demonstrates substantially lower resistivity of ~4 × 10² Ω·cm, an electron concentration of ~10¹⁶ cm⁻³, and electron mobility of 5 cm² V⁻¹ s⁻¹. The TiO₂ films possess a resistivity of ~10⁵ Ω·cm. The high resistivity of CSS-CdS, which is higher than that of the Sb₂Se₃ absorber, suggests that the depletion region extends into the ETL at the CdS/Sb₂Se₃ interface, resulting in ineffective charge separation and increased blocking transport behavior at the ETL/absorber interface. This leads to a pronounced roll-over effect in the J-V response of the solar cell, as observed in Fig. 27a. The measured carrier density of ~10¹⁴ cm⁻³ in the absorber indicates the contribution of defect levels in the Sb₂Se₃ material. To assess the location and distribution of defect-induced energy

levels in the bandgap of the Sb_2Se_3 absorber film, TAS measurements were employed, as shown in Fig. 28b and c.

The obtained value is three orders of magnitude lower than the recently reported 10^{17} cm^{-3} carrier density in the absorber of the $\text{TiO}_2/\text{Sb}_2\text{Se}_3$ n-n isotype cell configuration. This could explain lower J_{sc} value of 24.6 mA cm^{-2} for the $\text{TiO}_2/\text{Sb}_2\text{Se}_3$ n-p heterojunction cells developed in this study compared to 31.7 mA cm^{-2} $\text{TiO}_2/\text{Sb}_2\text{Se}_3$ n-n isotype device [47]. At the same time, the temperature-dependence evolution of the PV parameters for both $\text{TiO}_2/\text{Sb}_2\text{Se}_3$ device as well as for the cells with CdS ETLs showed the dominant interface-recombination. The transport limitation is also evident by the presence of roll-over effect (photocurrent saturation at high forward bias) in the J - V curves of all three devices at low temperatures, as shown in Figures 27a–c. Such an anomaly usually is observed in CdTe solar cells due to the Schottky barrier between CdTe and the metal back contact [128], [162]. However, the fact that the roll-over effect in Fig. 27 is less pronounced for the $\text{TiO}_2/\text{Sb}_2\text{Se}_3$ cell and is highlighted in CdS-based devices suggest that the back contact barrier might not be the only reason and the ETL/absorber interface has a large contribution to this effect.

Given that high resistivities can also point to the presence of deep defects in Sb_2Se_3 , we conducted TAS measurement on the three devices. Figures 28b and c display trap densities (N_{T}) for potential defect levels, which were determined from the Arrhenius plot of relaxation frequencies. All potential defect bands had densities between 10^{15} – $10^{16} \text{ cm}^{-3} \text{ eV}^{-1}$. We detected two activation energies when analyzing devices with CdS ETLs. The activation energy of 0.39 eV above VBM was found for the CSS-CdS/ Sb_2Se_3 device and another at 0.62 eV above VBM for the CBD-CdS/ Sb_2Se_3 device, as seen in Fig. 28b. As for the $\text{TiO}_2/\text{Sb}_2\text{Se}_3$ device, as shown in Fig. 28c, there are three bands peaking at around 0.40 eV, 0.52 eV, and 0.65 eV above VBM. Thermal activation energy at 0.39 eV above VBM was also found from the 3.7%-efficient $\text{TiO}_2/\text{Sb}_2\text{Se}_3$ device using a different TAS setup, as reported in Publication II. From first-principles calculations, transition energy levels were found for V_{Sb} acceptor defects, which lay close to 0.39 eV [112]. DFT study calculated transition energy levels of 0.33 eV and 0.40 eV for $\text{Sb}_{\text{Se}1}$ and $\text{Sb}_{\text{Se}2}$ antisite defects, which are deep acceptor defects [133]. Also, hybrid DFT study located Sb_{Se} antisite defects close to the 0.39 eV energy [22]. Given that the activation energies of 0.39–0.40 have been found in both CSS-CdS/ Sb_2Se_3 and $\text{TiO}_2/\text{Sb}_2\text{Se}_3$ devices, and the theoretical calculations predicted deep acceptor energy levels close to that, the activation energy obtained in the present study can be assigned to a deep acceptor defect. To compare, Tang's group used DLTS and found defect levels at 0.48–0.49 eV and 0.60–0.65 eV above VBM, attributing these to V_{Sb} acceptor and Sb_{Se} donor defects, respectively, with total densities at around 10^{15} cm^{-3} [11].

From a theoretical perspective, density functional calculation (DFT) studies offer a broader range of defects in Sb_2Se_3 , suggesting the Fermi level pinning toward the midgap due to deep defects [22], [133]. V_{Sb} behaves as a deep acceptor, with transition levels situated close to, but more than 0.025 eV away from the valence band maximum (VBM), whereas Se_{Sb} and Sb_{Se} exhibit amphoteric behavior, occupying positions in the middle of the bandgap and serving as deep recombination centers [22]. While various types of defects can coexist, typically one or two specific defect types predominate, determined by the composition of the vapor phase and the structure of the condensed phase.

Ghosh et al. [172] has reported the growth of Sb_2Se_3 films from vapor phase with slightly Se-rich composition in isothermal conditions, as shown in Equation 6:

$$nSb_2Se_3 = \frac{1}{4}Sb_{4(g)} + Sb_nSe_{n(g)} + Se_{2(g)} \quad (n = 1) \quad (6)$$

where n is the number of moles. Considering the Eq. 6 and assuming vacancies are the predominant defects in the CSS-deposited Sb_2Se_3 films, the formation of vacancy defects and the equilibrium constant in the lattice of Sb_2Se_3 could be expressed using Equations 7–10:

$$Sb_2Se_{3(s)} = [Sb_{(2-n)}Se_{(3-n)}nV_{Sb}nV_{Se}]_{(s)} + \frac{n}{2}Se_{2(g)} + \frac{n}{4}Sb_{4(g)} \quad (7)$$

$$K_p = [p_{Sb_4}]^{1/4} \cdot [p_{Se_2}]^{1/2} \quad (8)$$

$$2V_{Sb} + 3V_{Se} \Leftrightarrow 0 \quad (9)$$

$$K_{Schottky} = [V_{Sb}]^2 \times [V_{Se}]^3 \quad (10)$$

The charge carrier generation at temperature of the formation of solid Sb_2Se_3 film can be expressed as follows:

$$V_{Sb} = V_{Sb}^{3-} + 3h \rightarrow \text{generation of holes} \quad (11)$$

$$V_{Se} = V_{Se}^{2+} + 2e \rightarrow \text{generation of electrons} \quad (12)$$

Mass action law and electroneutrality conditions:

$$[n][p] = np = \text{const} \quad (13)$$

$$[V_{Sb}^{3-}]^2 + n = [V_{Se}^{2+}]^3 + p \quad (14)$$

Under slight Se-rich conditions:

$$[V_{Sb}^{3-}]^2 > [V_{Se}^{2+}]^3 \rightarrow n \ll p \rightarrow [V_{Sb}^{3-}] \sim p \quad (15)$$

Therefore, we claim that the p-type conductivity of CSS-deposited Sb_2Se_3 films could arise from the uncompensated antimony vacancies. From the fact that the admittance spectroscopy results were consistent with the results from CV profiling and that the hot-probe analysis has demonstrated poor, yet clear p-type conductivity for the Sb_2Se_3 absorber films on glass, it can be assumed that the free carrier density of $\sim 10^{14} \text{ cm}^{-3}$ stems from the deep acceptor at 0.39 eV above VBM.

To summarize, among all three devices developed in this work, the TiO_2/Sb_2Se_3 cells exhibit the highest performance of $\sim 5.3\%$ while the efficiency of CBD-CdS devices is drastically limited by the intermixing effect at the CdS– Sb_2Se_3 interface. For all the cells, the recombination at the interface was identified as a dominant recombination mechanism; this together with reduced hole density in the Sb_2Se_3 absorber has a large contribution to the modest cell efficiency. At the same time, the achieved 5.3% efficient TiO_2/Sb_2Se_3 n-p heterojunction device is well aligned in the top reported cell efficiencies [59], [65] with the same configuration and without the employment of back contact engineering strategy. Although optimization of back contact via incorporation of PCDTBT or PbS hole selective layer [59], [65] was proved to be effective for the improvement of device performance up to 7%, there is still tremendous room for development and

optimization in this direction. We are optimistic that the implementation of the same back contact approach, together with optimization of processing condition for the seed layer at the ETL-absorber interface would allow a similar boost in the efficiency of our $\text{TiO}_2/\text{Sb}_2\text{Se}_3$ device. Nevertheless, we consider that the main emphasis for further development should be on the development and optimization of doping strategies. Halide processing, (such as Cl , MgCl_2) [9] could be one solution in this direction, however, we consider that only implementation of controllable deliberative doping will allow for a significant boost in the efficiency and long term stability of Sb_2Se_3 based devices.

3.2 Developing growth strategy for depositing Sb_2S_3 thin films by CSS

3.2.1 The effect of CSS substrate temperature on Sb_2S_3 film morphology and grain orientation

A CSS growth approach similar to the Sb_2Se_3 thin films was developed also for Sb_2S_3 thin films. Considering the higher efficiencies for Sb_2S_3 devices had been achieved using chemical deposition methods, it was firstly important to understand why physically processed Sb_2S_3 solar cells underperform. Secondly, it gave us an opportunity to again determine the optimal conditions for depositing Sb_2S_3 films with CSS deposition. For the long run, it provides guidance to developing $\text{Sb}_2(\text{S},\text{Se})_3$ solar cells. Before proceeding, it is important to note that the following results were obtained with Sb_2S_3 films stacked on $\text{CdS}/\text{FTO}/\text{glass}$ substrates. Contrary to Sb_2Se_3 , TiO_2 substrates were not compatible with Sb_2S_3 films. A detailed discussion on the potential reasons to this phenomenon will not be a part of the following thesis.

Sb_2S_3 absorber layers were embedded in a superstrate $\text{glass}/\text{FTO}/\text{CdS}/\text{Sb}_2\text{S}_3/\text{Au}$ device. Sb_2S_3 films were deposited onto $\text{CdS}/\text{FTO}/\text{glass}$ substrates by CSS at substrate temperatures ranging from 240 to 400 °C. Fig. 29 displays XRD patterns of $\text{glass}/\text{FTO}/\text{CdS}/\text{Sb}_2\text{S}_3$ structures. Reflections at 17.5°, 22.3°, 25.0°, 28.6°, 32.6° can be assigned to orthorhombic Sb_2S_3 crystal structure with Pbnm space group symmetry (JCPDS 42–1393) [93]. No secondary phases were detected.

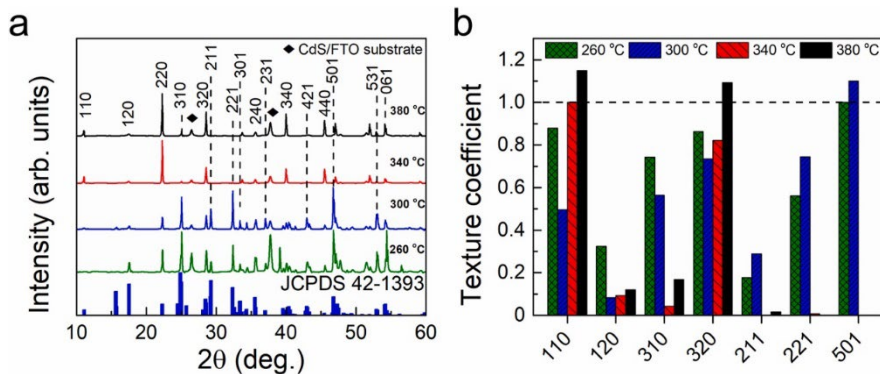


Figure 29. (a) Sb_2S_3 absorber films deposited by CSS at substrate temperatures 260–380 °C onto CdS/FTO substrates, (b) TC values calculated from integrated intensity ratios for main crystal planes in Sb_2S_3 films.

Sb_2S_3 crystal growth depending on the substrate temperature was investigated through texture coefficient (TC) analysis, as shown in Fig. 29b. TC values were calculated from Eq. 2. What can be noted from the calculated TC values is that Sb_2S_3 films deposited at 260 °C and 300 °C show gradually increasing TC values for 211, 221 and 501 planes, with largest TC values (exceeding 1) arising from the (501) planes. For Sb_2S_3 films deposited at 340 °C and 380 °C, the largest TC values correspond to (110) and (320) planes. It can be deduced that lower substrate temperatures help induce growth of (hk1) planes as compared to higher substrate temperatures. Previous reports on both Sb_2S_3 and Sb_2Se_3 absorbers have also deemed crystal grains with preference for (hk1) planes optimal for efficient charge transport across the Sb_2S_3 and Sb_2Se_3 films [12], [20], [46], [61].

The grain morphology in Sb_2S_3 films, deposited onto CdS/FTO/glass substrates, was analyzed by scanning electron microscopy (SEM). Top-down SEM images of Sb_2S_3 films, which were grown at substrate temperatures of 240–380 °C, as seen in Fig. 30a–d, illustrate well how the increase of substrate temperature converts to larger Sb_2S_3 grains. Ramp-up of substrate temperature caused Sb_2S_3 films to have bigger and denser plate-shaped grains as compared to smaller flakes at lower substrate temperatures – an observation that is consistent with previous CSS depositions of Sb_2Se_3 and SnS films [149], [173]. Cross-sectional SEM images in Fig. 30e–h showed that Sb_2S_3 films also grow more compact with increasing substrate temperature.

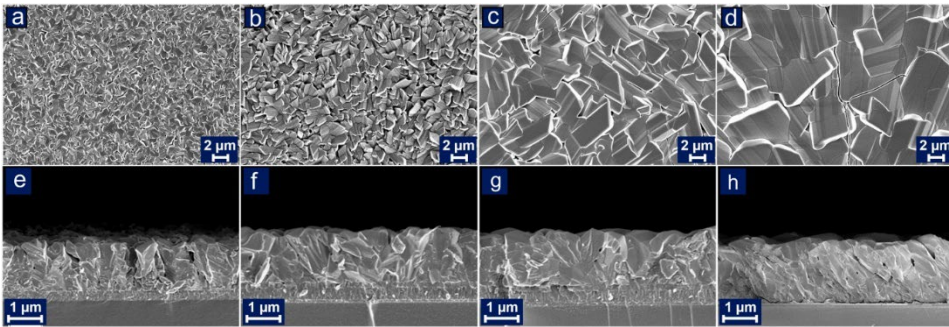


Figure 30. Top-down (a–d) and cross-sectional (e–h) SEM images of Sb_2S_3 absorber films, which are deposited at varying substrate temperatures of 260 °C (a, e), 300 °C (b, f), 340 °C (c, g), and 380 °C (d, h) onto CdS/FTO/glass substrates.

While the Sb_2S_3 film fabricated at lower substrate temperature of 260 °C, as seen in Fig. 30a, shows relatively large voids between the grains, only a small number of pinholes in Fig. 30b–d are seen for Sb_2S_3 films at higher substrate temperatures. More intriguing, however, was the occurrence of microcracks, as can be clearly noted in 30d, which were found in Sb_2S_3 films grown at substrate temperatures of 320 °C and above. Interestingly, no cracks were noted in the previously grown Sb_2Se_3 films, also made by the CSS process [173]. It is likely that there are multiple plausible factors that altogether led to the crack formation. First, it can be argued that the cracking could be related to the difference in the thermal expansion coefficients (TECs) of orthorhombic Sb_2S_3 and Sb_2Se_3 crystals. Gan et al. reported that the TEC of Sb_2S_3 in the [010] crystal direction is two to seven times larger than the TECs in the [100] and [001] crystal direction [174]. At the same time, Herrmann et al. showed that Sb_2Se_3 has nearly identical TECs values in all three crystal directions [175]. This implies that Sb_2S_3 films could be subject to greater residual stress during the deposition process at higher temperatures. If there is either substantial tensile or compressive stress within the film, it could lead to crack formation [176], [177].

Second, since Sb_2S_3 has a lower melting point ($550\text{ }^\circ\text{C}$) compared with Sb_2Se_3 ($611\text{ }^\circ\text{C}$) [47], it exhibits higher vapor pressure and sublimation is expected at lower temperatures. Therefore, substrate temperatures from $320\text{ }^\circ\text{C}$ onwards could have induced such an intense re-sublimation of the already deposited Sb_2S_3 film, which eventually led to the crack formation in the Sb_2S_3 films.

3.2.2 The effect of Sb_2S_3 film microstructure and grain orientation on the Sb_2S_3 PV device performance

Having noted systematic structural changes in the Sb_2S_3 film growth, the impact of CSS deposition temperature on the performance of superstrate glass/FTO/CdS/ Sb_2S_3 /Au solar cells was subsequently investigated. Fig. 31a–d shows main photovoltaic parameters with average values for devices with Sb_2S_3 deposited at substrate temperatures of $240\text{--}400\text{ }^\circ\text{C}$. Illuminated J–V curves are shown in Fig. 31a for the best devices. As seen in Fig. 31a–d, two distinct regions can be noted. In the first region, from $240\text{ }^\circ\text{C}$ to $300\text{ }^\circ\text{C}$, there is a gradual increase of all PV parameters, including open-circuit voltage (V_{oc}), current density (J_{sc}), fill factor (FF), and PCE. The maximum PV parameters, namely J_{sc} of 11.5 mA cm^{-2} , V_{oc} of 680 mV , FF of 48% , and PCE of 3.8% were obtained for the substrate temperature of $300\text{ }^\circ\text{C}$. In the second region, starting from substrate temperature of $320\text{ }^\circ\text{C}$, all the PV parameters start to decline. Interestingly, while the V_{oc} shows only a slight decrease before plateauing at 550 mV , both J_{sc} and FF undergo a significant drop, with J_{sc} reducing to microamperes.

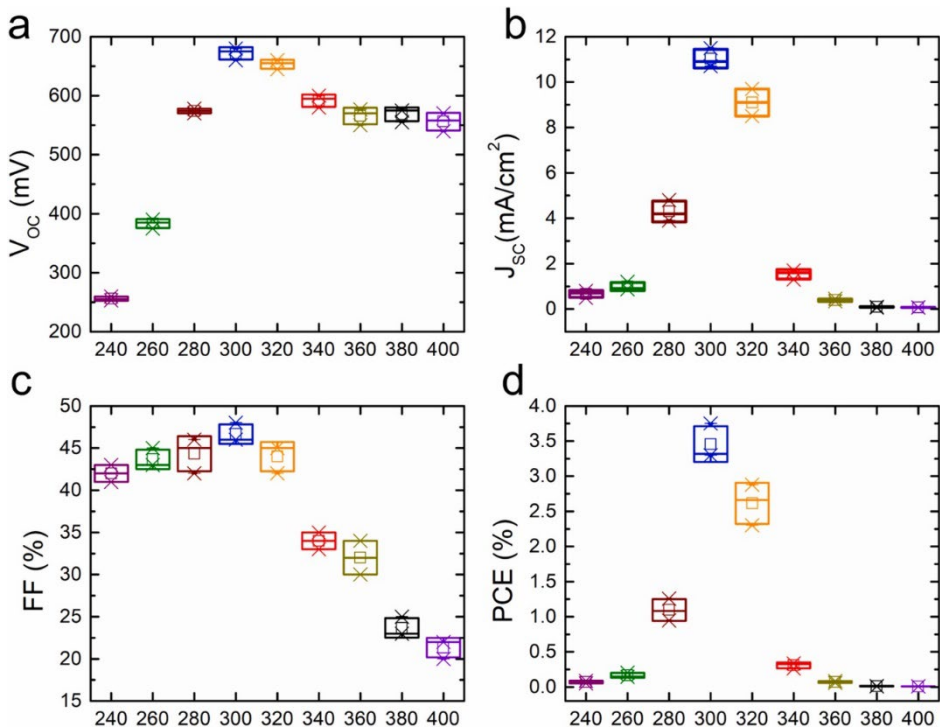


Figure 31. Main photovoltaic parameters including (a) open circuit voltage (V_{oc}), (b) short circuit current density (J_{sc}), (c) fill factor (FF) and (d) power conversion efficiency (PCE) with average values (marked as hollow squares) measured for Sb_2S_3 devices with Sb_2S_3 absorber deposited at substrate temperatures in the range of $240\text{--}400\text{ }^\circ\text{C}$.

External quantum efficiency (EQE) measurements, as seen in Fig. 31b, support the trend observed during the J–V measurements, with the best device showing highest EQE response for the whole wavelength region. The band gap energy of ~ 1.8 eV was determined for the best Sb_2S_3 device, as provided in the Supplementary material of Publication III. Nevertheless, the best device suffers a significant EQE response drop in the short wavelength region, which is associated with parasitic absorption in the CdS ETL [173]. Such absorption has been widely reported also in CdTe and Sb_2Se_3 cells, where a CdS ETL was employed [161], [178]. For all the devices obtained with Sb_2S_3 deposited at temperatures higher than 340°C , there was a futile EQE response throughout the whole wavelength region. This can be attributed to the detected microcracks, which inherently lead to the current leakage, further evidenced by low FF values shown in Fig. 31c.

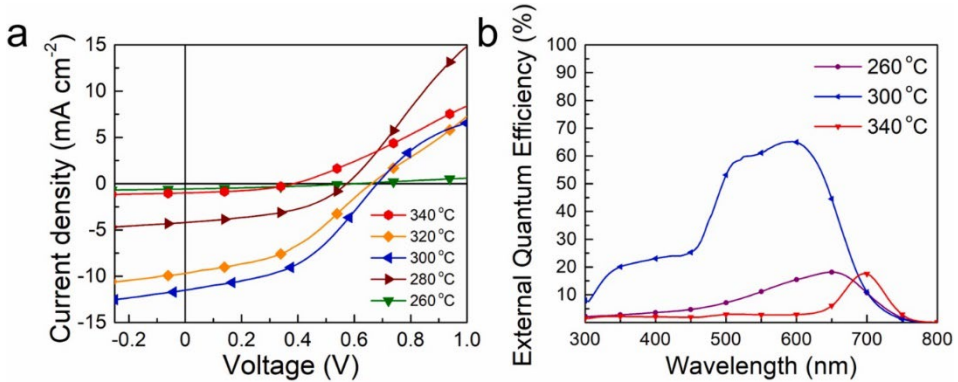


Figure 32. (a) Illuminated J–V curves of best Sb_2S_3 devices and (b) external quantum efficiency (EQE) plots of Sb_2S_3 devices with Sb_2S_3 absorber layer deposited at substrate temperatures of $260\text{--}340^\circ\text{C}$.

Based on the cumulative structural analysis of Sb_2S_3 absorber films and device characterization of respective Sb_2S_3 solar cells, it was demonstrated that the optimal CSS deposition of Sb_2S_3 films takes place at a substrate temperature of 300°C , where a compact Sb_2S_3 grain growth is achieved together with increased presence of favorable (hk1) planes. When compared with recent reports on the Sb_2S_3 fabrication with CSS and VTD techniques, the optimal processing temperature found in the current work is clearly lower than the deposition temperature interval of $350\text{--}450^\circ\text{C}$ reported elsewhere [18], [61], [64]. For instance, Hiu et al. reported a VTD deposition temperature of 495°C for depositing Sb_2S_3 films and achieved a PCE of 4.7% for the superstrate glass/ITO/CdS/ Sb_2S_3 /Au device [61]. Zeng et al. reported a 1.4%-efficient CdS/ Sb_2S_3 device, where a higher CSS processing temperature (no exact values were given) was found optimal for high-quality Sb_2S_3 absorber [63]. Employing a similar CSS deposition technique, although with an additional selenization process, Xie et al. produced a device with PCE of 4.5% [18]. In this work, the optimal source and substrate temperatures in the CSS reactor were 450°C and 370°C , respectively [18]. Guo et al. used an identical CSS technique and obtained a device efficiency of 3.8% after screening substrate temperatures of $300\text{--}400^\circ\text{C}$ [119]. However, for the best Sb_2S_3 device, optimal substrate temperature was not provided. When looking at studies where TE method was used, e.g., Chen et al. similarly found optimal substrate temperatures being in the $300\text{--}320^\circ\text{C}$ range, with the device achieving PCE of 3.0% [107]. Lian et al. followed a similar approach, employing a substrate temperature of 300°C , yet also including a selenization step for

the Sb_2S_3 absorber and a spiro-OMeTAD HTM atop the absorber, which yielded a device with PCE of 6.2% [93]. As can be seen, the latter findings reported substrate temperatures that match well with the results obtained in this study. In addition, we revealed a physical phenomenon that had not been reported before. It is important to emphasize that the cracking phenomenon of Sb_2S_3 films, observed during the CSS deposition at temperatures 340–400 °C, had a clear impact on the eventual solar cell performance. Had the cracking phenomena not occurred, then inferring from previous experience with the CSS deposition of CdTe and Sb_2Se_3 [163], [173], e.g., Sb_2S_3 films grown at higher substrate temperatures, such as seen in Fig. 30c and d, would have probably performed better, given that the films have larger grains and higher level of compactness. Although cracking might be an expected occurrence at elevated temperatures in thin film technologies, it was still unusual for an antimony chalcogenide material, and it could have direct implications for some of the proposed applications. For instance, such physical phenomena could mean Sb_2S_3 is not compatible as a bottom cell for the recently proposed Sb_2Se_3 – Sb_2S_3 monolithic tandem solar cell [179].

3.2.3 Recombination pathways and heterojunction band alignment in CdS/ Sb_2S_3 devices

Figure 33a shows I–V–T curves, which were measured to acquire better understanding of potential recombination processes for the best CdS/ Sb_2S_3 device (PCE = 3.8%). Fig. 33b shows a derived plot of logarithm of series resistance, R_s , vs. $1000/T$, where R_s increases with decreasing temperatures. Such behavior can be attributed to trapping of free carriers in the Sb_2S_3 bulk, which contributes to a significant R_s increase at lower temperatures [128]. The dominant recombination process in the CdS– Sb_2S_3 heterojunction was determined from the V_{oc} –T plot, as shown in Fig. 33c. Activation energy, E_A , for the recombination process was found according to Eq. 5. Linear extrapolation from higher temperatures to 0 K in the V_{oc} –T plot gave the activation energy of 0.88 ± 0.02 eV, which is much lower than the Sb_2S_3 band gap energy of 1.8 eV. This implies that interface recombination is the dominant recombination process in the CdS/ Sb_2S_3 device. In addition, PES was performed on CdS and Sb_2Se_3 films, as shown in Fig. 33d and e, respectively, to elucidate band alignment for the FTO/CdS/ Sb_2S_3 /Au device structure. Ionization potential (I_p) was found through extrapolation of the linear fit from valence band edge photoemission to 0 eV, giving ionization potentials of 5.65 ± 0.02 eV and 5.08 ± 0.03 eV for CdS and Sb_2S_3 , respectively. Considering the band gap values of CdS and Sb_2S_3 , a band diagram of the device was subsequently drawn, as shown in Fig. 33f, which revealed a small positive conduction band offset (CBO) of ≈ 0.1 eV between the CdS ETL and Sb_2S_3 absorber. Although it implies a formation of a spike, an electrostatic barrier to electrons moving to the front electrode, it has been argued that for such a small CBO, thermionic emission across the junction would still allow unimpeded charge transport [77], [180].

Deep defects could also explain substantial V_{oc} losses in the CdS/ Sb_2S_3 devices; TAS enabled characterization of deep defects in the Sb_2S_3 absorber. Similar to TAS measurements described in Section 1.3.2, relaxation frequencies, ω_0 , of capacitance steps were found from the maxima of a derivative capacitance ($-dC/d\omega$) plot. In the Arrhenius plot, natural logarithms of relaxation frequencies were plotted against inverse temperature to calculate the activation energy (E_A) and thermal emission prefactor (ξ_0) according to Eq. 1.

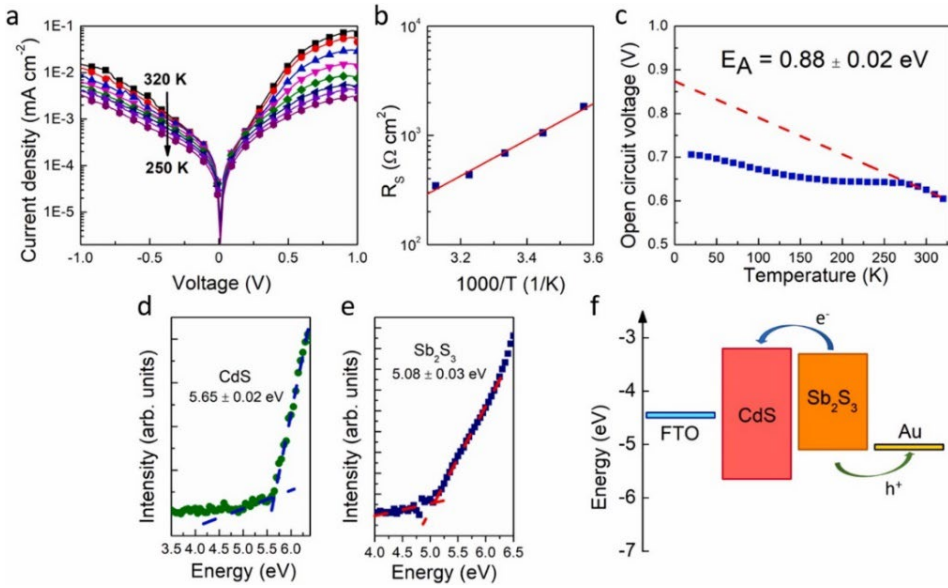


Figure 33. (a) C - f - T curves of CdS/Sb₂S₃ solar cell (PCE = 3.8%) measured from 80 to 320 K, (b) $-\omega dC(\omega)/d\omega$ vs E_ω plots that show two distinct peaks, (c) Arrhenius plot of $\ln(\omega/T^2)$ vs. $1/T$ used to calculate activation energies and thermal emission prefactors, PES spectra of (d) CdS on FTO/glass substrate and (e) Sb₂S₃ on CdS/FTO/glass substrates, (f) derived band diagram for the FTO/CdS/Sb₂S₃/Au solar cell structure.

Temperature-dependent capacitance-frequency (C - f - T) curves of a Sb₂S₃ device are shown in Fig. 34a. From the derivative capacitance plot, as shown in Fig. 34b, two distinct maxima could be discerned. Fig. 34c shows the Arrhenius plot with two activation energies: E_{A1} of 0.32 eV (ξ_0 of $4.2 \times 10^6 \text{ s}^{-1} \text{ K}^{-2}$) and E_{A2} of 0.37 eV (ξ_0 of $5.2 \times 10^6 \text{ s}^{-1} \text{ K}^{-2}$).

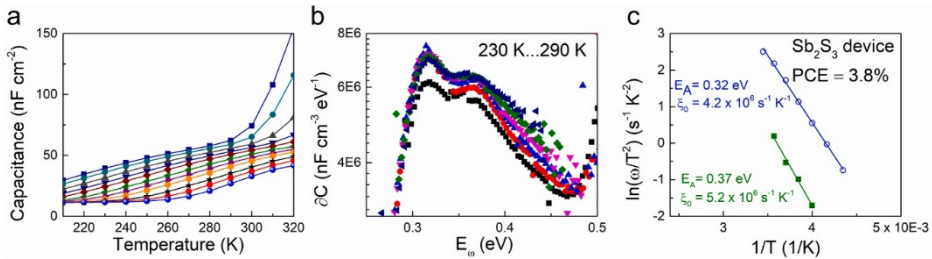


Figure 34. (a) C - f - T curves of CdS/Sb₂S₃ solar cell (PCE = 3.8%) measured from 80 to 320 K, (b) $-\omega dC(\omega)/d\omega$ vs E_ω plots that show two distinct peaks, (c) Arrhenius plot of $\ln(\omega/T^2)$ vs. $1/T$ used to calculate activation energies and thermal emission prefactors.

The activation energy of 0.32 eV has also been reported in a DLTS study on a TiO₂/Sb₂S₃ solar cell and was assigned to an Sb vacancy (V_{Sb}) [106]. A first-principles calculations study assigned comparable activation energies to a S antisite (S_{Sb}) defect and an Sb vacancy, respectively, and where both were reported to exist in high concentration due to low formation energy [119], [181]. Furthermore, a DFT study on intrinsic Sb₂S₃ found that V_{Sb} defects have two ionization energies between 0.3 and 0.4 eV, although these defects show relatively high defect formation energies [119]. Based on these reports and prior admittance measurements on the Sb₂Se₃ counterpart, presented in Section 3.1.7, at least one of the two activation energies could be tentatively assigned to the Sb vacancy.

Figure 35a shows PL spectra measured at 3–70 K for the Sb_2S_3 deposited at substrate temperature of 300 °C onto the CdS/FTO/glass substrate. It is important to mention that initial PL measurements were performed using a continuous wave He-Cd gas laser and an InGaAs detector [138], [149]. Since the continuous wave laser led to localized heating of the sample and given that a half-band was detected at around 1.35 eV, which was at the detection limit of the working range of the InGaAs photomultiplier tube (0.77–1.35 eV), a pulsed laser with a detection limit greater than 1.35 eV was opted. PL spectra revealed two PL bands: a narrow emission band peaked at 1.72 eV and a very broad asymmetric emission band peaked at around 1.40 eV.

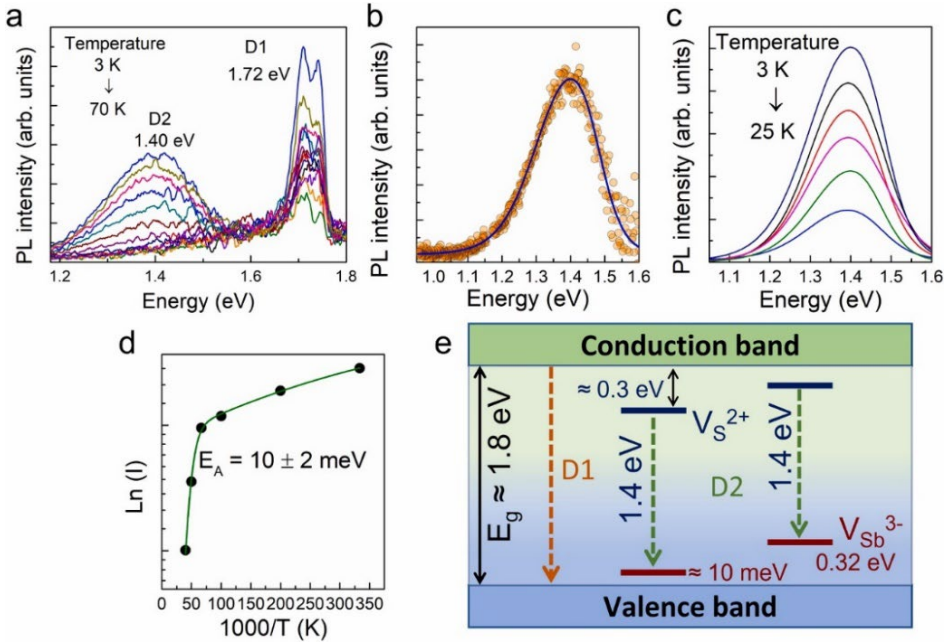


Figure 35. (a) Low-temperature PL spectra of Sb_2S_3 films deposited at substrate temperature of 300 °C on a CdS/FTO/glass substrate. For the given sample, (b) fitting of an asymmetric D2 band by using a single asymmetric sigmoidal function, and (c) temperature-dependent fitted PL spectra of D2 band measured in the temperature range of 3–25 K (d) Arrhenius plot giving thermal activation energy of the D2 band in Sb_2S_3 , which was obtained from fitted PL spectra, (e) model visualizing D1 band-to-band emission and D2 emission originating from a deep donor to shallow acceptor transition and/or from a deep donor to deep acceptor (V_{Sb}) transition.

The band D1 peaked at 1.72 eV was fitted by assuming there is a single peak and is related to a band-to-band transition. The broad band D2 was fitted by a single asymmetric sigmoidal function for the deconvolution of asymmetric band, as presented in Fig. 35b [138], [144]. Thereby, we obtained temperature-dependent PL spectra of band D2, as shown in Fig. 35c, which peak at approximately 1.40 eV. It is worth mentioning that while D1 band-to-band transition has been reported by a recent study employing room-temperature PL, to the best of our knowledge, the D2 band-related emission has not been reported thus far. To gain better understanding of the peculiarity of this band, the Arrhenius plot, as shown in Fig. 35d, was derived to E_A of the D2 band. Activation energy of 10 ± 2 meV was obtained, indicating that at least one shallow defect is involved in that recombination. In a classical approach, laser power dependence can provide supporting evidence if this D2 band originates from a donor-acceptor-pair (DAP)

recombination. However, since at higher laser power (≥ 10 mW) sample degradation was observed, and at lower laser power (< 3 mW) intensity of the signal was lost, we were not able to conduct laser power dependence measurements. Nevertheless, a subtle blue shift of the D2 band was observed with increasing temperature. Such a phenomenon, where a band is shifted toward higher energies with increasing temperature, has been related to a DAP recombination at low temperatures [138]. To satisfy this DAP mechanism, we should assume contribution from a certain deep donor defect, such as the S vacancy (V_S) (0.3–0.6 eV) [106], [181]. According to this scenario, the donor level will be occupied provided the temperature is increased, and recombination occurs between the conduction band and a deep acceptor.

According to TAS results, this deep acceptor can be assigned to the Sb vacancy (V_{Sb}). In theory, there is always one type of defect, which prevails over others in the crystal lattice. Given that the theoretical studies have provided low formation energies for vacancy defects (V_{Sb} , V_S) [106], [181], we consider these Schottky defects to be predominant and provide their formation mechanism in the Supplementary Material. Based on the above discussion and existence of possible defect levels, a DAP model is proposed in Fig. 35e. For the given model, it can be assumed the DAP transition could be related to either the transition between deep donor (DD) to shallow acceptor transition and/or between deep donor (V_S) and deep acceptor (V_{Sb} , as determined from TAS measurements). For better clarification, laser power dependence measurements would be needed to ascertain the shift of the band peak position per decade. Nevertheless, the presence of such complex defects is detrimental to the performance of Sb_2S_3 device, potentially limiting the built-in voltage and photocurrent collection.

In conclusion, we systematically studied the effect of substrate temperature on the Sb_2S_3 absorber microstructure and grain orientation with the CSS method, employing a wide substrate temperature range of 240–400 °C. It was found that CSS substrate temperature of 300 °C is optimal, resulting in compact crack-free films with increased presence of favorable (hk1) planes. Higher substrate temperatures (340–380 °C) caused Sb_2S_3 films to have bigger, more dense plate-shaped grains as compared to smaller flakes at lower substrate temperatures (240–280 °C). However, microcracks were detected in Sb_2S_3 films starting from substrate temperature of 320 °C. The maximum PV parameters, namely J_{sc} of 11.5 mA cm⁻², V_{oc} of 680 mV, FF of 48%, and PCE of 3.8% were obtained for the substrate temperature of 300 °C. For the same device the EQE showed the best response over the entire 300–800 nm wavelength range. For the best device, extraction of activation energy from the V_{oc} -T plot indicated that interface recombination is the dominant recombination mechanism in these devices. Based on the determined ionization potentials, a band diagram was derived, which showed favorable band alignment between the CdS ETL and Sb_2S_3 absorber. TAS study showed two deep defects with activation energies of 0.32 eV and 0.37 eV, while low-temperature PL measurement revealed a band-to-band emission at 1.72 eV and a broad band peaked at 1.40 eV, which was assigned to a donor-acceptor pair recombination. Although the device efficiency of 3.8% is a promising achievement and well-placed result within reported Sb_2S_3 based devices processed by physical deposition methods, the performance limiting factors like ETL/absorber interface recombination and existence of deep defects in the Sb_2S_3 absorber remain the key issues for this device structure. Further technological steps, such as post-deposition treatments and doping, combined with in-depth advanced characterization, need to be implemented to progress the development of emerging cost-efficient and environmentally friendly Sb_2S_3 thin film PV devices.

Conclusions

This doctoral work comprised of a development of growth strategies for depositing Sb_2Se_3 and Sb_2S_3 thin film solar cells by CSS and investigating deep defects in Sb_2Se_3 and Sb_2S_3 devices using TAS. Growth strategies, which included optimization of CSS source temperature, seed screening, and selection of a suitable ETL, were determined for optimal performance of Sb_2Se_3 and Sb_2S_3 PV devices with superstrate device architecture. The microstructure quality of both Sb_2Se_3 and Sb_2S_3 thin films were significantly affected by the CSS substrate temperature. The changes in the grain morphologies were explained by the theory of nucleation and grain growth.

1. Increasing substrate temperature from 300 to 450 °C yielded more compact and larger grain morphologies for the Sb_2Se_3 films deposited on the CSS-deposited CdS ETL.
2. Sb_2Se_3 thin films deposited at substrate temperature of 450 °C exhibited the highest performance with PCE of 2.8% when integrated into the PV device. This superior performance was attributed to the more compact Sb_2Se_3 films with larger grains and enhanced texture for (hk1) planes.
3. Similar evolution of grain morphology was also demonstrated in Sb_2S_3 thin films deposited at substrate temperatures from 240 to 400 °C. Microcracks started forming across the Sb_2S_3 films at substrate temperatures from 320 °C onwards. Previously unreported microcracks could be related to anisotropic thermal expansion coefficients of Sb_2S_3 and lattice mismatch between the CdS ETL and the Sb_2S_3 absorber.
4. Sb_2S_3 thin films deposited at substrate temperature of 300 °C showed the best performance with PCE of 3.8% when integrated into the PV device. Sb_2S_3 films were crack-free, compact and showed stronger presence for (hk1) planes than (hk0) planes.
5. The effect of heterojunction partner layers CdS, deposited by CSS and CBD, and TiO_2 , deposited by USP, and seed screening on the Sb_2S_3 film and device properties was also studied. PV device with the $\text{TiO}_2/\text{Sb}_2\text{Se}_3$ heterojunction achieved the highest efficiency with PCE of 5.3%, which was attributed to better Sb_2S_3 microstructure quality, improved photoresponse owing to the wider bandgap of TiO_2 , and enhanced grain orientation in the [001] direction.
6. Substrate temperature of 450 °C is suspected to induce chemical intermixing of Cd from the CBD-CdS ETL and Se from the Sb_2Se_3 absorber, which leads to the formation of a CdSe interface layer. This could explain the lowest performance and photoresponse for the PV device based on the CBD-CdS/ Sb_2Se_3 interface. Such phenomenon was not noted for the CSS-CdS/ Sb_2Se_3 device.
7. Seed screening approach, which involved a deposition of an amorphous Sb_2Se_3 film prior to the main Sb_2Se_3 absorber layer deposition, improved the grain orientation of the Sb_2Se_3 film in the [001] direction, as evidenced by TC analysis and pole figures measured by XRD.
8. In addition to common TC analysis, grain orientation of Sb_2Se_3 films grown with seed and no seed were analyzed deeper by pole figures measured by XRD and EBSD map. Pole figures measured by XRD revealed significantly stronger presence of (002) planes in the seed-assisted Sb_2Se_3 as compared to the Sb_2Se_3 film deposited without the seed layer. EBSD map of the seed-assisted Sb_2Se_3 film still showed a wide distribution of crystal orientations.

9. Deep defects were investigated for both Sb_2Se_3 and Sb_2S_3 PV devices by TAS measurements. Thermal activation energies of 0.4 eV, 0.5 eV, and 0.6–0.7 eV above VBM were found in Sb_2Se_3 devices, where the lowest energy was tentatively attributed to a deep acceptor defect, such as the V_{Sb} or Se_{Sb} defect. Two thermal activation energies between 0.3–0.4 eV were detected for a Sb_2S_3 PV device, which could originate from the V_{Sb} and S_{Sb} defects.
10. CV profiling of Sb_2Se_3 devices reveals a large defect density in the order of 10^{17} cm^{-3} , while the free carrier density of intrinsic Sb_2Se_3 is expected to be low in the order 10^{14} cm^{-3} .
11. Thermal activation energies, which were derived from the dark I–V–T measurements of both Sb_2Se_3 and Sb_2S_3 devices, are well below the respective bandgap energies of Sb_2Se_3 and Sb_2S_3 and therefore point to interface recombination as a dominant recombination mechanism.
12. Ionization energies measured for the CSS-CdS ETL and Sb_2S_3 absorber show that the CdS/ Sb_2S_3 heterojunction exhibits good band alignment. Despite a small positive CBO offset of 0.1 eV, thermionic emission is expected, allowing unimpeded electron transport.
13. Low-temperature PL measurements of Sb_2S_3 films revealed two PL bands D1 and D2. The D1 band peaked at 1.7 eV and was attributed to band-to-band transition, the previously unreported D2 band peaked at 1.4 eV and showed a subtle blue shift, which is indicative of a DAP recombination.

Acknowledgements

I would like to express my sincerest gratitude to my supervisors, Dr. Nicolae Spalatu and Dr. Ilona Oja Acik, for granting me the opportunity to pursue my doctoral degree in the Laboratory for Thin Film Energy Materials at Tallinn University of Technology. I greatly admire your motivation, passion, and dedication in driving our research to new heights.

I am also thankful to Dr. Arvo Mere for engaging in enlightening discussions that have significantly enhanced my understanding of semiconductor physics. Special thanks to Dr. Atanas Katerski for his invaluable technical assistance and to Dr. Malle Krunk for her guidance on research publications and doctoral seminars, which have honed my skills in concise scientific communication.

Furthermore, I extend my gratitude to Prof. Dr. Susan Schorr and Dr. Thomas Unold for providing me with the opportunity to conduct measurements at the Helmholtz-Zentrum Berlin for Materials and Energy. I am grateful to René Schwiddessen for his invaluable teachings on XRD measurements and analysis.

I would also like to acknowledge Raavo Josepson for his assistance with TAS measurements, Raitis Gržibovskis and Aivars Vembris from the University of Latvia for sharing their PES measurement results on our Sb_2S_3 devices, and Ramunas Nedzinskas and Rokas Kondrotas from the Lithuanian State Research Institute Center for Physical Sciences and Technology for conducting low-temperature PL measurements on our Sb_2S_3 films.

Their contributions have significantly enriched my research and I am sincerely thankful for their collaboration and support.

Lastly, I would like to express my heartfelt gratitude to my wife Mari and daughter Selma. Your unwavering support and constant encouragement have been instrumental in completing doctoral studies in time. I am also deeply grateful to my parents and Tartu family, especially Kaie and Agu, for creating a warm environment that facilitated the completion of my doctoral thesis.

This study was funded by the Estonian Research Council project PRG627 “Antimony chalcogenide thin films for next-generation semi-transparent solar cells applicable in electricity producing windows”, the Estonian Research Council project PSG689 “Bismuth Chalcogenide Thin-Film Disruptive Green Solar Technology for Next Generation Photovoltaics”, the Estonian Centre of Excellence project TK141 (TAR16016EK) “Advanced materials and high-technology devices for energy recuperation system”, and the EU H2020 program under the ERA Chair project 5GSOLAR grant agreement No 952509. R. Krautmann acknowledges Archimedes Foundation for financing the PhD student mobility through the Dora Plus Programme. This work has been partially supported by ASTRA “TUT Institutional Development Programme for 2016-2022” Graduate school of Functional Materials and Technologies (2014-2020.4.01.16-0032).

Abstract

Development of Sb_2Se_3 and Sb_2S_3 Thin Film Solar Cells by Close-Spaced Sublimation

Thin film photovoltaic (PV) technologies based on binary antimony chalcogenides Sb_2X_3 ($\text{X} = \text{S}, \text{Se}, \text{S/Se}$) have garnered significant attention due to their excellent optoelectronic properties, unique quasi-one-dimensional (Q-1D) characteristics, simple processing, low toxicity, earth-abundant constituents, and their applicability in innovative PV applications. These applications include tandem solar cells, internet-of-things (IoT) devices, flexible solar cells, and building-integrated PV (BIPV). Despite the rapid progress in Sb_2Se_3 and Sb_2S_3 PV devices, which have achieved impressive power conversion efficiencies (PCEs) of 10.1% and 8.0%, respectively, there are still technological challenges that need to be addressed to further enhance their performance. These challenges include unfavorable grain orientation and extensive defect-related recombination. Therefore, it is essential to develop growth strategies to improve the grain orientation and enhance the understanding of defect structures in Sb_2Se_3 and Sb_2S_3 films.

The primary aims of this doctoral thesis were to develop growth strategies for fabricating Sb_2Se_3 and Sb_2S_3 thin film solar cells using the close-spaced sublimation (CSS) method and to investigate deep defects in the Sb_2Se_3 and Sb_2S_3 devices using temperature-dependent admittance spectroscopy (TAS).

The thesis is based on three publications. Publications I and II focus on the fabrication and characterization of Sb_2Se_3 thin film PV devices, while Publication III centers around the development and characterization of Sb_2S_3 devices. The thesis comprises three chapters. Chapter I provides a literature overview of the material properties of Sb_2X_3 , state-of-the-art Sb_2X_3 PV devices, and the two main technological challenges currently limiting the performance of Sb_2Se_3 and Sb_2S_3 devices. Chapter II presents an overview of the experimental techniques used for fabricating the Sb_2Se_3 and Sb_2S_3 PV devices, along with details of the material and characterization techniques employed in the doctoral work. Chapter III is divided into two main sections. The first section focuses on the development of a growth strategy for depositing Sb_2Se_3 thin film solar cells using CSS. This includes the optimization of CSS substrate temperature, selection of a suitable electron transport layer (ETL), and the adoption of a seed screening approach. The chapter also demonstrates the analysis of grain orientation in the Sb_2Se_3 thin films through pole figure and electron backscatter diffraction (EBSD) measurements, along with the analysis of free carrier and defect densities using CV profiling and TAS. The second section concentrates on the development of a growth strategy for depositing Sb_2S_3 thin film solar cells using CSS, including the optimization of CSS substrate temperature. The section also investigates defects in Sb_2S_3 using TAS and low-temperature photoluminescence (PL) and discusses heterojunction band alignment and dominant recombination mechanisms.

In the fabrication of Sb_2Se_3 thin film solar cells by CSS, three different heterojunction layers were utilized: CSS-deposited CdS (CSS-CdS), spray-deposited TiO_2 , and CBD-deposited CdS (CBD-CdS). The optimized Sb_2Se_3 films employed a seed layer, which was deposited onto the electron transport layer (ETL) before the main absorber layer deposition. Sb_2S_3 thin films were also fabricated by CSS on the CSS-CdS ETL. Material characterization techniques such as scanning electron microscopy (SEM) and X-ray diffraction (XRD) were used. Pole figures and EBSD maps were generated for an Sb_2Se_3 film, while low-temperature photoluminescence (PL) and photoelectron spectroscopy (PES) were used to study Sb_2S_3

films. The Sb_2Se_3 and Sb_2S_3 PV devices were characterized using temperature-dependent current-voltage ($I-V-T$), external quantum efficiency (EQE), capacitance-voltage (CV) profiling, and TAS analysis methods.

The results demonstrated that the quality of the microstructure and grain orientation strongly depended on the CSS substrate temperature. Increasing the substrate temperature from 300 to 450 °C resulted in more compact and larger grain morphologies for the Sb_2Se_3 films deposited on the CSS-deposited CdS ETL. The Sb_2Se_3 thin films deposited at a substrate temperature of 450 °C exhibited the highest performance with a PCE of 2.8% when integrated into the PV device. This superior performance was attributed to the more compact Sb_2Se_3 films with larger grains and a stronger texture for (hk1) crystal planes. A similar evolution in grain morphology was observed in Sb_2S_3 thin films deposited at substrate temperatures ranging from 240 to 400 °C. However, microcracks started forming across the Sb_2S_3 films at substrate temperatures above 300 °C. These previously unreported microcracks could be attributed to the anisotropic thermal expansion coefficients of Sb_2S_3 and the lattice mismatch between the CdS ETL and the Sb_2S_3 absorber. Consequently, Sb_2S_3 thin films deposited at a substrate temperature of 300 °C exhibited the best performance with a PCE of 3.8% when integrated into the PV device. These films were crack-free, compact, and showed a stronger presence for (hk1) planes than (hk0) planes. Additionally, the properties of Sb_2S_3 films and devices were studied with different ETLs and a seed screening approach. The PV device based on the $\text{TiO}_2/\text{Sb}_2\text{Se}_3$ heterojunction achieved the highest efficiency with a PCE of 5.3%. This achievement was attributed to better Sb_2S_3 microstructure quality, improved photoresponse resulting from the wider bandgap of TiO_2 , and enhanced grain orientation in the [001] direction. It is suspected that a substrate temperature of 450 °C induces chemical intermixing through the outdiffusion of Cd from the CBD-CdS ETL and Se from the Sb_2Se_3 absorber, leading to the formation of a CdSe interface layer. This could explain the reduced photoresponse and lowest performance of the PV device based on the CBD-CdS/ Sb_2Se_3 interface. Pole figures measured by XRD mapping of the Sb_2Se_3 films deposited with and without a seed layer on the TiO_2 ETL confirmed the increase in texture for (002) planes in the seed-assisted Sb_2Se_3 film. An EBSD map of the grains in the seed-assisted Sb_2Se_3 film revealed a wide range of crystal orientations.

Deep defects in both Sb_2Se_3 and Sb_2S_3 PV devices were investigated using TAS analysis. Thermal activation energies of 0.4 eV, 0.5 eV, and 0.6–0.7 eV above the valence band maximum (VBM) were found in Sb_2Se_3 devices, with the lowest energy tentatively attributed to a deep acceptor defect such as the V_{Sb} or Se_{Sb} defect. Two thermal activation energies between 0.3–0.4 eV were detected for the Sb_2S_3 PV device, which could originate from the V_{Sb} and S_{Sb} defects. CV profiling of Sb_2Se_3 devices revealed a large defect density on the order of 10^{17} cm^{-3} , while the free carrier density of undoped Sb_2Se_3 is expected to be low, on the order of 10^{14} cm^{-3} . The thermal activation energies derived from dark $I-V-T$ measurements of both Sb_2Se_3 and Sb_2S_3 devices were well below the respective bandgap energies of Sb_2Se_3 and Sb_2S_3 , indicating interface recombination as a dominant recombination mechanism. Ionization energies measured for the CSS-CdS ETL and Sb_2S_3 absorber indicated that the CdS/ Sb_2S_3 heterojunction exhibited good band alignment. Despite a small positive conduction band offset of 0.1 eV, thermionic emission is expected, allowing unimpeded electron transport. Low-temperature PL measurements of Sb_2S_3 films revealed two PL bands, D1 and D2. The D1 band peaked at 1.7 eV and was attributed to band-to-band transition, while the previously unreported D2 band

peaked at 1.4 eV and showed a subtle blue shift, indicative of DAP recombination at low temperatures.

In conclusion, this doctoral work focused on the optimization of CSS substrate temperature, which was found to have a significant effect on the microstructure quality and grain orientation of Sb_2Se_3 and Sb_2S_3 films. The use of a seed screening approach was demonstrated as a processing route to enhance the Sb_2Se_3 film orientation along the [001] direction, as evidenced by the pole figures measured using XRD. The selection of TiO_2 as the ETL for Sb_2Se_3 resulted in the highest PCE of 5.3%. The detrimental effect of cracking phenomena in Sb_2S_3 thin films deposited at CSS substrate temperatures above 300 °C was revealed, and possible explanations were provided. TAS measurements provided insights into potential deep defects in Sb_2Se_3 and Sb_2S_3 devices. CV profiling revealed a high defect density of 10^{17} cm^{-3} in the Sb_2Se_3 device. Low-temperature PL of Sb_2S_3 revealed a wide band peaking at 1.4 eV, indicating extensive non-radiative recombination. Interface recombination was identified as the prevalent recombination mechanism. However, the CdS and Sb_2S_3 heterojunction exhibited very good band alignment.

The novelty of this doctoral work lies in the optimization of CSS substrate temperature, which was demonstrated to have a significant effect on the microstructure quality and grain orientation of Sb_2Se_3 and Sb_2S_3 films. The use of a seed screening approach provided insights into enhancing the Sb_2Se_3 film orientation along the [001] direction. The inclusion of pole figures measured by XRD and an EBSD map improved the analysis of grain orientation in Sb_2X_3 films, where preferred orientations are often claimed hastily. The occurrence of cracking phenomena in Sb_2S_3 thin films at CSS substrate temperatures above 300 °C was revealed, along with possible explanations. TAS measurements shed light on potential deep defects in Sb_2Se_3 and Sb_2S_3 absorbers. By developing a comprehensive deposition strategy and improving the understanding of defect chemistry in Sb_2Se_3 and Sb_2S_3 , this work has laid the groundwork for the future development of $\text{Sb}_2(\text{S,Se})_3$ solar cells using CSS.

Kokkuvõte

Sb₂Se₃ ja Sb₂S₃ õhukesekileliste päikesepatareide arendamine lähidistants-sublimatsiooni meetodil

Õhukesekilelised päikesepatareitehnoloogiad (*ingl thin film photovoltaic (PV) technologies*), mis põhinevad binaarsetel antimoni kalkogeniididel Sb₂X₃ (X = S, Se, S/Se), on pälvitud laialdast tähelepanu, sest neil on suurepärased optoelektronilised omadused ja unikaalne kvaasi-ühemõõtmeline (Q-1D) kristallikasv. Seejuures on materjalid lihtsasti valmistatavad, neil on madal toksilisus ja nad koosnevad maapõues rohkesti leiduvatest keemilistest elementidest. Need omadused võimaldavad Sb₂X₃ materjale kasutada uuenduslikes päikesepatareide rakendustes, nagu näiteks tandem-päikesepatareid, värvvõrguseadmed (*ingl internet-of-things – IoT*), painduvad päikesepatareid ja ehitisintegreeritud päikesepatareid (*ingl building-integrated PV – BIPV*). Vaatamata Sb₂Se₃ ja Sb₂S₃ päikesepatareide kiirele arengule viimase kümnendi jooksul, mille jooksul on päikesepatareide jõudlus küündinud efektiivsusteni vastavalt 10,1% ja 8,0%, tuleb nende jõudluste olulisemaks suurendamiseks lahendada mitmeid materjalitehnoloogilisi väljakutseid. Näiteks tuleb välja arendada kasvustrateegiaid Sb₂Se₃ ja Sb₂S₃ õhukestes kiledes laengute transporti soodustava kristalliidi orientatsiooni saavutamiseks ning saada ülevaade kiledes leiduvatest defektidest.

Käesoleva doktoritöö peamiseks eesmärgiks on välja töötada kasvustrateegiaid Sb₂Se₃ ja Sb₂S₃ õhukesekileliste päikesepatareide valmistamiseks lähidistants-sublimatsiooni (*ingl close-spaced sublimation – CSS*) meetodil ning uurida Sb₂Se₃ ja Sb₂S₃ kiledes esinevaid sügavaid defekte temperatuurist sõltuva kompleksjuhtivusspektroskoopia (*ingl temperature-dependent admittance spectroscopy – TAS*) abil.

Doktoritöö põhineb kolmel publikatsioonil. Artiklid I ja II keskenduvad Sb₂Se₃ õhukesekileliste päikesepatareide valmistamisele ja iseloomustamisele, samas kui artikkel III keskendub Sb₂S₃ päikesepatareide väljatöötamisele ja iseloomustamisele. Doktoritöö koosneb kolmest peatükist. Peatükk I annab ülevaate Sb₂X₃ materjali omadustest, Sb₂X₃ päikesepatareide arengust ning kahest peamisest tehnoloogilisest väljakutsest, mis hetkel Sb₂Se₃ ja Sb₂S₃ seadmete jõudlust piiravad. Peatükk II annab ülevaate Sb₂Se₃ ja Sb₂S₃ päikesepatareide valmistamiseks kasutatud eksperimentaalsetest meetoditest, samuti doktoritöös kasutatud materjali ja päikesepatarei iseloomustamiseks kasutatud meetoditest. Peatükk III jaguneb kaheks osaks. Esimene osa keskendub kasvustrateegia väljatöötamisele Sb₂Se₃ õhukeste kiledes ja päikesepatareide valmistamiseks CSS meetodiga. Selle hulka kuulub CSS substraadi temperatuuri optimeerimine, sobiva elektrontranspordi kihi (*ingl electron transport layer – ETL*) valimine ja idukihi (*ingl seed layer – SL*) meetodi juurutamine. Peatükk sisaldab ka Sb₂Se₃ õhukeste kiledes kristalliidi orientatsiooni analüüsi läbi pooluskujutiste (*ingl pole figures*) ja tagasihajunud elektronide difraktsiooni (*ingl electron backscatter diffraction – EBSD*) mõõtmiste ning vabade laengukandjate ja defektide tiheduse analüüsi mahtuvus-pinge (*ingl capacitance-voltage – CV*) mõõtmiste ja TAS meetodi abil. Teine osa keskendub kasvustrateegia väljatöötamisele Sb₂Se₃ õhukesekileliste päikesepatareide valmistamiseks CSS meetodiga, sealhulgas CSS substraadi temperatuuri optimeerimisele. Siin osas uuritakse Sb₂S₃ defekte, kasutades TAS ja madalatemperatuurilist fotoluminestsentsi (*ingl photoluminescence – PL*), ning heterosiirde energiatsoonide joondumist ja seadmes domineerivaid rekombinatsioonimehhanisme.

Sb_2Se_3 õhukesekileliste päikesepatareide valmistamisel CSS meetodiga kasutati kolme erinevat elektrontranspordi kihti: CSS-ga sadestatud CdS (CSS-CdS), keemiliselt pihustatud TiO_2 ja keemilise vannsadestamismeetodiga (ingl *chemical bath deposition – CBD*) sadestatud CdS (CBD-CdS). Optimeeritud Sb_2Se_3 kiled kasutasid idukihti, mis sadestati elektrontranspordi kihile enne põhikihi sadestamist. Sb_2S_3 õhukesi kilesid valmistati samuti CSS meetodiga, kuid ainult CSS-CdS elektrontranspordi kihile. Materjalide iseloomustamiseks kasutati skaneerivat elektronmikroskoopia (SEM) ja röntgendifraktsiooni (XRD) analüüsimeetodeid. Sb_2S_3 kiledede defektide uurimiseks kasutati madalatemperatuurilist fotoluminesentsi (PL), valentstsoonide maksimumide määramiseks fotoelektronspektroskoopiat (PES). Mõlemal, nii Sb_2Se_3 kui ka Sb_2S_3 päikesepatareid iseloomustati temperatuurist sõltuva voolu-pinge (I–V–T) karakteristike, välise kvantefektiivsuse (ingl *external quantum efficiency – EQE*) ja TAS analüüsimeetodite abil.

Tulemused näitasid, et Sb_2Se_3 ja Sb_2S_3 õhukeste kiledede mikrostruktuuri kvaliteet ja kristalliidi orientatsioon sõltusid oluliselt CSS substraadi temperatuurist. Substraadi temperatuuri suurendamine 300 °C-lt 450 °C-le muutis CSS-CdS partnerkihile sadestatud Sb_2Se_3 õhukeste kiledede kristalliteerimise suuremaks ja kile mikrostruktuuri kompaktsemaks. Nii saavutasid substraadi temperatuuril 450 °C sadestatud Sb_2S_3 õhukese kiled päikesepatareidesse integreerimisel kõrgeima, 2,8% efektiivsuse, mida seostati kompaktsemate ja suurimate teradega Sb_2Se_3 kiledega. Nendes kiledes leidis ka rohkem (hk1) kui (hk0) kristallitasandeid võrreldes teistel temperatuuridel sadestatud Sb_2Se_3 kiledega. Lisaks uuriti Sb_2S_3 kiledede ja päikesepatareide omadusi kasutades erinevaid elektrontranspordi kihte ja idukihti. Päikesepatarei, mis põhineb $\text{TiO}_2/\text{Sb}_2\text{Se}_3$ heterosiirdel ja kus Sb_2S_3 absorberikihi sadestamisel kasutati idukihti, saavutas kõrgeima, 5,3% efektiivsuse. Seda võimaldas veel kõrgema kvaliteediga Sb_2Se_3 mikrostruktuur, suurendatud kristalliidi orientatsioon [001] kristallisuunas ja kõrgem kvantefektiivsus tänu suuremale TiO_2 keelutsoonilaiusele võrreldes CSS-CdS ja CBD-CdS ETL-idega. Heterosiirde CBD-CdS/ Sb_2Se_3 puhul arvatakse, et substraadi temperatuur 450 °C põhjustab Cd ja Se difundeerimist vastavalt CdS ja Sb_2Se_3 kihtidest, moodustades kahe kihi piirpinnale CdSe vahekihi. Selle tulemusena väheneb CBD-CdS/ Sb_2Se_3 päikesepatarei kvantefektiivsus ja jõudlus võrreldes CSS-CdS/ Sb_2Se_3 ja $\text{TiO}_2/\text{Sb}_2\text{Se}_3$ päikesepatareiga. Kristalliidi orientatsiooni uuriti lähemalt idukihiga ja ilma idukihita TiO_2 ETL-ile sadestatud Sb_2Se_3 kiledelt. Röntgendifraktsiooni analüüsi meetodiga mõõdeti pooluskujutised, mis kinnitasid idukihiga sadestatud Sb_2Se_3 kile kristallitide joondumise paranemist [001] kristallisuunas.

Sarnast kiledede morfoloogia muutumist täheldati ka Sb_2S_3 õhukeste kiledede puhul, mis sadestati substraadi temperatuuridel vahemikus 240–400 °C. Substraadi temperatuuridel üle 300 °C hakkasid Sb_2S_3 kiledesse moodustuma mikropraod. Need kirjanduses varem mittemainitud mikropraod võivad olla seotud Sb_2S_3 soojuspaisumisteguri anisotroopsusega ja CdS ETL-i ning Sb_2S_3 absorberikihi kristallvõrepunktide mitte kattumisega. Seetõttu näitasid parimat jõudlust päikesepatareid, mis põhinesid substraadi temperatuuril 300 °C sadestatud Sb_2S_3 absorberkihtidel. Need kiled olid pragudeta, kompaktsed ning näitasid eelistatult (hk1) kui (hk0) kristallitasandite olemasolu.

TAS analüüsi abil uuriti Sb_2Se_3 ja Sb_2S_3 kiledes leiduvaid sügavaid defekte. Sb_2Se_3 seadmetes leiti kokku kolm aktivatsioonienergiat, mis on 0,4 eV, 0,5 eV ja 0,6–0,7 eV valentstsoonimaksimumi (ingl *valence band maximum – VBM*) suhtes, kusjuures madalaimat energianivood seostati esialgselt sügavale aktseptordefektile, nagu näiteks V_{Sb} või Se_{Sb} defekt. Sb_2S_3 PV seadme TAS mõõtmiste käigus leiti kaks aktiveerimisenergiat

vahemikus 0,3–0,4 eV, mis võisid pärineda V_{sb} ja S_{sb} defektidest. Sb_2Se_3 seadmete CV mõõtmised viitavad defektide suurele tiheduse suurusjärgus 10^{17} cm^{-3} , samas kui Sb_2Se_3 vabade laengukandjate tihedus on madal, umbes 10^{14} cm^{-3} . Sb_2Se_3 ja Sb_2S_3 seadmete V_{oc} -T kõveratest leitud aktivatsioonienergiad olid madalamad vastavalt Sb_2Se_3 ja Sb_2S_3 keelutsoonilaiustest, mis tähendab, et piirpinna rekombinatsioon on mõlemat tüüpi päikesepatareide domineerivaks rekombinatsioonimehhanismiks. CSS-CdS ETL-i ja Sb_2S_3 absorberikihi mõõdetud ionisatsioonienergiatest tuletati heterosiirde tsoonidiagramm, mis näitas, et CdS/ Sb_2S_3 heterosiirde juhtivustsooni miinimumid (ingl *conduction band minimum* – CBM) joonduvad väga hästi, võimaldades teoreetiliselt takistusteta elektronide transporti. Sb_2S_3 kilede madalatemperatuuriline PL mõõtmine andsid kaks PL piiki D1 ja D2. D1 piigi maksimum asus 1,7 eV juures ja seda seostati tsoonidevahelise üleminekuga, D2 piigi maksimum asus 1,4 eV juures ja näitas väikest sininihet, mis võib viidata doonor-aktseptor paari (DAP) rekombinatsioonile.

Kokkuvõttes keskendus see doktoritöö õhukesekiliste Sb_2Se_3 ja Sb_2S_3 päikesepatareide valmistamisele CSS meetodiga. Kasvustrateegiate väljatöötamisel optimeeriti CSS substraadi temperatuurid, millel oli märkimisväärne mõju Sb_2Se_3 ja Sb_2S_3 kilede mikrostruktuuri kvaliteedile ja kristalliidi orientatsioonile. Idukihi kasutamine näitas, et Sb_2S_3 kile orientatsiooni saab suurendada [001] suunas, nagu tõestasid XRD abil mõõdetud pooluskujutised. TiO_2 valimine elektrontranspordi kihiks Sb_2Se_3 -le tõi tulemuseks kõrgeima efektiivsuse 5,3%. Sb_2S_3 õhukeste kiledes esinesid mikropraod, mis tekkisid CSS substraadi temperatuuridel üle 300 °C. TAS mõõtmised andsid teavet potentsiaalsete sügavate defektide kohta Sb_2Se_3 ja Sb_2S_3 seadmetes. CV profiilide järgi oli Sb_2Se_3 päikesepatareides defektide tihedus ligikaudu 10^{17} cm^{-3} . Madalatemperatuuriline PL mõõtmine tõi Sb_2S_3 kiledes esile laia piigi maksimumiga 1,4 eV, mis viitab ulatuslikule mittekiirguslikule rekombinatsioonile Sb_2Se_3 kiledes. IV-kõverate temperatuursõltuvuse analüüsist leiti, et nii Sb_2Se_3 kui Sb_2S_3 seadmete peamiseks rekombinatsioonimehhanismiks on piirpinna rekombinatsioon. Ionisatsioonienergiatest tuletatud heterosiirde tsoonidiagramm näitasid CdS ja Sb_2S_3 juhtivustsoonide väga head ühilduvust.

Selle doktoritöö uudsus seisneb CSS substraadi temperatuuri optimeerimises, millel oli märkimisväärne mõju Sb_2S_3 ja Sb_2Se_3 kilede mikrostruktuuri kvaliteedile ja terade orientatsioonile. Idukihi rakendamine on üks töötlemisviise Sb_2Se_3 kile orientatsiooni suurendamiseks [001] kristallisuunas. XRD pooluskujutiste ja EBSD kaardi kasutamine parandab ortorombiliste Sb_2X_3 kilede kristalliidi orientatsiooni analüüsi täpsust, kus järeldusi eelistatud orientatsiooni olemasolust tehakse tihtipeale ennatlikult. Sb_2S_3 õhukestes kiledes toodi välja pragunemisega seotud nähtused CSS substraadi temperatuuridel üle 300 °C koos võimalike põhjuste ja tagajärgedega. TAS mõõtmiste abil leiti mitu potentsiaalselt sügavat defekti Sb_2Se_3 ja Sb_2S_3 absorberkihtides. Selle töö raames väljatöötatud sadestamisstrateegia Sb_2Se_3 ja Sb_2S_3 materjalide jaoks, parem ülevaade nende materjalide defektistruktuuridest ja teistest jõudlust piiravatest faktoritest panevad aluse tulevasele $Sb_2(S,Se)_3$ päikesepatareide arendustööle CSS meetodi abil.

References

- [1] D. Lugo-laguna, A. Arcos-Vargas, and F. Nuñez-herandez, "A European Assessment of the Solar Energy Cost: Key Factors and Optimal Technology," *Sustainability* 2021, Vol. 13, Page 3238, vol. 13, no. 6, p. 3238, Mar. 2021, doi: 10.3390/SU13063238.
- [2] E. Vartiainen, G. Masson, C. Breyer, D. Moser, and E. Román Medina, "Impact of weighted average cost of capital, capital expenditure, and other parameters on future utility-scale PV levelised cost of electricity," *Progress in Photovoltaics: Research and Applications*, vol. 28, no. 6, pp. 439–453, Jun. 2020, doi: 10.1002/PIP.3189.
- [3] "World Energy Outlook 2022 – Analysis - IEA." <https://www.iea.org/reports/world-energy-outlook-2022> (accessed May 03, 2023).
- [4] "Solar PV – Analysis - IEA." <https://www.iea.org/reports/solar-pv> (accessed May 03, 2023).
- [5] "COMMUNICATION FROM THE COMMISSION TO THE EUROPEAN PARLIAMENT, THE COUNCIL, THE EUROPEAN ECONOMIC AND SOCIAL COMMITTEE AND THE COMMITTEE OF THE REGIONS, EU Solar Energy Strategy." <https://eur-lex.europa.eu/legal-content/EN/TXT/?uri=COM%3A2022%3A221%3AFIN&qid=1653034500503> (accessed Mar. 03, 2023).
- [6] S. Barthwal, R. Kumar, and S. Pathak, "Present Status and Future Perspective of Antimony Chalcogenide (Sb_2X_3) Photovoltaics," *ACS Appl Energy Mater*, vol. 5, no. 6, pp. 6545–6585, Jun. 2022, doi: 10.1021/ACSAEM.2C00420/ASSET/IMAGES/LARGE/AE2C00420_0022.JPEG.
- [7] A. Zakutayev *et al.*, "Emerging inorganic solar cell Efficiency Tables (version 2)," *Journal of Physics: Energy*, no. 7, Mar. 2021, doi: 10.1088/2515-7655/abebca.
- [8] Y. C. Choi, D. U. Lee, J. H. Noh, E. K. Kim, and S. Il Seok, "Highly improved Sb_2S_3 sensitized-inorganic-organic heterojunction solar cells and quantification of traps by deep-level transient spectroscopy," *Adv Funct Mater*, vol. 24, no. 23, pp. 3587–3592, Jun. 2014.
- [9] S. Wang *et al.*, "A Novel Multi-Sulfur Source Collaborative Chemical Bath Deposition Technology Enables 8%-Efficiency Sb_2S_3 Planar Solar Cells," *Advanced Materials*, vol. 34, no. 41, p. 2206242, Oct. 2022, doi: 10.1002/ADMA.202206242.
- [10] Z. Duan *et al.*, " Sb_2Se_3 Thin-Film Solar Cells Exceeding 10% Power Conversion Efficiency Enabled by Injection Vapor Deposition Technology," *Advanced Materials*, vol. 34, no. 30, p. 2202969, Jul. 2022, doi: 10.1002/ADMA.202202969.
- [11] X. Wen *et al.*, "Vapor transport deposition of antimony selenide thin film solar cells with 7.6% efficiency," *Nat Commun*, vol. 9, no. 1, pp. 1–10, Dec. 2018, doi: 10.1038/s41467-018-04634-6.
- [12] Z. Li *et al.*, "9.2%-efficient core-shell structured antimony selenide nanorod array solar cells," *Nat Commun*, vol. 10, no. 1, pp. 1–9, Dec. 2019, doi: 10.1038/s41467-018-07903-6.

- [13] Y. Zhao *et al.*, “Regulating Energy Band Alignment via Alkaline Metal Fluoride Assisted Solution Post-Treatment Enabling $\text{Sb}_2(\text{S,Se})_3$ Solar Cells with 10.7% Efficiency,” *Adv Energy Mater*, vol. 12, no. 1, p. 2103015, Jan. 2022, doi: 10.1002/AENM.202103015.
- [14] G. Li, Z. Li, X. Liang, C. Guo, K. Shen, and Y. Mai, “Improvement in Sb_2Se_3 Solar Cell Efficiency through Band Alignment Engineering at the Buffer/Absorber Interface,” *ACS Appl Mater Interfaces*, vol. 11, no. 1, pp. 828–834, Jan. 2019, doi: 10.1021/acsami.8b17611.
- [15] Z. Li *et al.*, “ Sb_2Se_3 thin film solar cells in substrate configuration and the back contact selenization,” *Solar Energy Materials and Solar Cells*, vol. 161, pp. 190–196, Mar. 2017, doi: 10.1016/j.solmat.2016.11.033.
- [16] X. Liang *et al.*, “Crystallographic Orientation Control of 1D Sb_2Se_3 Nanorod Arrays for Photovoltaic Application by In Situ Back-Contact Engineering,” *Solar RRL*, vol. 4, no. 10, p. 2000294, Oct. 2020, doi: 10.1002/solr.202000294.
- [17] L. Wang *et al.*, “Stable 6%-efficient Sb_2Se_3 solar cells with a ZnO buffer layer,” *Nat Energy*, vol. 2, no. 4, p. 17046, Mar. 2017, doi: 10.1038/nenergy.2017.46.
- [18] H. Zhang *et al.*, “Controllable orientations for Sb_2S_3 solar cells by vertical VTD method,” *Progress in Photovoltaics: Research and Applications*, vol. 28, no. 8, pp. 823–832, Aug. 2020, doi: 10.1002/pip.3278.
- [19] P. Fan *et al.*, “Quasi-Vertically Oriented Sb_2Se_3 Thin-Film Solar Cells with Open-Circuit Voltage Exceeding 500 mV Prepared via Close-Space Sublimation and Selenization,” *ACS Appl Mater Interfaces*, vol. 13, no. 39, pp. 46671–46680, Oct. 2021, doi: 10.1021/ACSAMI.1C13223.
- [20] S. Yuan *et al.*, “Efficient planar antimony sulfide thin film photovoltaics with large grain and preferential growth,” *Solar Energy Materials and Solar Cells*, vol. 157, pp. 887–893, Dec. 2016, doi: 10.1016/J.SOLMAT.2016.07.050.
- [21] D. Ariosa, F. Elhordoy, E. A. Dalchiele, R. E. Marotti, and C. Stari, “Texture vs morphology in ZnO nano-rods: On the x-ray diffraction characterization of electrochemically grown samples,” *J Appl Phys*, vol. 110, no. 12, p. 124901, Dec. 2011, doi: 10.1063/1.3669026.
- [22] C. N. Savory and D. O. Scanlon, “The complex defect chemistry of antimony selenide,” *J Mater Chem A Mater*, vol. 7, no. 17, pp. 10739–10744, Apr. 2019, doi: 10.1039/c9ta02022e.
- [23] J. Dong, Y. Liu, Z. Wang, and Y. Zhang, “Boosting VOC of antimony chalcogenide solar cells: A review on interfaces and defects,” *Nano Select*, vol. 2, no. 10, pp. 1818–1848, Oct. 2021, doi: 10.1002/NANO.202000288.
- [24] C. Ballif, F. J. Haug, M. Boccard, P. J. Verlinden, and G. Hahn, “Status and perspectives of crystalline silicon photovoltaics in research and industry,” *Nature Reviews Materials* 2022 7:8, vol. 7, no. 8, pp. 597–616, Mar. 2022, doi: 10.1038/s41578-022-00423-2.
- [25] B. L. Smith, M. Woodhouse, K. A. W. Horowitz, T. J. Silverman, J. Zuboy, and R. M. Margolis, “Photovoltaic (PV) Module Technologies: 2020 Benchmark Costs and Technology Evolution Framework Results,” Nov. 2021, doi: 10.2172/1829459.
- [26] M. A. Green *et al.*, “Solar cell efficiency tables (Version 61),” *Progress in Photovoltaics: Research and Applications*, vol. 31, no. 1, pp. 3–16, Jan. 2023, doi: 10.1002/PIP.3646.

- [27] W. Shockley and H. J. Queisser, "Detailed Balance Limit of Efficiency of p-n Junction Solar Cells," *J Appl Phys*, vol. 32, no. 3, p. 510, Jun. 2004, doi: 10.1063/1.1736034.
- [28] P. K. Nayak, S. Mahesh, H. J. Snaith, and D. Cahen, "Photovoltaic solar cell technologies: analysing the state of the art," *Nature Reviews Materials* 2019 4:4, vol. 4, no. 4, pp. 269–285, Mar. 2019, doi: 10.1038/s41578-019-0097-0.
- [29] A. Romeo and E. Arregiani, "CdTe-Based Thin Film Solar Cells: Past, Present and Future," *Energies* 2021, Vol. 14, Page 1684, vol. 14, no. 6, p. 1684, Mar. 2021, doi: 10.3390/EN14061684.
- [30] "Directive 2011/65/EU of the European Parliament and of the Council of 8 June 2011 on the restriction of the use of certain hazardous substances in electrical and electronic equipment (recast)." <https://eur-lex.europa.eu/legal-content/EN/TXT/?uri=celex%3A32011L0065> (accessed Mar. 21, 2023).
- [31] R. A. Marques Lameirinhas, J. P. N. Torres, and J. P. de Melo Cunha, "A Photovoltaic Technology Review: History, Fundamentals and Applications," *Energies* 2022, Vol. 15, Page 1823, vol. 15, no. 5, p. 1823, Mar. 2022, doi: 10.3390/EN15051823.
- [32] T. D. Lee and A. U. Ebong, "A review of thin film solar cell technologies and challenges," *Renewable and Sustainable Energy Reviews*, vol. 70. Elsevier Ltd, pp. 1286–1297, Apr. 01, 2017. doi: 10.1016/j.rser.2016.12.028.
- [33] T. Unold, "Accelerating research on novel photovoltaic materials," *Faraday Discuss*, vol. 239, no. 0, pp. 235–249, Oct. 2022, doi: 10.1039/D2FD00085G.
- [34] H. Min *et al.*, "Perovskite solar cells with atomically coherent interlayers on SnO₂ electrodes," *Nature* 2021 598:7881, vol. 598, no. 7881, pp. 444–450, Oct. 2021, doi: 10.1038/s41586-021-03964-8.
- [35] Y. Ding *et al.*, "Single-crystalline TiO₂ nanoparticles for stable and efficient perovskite modules," *Nature Nanotechnology* 2022 17:6, vol. 17, no. 6, pp. 598–605, Apr. 2022, doi: 10.1038/s41565-022-01108-1.
- [36] "Best Research-Cell Efficiency Chart | Photovoltaic Research | NREL." <https://www.nrel.gov/pv/cell-efficiency.html> (accessed Mar. 21, 2023).
- [37] T. Yang *et al.*, "One-stone-for-two-birds strategy to attain beyond 25% perovskite solar cells," *Nature Communications* 2023 14:1, vol. 14, no. 1, pp. 1–10, Feb. 2023, doi: 10.1038/s41467-023-36229-1.
- [38] Z. Hu, C. Ran, H. Zhang, L. Chao, Y. Chen, and W. Huang, "The Current Status and Development Trend of Perovskite Solar Cells," *Engineering*, Dec. 2022, doi: 10.1016/J.ENG.2022.10.012.
- [39] C.-H. Chen *et al.*, "Toxicity, Leakage, and Recycling of Lead in Perovskite Photovoltaics," *Adv Energy Mater*, p. 2204144, 2023, doi: 10.1002/AENM.202204144.
- [40] R. Sun *et al.*, "18.2%-efficient ternary all-polymer organic solar cells with improved stability enabled by a chlorinated guest polymer acceptor," *Joule*, vol. 7, no. 1, pp. 221–237, Jan. 2023, doi: 10.1016/J.JOULE.2022.12.007.
- [41] Y. Li *et al.*, "Recent Progress in Organic Solar Cells: A Review on Materials from Acceptor to Donor," *Molecules*, vol. 27, no. 6, p. 1800, Mar. 2022, doi: 10.3390/MOLECULES27061800.

- [42] Y. Ren *et al.*, "Hydroxamic acid pre-adsorption raises the efficiency of cosensitized solar cells," *Nature* 2022 613:7942, vol. 613, no. 7942, pp. 60–65, Oct. 2022, doi: 10.1038/s41586-022-05460-z.
- [43] H. Zhu *et al.*, "Antimony selenide thin-film solar cells," *Semicond Sci Technol*, vol. 31, no. 6, p. 063001, Apr. 2016, doi: 10.1088/0268-1242/31/6/063001.
- [44] C. Chen *et al.*, "Characterization of basic physical properties of Sb₂Se₃ and its relevance for photovoltaics," *Frontiers of Optoelectronics*, vol. 10, no. 1, pp. 18–30, Mar. 2017, doi: 10.1007/s12200-017-0702-z.
- [45] U. Ali Shah *et al.*, "Wide Bandgap Sb₂S₃ Solar Cells," *Adv Funct Mater*, vol. 31, 7 no. 27, p. 2100265, Jul. 2021, doi: 10.1002/ADFM.202100265.
- [46] Y. Zhou *et al.*, "Thin-film Sb₂Se₃ photovoltaics with oriented one-dimensional ribbons and benign grain boundaries," *Nat Photonics*, vol. 9, no. 6, pp. 409–415, 2015, doi: 10.1038/nphoton.2015.78.
- [47] T. D. C. Hobson *et al.*, "Isotype Heterojunction Solar Cells Using n-Type Sb₂Se₃ Thin Films," *Chemistry of Materials*, Mar. 2020, doi: 10.1021/acs.chemmater.0c00223.
- [48] R. Kondrotas, C. Chen, and J. Tang, "Sb₂S₃ Solar Cells," *Joule*, vol. 2, no. 5, pp. 857–878, May 2018, doi: 10.1016/J.JOULE.2018.04.003.
- [49] J. Zhang *et al.*, "All Antimony Chalcogenide Tandem Solar Cell," *Solar RRL*, vol. 4, no. 4, p. 2000048, Apr. 2020, doi: 10.1002/SOLR.202000048.
- [50] M. M. Nicolás-Marín, J. R. González-Castillo, O. Vigil-Galán, and M. Courel, "The state of the art of Sb₂(S, Se)₃ thin film solar cells: current progress and future prospect," *J Phys D Appl Phys*, vol. 55, no. 30, p. 303001, Apr. 2022, doi: 10.1088/1361-6463/AC5F32.
- [51] X. Liu *et al.*, "Thermal evaporation and characterization of Sb₂Se₃ thin film for substrate Sb₂Se₃/CdS solar cells," *ACS Appl Mater Interfaces*, vol. 6, no. 13, pp. 10687–10695, Jul. 2014, doi: 10.1021/am502427s.
- [52] A. Mavlonov *et al.*, "A review of Sb₂Se₃ photovoltaic absorber materials and thin-film solar cells," *Solar Energy*, vol. 201, pp. 227–246, May 2020, doi: 10.1016/J.SOLENER.2020.03.009.
- [53] C. Chen, K. Li, and J. Tang, "Ten Years of Sb₂Se₃ Thin Film Solar Cells," *Solar RRL*, vol. 6, no. 7, p. 2200094, Jul. 2022, doi: 10.1002/SOLR.202200094.
- [54] U. S. G. Survey, "Mineral commodity summaries 2023," *Mineral Commodity Summaries*, 2023, doi: 10.3133/MCS2023.
- [55] A. Mavlonov *et al.*, "A review of Sb₂Se₃ photovoltaic absorber materials and thin-film solar cells," *Solar Energy*, vol. 201, pp. 227–246, May 2020, doi: 10.1016/J.SOLENER.2020.03.009.
- [56] B. Roy, B. R. Chakraborty, R. Bhattacharya, and A. K. Dutta, "Electrical and magnetic properties of antimony sulphide (Sb₂S₃) crystals and the mechanism of carrier transport in it," *Solid State Commun*, vol. 25, no. 11, pp. 937–940, Mar. 1978, doi: 10.1016/0038-1098(78)90306-X.
- [57] R. E. Williams *et al.*, "Evidence for Self-healing Benign Grain Boundaries and a Highly Defective Sb₂Se₃-CdS Interfacial Layer in Sb₂Se₃ Thin-Film Photovoltaics," *ACS Appl Mater Interfaces*, vol. 12, no. 19, pp. 21730–21738, May 2020, doi: 10.1021/acsami.0c03690.

- [58] X. Wang, R. Tang, C. Wu, C. Zhu, and T. Chen, "Development of antimony sulfide–selenide $\text{Sb}_2(\text{S}, \text{Se})_3$ -based solar cells," *Journal of Energy Chemistry*, vol. 27, no. 3, pp. 713–721, May 2018, doi: 10.1016/J.JEACHEM.2017.09.031.
- [59] O. S. Hutter, L. J. Phillips, K. Durose, and J. D. Major, "6.6% efficient antimony selenide solar cells using grain structure control and an organic contact layer," *Solar Energy Materials and Solar Cells*, vol. 188, pp. 177–181, Dec. 2018, doi: 10.1016/j.solmat.2018.09.004.
- [60] H. Deng *et al.*, "Efficient and stable $\text{TiO}_2/\text{Sb}_2\text{S}_3$ planar solar cells from absorber crystallization and Se-atmosphere annealing," *Mater Today Energy*, vol. 3, pp. 15–23, Mar. 2017, doi: 10.1016/J.MTENER.2017.02.001.
- [61] Y. Zeng *et al.*, "Quasi-Vertically-Orientated Antimony Sulfide Inorganic Thin-Film Solar Cells Achieved by Vapor Transport Deposition," *ACS Appl Mater Interfaces*, vol. 12, no. 20, pp. 22825–22834, May 2020, doi: 10.1021/ACSAMI.0C02697.
- [62] Z. Duan *et al.*, " Sb_2S_3 Thin-Film Solar Cells Exceeding 10% Power Conversion Efficiency Enabled by Injection Vapor Deposition Technology," *Advanced Materials*, vol. 34, no. 30, p. 2202969, Jul. 2022, doi: 10.1002/ADMA.202202969.
- [63] Y. Zeng, F. Liu, and X. Hao, "Fabrication of Sb_2S_3 planar thin film solar cells with closed-space sublimation method," *2018 IEEE 7th World Conference on Photovoltaic Energy Conversion, WCPEC 2018 - A Joint Conference of 45th IEEE PVSC, 28th PVSEC and 34th EU PVSEC*, pp. 870–872, Nov. 2018, doi: 10.1109/PVSC.2018.8547305.
- [64] Y. Xie *et al.*, "Fabrication of Sb_2S_3 solar cells by close space sublimation and enhancing the efficiency via co-selenization," *Mater Sci Semicond Process*, vol. 142, p. 106451, May 2022, doi: 10.1016/J.MSSP.2022.106451.
- [65] K. Li *et al.*, "Orientation Engineering in Low-Dimensional Crystal-Structural Materials via Seed Screening," *Advanced Materials*, vol. 31, no. 44, p. 1903914, Nov. 2019, doi: 10.1002/adma.201903914.
- [66] J. S. Eensalu, "Deposition of Sb_2S_3 Thin Films by Ultrasonic Spray Pyrolysis for Photovoltaic Applications," Tallinn University of Technology, 2022. doi: 10.23658/taltech.1/2022.
- [67] J. Han *et al.*, "Solution-Processed Sb_2S_3 Planar Thin Film Solar Cells with a Conversion Efficiency of 6.9% at an Open Circuit Voltage of 0.7 V Achieved via Surface Passivation by a SbCl_3 Interface Layer," *ACS Appl Mater Interfaces*, vol. 12, no. 4, pp. 4970–4979, Jan. 2020, doi: 10.1021/ACSAMI.9B15148.
- [68] Y. Ma *et al.*, "Efficient defect passivation of Sb_2S_3 film by tellurium doping for high performance solar cells," *J Mater Chem A Mater*, vol. 8, no. 14, pp. 6510–6516, Apr. 2020, doi: 10.1039/D0TA00443J.
- [69] S. Mandati *et al.*, "4.9% Efficient Sb_2S_3 Solar Cells from Semitransparent Absorbers with Fluorene-Based Thiophene-Terminated Hole Conductors," *ACS Appl Energy Mater*, vol. 6, p. 3833, Apr. 2022, doi: 10.1021/ACSAEM.2C04097.
- [70] C. Zhen, T. Wu, R. Chen, L. Wang, G. Liu, and H. M. Cheng, "Strategies for Modifying TiO_2 Based Electron Transport Layers to Boost Perovskite Solar Cells," *ACS Sustain Chem Eng*, vol. 7, no. 5, pp. 4586–4618, Mar. 2019, doi: 10.1021/acssuschemeng.8b06580.

- [71] T. Dittrich *et al.*, "Synthesis Control of Charge Separation at Anatase TiO₂ Thin Films Studied by Transient Surface Photovoltage Spectroscopy," *ACS Appl Mater Interfaces*, vol. 14, no. 38, pp. 43163–43170, Sep. 2022, doi: 10.1021/ACSAMI.2C09032.
- [72] M. K. Nowotny, and T. Bak, and J. Nowotny, "Electrical Properties and Defect Chemistry of TiO₂ Single Crystal. I. Electrical Conductivity," *J Phys Chem B*, vol. 110, no. 33, pp. 16270–16282, Aug. 2006, doi: 10.1021/JP0606210.
- [73] Y. S. Kim *et al.*, "Reduced extrinsic recombination process in anatase and rutile TiO₂ epitaxial thin films for efficient electron transport layers," *Scientific Reports 2021 11:1*, vol. 11, no. 1, pp. 1–10, Mar. 2021, doi: 10.1038/s41598-021-86422-9.
- [74] V. C. Anitha, A. N. Banerjee, and S. W. Joo, "Recent developments in TiO₂ as n- and p-type transparent semiconductors: synthesis, modification, properties, and energy-related applications," *Journal of Materials Science 2015 50:23*, vol. 50, no. 23, pp. 7495–7536, Aug. 2015, doi: 10.1007/S10853-015-9303-7.
- [75] W. Hu, S. Yang, and S. Yang, "Surface Modification of TiO₂ for Perovskite Solar Cells," *Trends Chem*, vol. 2, no. 2, pp. 148–162, Feb. 2020, doi: 10.1016/J.TRECHM.2019.11.002.
- [76] A. Morales-Acevedo, "Thin film CdS/CdTe solar cells: Research perspectives," *Solar Energy*, vol. 80, no. 6, pp. 675–681, Jun. 2006, doi: 10.1016/J.SOLENER.2005.10.008.
- [77] H. Shiel *et al.*, "Natural Band Alignments and Band Offsets of Sb₂Se₃ Solar Cells," *ACS Appl Energy Mater*, vol. 3, no. 12, pp. 11617–11626, Dec. 2020, doi: 10.1021/acsaem.0c01477.
- [78] L. J. Phillips *et al.*, "Current Enhancement via a TiO₂ Window Layer for CSS Sb₂Se₃ Solar Cells: Performance Limits and High Voc," *IEEE J Photovolt*, vol. 9, no. 2, pp. 544–551, Mar. 2019, doi: 10.1109/JPHOTOV.2018.2885836.
- [79] A. Pan and X. Zhu, "Optoelectronic properties of semiconductor nanowires," *Semiconductor Nanowires: Materials, Synthesis, Characterization and Applications*, pp. 327–363, Jan. 2015, doi: 10.1016/B978-1-78242-253-2.00012-8.
- [80] Q. Li, X. Li, and J. Yu, "Surface and interface modification strategies of CdS-based photocatalysts," *Interface Science and Technology*, vol. 31, pp. 313–348, Jan. 2020, doi: 10.1016/B978-0-08-102890-2.00010-5.
- [81] S. Messina, M. T. S. Nair, and P. K. Nair, "Antimony Selenide Absorber Thin Films in All-Chemically Deposited Solar Cells," *J Electrochem Soc*, vol. 156, no. 5, p. H327, Mar. 2009, doi: 10.1149/1.3089358.
- [82] Y. C. Choi *et al.*, "Sb₂Se₃-Sensitized Inorganic–Organic Heterojunction Solar Cells Fabricated Using a Single-Source Precursor," *Angewandte Chemie International Edition*, vol. 53, no. 5, pp. 1329–1333, Jan. 2014, doi: 10.1002/ANIE.201308331.
- [83] C. Chen *et al.*, "6.5% Certified Efficiency Sb₂Se₃ Solar Cells Using PbS Colloidal Quantum Dot Film as Hole-Transporting Layer," *ACS Energy Lett*, vol. 2, no. 9, pp. 2125–2132, Sep. 2017, doi: 10.1021/acscenergylett.7b00648.
- [84] Shangwei Dong *et al.*, "Deep defects limiting the conversion efficiency of Sb₂Se₃ thin-film solar cells," *Physical Chemistry Chemical Physics*, vol. 25, no. 6, pp. 4617–4623, Feb. 2023, doi: 10.1039/D2CP05585F.

- [85] O. Savadogo and K. C. Mandal, "Low Cost Schottky Barrier Solar Cells Fabricated on CdSe and Sb₂S₃ Films Chemically Deposited with Silicotungstic Acid," *J Electrochem Soc*, vol. 141, no. 10, pp. 2871–2877, Oct. 1994, doi: 10.1149/1.2059248.
- [86] Y. Itzhaik, O. Niiitsoo, M. Page, and G. Hodes, "Sb₂S₃-sensitized nanoporous TiO₂ solar cells," *Journal of Physical Chemistry C*, vol. 113, no. 11, pp. 4254–4256, Mar. 2009, doi: 10.1021/jp900302b.
- [87] J. A. Chang *et al.*, "High-performance nanostructured inorganic-organic heterojunction solar cells," *Nano Lett*, vol. 10, no. 7, pp. 2609–2612, Jul. 2010, doi: 10.1021/nl101322h.
- [88] J. A. Chang *et al.*, "Panchromatic photon-harvesting by hole-conducting materials in inorganic-organic heterojunction sensitized-solar cell through the formation of nanostructured electron channels," *Nano Lett*, vol. 12, no. 4, pp. 1863–1867, Apr. 2012, doi: 10.1021/nl204224v.
- [89] D. H. Kim *et al.*, "Highly reproducible planar Sb₂S₃-sensitized solar cells based on atomic layer deposition," *Nanoscale*, vol. 6, no. 23, pp. 14549–14554, Nov. 2014, doi: 10.1039/C4NR04148H.
- [90] C. Jiang, R. Tang, X. Wang, H. Ju, G. Chen, and T. Chen, "Alkali Metals Doping for High-Performance Planar Heterojunction Sb₂S₃ Solar Cells," *Solar RRL*, vol. 3, no. 1, p. 1800272, Jan. 2019, doi: 10.1002/SOLR.201800272.
- [91] J. S. Eensalu *et al.*, "Semitransparent Sb₂S₃ thin film solar cells by ultrasonic spray pyrolysis for use in solar windows," vol. 10, no. 1, pp. 2396–2409, Dec. 2019, doi: 10.3762/bjnano.10.230.
- [92] H. Ning *et al.*, "Enhancing the efficiency of Sb₂S₃ solar cells using dual-functional potassium doping," *Solar Energy Materials and Solar Cells*, vol. 221, p. 110816, Mar. 2021, doi: 10.1016/J.SOLMAT.2020.110816.
- [93] W. Lian *et al.*, "Revealing composition and structure dependent deep-level defect in antimony trisulfide photovoltaics," *Nature Communications 2021 12:1*, vol. 12, no. 1, pp. 1–7, May 2021, doi: 10.1038/s41467-021-23592-0.
- [94] H. Deng *et al.*, "Efficient All-Inorganic Sb₂S₃ Solar Cells with Matched Energy Levels Using Sb₂Se₃ as Hole Transport Layers," *Solar RRL*, vol. 6, no. 4, p. 2101017, Apr. 2022, doi: 10.1002/SOLR.202101017.
- [95] C. Gao *et al.*, "Fabrication of Sb₂S₃ thin films by sputtering and post-annealing for solar cells," *Ceram Int*, vol. 45, no. 3, pp. 3044–3051, Feb. 2019, doi: 10.1016/J.CERAMINT.2018.10.155.
- [96] G. Pan *et al.*, "Substrate structured Sb₂S₃ thin film solar cells fabricated by rapid thermal evaporation method," *Solar Energy*, vol. 182, pp. 64–71, Apr. 2019, doi: 10.1016/J.SOLENER.2019.02.014.
- [97] Y. Chan Choi *et al.*, "Efficient Inorganic-Organic Heterojunction Solar Cells Employing Sb₂(S_x/Se_{1-x})₃ Graded-Composition Sensitizers," *Adv Energy Mater*, vol. 4, no. 7, p. 1301680, May 2014, doi: 10.1002/AENM.201301680.
- [98] B. Yang *et al.*, "In situ sulfurization to generate Sb₂(Se_{1-x}S_x)₃ alloyed films and their application for photovoltaics," *Progress in Photovoltaics: Research and Applications*, vol. 25, no. 1, pp. 113–122, Jan. 2017, doi: 10.1002/PIP.2819.
- [99] W. Wang *et al.*, "Over 6% Certified Sb₂(S,Se)₃ Solar Cells Fabricated via In Situ Hydrothermal Growth and Postselenization," *Adv Electron Mater*, vol. 5, no. 2, p. 1800683, Feb. 2019, doi: 10.1002/AELM.201800683.

- [100] F. De Bray Sánchez, M. T. S. Nair, and P. K. Nair, "Optimum chemical composition of antimony sulfide selenide for thin film solar cells," *Appl Surf Sci*, vol. 454, pp. 305–312, Oct. 2018, doi: 10.1016/J.APSUSC.2018.05.076.
- [101] R. Tang *et al.*, "Hydrothermal deposition of antimony selenosulfide thin films enables solar cells with 10% efficiency," *Nature Energy* 2020 5:8, vol. 5, no. 8, pp. 587–595, Jul. 2020, doi: 10.1038/s41560-020-0652-3.
- [102] X. Wang *et al.*, "Manipulating the Electrical Properties of Sb₂(S,Se)₃ Film for High-Efficiency Solar Cell," *Adv Energy Mater*, vol. 10, no. 40, p. 2002341, Oct. 2020, doi: 10.1002/AENM.202002341.
- [103] K. Li *et al.*, "Fabrication of closed-space sublimation Sb₂(S_{1-x}Se_x)₃ thin-film based on a single mixed powder source for photovoltaic application," *Opt Mater (Amst)*, vol. 122, p. 111659, Dec. 2021, doi: 10.1016/J.OPTMAT.2021.111659.
- [104] X. Pan *et al.*, "All-Vacuum-Processed Sb₂(S,Se)₃ Thin Film Photovoltaic Devices via Controllable Tuning Seed Orientation," *Adv Funct Mater*, p. 2214511, 2023, doi: 10.1002/ADFM.202214511.
- [105] H. Deng *et al.*, "Quasiepitaxy Strategy for Efficient Full-Inorganic Sb₂S₃ Solar Cells," *Adv Funct Mater*, vol. 29, no. 31, p. 1901720, Aug. 2019, doi: 10.1002/ADFM.201901720.
- [106] L. Zhang, W. Lian, X. Zhao, Y. Yin, T. Chen, and C. Zhu, "Sb₂S₃ Seed-Mediated Growth of Low-Defect Sb₂S₃ on a TiO₂ Substrate for Efficient Solar Cells," *ACS Appl Energy Mater*, vol. 3, no. 12, pp. 12417–12422, Dec. 2020, doi: 10.1021/ACSAEM.0C02400.
- [107] X. Chen *et al.*, "CdS/Sb₂S₃ heterojunction thin film solar cells with a thermally evaporated absorber," *J Mater Chem C Mater*, vol. 5, no. 36, pp. 9421–9428, Sep. 2017, doi: 10.1039/C7TC02460F.
- [108] L. Zhang *et al.*, "Role of Grain Growth in Controlling the Crystal Orientation of Sb₂S₃ Film for efficient Solar Cell," *J Mater Chem A Mater*, vol. 6, pp. 4883–5230, 2023, doi: 10.1039/D3TA00678F.
- [109] U. Wijesinghe, G. Longo, and O. S. Hutter, "Defect engineering in antimony selenide thin film solar cells," *Energy Advances*, vol. 2, no. 1, pp. 12–33, Jan. 2023, doi: 10.1039/D2YA00232A.
- [110] A. Kyono, M. Kimata, M. Matsuhisa, Y. Miyashita, and K. Okamoto, "Low-temperature crystal structures of stibnite implying orbital overlap of Sb 5s² inert pair electrons," *Phys Chem Miner*, vol. 29, no. 4, pp. 254–260, 2002, doi: 10.1007/s00269-001-0227-1.
- [111] N. W. Tideswell, F. H. Kruse, J. D. McCullough, and IUCr, "The crystal structure of antimony selenide, Sb₂Se₃," vol. 10, no. 2, pp. 99–102, Feb. 1957, doi: 10.1107/S0365110X57000298.
- [112] M. Huang, P. Xu, D. Han, J. Tang, and S. Chen, "Complicated and Unconventional Defect Properties of the Quasi-One-Dimensional Photovoltaic Semiconductor Sb₂Se₃," vol. 11, no. 17, pp. 15564–15572, May 2019, doi: 10.1021/acscami.9b01220.
- [113] Z. Cai, C. M. Dai, and S. Chen, "Intrinsic Defect Limit to the Electrical Conductivity and a Two-Step p-Type Doping Strategy for Overcoming the Efficiency Bottleneck of Sb₂S₃-Based Solar Cells," *Solar RRL*, vol. 4, no. 4, p. 1900503, Apr. 2020, doi: 10.1002/SOLR.201900503.

- [114] R. Zhao, X. Yang, H. Shi, and M. H. Du, "Intrinsic and complex defect engineering of quasi-one-dimensional ribbons Sb_2S_3 for photovoltaics performance," *Phys Rev Mater*, vol. 5, no. 5, p. 054605, May 2021, doi: 10.1103/PhysRevMaterials.5.054605.
- [115] M. I. Medina-Montes, Z. Montiel-González, F. Paraguay-Delgado, N. R. Mathews, and X. Mathew, "Structural, morphological and spectroscopic ellipsometry studies on sputter deposited Sb_2S_3 thin films," *Journal of Materials Science: Materials in Electronics*, vol. 27, no. 9, pp. 9710–9719, Sep. 2016, doi: 10.1007/S10854-016-5033-0/FIGURES/11.
- [116] K. Y. Rajpure and C. H. Bhosale, "Preparation and characterization of spray deposited photoactive Sb_2S_3 and Sb_2Se_3 thin films using aqueous and non-aqueous media," *Mater Chem Phys*, vol. 73, no. 1, pp. 6–12, Jan. 2002, doi: 10.1016/S0254-0584(01)00350-9.
- [117] Y. Zhou *et al.*, "Solution-processed antimony selenide heterojunction solar cells," *Adv Energy Mater*, vol. 4, no. 8, Jun. 2014, doi: 10.1002/aenm.201301846.
- [118] Y. Zhou *et al.*, "Buried homojunction in $\text{CdS}/\text{Sb}_2\text{Se}_3$ thin film photovoltaics generated by interfacial diffusion," *Appl Phys Lett*, vol. 111, no. 1, p. 013901, Jul. 2017, doi: 10.1063/1.4991539.
- [119] L. Guo *et al.*, "Scalable and efficient Sb_2S_3 thin-film solar cells fabricated by close space sublimation," *APL Mater*, vol. 7, no. 4, p. 041105, Apr. 2019, doi: 10.1063/1.5090773.
- [120] X. Liu *et al.*, "Enhanced Sb_2Se_3 solar cell performance through theory-guided defect control," *Progress in Photovoltaics: Research and Applications*, vol. 25, no. 10, pp. 861–870, Oct. 2017, doi: 10.1002/PIP.2900.
- [121] B. Zhang and X. Qian, "Competing Superior Electronic Structure and Complex Defect Chemistry in Quasi-One-Dimensional Antimony Chalcogenide Photovoltaic Absorbers," *ACS Appl Energy Mater*, vol. 5, no. 1, pp. 492–502, Jan. 2022, doi: 10.1021/acsaem.1c03023.
- [122] B. Teymur *et al.*, "Optoelectronic and material properties of solution-processed Earth-abundant $\text{Cu}_2\text{BaSn}(\text{S}, \text{Se})_4$ films for solar cell applications," *Nano Energy*, vol. 80, p. 105556, Feb. 2021, doi: 10.1016/j.nanoen.2020.105556.
- [123] S. Levchenko *et al.*, "Deep Defects in $\text{Cu}_2\text{ZnSn}(\text{S}, \text{Se})_4$ Solar Cells with Varying Se Content," *Phys Rev Appl*, vol. 5, no. 2, p. 024004, Feb. 2016, doi: 10.1103/PhysRevApplied.5.024004.
- [124] J. Heath and P. Zabierowski, "Capacitance Spectroscopy of Thin-Film Solar Cells," *Advanced Characterization Techniques for Thin Film Solar Cells: Second Edition*, vol. 1–2, pp. 93–119, Sep. 2016, doi: 10.1002/9783527699025.CH4.
- [125] E. Kask, J. Krustok, S. Giraldo, M. Neuschitzer, S. López-Marino, and E. Saucedo, "Temperature dependent electrical characterization of thin film $\text{Cu}_2\text{ZnSnSe}_4$ solar cells," *J Phys D Appl Phys*, vol. 49, no. 8, p. 085101, Mar. 2016, doi: 10.1088/0022-3727/49/8/085101.
- [126] M. Grossberg, "Optical Properties of Multinary Semiconductor Compounds for Photovoltaic Applications," Tallinn University of Technology, 2010.
- [127] A. Penežko, "Properties of CuSbSe_2 and Sb_2Se_3 Absorber Materials for Solar Cell Applications," Tallinn University of Technology, 2022.

- [128] R. Scheer and H.-W. Schock, *Chalcogenide Photovoltaics*. Weinheim, Germany: Wiley-VCH Verlag GmbH & Co. KGaA, 2011. doi: 10.1002/9783527633708.
- [129] R. M. Fleming, C. H. Seager, D. V. Lang, and J. M. Campbell, "Injection deep level transient spectroscopy: An improved method for measuring capture rates of hot carriers in semiconductors," *J Appl Phys*, vol. 118, no. 1, p. 015703, Jul. 2015, doi: 10.1063/1.4923358.
- [130] F. D. Auret and M. Nel, "Detection of minority-carrier defects by deep level transient spectroscopy using Schottky barrier diodes," *J Appl Phys*, vol. 61, no. 7, pp. 2546–2549, 1987, doi: 10.1063/1.337931.
- [131] T. D. C. Hobson, L. J. Phillips, O. S. Hutter, K. Durose, and J. D. Major, "Defect properties of Sb₂Se₃ thin film solar cells and bulk crystals," *Appl Phys Lett*, vol. 116, no. 26, p. 261101, Jul. 2020, doi: 10.1063/5.0012697.
- [132] Y. Ma *et al.*, "Efficient defect passivation of Sb₂Se₃ film by tellurium doping for high performance solar cells," *J Mater Chem A Mater*, vol. 8, no. 14, pp. 6510–6516, Apr. 2020, doi: 10.1039/D0TA00443J.
- [133] A. Stolaroff *et al.*, "Deciphering the Role of Key Defects in Sb₂Se₃, a Promising Candidate for Chalcogenide-Based Solar Cells," *ACS Appl Energy Mater*, vol. 3, no. 3, pp. 2496–2509, Mar. 2020, doi: 10.1021/acsaem.9b02192.
- [134] X. Hu *et al.*, "Improving the efficiency of Sb₂Se₃ thin-film solar cells by post annealing treatment in vacuum condition," *Solar Energy Materials and Solar Cells*, vol. 187, pp. 170–175, Dec. 2018, doi: 10.1016/j.solmat.2018.08.006.
- [135] X. Hu *et al.*, "5.91%-efficient Sb₂Se₃ solar cells with a radio-frequency magnetron-sputtered CdS buffer layer," *Appl Mater Today*, vol. 16, pp. 367–374, Sep. 2019, doi: 10.1016/j.apmt.2019.06.001.
- [136] X. Hu *et al.*, "Investigation of electrically-active defects in Sb₂Se₃ thin-film solar cells with up to 5.91% efficiency via admittance spectroscopy," *Solar Energy Materials and Solar Cells*, vol. 186, pp. 324–329, Nov. 2018, doi: 10.1016/j.solmat.2018.07.004.
- [137] R. Tang *et al.*, "Highly efficient and stable planar heterojunction solar cell based on sputtered and post-selenized Sb₂Se₃ thin film," *Nano Energy*, vol. 64, p. 103929, Oct. 2019, doi: 10.1016/j.nanoen.2019.103929.
- [138] M. Grossberg, O. Volobujeva, A. Penežko, R. Kaupmees, T. Raadik, and J. Krustok, "Origin of photoluminescence from antimony selenide," *J Alloys Compd*, vol. 817, p. 152716, Mar. 2020, doi: 10.1016/j.jallcom.2019.152716.
- [139] R. Wang *et al.*, "Optimisation of Sb₂S₃ thin-film solar cells via Sb₂Se₃ post-treatment," *J Power Sources*, vol. 556, p. 232451, Feb. 2023, doi: 10.1016/J.JPOWSOUR.2022.232451.
- [140] Chunyan Wu *et al.*, "The role of grain growth in controlling the crystal orientation of Sb₂S₃ films for efficient solar cells," *J Mater Chem A Mater*, vol. 11, no. 15, pp. 8184–8191, Apr. 2023, doi: 10.1039/D3TA00678F.
- [141] D. Qin *et al.*, "Effects of working pressure on the material and defect properties of Sb₂S₃ thin-film solar cells achieved by the VTD method," *Appl Opt*, vol. 61, no. 23, p. 6879, Aug. 2022, doi: 10.1364/ao.461238.

- [142] Y. Di Luo *et al.*, “An effective combination reaction involved with sputtered and selenized Sb precursors for efficient Sb_2Se_3 thin film solar cells,” *Chemical Engineering Journal*, vol. 393, p. 124599, Aug. 2020, doi: 10.1016/J.CEJ.2020.124599.
- [143] M. I. Medina-Montes, Z. Montiel-González, N. R. Mathews, and X. Mathew, “The influence of film deposition temperature on the subsequent post-annealing and crystallization of sputtered Sb_2S_3 thin films,” *Journal of Physics and Chemistry of Solids*, vol. 111, pp. 182–189, Dec. 2017, doi: 10.1016/J.JPCS.2017.07.035.
- [144] M. E. Uslu *et al.*, “Study of the optical properties of $\text{Sb}_2(\text{Se}_{1-x}\text{S}_x)_3$ ($x = 0-1$) solid solutions,” *Mater Sci Semicond Process*, vol. 144, p. 106571, Jun. 2022, doi: 10.1016/J.MSSP.2022.106571.
- [145] T. D. C. Hobson *et al.*, “P-type conductivity in Sn-doped Sb_2Se_3 ,” *Journal of Physics: Energy*, vol. 4, no. 4, p. 045006, Sep. 2022, doi: 10.1088/2515-7655/AC91A6.
- [146] W. H. Li *et al.*, “Enhanced performance of antimony selenide thin film solar cell using PbI_2 as a dopant,” *Appl Phys Lett*, vol. 118, no. 9, p. 93903, Mar. 2021, doi: 10.1063/5.0040940/236143.
- [147] C. Chen *et al.*, “Efficiency Improvement of Sb_2Se_3 Solar Cells via Grain Boundary Inversion,” *ACS Energy Lett*, vol. 3, no. 10, pp. 2335–2341, Oct. 2018, doi: 10.1021/ACSENERGYLETT.8B01456/SUPPL_FILE/NZ8B01456_SI_001.PDF.
- [148] Y. Ma *et al.*, “Efficient defect passivation of Sb_2Se_3 film by tellurium doping for high performance solar cells,” *J Mater Chem A Mater*, vol. 8, no. 14, pp. 6510–6516, Apr. 2020, doi: 10.1039/D0TA00443J.
- [149] N. Spalatu *et al.*, “Postdeposition Processing of SnS Thin Films and Solar Cells: Prospective Strategy to Obtain Large, Sintered, and Doped SnS Grains by Recrystallization in the Presence of a Metal Halide Flux,” *ACS Appl Mater Interfaces*, vol. 11, no. 19, pp. 17539–17554, May 2019, doi: 10.1021/acsami.9b03213.
- [150] N. Maticiu, J. Hiie, V. Mikli, T. Potlog, and V. Valdna, “Structural and optical properties of cadmium sulfide thin films modified by hydrogen annealing,” *Mater Sci Semicond Process*, vol. 26, no. 1, pp. 169–174, Oct. 2014, doi: 10.1016/j.mssp.2014.04.031.
- [151] N. Maticiu, N. Spalatu, V. Mikli, and J. Hiie, “Impact of CdS annealing atmosphere on the performance of CdS-CdTe solar cell,” in *Applied Surface Science*, Elsevier B.V., Sep. 2015, pp. 14–18. doi: 10.1016/j.apsusc.2015.01.172.
- [152] L. Ph. Bérubé and G. L’Espérance, “A Quantitative Method of Determining the Degree of Texture of Zinc Electrodeposits,” *J Electrochem Soc*, vol. 136, no. 8, pp. 2314–2315, Aug. 1989, doi: 10.1149/1.2097318.
- [153] L. Guo *et al.*, “Tunable Quasi-One-Dimensional Ribbon Enhanced Light Absorption in Sb_2Se_3 Thin-film Solar Cells Grown by Close-Space Sublimation,” *Solar RRL*, vol. 2, no. 10, p. 1800128, Oct. 2018, doi: 10.1002/SOLR.201800128.
- [154] L. Guo *et al.*, “Interface Engineering via Sputtered Oxygenated CdS:O Window Layer for Highly Efficient Sb_2Se_3 Thin-Film Solar Cells with Efficiency Above 7%,” *Solar RRL*, vol. 3, no. 10, p. 1900225, Oct. 2019, doi: 10.1002/SOLR.201900225.
- [155] H. Guo *et al.*, “Enhancement in the Efficiency of Sb_2Se_3 Thin-Film Solar Cells by Increasing Carrier Concentration and Inducing Columnar Growth of the Grains,” *Solar RRL*, vol. 3, no. 3, p. 1800224, Mar. 2019, doi: 10.1002/SOLR.201800224.

- [156] F. Pattini *et al.*, "Role of the substrates in the ribbon orientation of Sb_2Se_3 films grown by Low-Temperature Pulsed Electron Deposition," *Solar Energy Materials and Solar Cells*, vol. 218, p. 110724, Dec. 2020, doi: 10.1016/j.solmat.2020.110724.
- [157] J. Zhou *et al.*, "Substrate dependence on $(\text{Sb}_4\text{Se}_6)_n$ ribbon orientations of antimony selenide thin films: Morphology, carrier transport and photovoltaic performance," *J Alloys Compd*, vol. 862, p. 158703, May 2021, doi: 10.1016/J.JALLCOM.2021.158703.
- [158] I. Dundar, M. Krichevskaya, A. Katerski, and I. O. Acik, "TiO₂ thin films by ultrasonic spray pyrolysis as photocatalytic material for air purification," *R Soc Open Sci*, vol. 6, no. 2, Feb. 2019, doi: 10.1098/rsos.181578.
- [159] E. Kärber, A. Katerski, I. Oja Acik, A. Mere, V. Mikli, and M. Krunks, "Sb₂S₃ grown by ultrasonic spray pyrolysis and its application in a hybrid solar cell," *Beilstein Journal of Nanotechnology*, vol. 7, no. 1, pp. 1662–1673, Nov. 2016, doi: 10.3762/bjnano.7.158.
- [160] R. Parize *et al.*, "ZnO/TiO₂/Sb₂S₃ Core–Shell Nanowire Heterostructure for Extremely Thin Absorber Solar Cells," *The Journal of Physical Chemistry C*, vol. 121, no. 18, pp. 9672–9680, May 2017, doi: 10.1021/acs.jpcc.7b00178.
- [161] A. Graf *et al.*, "Electrical characterization of annealed chemical-bath-deposited CdS films and their application in superstrate configuration CdTe/CdS solar cells," in *Thin Solid Films*, Elsevier, May 2015, pp. 351–355. doi: 10.1016/j.tsf.2014.11.003.
- [162] N. Spalatu *et al.*, "Effect of CdCl₂ annealing treatment on structural and optoelectronic properties of close spaced sublimation CdTe/CdS thin film solar cells vs deposition conditions," *Thin Solid Films*, vol. 582, pp. 128–133, May 2015, doi: 10.1016/J.TSF.2014.11.066.
- [163] N. Spalatu, M. Krunks, and J. Hiie, "Structural and optoelectronic properties of CdCl₂ activated CdTe thin films modified by multiple thermal annealing," *Thin Solid Films*, vol. 633, pp. 106–111, Jul. 2017, doi: 10.1016/j.tsf.2016.09.042.
- [164] V. Tomashyk, "Quaternary alloys based on II-VI semiconductors," *Quaternary Alloys Based on II - VI Semiconductors*, pp. 1–481, Jan. 2014, doi: 10.1201/b17523.
- [165] B. Cordero *et al.*, "Covalent radii revisited," *Dalton Transactions*, no. 21, pp. 2832–2838, May 2008, doi: 10.1039/B801115J.
- [166] D. Abou-Ras *et al.*, "Advanced characterization and in-situ growth monitoring of Cu(In,Ga)Se₂ thin films and solar cells," *Solar Energy*, vol. 170, pp. 102–112, Aug. 2018, doi: 10.1016/j.solener.2018.04.032.
- [167] J. Krustok, R. Josepson, M. Danilson, and D. Meissner, "Temperature dependence of Cu₂ZnSn(SexS_{1-x})₄ monograin solar cells," *Solar Energy*, vol. 84, no. 3, pp. 379–383, Mar. 2010, doi: 10.1016/J.SOLENER.2009.09.011.
- [168] T. K. Todorov *et al.*, "Ultrathin high band gap solar cells with improved efficiencies from the world's oldest photovoltaic material," *Nature Communications 2017 8:1*, vol. 8, no. 1, pp. 1–8, Sep. 2017, doi: 10.1038/s41467-017-00582-9.
- [169] O. Gunawan, T. Gokmen, and D. B. Mitzi, "Suns- V_{oc} characteristics of high performance kesterite solar cells," *J Appl Phys*, vol. 116, no. 8, Aug. 2014, doi: 10.1063/1.4893315/1016582.

- [170] S. S. Hegedus and W. N. Shafarman, "Thin-film solar cells: device measurements and analysis," *Progress in Photovoltaics: Research and Applications*, vol. 12, no. 2–3, pp. 155–176, Mar. 2004, doi: 10.1002/PIP.518.
- [171] S. Polivtseva, N. Spalatu, A. Abdalla, O. Volobujeva, J. Hiie, and S. Bereznev, "Pulsed Laser Deposition of Zn(O,Se) Layers for Optoelectronic Application," *ACS Appl Energy Mater*, vol. 1, no. 11, pp. 6505–6512, Nov. 2018, doi: 10.1021/acsaem.8b01431.
- [172] G. Ghosh, "The sb-se (antimony-selenium) system," *Journal of Phase Equilibria*, vol. 14, no. 6, pp. 753–763, Dec. 1993, doi: 10.1007/BF02667889.
- [173] N. Spalatu *et al.*, "Screening and optimization of processing temperature for Sb₂Se₃ thin film growth protocol: Interrelation between grain structure, interface intermixing and solar cell performance," *Solar Energy Materials and Solar Cells*, vol. 225, p. 111045, Jun. 2021, doi: 10.1016/j.solmat.2021.111045.
- [174] C. K. Gan, J. R. Soh, and Y. Liu, "Large anharmonic effect and thermal expansion anisotropy of metal chalcogenides: The case of antimony sulfide," *Phys Rev B Condens Matter Mater Phys*, vol. 92, no. 23, Oct. 2015, doi: 10.1103/PhysRevB.92.235202.
- [175] M. G. Herrmann *et al.*, "Lattice Dynamics of Sb₂Se₃ from Inelastic Neutron and X-Ray Scattering," *physica status solidi (b)*, vol. 257, no. 6, p. 2000063, Jun. 2020, doi: 10.1002/PSSB.202000063.
- [176] Z. B. Zhao, S. M. Yalisove, Z. U. Rek, and J. C. Bilello, "Evolution of anisotropic microstructure and residual stress in sputtered Cr films," *J Appl Phys*, vol. 92, no. 12, p. 7183, Nov. 2002, doi: 10.1063/1.1521791.
- [177] S. Mani and T. M. Saif, "Mechanism of controlled crack formation in thin-film dielectrics," *Appl Phys Lett*, vol. 86, no. 20, p. 201903, May 2005, doi: 10.1063/1.1927267.
- [178] N. Spalatu *et al.*, "Properties of the CdCl₂ air-annealed CSS CdTe thin films," in *Energy Procedia*, Elsevier, Jan. 2014, pp. 85–95. doi: 10.1016/j.egypro.2013.12.013.
- [179] Y. Cao *et al.*, "Rotational design of charge carrier transport layers for optimal antimony trisulfide solar cells and its integration in tandem devices," *Solar Energy Materials and Solar Cells*, vol. 206, p. 110279, Mar. 2020, doi: 10.1016/J.SOLMAT.2019.110279.
- [180] A. Niemegeers, M. Burgelman, and A. de Vos, "On the CdS/CuInSe₂ conduction band discontinuity," *Appl Phys Lett*, vol. 67, no. 6, p. 843, Jun. 1998, doi: 10.1063/1.115523.
- [181] Z. Cai, C. M. Dai, and S. Chen, "Intrinsic Defect Limit to the Electrical Conductivity and a Two-Step p-Type Doping Strategy for Overcoming the Efficiency Bottleneck of Sb₂S₃-Based Solar Cells," *Solar RRL*, vol. 4, no. 4, p. 1900503, Apr. 2020, doi: 10.1002/SOLR.201900503.

Appendix 1

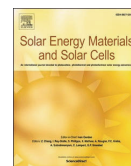
PUBLICATION I

N. Spalatu, **R. Krautmann**, A. Katerski, E. Kärber, R. Josepson, J. Hiie, I. Oja Acik, M. Krunks, “Screening and optimization of processing temperature for Sb₂Se₃ thin film growth protocol: Interrelation between grain structure, interface intermixing and solar cell performance”, Solar Energy Materials and Solar Cells, vol. 225, 2021, DOI: 10.1016/j.solmat.2021.111045



Contents lists available at ScienceDirect

Solar Energy Materials and Solar Cells

journal homepage: <http://www.elsevier.com/locate/solmat>

Screening and optimization of processing temperature for Sb_2Se_3 thin film growth protocol: Interrelation between grain structure, interface intermixing and solar cell performance

Nicolae Spalatu^{a,*}, Robert Krautmann^a, Atanas Katerski^a, Erki Karber^a, Raavo Josepson^b, Jaan Hiie^a, Ilona Oja Acik^a, Malle Krunks^a

^a Department of Materials and Environmental Technology, Tallinn University of Technology, Ehitajate tee 5, 19086, Tallinn, Estonia

^b Division of Physics, Tallinn University of Technology, Ehitajate tee 5, 19086, Tallinn, Estonia

ARTICLE INFO

Keywords:

Antimony selenide
 Sb_2Se_3
 Close-spaced sublimation
 Thin-film growth
 Grain structure
 Interface intermixing
 Solar cell efficiency

ABSTRACT

Deliverability of controllable deposition processes represents the current state-of-the-art strategy for the development of emerging 1D crystal-structure photovoltaic (PV) materials. For Sb_2Se_3 , a compound with tremendous potential for next-generation cost-efficient thin-film PV, the current reported findings proposed that columnar grain growth protocol is required to promote efficient carrier transport and to achieve highly efficient solar cells. It is still a matter of debate, however, whether the growth of the thin-film absorber should follow the weak contacted nanorod grain structure or the columnar-sintered large grain protocol, in relation with the processing temperature, the under-layer junction partner, and interface intermixing. In this work, close-spaced sublimation processing temperature in conjunction with CdS and TiO_2 junction partner layers is systematically investigated towards optimization of Sb_2Se_3 thin film growth conditions. The desideratum of columnar-sintered large grains protocol is validated and insights into the mechanism of absorber-buffer interface intermixing are provided. Following a systematic technological approach, a solar cell efficiency of 5.3% is demonstrated. Combining classical and advanced measurement techniques, insights into physicochemical processes and device functionality in connection with grain structure, defect density, carrier concentration, and recombination mechanism in Sb_2Se_3 absorber are provided.

1. Introduction

Cost-efficient solar cells can help fulfill future energy demand and curb increasing carbon emissions. Currently, crystalline silicon (c-Si) panels make up 90% of the global solar PV market [1]. Inorganic cadmium telluride (CdTe) and copper indium gallium diselenide (CIGS) semiconductor thin-film photovoltaics demonstrated efficiencies exceeding 22% [2] and have an enormous potential to produce high efficiencies at significantly lower manufacturing costs. Yet despite successful deployment, factors like the toxicity of Cd, scarcity of In and Te, and high material cost of In and Ga, altogether hinder further market expansion [3]. This necessitates extensive research into alternative photovoltaic materials that are non-toxic and earth-abundant.

The antimony selenide (Sb_2Se_3) is an attractive photovoltaic absorber material for its suitable optical bandgap of 1.1–1.3 eV, high absorption coefficient ($>10^5 \text{ cm}^{-1}$) at shorter wavelengths [3,4], high

elemental abundance, and low toxicity. Sb_2Se_3 exhibits orthorhombic phase [5,6] and its crystal structure is one-dimensional (1D), as $(\text{Sb}_4\text{Se}_6)_n$ units stack via covalent bonds, forming vertical ribbons [7]. This implies the adjacent ribbons bond through weak van der Waals forces that prevent the formation of dangling bonds at the interface between grains, making them grain boundary (GB) defect tolerant. The GB tolerance peculiarity has allowed a variety range of deposition techniques to be deployed for Sb_2Se_3 growth as a thin film absorber, including physical deposition methods such as vacuum evaporation (VE) [8], close-spaced sublimation (CSS) [9], magnetron sputtering [10], as well as low-temperature solution-processed methods [11–14]. Nevertheless, the large negative formation enthalpy, the low melting point of 608 °C, and the correspondingly high vapor pressure ($\sim 1200 \text{ Pa}$ at 550 °C) [15] make Sb_2Se_3 more compatible for congruent sublimation via VE and CSS, such as in CdTe PV. A number of studies investigated Sb_2Se_3 thin films and solar cells by sputtering, VE, and CSS reporting

* Corresponding author.

E-mail address: nicolae.spalatu@taltech.ee (N. Spalatu).

<https://doi.org/10.1016/j.solmat.2021.111045>

Received 9 December 2020; Received in revised form 21 February 2021; Accepted 28 February 2021

Available online 11 March 2021

0927-0248/© 2021 The Authors.

Published by Elsevier B.V. This is an open access article under the CC BY-NC-ND license

(<http://creativecommons.org/licenses/by-nc-nd/4.0/>).

device efficiency between 2–4% [5,8,16–19]. Like in CdTe technology, CdS is the most widely used heterojunction partner layer in Sb₂Se₃ based solar cells. A great emphasis is on the development and optimization of Sb₂Se₃ thin-film absorbers consisting of [211] and [221] oriented ribbon-shaped grains, perpendicularly aligned to the substrate; the [001] ribbon axis being the preferred direction for the efficient charge transport in Sb₂Se₃ absorber [3,4,7,9,20]. Although this approach appears to be simple in concept, its implementation in practice is rather complicated since the 1D materials are always inclined to grow with low energy crystal faces parallel to the substrate, towards minimization of the free energy of the system. This effect is widely observed in Sb₂Se₃ thin films grown by the “non-equilibrium” sputtering process [10, 21–23]. So far, only employment of controllable CSS and VTD “equilibrium” deposition processes allowed the achievement of Sb₂Se₃ absorber films with columnar grains and highlighted [211] and/or [221] orientation [3,4,9,16]. This approach enabled to obtain Sb₂Se₃ based solar cells with efficiencies of 7.6% [4] and 9.2% [3], for superstrate CdS/Sb₂Se₃ and substrate CdS/TiO₂/Sb₂Se₃ configurations, respectively. Although the 7.6% and 9.2% are the highest reported efficiencies for Sb₂Se₃ based device, there are some contradictory results in terms of established processing temperature regime for the grain growth protocol of the absorber and the interrelation between absorber grain structure and device performance in these two configurations. In the case of a 7.6% efficient device [4], a high-temperature CSS processing (≥ 400 °C) was established to be optimal for growing of Sb₂Se₃ absorber with (211) and (221) oriented columnar large grains. In contrast, for the 9.2% device [3], a low temperature (~ 270 °C) CSS processing regime was settled to be optimal for the synthesis of the absorber with the same orientation but with non-sintered nanorod-shaped grains. This discrepancy between the results generates a number of questions; (i) which grain structure and texture is truly optimal for the efficient carrier transport and solar cell performance - large columnar sintered grains or weakly contacted nanorods? (ii) are the GBs in the Sb₂Se₃ solar cell benign? [24] Another critical aspect of this technology is the conductivity type and carrier concentration in the Sb₂Se₃ absorber. A number of reports simply rely on the analogy with CdTe absorber, assuming that Sb₂Se₃ has p-type conductivity [4,5,7,12]. Hall measurements seem to be difficult to perform since, similar to CdTe, in most cases the as-grown Sb₂Se₃ thin films are highly resistive, exhibiting semi-insulating behavior. Despite the fact, several reports showed n-type conductivity and a high value of carrier concentrations, in the range of 10^{16} – 10^{17} cm⁻³ [9,20]. The n-type conductivity and 10^{17} cm⁻³ carrier density in Sb₂Se₃ crystals and thin films were recently related to the presence of chlorine impurities in the Sb₂Se₃ source material [9]. The origin of n-type conductivity was also explained to be due to elemental Cd diffusion from the CdS buffer [25], nevertheless the mechanism by which Cd diffuses at the interface and promotes n-type conductivity in Sb₂Se₃ was not identified. There is still no consensus regarding the understanding of the intermixing effect (which occurs at the interface between CdS and Sb₂Se₃ absorber) on the device performance. Some groups found the intermixing as potentially beneficial for the device performance, claiming that the alloy formation at the interface reduces the interfacial lattice mismatch and defects [4]. Other groups reported the intermixing as being detrimental for the device efficiency assuming the formation of CdSe at the interface could introduce a potential barrier, impeding the charge transport in the device [16]. Development of alternative window/buffer layers like TiO₂ [9,16,26, 27], ZnO [28], Zn(O,S) [29], Zn(O,Se) [30] and seed layer screening strategies for the grain growth control [26] and optimization of band offsets at the heterostructure interface [28,29] are promising and active areas of research. Sb₂Se₃/TiO₂ solar cells (i.e., Cd-free buffer partner) with efficiencies between 6–7% were recently demonstrated [9,16,26, 27]. However, the fact that a very limited number of research groups were able to reproduce and confirm the state of the art of the reported high efficiencies, indicate the lack of systematic knowledge on the development and optimization of processing conditions, identification

of suitable partner layer, as well as device operation and its limitations via advanced characterization techniques.

Considering these approaches, the present study is focused on screening and optimization of CSS processing temperature and identification of optimal buffer partner layer, towards the development of a protocol for growing of Sb₂Se₃ absorber with columnar grains and desired orientation for efficient carrier transport in solar cell device. The novelty lies in the systematically technological approach combined with advanced characterization techniques, bringing new insights into physicochemical processes, the interrelation between absorber grain structure, absorber-buffer interface intermixing, defect density, carrier concentration, and recombination mechanism in Sb₂Se₃ absorber films and solar cell device.

2. Materials and methods

2.1. Fabrication of thin films and solar cells

A specially designed vacuum setup with the capability to reach a vacuum level of 10^{-6} torr was used for the fabrication of thin films and solar cells [31]. Soda-lime glass substrates coated with a 200 nm thick $20 \Omega \text{ sq}^{-1}$ fluorine-doped tin oxide (FTO) were used to develop Sb₂Se₃/CdS and Sb₂Se₃/TiO₂ superstrate configuration thin-film heterostructures. Prior to the deposition, the substrates were properly cleaned following procedures described in previous works [31]. CdS buffer films of 100 nm thickness were deposited by close-spaced sublimation (CSS) [31] and chemical bath deposition (CBD) [32,33] onto the freshly cleaned substrates. The chemical bath for CBD CdS consisted of a water solution of 1 mM CdSO₄, 10 mM thiourea, 0.2 M NH₄OH, 30 mM (NH₄)₂SO₄, and a low concentration of NH₄Cl solution (0.1 μM). The temperature and agitation speed of the solution were 85 °C and 500 rpm, respectively. After deposition CBD CdS films were vacuum dried in a closed quartz tube at 120 °C for 1 h. TiO₂ films of 200 nm thickness were deposited by ultrasonic spray pyrolysis (USP) at 350 °C using precursor solution of titanium (IV) isopropoxide (TTIP) with a concentration of 0.1 M and acetylacetone (AcacH) with a molar ratio of 1:4 dissolved in ethanol. After deposition, TiO₂ films underwent two subsequent annealing steps, in a vacuum at 120 °C, and in the air at 450 °C for 30 min. With all buffer layers, complete Sb₂Se₃ solar cells were fabricated, in which the Sb₂Se₃ absorber layers of $\sim 1.5 \mu\text{m}$ thickness were deposited by CSS (from 5 N granulated Sb₂Se₃ source material, Sigma-Aldrich) at a source temperature of 490 °C keeping a deposition rate of $\sim 1 \mu\text{m}/\text{min}$. A series of Sb₂Se₃ thin films were deposited at the same conditions onto chemically and thermally etched $20 \times 20 \times 1 \text{ mm}^2$ roughened glass substrates. Roughened glass plates with a root-mean-square roughness, R_q, of 2.66 nm (O. Kindler) were used to ensure better adhesion of the Sb₂Se₃ layers. For solar cell structure with CSS-CdS, the deposition temperature of the Sb₂Se₃ absorber was varied in between 300 and 450 °C in steps of $\Delta T = 50$ °C. The solar cell structures with CBD-CdS and TiO₂ buffers layers were developed with and without a $\sim 60 \text{ nm}$ thick Sb₂Se₃ seed layer deposited at the interface between buffer and absorber layers by CSS at 300 °C. To complete the cells, Au back contacts with square geometries (25 mm^2) were deposited by VE through a mica mask placed between the evaporation source and the sample.

2.2. Materials and device characterization

Top-view and cross-sectional images of layers were made by Zeiss EVO-MA15 scanning electron microscope (SEM) equipped with a Zeiss HR FESEM Ultra 55 system. X-ray diffraction (XRD) patterns were recorded using a Rigaku Ultima IV diffractometer with Cu K α radiation ($\lambda = 1.54 \text{ \AA}$, 40 kV, 40 mA). *J-V* curves were measured using an AUTOLAB PGSTAT 30 and an Oriel class A solar simulator 91159A (100 mW cm^{-2} , AM1.5) in air ambient at room temperature. The external quantum efficiency (EQE) spectra were measured using a

monochromatized light source (Newport 300 W Xenon lamp, 69911 with a monochromator Newport Cornerstone 260), a digital lock-in detector (Merlin), and a factory-calibrated Si reference detector.

For temperature-dependent measurements, $\text{Sb}_2\text{Se}_3/\text{CdS}$ and $\text{Sb}_2\text{Se}_3/\text{TiO}_2$ cells were placed in a Janis closed-cycle He cryostat. Temperature-dependent J - V curves of $\text{Sb}_2\text{Se}_3/\text{CdS}$ and $\text{Sb}_2\text{Se}_3/\text{TiO}_2$ solar cells were measured with a KEITHLEY 2400 SourceMeter under 100 mW cm^{-2} illumination, where the temperature was varied from 20 K to 320 K with temperature step of $\Delta T = 20 \text{ K}$. The resistivity, charge carrier concentration, and mobility of the films were measured at RT using MMR's variable-temperature Hall system and van der Pauw controller H-50. Capacitance-voltage (C - V) profiling was performed at room temperature with a KEITHLEY 2400 SourceMeter using a frequency of 1 MHz and a.c. the amplitude of 30 mV. DC bias was scanned from -1.0 V to 1.0 V . Temperature-dependent admittance spectroscopy measurements were made using a Wayne Kerr 6500B impedance analyzer. The temperature ranged from 20 K to 320 K with temperature step of $\Delta T = 10 \text{ K}$. Impedance Z and phase angle θ were measured as a function of frequency f and temperature T . Frequency f was varied from 20 Hz to 10 MHz. AC voltage was kept as low as 30 mV to remove the background noise. Dark measurement was carried out at a DC bias of 0 V. The combination of high temperatures and low frequencies f allow probing of the deeper states from the so-called demarcation energy according to eq (1):

$$E_f = kT \ln \left(\frac{\nu_0}{\pi f} \right) \quad (1)$$

where k is the Boltzmann constant and ν_0 is the attempt-to-escape frequency. Defect density N_t is calculated for each E_f as the derivative of the capacitance by eq (2):

$$N_t(E_f) = - \frac{V_{bi} f}{w q_e k T} \frac{dC}{df} \quad (2)$$

Where V_{bi} is the built-in voltage, w is the absorber thickness and q_e is the electron charge, and C is the cell area normalized capacitance. N_t is plotted at varied temperatures and then overlapped through the proper choice of ν_0 .

3. Results and discussion

3.1. Screening and optimization of CSS deposition temperature for Sb_2Se_3 absorber growth protocol

3.1.1. Structural and morphological properties

The first approach towards the development of Sb_2Se_3 thin-film absorber and solar cells in this study was focused on screening and optimization of CSS deposition temperature. The idea was to find the optimal processing conditions for grain growth, grain orientation, and to understand their interrelation with the device performance. For this purpose, a single CdS buffer layer deposited by CSS on FTO/glass

substrates (Figure S1a, Supplementary material) was used for all experiments assuming that this is a "suitable" buffer layer, while Sb_2Se_3 absorber layers were deposited at temperatures between 300 and 450 °C following the superstrate configuration. The CSS source regime temperature was set to 490 °C and was selected in a way to enable the deposition rate of 1 $\mu\text{m}/\text{min}$. Such CSS deposition rate is well established for CdTe and SnS PV thin-film technologies [31,34,35]. The changes in the Sb_2Se_3 thin-film structure depending on the CSS deposition temperature were analyzed by SEM and XRD.

SEM images (Fig. 1) revealed a strong dependence between deposition temperature and the resulting grain structure of the films. Fig. 1a shows that Sb_2Se_3 films deposited at 300 °C exhibit highly dispersed and porous ribbon-like structures. Deposition at 350 °C leads to denser absorber films with larger grain size and more homogeneous distribution (Fig. 1b). By increasing the deposition temperature to 400 °C, the grain size increased significantly resulting in absorber films with a close-packed morphology near to the interface between Sb_2Se_3 and CdS; the faceted shaped grains with sharp edges increase the surface roughness giving rise to open column boundaries close to the rear surface (Fig. 1c). Ramping up the deposition temperature to 450 °C resulted in films with large columnar and sintered grains and smooth crystal facets (Fig. 1d).

Fig. 2 displays XRD patterns of CSS Sb_2Se_3 absorber layers grown at temperatures between 300 and 450 °C onto CdS/FTO/glass stacked substrates. The diffractograms show the primary peaks from the (211), (221), and (301) planes corresponding to the orthorhombic Sb_2Se_3 crystal structure (PDF card no: 01-089-0821) and matching well with those reported in the literature for Sb_2Se_3 absorber films deposited by the CSS and VTD techniques [3,4,9,16]. Interestingly, the (120) and (020) XRD peaks which are frequently observed in the diffractogram of Sb_2Se_3 films grown by various physical and chemical techniques [5, 8–14] were barely detectable in the XRD patterns of the absorbers deposited in this study at temperatures between 300 and 450 °C (Fig. 2). It is widely accepted that the presence of such XRD peaks in the diffractogram is an indication of the grains in the films lying parallel on the CdS/FTO/glass substrate [19,26].

To evaluate quantitatively the degree of orientation preference of the crystalline planes, the texture coefficient (TC) was calculated using by Harris formula (eq (3)) [36]:

$$TC(hkl) = \frac{I(hkl)}{I_0(hkl)} \left[\frac{1}{N} \sum_{i=1}^N \frac{I(h_i k_i l_i)}{I_0(h_i k_i l_i)} \right]^{-1} \quad (3)$$

where $TC(hkl)$ is the texture coefficient of the plane defined by Miller indices (hkl); $I(hkl)$ and $I_0(hkl)$ are the integrated intensity ratios of the thin films and randomly oriented Sb_2Se_3 powder respectively, for a given peak and N is the number of diffraction peaks. The Lorentzian function was used for the peak integration and before the fitting, the background noise of the diffractogram was deconvoluted and integrated intensity corresponding to each peak was calculated. It is well established that an increase (decrease) from the unit of the TC indicates a higher (lower) degree of preferential orientation along a particular

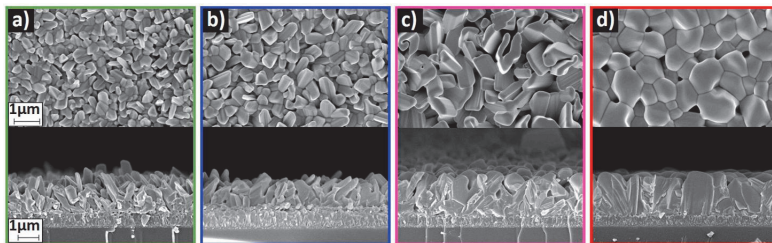


Fig. 1. Top-and cross-sectional view SEM images of CSS Sb_2Se_3 absorber films deposited on CdS/FTO/glass stacked substrates at temperatures: (a) 300 °C, (b) 350 °C, (c) 400 °C, and (d) 450 °C.

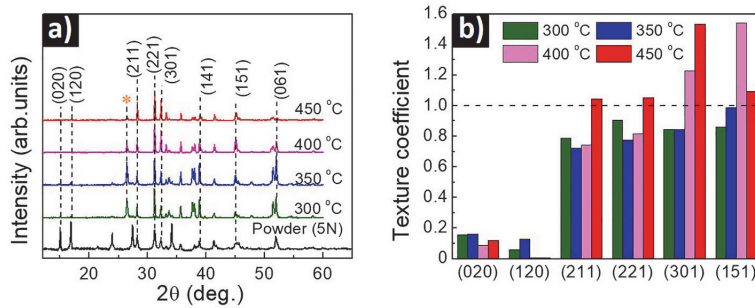


Fig. 2. a) XRD patterns of CSS Sb_2Se_3 absorber films deposited at 300–450 °C onto CdS/FTO/glass substrates (XRD peak labeled with asterisk symbol belongs to CdS underlayer). b) Texture coefficients (TC) calculated from integrated intensity ratios for the dominant miller planes of Sb_2Se_3 absorber.

crystalline plane of the film with respect to powder material [37,38]. A higher (lower) TC value also indicates an increase (decrease) in the packing density along a particular crystal plane as compared to ideal values. No evident trend has been observed in the TC of (211) and (221) planes with increasing the deposition temperature from 300 to 400 °C, nevertheless, the planar density was the highest for (221) plane (Fig. 2a) in the entire deposition temperature interval. For the Sb_2Se_3 absorber films deposited at 450 °C, the TC of (211) and (221) planes increases significantly and exceeded the unit, indicating the preferred orientation of the absorber grains along [211] and [221] crystal directions. At the same time, by increasing the deposition temperature from 300 to 450 °C the TC value of (301) and (151) planes increased systematically, with concomitant TC decrease of the (020) and (120) planes.

The trend in the texture of Sb_2Se_3 absorber layers deposited at 300–450 °C is consistent with the changes in the grain morphology of the films shown by SEM (Fig. 1a–d) and can be explained by differences in the nucleation density and grain coalescence rates at different CSS temperatures. All these processes depend on the temperature gradient (source–substrate temperature) and supersaturation of the gas phase in the CSS system [31,34]. The lower the CSS substrate temperature (the higher source–substrate temperature gradient), the greater the supersaturation of the gas phase close to the substrate, the lower the adatom mobility and surface diffusion, and the higher the saturation of nucleation density on the substrate. The higher the CSS substrate temperature (the smaller the source–substrate temperature gradient), the lower the gas phase supersaturation close to the substrate, the higher the adatom surface diffusion and lower nucleation sites on the substrate. Thus, at deposition temperatures of 300 and 350 °C, the initial in-plane grain sizes are set by the saturation nucleation density, resulting in an anisotropic film growth with a wide distribution of grain sizes and hence a highly dispersed structure (Fig. 1a and b). As the orientation of the grains is determined by the orientation of the initial nuclei, this leads to the orientation of the crystallites along the planes with the highest growth rate; for the orthorhombic 1D Sb_2Se_3 , these planes being the densely populated (211) and (221) planes (Fig. 2). At 400 °C deposition temperature, the adatom surface diffusion is significant, resulting in local epitaxial growth on individual grains. The grain coarsening occurs during the coalescence of small islands with large surface-to-volume ratios, whereas GBs become immobile in continuous layers. A columnar structure develops, in which the columns are actually elongated grains. The faceted column tops increase the surface roughness, which increases with increasing thickness, giving rise to open column boundaries. The films preserve the same texture along (211) and (221) planes, and since the growth take place in both perpendicular and lateral directions the TC of (301) and (151) planes increases, with a concomitant TC drop of the (020) and (120) planes (Fig. 2). By increasing the deposition temperature to 450 °C, the adatoms have high mobility on the surface, leading to fewer nucleation sites. Therefore, complete coalescence will occur for relatively large islands because the rate of

material transfer between islands is high. GB migration takes place not only during coalescence but throughout the film-thickening process. The orientation selection during the coalescence stage is more pronounced, as it is driven by a decrease in the total GB area as well as by minimization of the interfacial and surface energies. Thus, Sb_2Se_3 films with columnar large and sintered grains, oriented preferably along [211] and [221] crystal directions were developed.

3.1.2. Efficiency of CSS-CdS/ Sb_2Se_3 solar cells depending on the absorber grain morphology and texture

It is well understood that Sb_2Se_3 films consisting of grains orientating preferably along [211] and [221] crystal directions are beneficial for the carrier transport in the solar cells, all the high-performance Sb_2Se_3 devices relying on [211]- and [221]- preferential oriented Sb_2Se_3 absorber films [3,4,7,9,20]. In our case, this orientation was present in all the films deposited at 300–450 °C and highlighted for the films deposited at 450 °C. To understand the effect of Sb_2Se_3 thin film morphology and texture on the device performance, a series of glass-/FTO/CdS/ Sb_2Se_3 /Au solar cells with a superstrate configuration were fabricated.

Fig. 3(a–c) shows J - V characteristics and evolution of the PV parameters of the glass/FTO/CdS/ Sb_2Se_3 /Au solar cells with Sb_2Se_3 absorber deposited at temperatures between 300 and 450 °C. It is clear, the solar cells with Sb_2Se_3 deposited at temperatures of 300 °C and 350 °C showed little to no performance. Negligible photocurrent can be attributed to the low-quality of the Sb_2Se_3 absorber, incorporating a high density of channels that increase shunting pathways across the junction, as was seen in Fig. 1 (a, b). However, the devices with Sb_2Se_3 absorber obtained at 400 °C marked great improvement, producing V_{OC} of 360 ± 10 mV, J_{SC} of 16.5 ± 0.4 mA/cm², FF of $28 \pm 3\%$, and efficiency of $\sim 1.6\%$. Furthermore, the cells with Sb_2Se_3 grown at 450 °C achieved the highest efficiency of $\sim 2.8\%$, showing an increase of J_{SC} to 19.5 ± 0.5 mA cm⁻², V_{OC} to 380 ± 10 mV, and FF to $38 \pm 3\%$. These results indicate that the higher deposition temperature prompting larger columnar Sb_2Se_3 grains, the lower density of GBs, and void-free junction interface proved vital for the performance of the superstrate configuration CdS/ Sb_2Se_3 solar cells. It must be noted that the solar cell efficiency was greatly limited by modest FF values, indicating to the highly resistive Sb_2Se_3 absorber material.

The EQE of the glass/FTO/CdS/ Sb_2Se_3 /Au solar cells with Sb_2Se_3 absorber deposited at temperatures between 300 and 450 °C are given in Fig. 3b. The four curves reveal that the solar cells with Sb_2Se_3 obtained at 400 and 450 °C have the largest EQE response in the entire wavelength interval. As for the device with Sb_2Se_3 deposited at 400 °C, the EQE maximum is close to 60% in the wavelength region between 600 and 900 nm. The cell with Sb_2Se_3 obtained at 450 °C has a larger EQE that explains its superior performance. This can again be attributed to the superior Sb_2Se_3 film quality at 450 °C, where a denser structure with larger grains enables efficient charge separation and transport in the

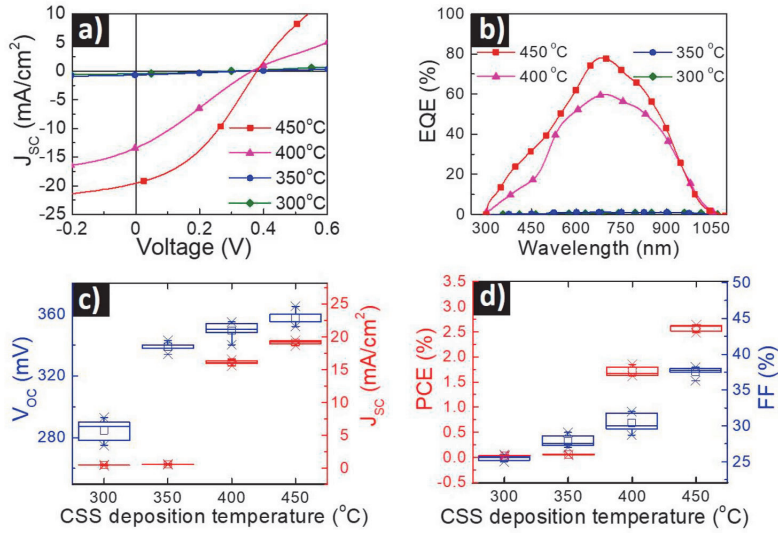


Fig. 3. a) J - V characteristics of the glass/FTO/CdS/Sb₂Se₃/Au thin film solar cells with Sb₂Se₃ absorber deposited at 300–450 °C; b) EQE spectra of the devices with Sb₂Se₃ deposited at 300–450 °C; c) and d) Evolution of the corresponding PV parameters; 5 cells were used for each deposition temperature and the average values of the PV parameters are presented.

device. However, the EQE has steep declines at both shorter and longer wavelengths. Parasitic absorption at lower wavelengths is related to the light absorption by the CdS buffer layer [3]. Despite this, the EQE of the cells with Sb₂Se₃ grown at 450 °C is still larger below ~500 nm, which marks the absorption edge of the CdS buffer ($E_g \sim 2.5$ eV, Figure S2a, Supplementary material). Low EQE at longer wavelengths is related to back surface recombination and small diffusion lengths of the minority carrier (electrons). It was reported that [221]-orientated Sb₂Se₃ films have intragrain carrier diffusion length in the range of 0.3–0.6 μm [39], which is at least two times smaller than the absorber thickness (~1.5 μm) obtained in this study at temperatures between 300 and 450 °C which may affect the carrier collection.

It is worth mentioning that the impact of CSS deposition conditions on the grain morphology and structure of Sb₂Se₃ thin films and their correlation with the CdS/Sb₂Se₃ solar cell efficiency has been investigated by several groups. Guo et al. [40] varied the CSS deposition temperature between 250 and 350 °C and found that the substrate temperature should be lower than 300 °C to prevent the [120]-oriented grain growth during CSS deposition. Therein it was shown that [211]-preferred orientation leads to the minimum series resistance, enhanced light absorbance, and 4.2% efficient CdS/Sb₂Se₃ solar cells. The same group reported in another study use of sputtered oxygenated CdS buffer, as an effective approach to improving the grain growth of Sb₂Se₃ absorber and performance of CdS:O/Sb₂Se₃ solar cells [41]. The last approach was proven to be efficient using also an oxygen plasma treatment and deposition of a monoatomic Al₂O₃ layer at the CdS–Sb₂Se₃ interface [42]. The introduction of oxygen was considered to be beneficial for preventing the Cd diffusion and formation of detrimental Cd interstitials. In contrast with these studies Wen et al. [4] demonstrated 7.6% efficient CdS/Sb₂Se₃ solar cells (the highest reported efficiency for such configuration) with the necessity of high deposition VTD temperature (≥ 400 °C) to obtain dense and high quality [221]-orientated Sb₂Se₃ absorber films. Therein it was claimed that diffusion of Cd into absorber reduces the interface defects and recombination at the heterojunction interface, both beneficial for device performance. At the same time, a common particularity for all these studies is that the CdS buffer layer, deposited by CBD or sputtering always undergoes air, CdCl₂, and/or oxygen treatments which might be crucial for

the final cell efficiency. In terms of CSS processing temperature, our results seem to support the findings by Wen et al. [4], rather than the results reported by Guo et al. [40], as the 450 °C was the only deposition temperature enabling deposition of the Sb₂Se₃ absorber layers with columnar sintered grains and [221] preferential orientation. Nevertheless, the obtained ~2.8% CSS-CdS/Sb₂Se₃ cell efficiency is still modest in comparison with the record performance of CdS based devices. The role of the substrate on the ribbon orientation of Sb₂Se₃ absorber thin films was recently investigated in Refs. [43,44], showing the great impact of various buffer layers on the growth direction of the absorber. Cumulatively, all these recent investigations show that the selection of the buffer partner layer significantly can affect the Sb₂Se₃ absorber grain structure and orientation, interface intermixing, and hence impacting heterojunction formation and final device efficiency. Thus, our next strategy was to investigate the impact of CBD-CdS and USP-TiO₂ buffer layers on the Sb₂Se₃ absorber grain structure and intermixing phenomenon at the buffer-absorber interface.

3.2. Grain structure and intermixing effect with CdS and TiO₂ heterojunction partner layers

As demonstrated above, the 450 °C was the optimal CSS processing temperature which enabled the fabrication of the Sb₂Se₃ absorber layers with columnar sintered grains and [221] preferential orientation. With this result, we validated the desideratum of the columnar-sintered large grains protocol for an efficient CSS-CdS/Sb₂Se₃ device. However, a big challenge for the next step was to prove that the 450 °C CSS processing temperature allows to control and keep the same columnar sintered grain feature in the absorber film when deposited on top of CBD-CdS and USP TiO₂ buffer layers (Figure S1, Supplementary material). The CBD CdS was selected from the consideration of its wide applicability in the Sb₂Se₃ solar cell devices and to study the intermixing phenomenon at the Sb₂Se₃–CdS interface, comparing low-temperature (85 °C) deposited CBD-CdS with high-temperature (300 °C) processed CSS-CdS buffer layer. As described in the experimental part, CSS-CdS did not undergo any annealing step, while CBD-CdS and TiO₂ received, unlike treatments prior to absorber deposition. For USP-TiO₂, the standard annealing step in the air at 450 °C for 30 min provides a higher degree of crystallinity

and better optoelectronic properties [45–47]. Annealing at 120 °C, 1 h for CBD-CdS films is a well-established procedure for the removal of secondary phases of water and organic impurities from the surface of the layers [33,48]. Both, CBD-CdS and TiO₂ based heterostructures were developed with and without a ~60 nm thick Sb₂Se₃ seed layer deposited by CSS at 300 °C (Figure S1d, Supplementary material), prior to the deposition of the Sb₂Se₃ absorber. The 300 °C CSS deposition temperature for the seed film was selected as optimal after scanning the CSS processing conditions in the temperature interval of 250–350 °C.

Fig. 4 shows the top-and cross-sectional view SEM images of CSS Sb₂Se₃ absorber films deposited at 450 °C on CBD-CdS and USP-TiO₂ with and without a CSS Sb₂Se₃ seed layer. Sb₂Se₃ films deposited onto CBD-CdS, without seed layer (Fig. 4a) exhibit similar features with the morphology of the absorber previously observed at 350–400 °C deposition temperatures onto CSS-CdS (Fig. 1c and d). Inclined ribbon-like grains and dense structures close to the absorber-buffer interface, whereas accommodation of high concentration of microvoids near to the rear surface.

The morphology is drastically changed however for the absorber grown onto TiO₂ films without seed layer, in which a highly anisotropic flake-like grain growth is discerned (Fig. 4c). For both absorber depositions, onto CBD-CdS and TiO₂ buffer layers, the use of a seed layer leads to dense absorber films with larger sintered grains and smooth crystal facets (Fig. 4b, d). While the columnar sintered grain feature is clearly distinguished in the absorber grown onto TiO₂, the same picture is not so evident for the films deposited onto CBD CdS; it looks like the grains grow more laterally to the substrate (Fig. 4b).

Fig. 5a displays XRD patterns of CSS Sb₂Se₃ absorber films deposited at 450 °C onto CBD-CdS and USP-TiO₂ layers, and Fig. 5b reveals the texture coefficients for the dominant reflection planes of the absorber. The diffractograms of the heterostructures without the seed layer show the primary peaks from the (211), (221), and (301) planes. At the same time, the (120) and (020) XRD peaks were quite pronounced in the structure with TiO₂ and without a seed layer (Fig. 5a and b), indicating the presence of the absorber grains lying parallel to the TiO₂/FTO/glass substrate. Interestingly, for the sample with CBD-CdS buffer and without a seed layer, the same reflection planes were barely detectable in the XRD pattern.

The trend in the texture of Sb₂Se₃ absorber layers deposited onto CdS and TiO₂ buffers are consistent with the changes in the grain morphology of the films shown by SEM (Fig. 4). Thus, for the Sb₂Se₃ absorber obtained with a seed layer on TiO₂, the TC of (020) and (120) planes are barely detectable, while the TC of (211), (221), and (002) planes have the highest value (Fig. 5b), indicating to the preferred orientation of the grains along with those crystal directions and hence to the columnar growth (Fig. 4d). The TC value of the (002) plane in the absorbers obtained onto CBD-CdS is significantly lower compared to the TC of the same plane of the film grown on TiO₂, nevertheless, the absorber layers preserve the same [211], [221] orientation texture. For the same structures, the high TC value of the (301) and (151) planes indicates significant lateral grain growth.

All these results generate a number of questions, such as: (i) what is the reason for the high inner porosity of the absorber grown onto CBD CdS? (ii) what makes it difficult for the absorber to grow as columnar sintered grains on TiO₂/FTO substrate when deposited without a seed layer? and (iii) what is the effect of the seed at the absorber-buffer interface? An answer to the first question may lie in the physicochemical aspects of the chemical bath deposition process which involves the presence of hydroxide groups in CBD CdS films. The mechanism of hydroxide groups in CBD CdS, together with XPS analysis are presented in the supplementary material (Figure S1 and Table S1). An explanation of the second question could be related to the presence of organic residuals in the TiO₂ layers. The USP TiO₂ films are deposited from water and/or alcohol precursor solution which contains a high concentration of residues of hydroxide and organic complexes [45,49,50]. It was previously shown that organic residuals in TiO₂ are located on the surface and at the GBs of the layers, being very stable and not easy to outdiffuse even at temperatures ≥400 °C [49]. XPS analysis of USP TiO₂ films, before and after air annealing at 450 °C (Figure S4, Supplementary material) indicates the presence of carbon species in the films. Thus, during the deposition of the absorber layer at 450 °C, the presence of such organic species could create a contra gas pressure which lowers the deposition rate of the main material on the substrate due to the high re-evaporation rate. This effect was proved experimentally, as for the absorber deposition on TiO₂ the sublimation rate was lower than 1 μm/min, and to keep the same ~1.5 μm thickness of the absorber, the CSS source temperature and the deposition time were slightly increased and prolonged, respectively. The hydroxide complexes and organic in CdS and TiO₂ have much higher vapor pressure than the pure compounds and strongly contribute to the vapor transport and grain growth on the free surface of the sublimated material resulting in porous and dispersed thin film structure (Fig. 4a, c).

The dispersed absorber structure on the TiO₂ layer in Fig. 4c can be also explained as being due to the high inert surface of the TiO₂. The oxygen is more electronegative than sulfur consequently, the oxygen is strongly bonded with the titanium in the TiO₂ having bond energy of ~660 kJ mol⁻¹ which is much stronger compared to ~200 kJ mol⁻¹ bond energy of the Cd-S [51]. This implies that the density of dangling bonds on the surface of TiO₂ is lower, making difficult formation of the initial stable nucleation sites during the deposition of the Sb₂Se₃ from the vapor phase and consequently to the growth of dense and continuous layers. This phenomenon has been observed by many other groups showing anisotropic grain growth and [020], [120] oriented Sb₂Se₃ films when deposited on TiO₂ layers [9,16,20,26,27]. As shown above the initial seed layer plays a significant role in the final film orientation. In this context, two very recent reports by Hobson et al. [9] and by Li et al. [26] showed the application of a Sb₂Se₃ seed layer as an efficient technological approach to control the growth of Sb₂Se₃ thin-film absorber. It is well understood that the processing conditions for the seed layer will impact the subsequent growth of the absorber, however, the research efforts in this direction are at the very beginning stage and the technological aspects are not yet disclosed even in the

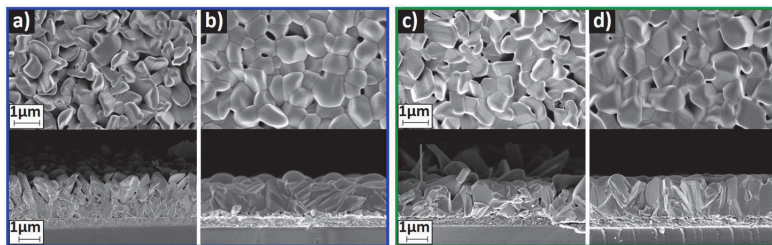


Fig. 4. Top-and cross-sectional view SEM images of CSS Sb₂Se₃ absorber films deposited at 450 °C: (a) and (b) CBD-CdS without and with a CSS Sb₂Se₃ seed layer, respectively; (c) and (d) USP-TiO₂ without and with a seed layer, respectively. In both structures, an ~60 nm thick Sb₂Se₃ seed layer was deposited by CSS at 300 °C.

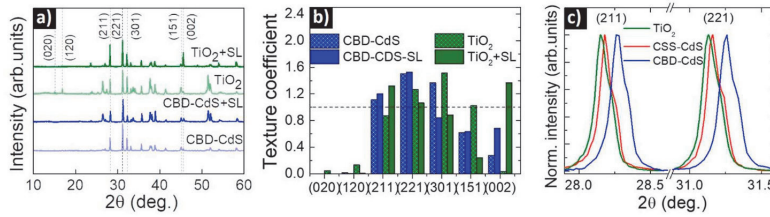


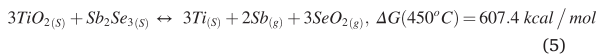
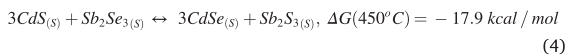
Fig. 5. a) XRD patterns of CSS Sb_2Se_3 absorber films deposited at 450°C on CBD-CdS and USP- TiO_2 layers. b) Texture coefficients calculated from integrated intensity ratios of dominant reflection planes of Sb_2Se_3 absorber. c) Displacement of the (211) and (221) XRD peaks of Sb_2Se_3 deposited on TiO_2 , CSS-CdS, and CBD-CdS layers.

forementioned two reports.

In our case, the Sb_2Se_3 seed film deposited by CSS onto TiO_2 at 300°C (Figure S1d, Supplementary material) had a nanorod grain structure, displaying some similarity to the morphology of the Sb_2Se_3 absorber film grown at 300°C onto CSS CdS shown in Fig. 1a but with a much lower thickness (60–80 nm). As explained before, at 300°C deposition temperature the initial in-plane grain sizes are set by the saturation nucleation density with the orientation of the crystallites along the (211) and (221) planes (Fig. 2). During the subsequent CSS deposition of the absorber at 450°C , the nanorod seeds aligned parallel to the substrate are easily re-evaporated, as they are bonded with the TiO_2/FTO substrate via weak van der Waals forces. Only those vertically standing nanorods, that are bonded through the strong covalent bonds with the substrate and are stable enough to resist re-evaporation, continue to grow by the addition of material from the vapor and by the high adatom surface diffusion at 450°C . Thus, large Sb_2Se_3 columnar sintered grains with low surface energies grow perpendicular to the TiO_2/FTO substrate, leading to the formation of dense, continuous, and [221] oriented Sb_2Se_3 absorber layers (Fig. 4d).

To study the possible intermixing effect between CdS and Sb_2Se_3 , we analyzed the diffraction patterns in the region of $28\text{--}32^\circ$ at a higher resolution (Fig. 5c). The displacement of the (211) and (221) main peaks towards higher 2θ values with respect to $\text{TiO}_2\text{--Sb}_2\text{Se}_3$ was observed. A similar effect was previously seen for the (511) and (111) XRD peaks in the halide processed CdS/CdTe heterostructures [35] and SnS films [31] deposited by CSS. Therein the phenomenon was explained by the intermixing at the CdS/CdTe interface with the formation of a $\text{Cd}_{1-x}\text{S}_x$ alloy and/or incorporation of chlorine impurity in the lattice of CdTe and SnS [31,34,35]. Analogous to CdS/CdTe interface, we explain the displacement of the (211) and (221) XRD peak shown in Fig. 5c as being due to the interdiffusion of sulfur from CdS into Sb_2Se_3 absorber and of the Se into the CBD-CdS buffer with the formation of $\text{CdS}_{1-x}\text{Se}_x/\text{Sb}_2\text{Se}_{3-y}\text{S}_y$ alloy at the interface. It is important to note that herein the interdiffusion took place due to subsequent absorber deposition at 450°C .

To prove these statements, we analyzed the possible thermodynamic reactions in the $\text{Sb}_2\text{Se}_3\text{--CdS}$ and $\text{Sb}_2\text{Se}_3\text{--TiO}_2$ systems (eq (4) and (5)).



For eq (4), the Gibbs free energy (ΔG) is negative, which means the reaction is thermodynamically favored toward the formation of solid CdSe and Sb_2Se_3 . This implies full transformation to CdSe and Sb_2Se_3 depending on the kinetics and quantities of the starting compounds (Table S2, Supplementary material). According to the phase diagrams of $\text{Sb}_2\text{Se}_3\text{--CdS}$ and $\text{Sb}_2\text{Se}_3\text{--CdSe}$ [52], there is high mutual solubility and probability for the formation of compounds like CdSb_2Se_4 . In contrast, the ΔG of the reaction between TiO_2 and Sb_2Se_3 (eq (5)) is largely

positive indicating the thermodynamically unfavorable reaction in this system. Considering eq (2), we claim that the intermixing occurs at the CdS/ Sb_2Se_3 interface, converting this interface into a $\text{CdS}_{1-x}\text{Se}_x/\text{Sb}_2\text{Se}_{3-y}\text{S}_y$ solid alloy. At the temperature under investigation (450°C), the solubility of selenium into CdS is higher than the solubility of the sulfur in Sb_2Se_3 [52] which favors the formation of CdSe to a higher extent at the interface. The ionic radius of sulfur (S^{2-} : 170 p.m.) [53] is smaller than the ionic radius of the selenium (Se^{2-} : 190 p.m.) [53] causing contraction of the Sb_2Se_3 sublattices and hence the shift of the (211) and (221) peaks toward higher 2θ values in Fig. 5c. At the same time, the incorporation of Se into CdS lattice prompts a shift in the (111) peak (CBD-CdS cubic modification) toward lower 2θ values (Figure S5, Supplementary material), an indication of lattice expansion. The cubic zinc blende CdSe has a lattice parameter of 0.608 nm, which is higher compared to the 0.582 nm lattice parameter of CdS with the same crystal modification [54]. Interestingly, for Sb_2Se_3 films deposited on CSS-CdS a very little shift in the XRD peaks was observed compared to CBD-CdS based structure (Fig. 5c). This result suggests that the CBD-CdS deposited from the solution at 85°C , having smaller grains [33] (Figure S1b, Supplementary material) with high surface energy, are more active for interdiffusion by mass transport through the gas phase, and consequently leads to a high degree of alloy formation at the interface during the sublimation process at 450°C .

There is still no consensus regarding the impact of the CdS– Sb_2Se_3 intermixing on the device performance. Some groups found the intermixing as potentially beneficial for the device efficiency, relying on the classical analogy with the CdTe–CdS system [4]. A more recent report suggests the interface layer establishes a potential barrier that impedes charge transport [16]. To understand the impact of the intermixing effect on the cell performance we further compared and analyzed the Sb_2Se_3 devices with CSS-CdS, CBD-CdS, and TiO_2 buffer layers.

3.3. Device performance and characterization

3.3.1. Efficiency and EQE of the cells with CdS and TiO_2 buffer layers

Fig. 6(a–c) shows the schematic of stack configurations and the comparison between $J\text{--}V$ curves and EQE spectral responses of the three solar cells: $\text{FTO}/\text{CSS-CdS}/\text{Sb}_2\text{Se}_3/\text{Au}$, $\text{FTO}/\text{CBD-CdS}/\text{Sb}_2\text{Se}_3/\text{Au}$, and $\text{FTO}/\text{USP-TiO}_2/\text{Sb}_2\text{Se}_3/\text{Au}$. To demonstrate the feasibility of large contact cells, Au with square contact geometries of 0.25 cm^2 were deposited by VE. The peak and average $J\text{--}V$ performance parameters of Sb_2Se_3 devices with three different buffer layers are displayed in Table 1. Among these three devices, the CBD-CdS– Sb_2Se_3 solar cell exhibits the lowest performance with a peak device efficiency of $\sim 2\%$, V_{OC} of 350 mV, J_{SC} of 15.6 mA cm^{-2} , and FF of 38%. Interestingly, for the same device, the inclusion of a Sb_2Se_3 seed layer at the buffer-absorber interface did not improve the cell performance. Except for the V_{OC} , which was slightly enhanced to 360 mV, all the other PV parameters remained practically unchanged. Compared to CBD-CdS based device, the cell with CSS-CdS shows a higher performance of $\sim 2.8\%$ with the peak values of V_{OC} , J_{SC} , and FF of 380 mV, 19.5 mA cm^{-2} , and 38%,

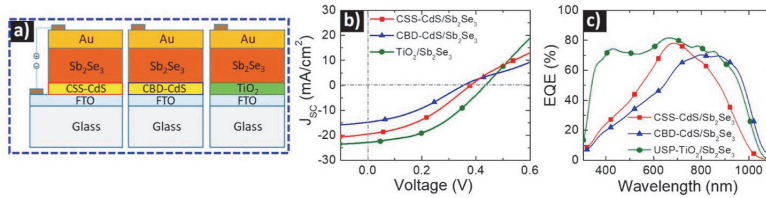


Fig. 6. a) Schematic configurations of three devices developed in this study: CSS-CdS/Sb₂Se₃, CBD-CdS/Sb₂Se₃, and USP-TiO₂/Sb₂Se₃; b) and c) Representative *J-V* curves and EQE spectral response of the corresponding solar cells.

Table 1

Peak and average *J-V* performance parameters of Sb₂Se₃ devices with three different buffer layers.

Device	Peak (P) Average (A)	V _{OC} [mV]	J _{SC} [mAcm ⁻²]	FF [%]	Eff [%]
TiO ₂ / Sb ₂ Se ₃ +SL ^a	P	430	24.6	50	5.28
	A	410 ± 10	23.9 ± 0.5	48.5 ± 1.2	4.9 ± 0.7
TiO ₂ /Sb ₂ Se ₃	P	240	19.8	35	1.66
	A	220 ± 20	18.4 ± 0.9	33 ± 2.7	1.4 ± 0.7
CSS-CdS/ Sb ₂ Se ₃	P	380	19.5	38	2.82
	A	360 ± 10	17.6 ± 0.8	36 ± 2.5	2.5 ± 0.9
CBD-CdS/ Sb ₂ Se ₃	P	350	15.6	38	2.07
	A	320 ± 15	14.2 ± 1.1	37 ± 3.4	1.8 ± 1.5

^a SL-CSS Sb₂Se₃ seed layer deposited at 300 °C.

respectively. The best performance was achieved with TiO₂/Sb₂Se₃ cell architecture with the inclusion of Sb₂Se₃ seed layer at the interface, enabling efficiency of ~5.3% with a V_{OC} of 430 mV, FF of 50%, and J_{SC} of 24.6 mA cm⁻² peak values. The same device, without incorporation of the seed layer, showed an efficiency of ~1.6% with a V_{OC} of 240 mV, FF of 35%, and J_{SC} of 19.8 mA cm⁻².

It is well understood that the previously described differences in the grain structure and texture of the Sb₂Se₃ absorber films (Fig. 4) deposited on these three buffer layers (with and without deposition of the seed layer) are reflected in the final device performance. The large, columnar, and sintered Sb₂Se₃ grains contributed to the enhanced PV parameters and efficient CSS-CdS/Sb₂Se₃ and TiO₂/Sb₂Se₃ solar cells. While for these two configurations the enhancement was highlighted, the grain sintering effect was minimal for the CBD-CdS based devices. This result indicates that the intermixing between CdS and Sb₂Se₃ with the formation of CdS_{1-x}Se_x alloy at the interface has the most detrimental effect on the CdS/Sb₂Se₃ cell performance.

The above conclusion is also supported by the changes in the EQE spectra of these three devices (Fig. 6 c). Thus, the CBD-CdS based cells with the lowest performance show the lowest EQE response in the short-wavelength region, 400–700 nm (Fig. 6c) indicating the high degree of alloy formation at the front interface. In comparison with the CBD-CdS-based device, the CSS-CdS/Sb₂Se₃ cell has a higher EQE response in the short-wavelength region, however, the response is significantly reduced in the long-wavelength region (800–1100 nm). The low blue response and low red response usually is an indication of small values of the collection function close to the buffer-absorber interface, i.e., high recombination velocity at the interface and small diffusion length of the minority carriers in the absorber bulk [55]. Phillips et al. [16] argued that the low external quantum efficiency in the region between 700 and 1050 nm is due to the CdSe layer implying a limiting conduction-band offset, hence impeding charge transport between CSS-CdS and Sb₂Se₃ layer.

At this point, it is worth noting that champion solar cells both in superstrate (7.6%) and substrate configuration (9.2%) have employed

CBD-CdS buffer layer [3,4]. Moreover, it has been shown that CdS/Sb₂Se₃ band alignments at the interface are superior to TiO₂/Sb₂Se₃ (assuming ideal grain structure), being near-optimal for charge transfer [3]. Important to mention that in both aforementioned record devices, the CBD-CdS buffer was subjected to CdCl₂ post-deposition treatment in air at ~400 °C – a well-established key processing step in CdTe PV technology. Our attempts to perform CdCl₂ treatment for CBD-CdS and to use it in Sb₂Se₃ solar cells did not succeed, although the functionality of the same buffer layer was successfully demonstrated in CdTe solar cells [33]. The main challenge we encountered when performing the CdCl₂ processing step for CdS buffer was the uncontrollability of the residual oxychlorides (as secondary phases results of the treatment) which had a great impact on the absorber morphology and buffer-absorber interface quality. The fact that only those few groups reported relatively highly efficient CdS/Sb₂Se₃ devices and that the many other groups have not yet succeeded with the same cell configuration indicates that the control of the intermixing effect remains a key issue for the CdS/Sb₂Se₃ device.

So far, the best performing 5.3% TiO₂/Sb₂Se₃ device in the study at hand also showed the highest EQE response in the entire 350–1100 nm, implying better collection efficiency. Although a promising result, the achieved cell efficiency is still lower in comparison with the recently reported ~5.6 [26] and ~7% [9,20] efficiencies for the same device configuration. The obtained V_{OC} of 430 mV and FF of 49% are comparable with the highest reported values of the aforementioned record devices, nevertheless, the main limitation comes from the low value of J_{SC} of ~24.6 mA/cm².

3.3.2. Recombination mechanisms in Sb₂Se₃ device with CdS and TiO₂ buffer layers

To identify the limiting factors for the J_{SC} and other PV parameters and to investigate the possible recombination mechanisms in the Sb₂Se₃ solar cell structures, we conducted temperature-dependent *J-V* measurements, as shown in Fig. 7(a–c). We first analyzed the V_{OC}-*T* dependence for all three devices (insets of Fig. 7a–c) that can be described by eq (6):

$$V_{OC} = \frac{E_A}{q} - \frac{A k_B T}{q} \ln \left(\frac{J_{00}}{J_L} \right) \quad (6)$$

where E_A is the activation energy of the dominant recombination path in heterojunction, *q* is the elementary charge, *A* is the ideality factor, *k_B* is the Boltzmann constant, *T* is temperature, J₀₀ is the reverse saturation diode current prefactor and J_L is photocurrent density.

For all the samples, the V_{OC}-*T* plot shows the usual initial increase at low temperature, which is expected as recombination is reduced at lower temperatures, decreasing the reverse dark saturation current. Below 240 K the V_{OC} starts to level off for the device with CSS-CdS, whereas a plateau was reached for the cells with CBD-CdS and TiO₂. A possible reason for such behavior in CSS-CdS based cell is the so-called carrier freeze-out effect that usually occurs in materials with deep defect levels and increasing blocking transport behavior at the interfaces (i.e., buffer/absorber or absorber/back contact); due to the low carrier density absorber, the device can no longer sustain high V_{OC} [56–58]. The

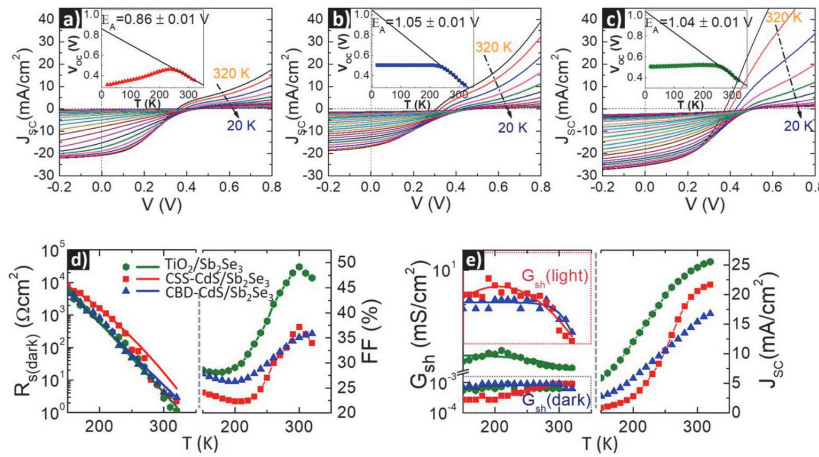


Fig. 7. Temperature-dependent J - V curves of three solar cells: a) CSS-CdS/Sb₂Se₃, b) CBD-CdS/Sb₂Se₃, and c) TiO₂/Sb₂Se₃. Insets display the V_{OC} temperature dependence together with the extrapolation to 0 K showing the activation energy (E_A) for the corresponding devices, d) Temperature dependence of FF and series resistance (R_S) extracted from dark J - V measurements e) Temperature dependence of J_{SC} and shunt conductance (G_{sh}) extracted from the illuminated and dark J - V measurements.

carrier freeze-out effect is present in all three devices, nevertheless, the abrupt behavior of the V_{OC} - T below 240 K for the CSS-CdS based cell indicates that the effect is more drastic in this device.

Extrapolation of the linear part of the V_{OC} plots to $T = 0$ K gave the activation energies of 0.86, 1.05 eV, and 1.04 eV for the solar cells with CSS-CdS, CBD-CdS, and TiO₂, respectively (Fig. 7 insets). All these values are smaller than the $E_g \sim 1.17$ eV (determined from modified EQE plot in Figure S2d, Supplementary material) of the Sb₂Se₃ absorber, indicating to the interface recombination as a predominant factor for limiting V_{OC} in these devices. For all three devices, the dominant contributor to the temperature-dependent efficiency behavior is the FF and J_{SC} behavior vs. temperature; the values of these parameters decrease monotonically with decreasing temperature (Fig. 7d and e). Generally, in an ideal solar cell, J_{SC} only changes a little with respect to temperature [55]. To identify the limiting factors for these two parameters, the temperature-dependence of the series resistance (R_S) and shunt conductance (G_{sh}) was analyzed (Fig. 7d and e). The analysis shows that the marked drop in the FF and J_{SC} is due to the significant increase of the R_S at low temperatures that distort the J - V curve and lower FF and J_{SC} values at low temperatures. The dark shunt conductance is very low ($G_{sh(D)} \sim 10^{-4}$ mS/cm²) indicating no physical shunt or leakage problem across the cells, nevertheless, the light shunt conductance ($G_{sh(L)}$) is increased by four orders of magnitude under illumination, indicating that the FF is affected by the nonequilibrium phenomena. Such an effect may imply a voltage-dependent collection-efficiency problem under light [59] caused by a high recombination rate and resulting short minority carrier collection length. In this case, increasing the forward bias will reduce the width of the space charge region (SCR), and consequently the carrier collection, as the collection due to diffusion is minimal [59]. The latter effect results in a positive slope near 0 V or higher shunt conductance under illumination $G_{sh(L)}$. The width of the SCR in a p-n heterojunction depends on many factors, but among these parameters, the carrier concentration is crucial in both n-type and p-type components.

3.3.3. Carrier concentration and defect density in Sb₂Se₃ absorber

It is worth mentioning that the conductivity type and carrier density measurements for the Sb₂Se₃ absorber are quite challenging since very few groups were able to perform carrier-type measurements and the reported values are quite dispersed. Several groups reported p-type conductivity and $\sim 10^{13}$ cm⁻³ carrier density in the Sb₂Se₃ absorber films [5,12,41,42]. The p-type conductivity behavior of thermally evaporated Sb₂Se₃ films was shown by Seebeck analysis [5] and via cyclic voltammetry [12]. A very recent report by Hobson et al. [9]

demonstrated n-type conductivity and carrier concentration of $\sim 10^{17}$ cm⁻³ in Sb₂Se₃ single crystals and CSS Sb₂Se₃ films, establishing that the $\sim 7.3\%$ efficient TCO/TiO₂/n-Sb₂Se₃/Au cell structure (one of the highest reported device performance) is, in fact, an n-n isotype heterojunction device. Therein, the chlorine was validated as an n-type dopant via intentional MgCl₂ doping of Sb₂Se₃ crystals. It is not clear, however, whether the Cl impurity in the Sb₂Se₃ source material out-diffuses or remains in the material after repeatable sublimation processes and consequently how the conductivity type and carrier density in Sb₂Se₃ films are affected. This striking result prompted us to analyze the conductivity type and carrier density of our CSS-deposited Sb₂Se₃ absorber films. The conductivity type of the absorber was analyzed by the hot-point probe technique for single Sb₂Se₃ absorber layers deposited onto glass substrates. SnS thin film deposited by CSS on the same glass substrates was used as a p-type standard [31]. The Sb₂Se₃ absorber layers always showed p-type conductivity. The films also exhibited a high dark resistivity $\rho_D \sim 2$ - $5 \cdot 10^6$ Ω cm, suggesting the self-compensation of native defects. Furthermore, the layers exhibited photoconductivity, with a dark-to-light resistance ratio of $K_{FL} \sim 30$ (having a light resistivity $\rho_L \sim 10^5$ Ω cm). Following the classical analogy with CdTe, such behavior was previously observed in CSS CdTe films only after the CdCl₂ processing step, while the as-grown CdTe films always exhibiting a semi-insulating character ($\rho_D > 10^{10}$ Ω cm) and no photosensitivity [34]. This difference between the resistivity and photosensitivity of as-deposited CSS Sb₂Se₃ and CdTe films indicates the higher carrier density and mobility in the Sb₂Se₃ absorber and may explain why the efficiency of the solar cells with untreated Sb₂Se₃ absorber is much higher compared to the devices with as-grown CdTe absorber [30]. Still, for Sb₂Se₃ films having a resistivity of $\sim 10^6$ Ω cm, it was difficult to perform Hall measurements for determination of carrier-type and density in the absorber. Thus, the carrier concentration in the Sb₂Se₃ was determined from the analysis of capacitance-voltage (C - V) measurements of the device junction (Fig. 8a). Since the hot-probe analysis showed systematic p-type conductivity of the Sb₂Se₃ absorber films, the holes were assumed as majority carriers and their density was measured to be $\sim 10^{14}$ cm⁻³.

The obtained value is three orders of magnitude lower than the recently reported 10^{17} cm⁻³ carrier density in the absorber of the TiO₂/Sb₂Se₃ n-n isotype cell configuration [9,20]. This result could be one explanation for the lower J_{SC} value of ~ 24.6 mA cm⁻² for the TiO₂/Sb₂Se₃ n-p heterojunction cells developed in this study compared to 31.7 mA cm⁻² TiO₂/Sb₂Se₃ n-n isotype device. At the same time, the temperature-dependence evolution of the PV parameters for both TiO₂/Sb₂Se₃ device as well as for the cells with CdS buffers showed the

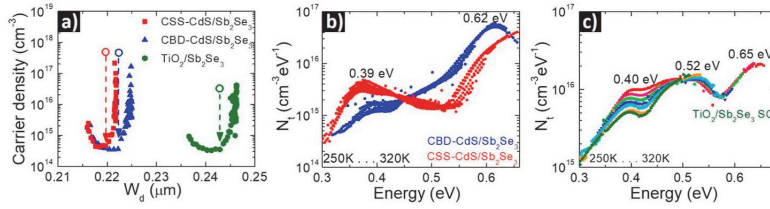


Fig. 8. a) Depth carrier density profile versus depletion width calculated from capacitance-voltage (C - V) measurements (circles denoting 0 V) for three solar cells: CSS-CdS/Sb₂Se₃, CBD-CdS/Sb₂Se₃, and USP-TiO₂/Sb₂Se₃; b) and c) Defect density profile of absorber films in the corresponding devices.

dominant interface-recombination. The transport limitation is also evident by the presence of roll-over effect (photocurrent saturation at high forward bias) in the J - V curves of all three devices at low temperatures, as shown in Fig. 7(a–c). Such an anomaly usually is observed in CdTe solar cells due to the Schottky barrier between CdTe and the metal back contact [35,60]. However, the fact that the roll-over effect in Fig. 7 is less pronounced (or even missing at 320–300 K) for the TiO₂/Sb₂Se₃ cell and is highlighted in CdS-based devices suggest that the back contact barrier might not be the only reason and the buffer-absorber interface has a large contribution to this effect. For the CdS based cells the roll-over occurs due to interaction of both effects: (i) formation of Cd_{1-x}S_x solid alloy at the interface, introducing an offset at the conduction band or valence band due to intermediate layer, and (ii) due to the low concentration of holes in the absorber and similar densities of the compensating recombination centers in buffer and absorber. As shown, the intermixing is not present in TiO₂/Sb₂Se₃ cell meaning that the deficit of hole density in the absorber still has a large contribution to the roll-over effect at low temperatures, nevertheless the positive conduction band offset at the TiO₂ buffer-FTO window interface could be also involved. If the electron barrier is fixed due to Fermi level pinning at the buffer/window interface and the electron barrier is large enough, the diode current is totally blocked and only photocurrent can pass the barrier resulting also in a roll-over anomaly of the light J - V curve [55]. In this context, the carrier density in the buffer also plays a critical role. Indeed, among all the three buffer layers used in this work, the CSS-CdS has the highest resistivity ($>10^{10} \Omega \text{ cm}$). In striking contrast with CSS-CdS, the CBD-CdS buffer layer exhibits substantially lower resistivity of $\sim 4 \times 10^2 \Omega \text{ cm}$, an electron concentration of $\sim 10^{16} \text{ cm}^{-3}$, and electron mobility of $5 \text{ cm}^2 \text{ V}^{-1} \text{ s}^{-1}$. For the TiO₂ films, a resistivity of $\sim 10^5 \Omega \text{ cm}$ was measured. The high resistivity of CSS CdS (higher than of Sb₂Se₃ absorber) implies that the SCR region extends into the buffer layer at the CdS/Sb₂Se₃ interface, leading to ineffective charge separation and increasing blocking transport behavior at the buffer/absorber interface and hence to a pronounced roll-over in the J - V response of the solar cell (Fig. 7a).

The obtained $\sim 10^{14} \text{ cm}^{-3}$ carrier density in the absorber indicates the contribution of the defect levels in Sb₂Se₃ material. To evaluate the location and distribution of defect-induced energy levels in the bandgap of the Sb₂Se₃ absorber film we used thermal admittance spectroscopy measurements [61], as shown in Fig. 8 (b, c).

For the devices with CdS buffers, there is a contribution from two bands, one centered at 0.39 eV and another, extending from 0.5 eV toward the midgap, peaking at 0.62 eV for CBD-CdS based cell (Fig. 8b). For the cell with TiO₂ buffer, it is possible to distinguish contribution from bands centered at around 0.40 eV, at 0.52 eV, and possibly also at around 0.65 eV (Fig. 8c). Wide defect bands, such as the ones observed, are generally expected to be of bulk material by the current measurement technique is employed [61]. CSS-CdS based cell also appears to show a slight hump near 0.42 eV indicating Sb₂Se₃ related origin, however, no sign of any maxima near 0.52 eV. Interestingly, the band at 0.37 eV has a somewhat lower intensity for the CBD-CdS/Sb₂Se₃ cell despite its lower V_{OC} compared to the CSS-CdS based device. However, the close-to-midgap defect levels should in fact play a more dominant

role for non-radiative type recombination and, indeed, there is indication that the $>0.45 \text{ eV}$ range has a higher density of defect levels in the cell with CBD-CdS, as seen in Fig. 8b.

The physical location as well as the physical origin of the defects is still under question and needs further insight, in particular, because the nature of the defect structure on Sb-compounds is far from trivial [62]. In the scope of the current work, peak values of defect densities between 10^{15} – $10^{16} \text{ cm}^{-3} \text{ eV}^{-1}$ were determined. For comparison, investigations of the 7.6% efficient VTD CdS/Sb₂Se₃ solar cell [4] revealed defect levels at energies at 0.48–0.49 eV (attributed to V_{Sb} acceptor) and 0.60–0.65 eV (attributed to Sb_{Se} donor), however, with total defect densities barely above 10^{15} cm^{-3} . From a theoretical perspective, the density functional calculations (DFT) [63] provide a larger variety of defects in Sb₂Se₃, with a general suggestion to the Fermi level midgap pinning due to native defects. V_{Sb} acts as a deep acceptor, with all transition levels lying close to, but further than 0.025 eV from, the valence band edge, while Se_{Sb} and Sb_{Se} exhibit amphoteric behavior, lying in the middle of the band-gap and acting as deep recombination centers [63]. Although all types of disorders (including Schottky, Frenkel, and antisite defects) are simultaneously possible in Sb₂Se₃, in general, only one type of disorder will predominate, which depends on the composition of the vapor phase and structure of the condensed phase [64]. The studies of vapor phase crystal growth of Sb₂Se₃ has shown that its sublimates congruently with slightly Se rich composition in isothermal conditions [6] (eq (7)).

$$nSb_2Se_3 = \frac{1}{4} Sb_{4(g)} + Sb_n Se_{n(g)} + Se_{2(g)} \quad (n=1) \quad (7)$$

Considering eq (7) and based on the vacancy-type mechanism as a predominant disorder in the CSS Sb₂Se₃ films, the formation of Schottky defects and the equilibrium constant in the lattice of Sb₂Se₃ films could be expressed as follow:

$$Sb_2Se_{3(s)} = [Sb_{(2-n)}Se_{(3-n)}nV_{Sb}nV_{Se}] + n_2Se_{2(g)} + n_4Sb_{4(g)} \quad (8)$$

$$K_p = [p_{Sb_4}]^{1/4} \cdot [p_{Se_2}]^{1/2} \quad (9)$$

$$2V_{Sb} + 3V_{Se} \Leftrightarrow 0 \quad (10)$$

$$K_{Schottky} = [V_{Sb}]^2 \times [V_{Se}]^3 \quad (11)$$

The charge carrier generation at a temperature of the formation of solid Sb₂Se₃ film can be expressed as follow:

$$V_{Sb} = V_{Sb}^{3-} + 3h \rightarrow \text{generation of holes} \quad (12)$$

$$V_{Se} = V_{Se}^{2+} + 2e \rightarrow \text{generation of electrons} \quad (13)$$

Mass action law and electroneutrality conditions:

$$[n][p] = np = \text{const} \quad (14)$$

$$[V_{Sb}^{3-}]^2 + n = [V_{Se}^{2+}]^3 + p \quad (15)$$

Under slight Se-rich conditions:

$$[V_{Sb}^{3-}]^2 > [V_{Se}^{2+}]^3 \rightarrow n \ll p \rightarrow [V_{Sb}^{3-}] \sim p \quad (16)$$

Thus, the concentration of uncompensated antimony vacancies generated in the absorber material at 450 °C CSS processing temperature and then freeze-in during the cooling-down process, determines the p-type conductivity and hole concentration at room temperature in Sb₂Se₃ absorber films. On the other hand, the measured $\sim 10^6$ Ω cm dark resistivity indicates the high self-compensation and thus, the concentration of the holes in the valence band should be also low. This argument is valid as the obtained carrier density $\sim 10^{14}$ cm⁻³ from C–V measurements represents in fact the concentration of uncompensated defects ($N_A - N_D$) in the absorber which may differ by several orders of magnitude and cannot be identified with the density of holes in the valence band. At the same time, it is possible that the valence and conduction band have so low carriers that a high defect density (Fig. 8b and c) in the band gap can open up a defect conduction channel that exhibits higher carrier concentration (but not higher mobility) than the normal extended state transport.

To summarize, among all three devices developed in this work, the TiO₂/Sb₂Se₃ cells exhibit the highest performance of $\sim 5.3\%$ while the efficiency of CdS-based cells is drastically limited by the intermixing effect at the CdS–Sb₂Se₃ interface. For all the cells, the recombination at the interface was identified as a dominant recombination mechanism; this together with reduced hole density in the Sb₂Se₃ absorber has a large contribution to the modest cell efficiency. At the same time, the achieved 5.3% efficient TiO₂/Sb₂Se₃ n–p heterojunction device is well aligned in the top reported cell efficiencies [20,26] with the same configuration and without the employment of back contact engineering strategy. Although optimization of back contact via incorporation of PCDTBT or PbS hole selective layer [20,26] was proved to be effective for the improvement of device performance up to 7%, there is still tremendous room for development and optimization in this direction. We are optimistic that the implementation of the same back contact approach, together with optimization of processing condition for the seed layer at the buffer-absorber interface would allow a similar boost in the efficiency of our TiO₂/Sb₂Se₃ device. Nevertheless, we consider that the main emphasis for further development should be on the development and optimization of doping strategies. Halide processing, (such as Cl, MgCl₂) [9] could be one solution in this direction, however, we consider that only implementation of controllable deliberative doping will allow for a significant boost in the efficiency and long term stability of Sb₂Se₃ based devices.

4. Conclusions

A systematic study focused on screening and optimization of CSS processing temperature and identification of optimal buffer junction partner layer was carried out to develop a protocol for growing of Sb₂Se₃ absorber with columnar grains and desired orientation for efficient solar cell device.

Different morphological and structural properties of Sb₂Se₃ absorber films obtained at deposition temperatures between 300 °C and 450 °C onto CSS CdS were explained in terms of nucleation and growth theory. Deposition at 450 °C gave absorber films with large, columnar, and sintered [221]-orientated grains which proved vital for efficient light-harvesting in CSS-CdS/Sb₂Se₃ solar cell. The grain structure and texture of the absorber deposited at 450 °C onto CBD-CdS and USP-TiO₂ buffer layers, with and without a Sb₂Se₃ seed layer, as well as an intermixing phenomenon at the buffer-absorber interface were investigated. Absorber layers with columnar [221]- oriented grains but having high inner porosity were developed on CBD-CdS, while a dispersed structure with flake-like shaped grains, lying to the substrate were obtained onto TiO₂ when the depositions were performed without a Sb₂Se₃ seed layer. For both, absorber depositions onto CBD-CdS, and TiO₂ buffer layers, the use of a seed layer at the interface lead to dense [221]-orientated absorber films with larger sintered grains and smooth crystal facets. Deposition at 450 °C was validated as optimal temperature for the development of columnar sintered grain protocol of the absorber,

but during the processing onto CdS buffer, intermixing occurred at the CdS/Sb₂Se₃ interface, converting this interface into a CdS_{1-x}Se_x/Sb₂Se_{3-y}S_y solid alloy. The alloy formation was proved by displacement of the main (211) and (221) XRD peaks, thermodynamic computation, and EQE response of the devices. While the intermixing effect was minimal for the cell with CSS-CdS and absent for the TiO₂-based device, the same effect was highlighted for the cells with CBD-CdS, resulting in the lowest device performance. So far, these results indicate that the use of CdS buffer as a heterojunction partner layer in Sb₂Se₃ solar cells is suitable for understanding the physicochemical processes in the device, nevertheless, the intermixing effect in this system represents a major impediment for further progress in the efficiency of CdS/Sb₂Se₃ cells.

TiO₂/Sb₂Se₃ n–p heterojunction type cells with an efficiency of $\sim 5.3\%$ were achieved via screening and optimization of absorber processing temperature and implementation of a seed layer at the interface. Although a promising achievement and well placed in the top reported TiO₂/Sb₂Se₃ device efficiencies, the limitation factors, like buffer-absorber interface recombination, low hole concentration, and high defect density in the absorber material remains the key issues in this device. Further, advanced characterization techniques together with systematic technological approaches, such as controlled post-deposition treatments and doping are required to get more insights into device functionality and to progress the development of emerging, cost-efficient, and low toxic Sb₂Se₃ based thin-film solar cells.

Funding

No funding was received for this work.

CRediT authorship contribution statement

Nicolae Spalatu: Conceptualization, Validation, Methodology, Formal analysis, Data curation, Writing – original draft, Writing – review & editing, Visualization. **Robert Krautmann:** Formal analysis, Writing – original draft. **Atanas Katerski:** Formal analysis, Software, Visualization, Data curation. **Erki Karber:** Writing – original draft, Formal analysis. **Raavo Josepson:** Data curation, Formal analysis. **Jaan Hiie:** Formal analysis. **Ilona Oja Acik:** Formal analysis, Writing – review & editing. **Malle Krunks:** Formal analysis, Writing – review & editing.

Declaration of competing interest

The authors declare that they have no known competing financial interests or personal relationships that could have appeared to influence the work reported in this paper.

Acknowledgments

This study was funded by the Estonian Research Council project PRG627 “Antimony chalcogenide thin films for next-generation semi-transparent solar cells applicable in electricity producing windows”, the Estonian Centre of Excellence project TK141 (TAR160166K) “Advanced materials and high-technology devices for energy recuperation systems”, and the European Union’s H2020 programme under the ERA Chair project 5GSOLAR grant agreement No 952509.

Appendix A. Supplementary data

Supplementary data to this article can be found online at <https://doi.org/10.1016/j.solmat.2021.111045>.

References

- [1] T.D. Lee, A.U. Ebong, A review of thin film solar cell technologies and challenges, *Renew. Sustain. Energy Rev.* 70 (2017) 1286–1297, <https://doi.org/10.1016/j.rser.2016.12.028>.

- [2] M.A. Green, E.D. Dunlop, J. Hohl-Ebinger, M. Yoshita, N. Kopidakis, A.W.Y. Ho-Baillie, Solar cell efficiency tables (Version 55), *Prog. Photovoltaics Res. Appl.* 28 (2020) 3–15, <https://doi.org/10.1002/pp.3228>.
- [3] Z. Li, X. Liang, G. Li, H. Liu, H. Zhang, J. Guo, J. Chen, K. Shen, X. San, W. Yu, R.E.I. Schropp, Y. Mai, 9.2%-efficient core-shell structured antimony selenide nanorod array solar cells, *Nat. Commun.* 10 (2019) 1–9, <https://doi.org/10.1038/s41467-018-07903-6>.
- [4] X. Wen, C. Chen, S. Lu, K. Li, R. Kondrotas, Y. Zhao, W. Chen, L. Gao, C. Wang, J. Zhang, G. Niu, J. Tang, Vapor transport deposition of antimony selenide thin film solar cells with 7.6% efficiency, *Nat. Commun.* 9 (2018) 1–10, <https://doi.org/10.1038/s41467-018-04634-6>.
- [5] X. Liu, J. Chen, M. Luo, M. Leng, Z. Xia, Y. Zhou, S. Qin, D.J. Xue, L. Lv, H. Huang, D. Niu, J. Tang, Thermal evaporation and characterization of Sb₂Se₃ thin film for substrate Sb₂Se₃/CdS solar cells, *ACS Appl. Mater. Interfaces* 6 (2014) 10687–10695, <https://doi.org/10.1021/am502427s>.
- [6] G. Ghosh, The sb-se (antimony-selenium) system, *J. Phase Equil.* 14 (1993) 753–763, <https://doi.org/10.1007/BF02667889>.
- [7] Y. Zhou, L. Wang, S. Chen, S. Qin, X. Liu, J. Chen, D.J. Xue, M. Luo, Y. Cao, Y. Cheng, E.H. Sargent, J. Tang, Thin-film Sb₂Se₃ photovoltaics with oriented one-dimensional ribbons and benign grain boundaries, *Nat. Photon.* 9 (2015) 409–415, <https://doi.org/10.1038/nphoton.2015.78>.
- [8] V. Kumar, E. Argezianni, A. Kumar, G. Mariotto, F. Piccinelli, A. Romeo, Effects of post-deposition annealing and copper inclusion in superstrate Sb₂Se₃ based solar cells by thermal evaporation, *Sol. Energy* 193 (2019) 452–457, <https://doi.org/10.1016/j.solener.2019.09.069>.
- [9] T.D.C. Hobson, L.J. Phillips, O.S. Hutter, H. Shiel, J.E.N. Swallow, C.N. Savory, P. K. Nayak, S. Mariotti, B. Das, L. Bowen, L.A.H. Jones, T.J. Featherstone, M. J. Smiles, M.A. Farnworth, G. Zoppi, P.K. Thakur, T.-L. Lee, H.J. Snaith, C. Leighton, D.O. Scanlon, V.R. Dhanak, K. Durose, T.D. Veal, J.D. Major, Isotype heterojunction solar cells using n-type Sb₂Se₃ thin films, *Chem. Mater.* (2020), <https://doi.org/10.1021/acs.chemmater.0c00223>.
- [10] R. Tang, X.Y. Chen, G.X. Liang, Z.H. Su, J. ting Luo, P. Fan, Magnetron sputtering deposition and selenization of Sb₂Se₃ thin film for substrate Sb₂Se₃/CdS solar cells, *Surf. Coating. Technol.* 360 (2019) 68–72, <https://doi.org/10.1016/j.surfcoat.2018.12.102>.
- [11] Y.C. Choi, D.U. Lee, J.H. Noh, E.K. Kim, S. Il Seok, Highly improved Sb₂Se₃ sensitized-inorganic-organic heterojunction solar cells and quantification of traps by deep-level transient spectroscopy, *Adv. Funct. Mater.* 24 (2014) 3587–3592, <https://doi.org/10.1002/adfm.201304238>.
- [12] Y. Zhou, M. Leng, Z. Xia, J. Zhong, H. Song, X. Liu, B. Yang, J. Zhang, J. Chen, K. Zhou, J. Han, Y. Cheng, J. Tang, Solution-processed antimony selenide heterojunction solar cells, *Adv. Energy Mater.* (2014), <https://doi.org/10.1002/aenm.201301846>.
- [13] T.T. Ngo, S. Chavhan, I. Kosta, O. Miguel, H.J. Grande, R. Tena-Zaera, Electrodeposition of antimony selenide thin films and application in semiconductor sensitized solar cells, *ACS Appl. Mater. Interfaces* 6 (2014) 2836–2841, <https://doi.org/10.1021/am405416a>.
- [14] J. Yang, Y. Lai, Y. Fan, Y. Jiang, D. Tang, L. Jiang, F. Liu, J. Li, Photoelectrochemically deposited Sb₂Se₃ thin films: deposition mechanism and characterization, *RSC Adv.* 5 (2015) 85592–85597, <https://doi.org/10.1039/c5ra16055c>.
- [15] S.A. Semenkovich, B.T. Melekch, Thermodynamic properties of Bi₂Te₃, Bi₂Se₃, Sb₂Te₃, and Sb₂Se₃, in: *Chem. Bond. Solids*, Springer US, 1972, pp. 159–162, https://doi.org/10.1007/978-1-4684-1686-2_27.
- [16] L.J. Phillips, C.N. Savory, O.S. Hutter, P.J. Yates, H. Shiel, S. Mariotti, L. Bowen, M. Birkett, K. Durose, D.O. Scanlon, J.D. Major, Current enhancement via a TiO₂ window layer for CSS Sb₂Se₃ solar cells: performance limits and high Voc, *IEEE J. Photovoltaics* 9 (2019) 544–551, <https://doi.org/10.1109/JPHOTOV.2018.2885836>.
- [17] Z. Li, X. Chen, H. Zhu, J. Chen, Y. Guo, C. Zhang, W. Zhang, X. Niu, Y. Mai, Sb₂Se₃ thin film solar cells in substrate configuration and the back contact selenization, *Sol. Energy Mater. Sol. Cells* 161 (2017) 190–196, <https://doi.org/10.1016/j.solmat.2016.11.033>.
- [18] S.N. Park, S.Y. Kim, S.J. Lee, S.J. Sung, K.J. Yang, J.K. Kang, D.H. Kim, Controlled synthesis of (hk1) preferentially oriented Sb₂Se₃ rod arrays by co-evaporation for photovoltaic applications, *J. Mater. Chem. A* 7 (2019) 25900–25907, <https://doi.org/10.1039/c9ta08289a>.
- [19] K.J. Tiwari, M. Neuschitzer, M. Espindola-Rodriguez, Y. Sánchez, Z. Jehl, P. Vidal-Fuentes, E. Saucedo, P. Malar, Efficient Sb₂Se₃/CdS planar heterojunction solar cells in substrate configuration with (hk0) oriented Sb₂Se₃ thin films, *Sol. Energy Mater. Sol. Cells* 215 (2020), 110603, <https://doi.org/10.1016/j.solmat.2020.110603>.
- [20] O.S. Hutter, L.J. Phillips, K. Durose, J.D. Major, 6.6% efficient antimony selenide solar cells using grain structure control and an organic contact layer, *Sol. Energy Mater. Sol. Cells* 188 (2018) 177–181, <https://doi.org/10.1016/j.solmat.2018.09.004>.
- [21] X. Liang, X. Chen, Z. Li, G. Li, J. Chen, L. Yang, K. Shen, Y. Xu, Y. Mai, Effect of deposition pressure on the properties of magnetron sputtering-deposited Sb₂Se₃ thin-film solar cells, *Appl. Phys. Mater. Sci. Process* 125 (2019) 1–7, <https://doi.org/10.1007/s00339-019-2677-7>.
- [22] G.X. Liang, Z.H. Zheng, P. Fan, J.T. Luo, J.G. Hu, X.H. Zhang, H.L. Ma, B. Fan, Z. K. Luo, D.P. Zhang, Thermally induced structural evolution and performance of Sb₂Se₃ films and nanorods prepared by an easy sputtering method, *Sol. Energy Mater. Sol. Cells* 174 (2018) 263–270, <https://doi.org/10.1016/j.solmat.2017.09.008>.
- [23] G.X. Liang, X.H. Zhang, H.L. Ma, J.G. Hu, B. Fan, Z.K. Luo, Z.H. Zheng, J.T. Luo, P. Fan, Facile preparation and enhanced photoelectrical performance of Sb₂Se₃ nano-rods by magnetron sputtering deposition, *Sol. Energy Mater. Sol. Cells* 160 (2017) 257–262, <https://doi.org/10.1016/j.solmat.2016.10.042>.
- [24] R.E. Williams, Q.M. Ramasse, K.P. McKenna, L.J. Phillips, P.J. Yates, O.S. Hutter, K. Durose, J.D. Major, B.G. Mendis, Evidence for self-healing benign grain boundaries and a highly defective Sb₂Se₃-CdS interfacial layer in Sb₂Se₃ thin-film photovoltaics, *ACS Appl. Mater. Interfaces* 12 (2020) 21730–21738, <https://doi.org/10.1021/acami.0c03690>.
- [25] Y. Zhou, Y. Li, J. Luo, D. Li, X. Liu, C. Chen, H. Song, J. Ma, D.J. Xue, B. Yang, J. Tang, Buried homojunction in CdS/Sb₂Se₃ thin film photovoltaics generated by interfacial diffusion, *Appl. Phys. Lett.* 111 (2017) 13901, <https://doi.org/10.1063/1.4991539>.
- [26] K. Li, C. Chen, S. Lu, C. Wang, S. Wang, Y. Lu, J. Tang, Orientation engineering in low-dimensional crystal-structural materials via seed screening, *Adv. Mater.* 31 (2019), 1903914, <https://doi.org/10.1002/adma.201903914>.
- [27] C. Chen, Y. Zhao, S. Lu, K. Li, Y. Li, B. Yang, W. Chen, L. Wang, D. Li, H. Deng, F. Yi, J. Tang, Accelerated optimization of TiO₂/Sb₂Se₃ thin film solar cells by high-throughput combinatorial approach, *Adv. Energy Mater.* 7 (2017), 1700866, <https://doi.org/10.1002/aenm.201700866>.
- [28] L. Wang, D.B. Li, K. Li, C. Chen, H.X. Deng, L. Gao, Y. Zhao, F. Jiang, L. Li, F. Huang, Y. He, H. Song, G. Niu, J. Tang, Stable 6%-efficient Sb₂Se₃ solar cells with a ZnO buffer layer, *Nat. Energy* 2 (2017) 17046, <https://doi.org/10.1038/energy.2017.46>.
- [29] I. Gharibshahian, A.A. Orouji, S. Sharbati, Towards high efficiency Cd-Free Sb₂Se₃ solar cells by the band alignment optimization, *Sol. Energy Mater. Sol. Cells* 212 (2020), 110581, <https://doi.org/10.1016/j.solmat.2020.110581>.
- [30] S. Polivtseva, N. Spalatu, A. Abdalla, O. Volobujeva, J. Hiie, S. Bereznev, Pulsed laser deposition of Zn(O,Se) layers for optoelectronic application, *ACS Appl. Energy Mater.* 1 (2018) 6505–6512, <https://doi.org/10.1021/acsaem.8b01431>.
- [31] N. Spalatu, J. Hiie, R. Kaupmees, O. Volobujeva, J. Krustok, I.O. Acik, M. Krunk, Postdeposition processing of SnS thin films and solar cells: prospective strategy to obtain large, sintered, and doped SnS grains by recrystallization in the presence of a metal halide flux, *ACS Appl. Mater. Interfaces* 11 (2019) 17539–17554, <https://doi.org/10.1021/acami.9b03213>.
- [32] N. Maticiu, J. Hiie, V. Mikli, T. Potlog, V. Valdna, Structural and optical properties of cadmium sulfide thin films modified by hydrogen annealing, *Mater. Sci. Semicond. Process.* 26 (2014) 169–174, <https://doi.org/10.1016/j.mssp.2014.04.031>.
- [33] N. Maticiu, N. Spalatu, V. Mikli, J. Hiie, Impact of CdS annealing atmosphere on the performance of CdS-CdTe solar cell, in: *Appl. Surf. Sci.*, Elsevier B.V., 2015, pp. 14–18, <https://doi.org/10.1016/j.apsusc.2015.01.172>.
- [34] N. Spalatu, M. Krunk, J. Hiie, Structural and optoelectronic properties of CdCl₂ activated CdTe thin films modified by multiple thermal annealing, *Thin Solid Films* 633 (2017) 106–111, <https://doi.org/10.1016/j.tsf.2016.09.042>.
- [35] N. Spalatu, J. Hiie, V. Mikli, M. Krunk, V. Valdna, N. Maticiu, T. Raadik, M. Caraman, Effect of CdCl₂ annealing treatment on structural and optoelectronic properties of close spaced sublimation CdTe/CdS thin film solar cells vs deposition conditions, in: *Thin Solid Films*, Elsevier, 2015, pp. 128–133, <https://doi.org/10.1016/j.tsf.2014.11.066>.
- [36] G.B. Harris, Quantitative measurement of preferred orientation in rolled uranium bars, London, Edinburgh, Dublin Philos. Mag. J. Sci. 43 (1952) 113–123, <https://doi.org/10.1080/14786440108520972>.
- [37] H.J. Bunge, Influence of texture on powder diffraction, *Textures Microstruct.* 29 (1997) 1–26, <https://doi.org/10.1155/tsm.29.1>.
- [38] M. Kumar, A. Kumar, A.C. Abhyankar, Influence of texture coefficient on surface morphology and sensing properties of W-doped nanocrystalline tin oxide thin films, *ACS Appl. Mater. Interfaces* 7 (2015) 3571–3580, <https://doi.org/10.1021/am507397z>.
- [39] C. Chen, D.C. Bobela, Y. Yang, S. Lu, K. Zeng, C. Ge, B. Yang, L. Gao, Y. Zhao, M. C. Beard, J. Tang, Characterization of basic physical properties of Sb₂Se₃ and its relevance for photovoltaics, *Front. Optoelectron.* 10 (2017) 18–30, <https://doi.org/10.1007/s12200-017-0702-z>.
- [40] L. Guo, B. Zhang, Y. Qin, D. Li, L. Li, X. Qian, F. Yan, Tunable quasi-one-dimensional ribbon enhanced light absorption in Sb₂Se₃ thin-film solar cells grown by close-space sublimation, *Sol. RRL* (2018), <https://doi.org/10.1002/solr.201800128>.
- [41] L. Guo, B. Zhang, S. Ranjit, J. Wall, S. Saurav, A.J. Hauser, G. Xing, L. Li, X. Qian, F. Yan, Interface engineering via sputtered oxygenated CdS:O window layer for highly efficient Sb₂Se₃ thin-film solar cells with efficiency above 7%, *Sol. RRL* (2019) <https://doi.org/10.1002/solr.201900225>.
- [42] H. Guo, Z. Chen, X. Wang, Q. Cang, X. Jia, C. Ma, N. Yuan, J. Ding, Enhancement in the efficiency of Sb₂Se₃ thin-film solar cells by increasing carrier concentration and inducing columnar growth of the grains, *Sol. RRL* (2019), <https://doi.org/10.1002/solr.201800224>.
- [43] F. Pattini, S. Rampino, F. Mezzadri, D. Calestani, G. Spaggiari, M. Sidoli, D. Delmonte, A. Sala, E. Gilio, M. Mazzer, Role of the substrates in the ribbon orientation of Sb₂Se₃ films grown by Low-Temperature Pulsed Electron Deposition, *Sol. Energy Mater. Sol. Cells* 218 (2020), <https://doi.org/10.1016/j.solmat.2020.110724>.
- [44] J. Zhou, H. Chen, X. Zhang, K. Chi, Y. Cai, Y. Cao, J. Pang, Substrate dependence on (Sb₄Se₆)_n ribbon orientations of antimony selenide thin films: morphology, carrier transport and photovoltaic performance, *J. Alloys Compd.* 862 (2021), 158703, <https://doi.org/10.1016/j.jallcom.2021.158703>.

- [45] I. Dundar, M. Krichevskaya, A. Katerski, I.O. Acik, TiO₂ thin films by ultrasonic spray pyrolysis as photocatalytic material for air purification, *R. Soc. Open Sci.* 6 (2019), <https://doi.org/10.1098/rsos.181578>.
- [46] E. Kärber, A. Katerski, I. Oja Acik, A. Mere, V. Mikli, M. Krunks, Sb₂S₃ grown by ultrasonic spray pyrolysis and its application in a hybrid solar cell, *Beilstein J. Nanotechnol.* 7 (2016) 1662–1673, <https://doi.org/10.3762/bjnano.7.158>.
- [47] R. Parize, A. Katerski, I. Gromyko, L. Rapenne, H. Roussel, E. Kärber, E. Appert, M. Krunks, V. Consonni, ZnO/TiO₂/Sb₂S₃ core–shell nanowire heterostructure for extremely thin absorber solar cells, *J. Phys. Chem. C* 121 (2017) 9672–9680, <https://doi.org/10.1021/acs.jpcc.7b00178>.
- [48] A. Graf, N. Maticiu, N. Spalatu, V. Mikli, A. Mere, A. Gavrilov, J. Hiie, Electrical characterization of annealed chemical-bath-deposited CdS films and their application in superstrate configuration CdTe/CdS solar cells, in: *Thin Solid Films*, Elsevier, 2015, pp. 351–355, <https://doi.org/10.1016/j.tsf.2014.11.003>.
- [49] I. Oja, A. Mere, M. Krunks, C.-H. Solterbeck, M. Es-Souni, Properties of TiO₂ films prepared by the spray pyrolysis method, *Solid State Phenom.* 99–100 (2004) 259–264. <https://doi.org/10.4028/www.scientific.net/SSP.99-100.259>.
- [50] N. Maticiu, A. Katerski, M. Danilson, M. Krunks, J. Hiie, XPS study of OH impurity in solution processed CdS thin films, *Sol. Energy Mater. Sol. Cells* 160 (2017) 211–216, <https://doi.org/10.1016/j.solmat.2016.10.040>.
- [51] Outokumpu Research Oy, Database of HSC Chemistry, ((n.d.)).
- [52] V. Tomashyk, Quaternary Alloys Based on II-VI Semiconductors, CRC Press, 2014, <https://doi.org/10.1201/b17523>.
- [53] B. Cordero, V. Gómez, A.E. Platero-Prats, M. Revés, J. Echeverría, E. Cremades, F. Barragán, S. Alvarez, Covalent radii revisited, *J. Chem. Soc. Dalton Trans.* (2008) 2832–2838, <https://doi.org/10.1039/b801115j>.
- [54] S. Adachi, Properties of Group-IV, III-V and II-VI Semiconductors, John Wiley & Sons, Ltd, Chichester, 2005, <https://doi.org/10.1002/0470090340>.
- [55] R. Scheer, H.-W. Schock, Chalcogenide Photovoltaics, Wiley-VCH Verlag GmbH & Co. KGaA, Weinheim, 2011, <https://doi.org/10.1002/9783527633708>.
- [56] J. Krustok, R. Josepson, M. Danilson, D. Meissner, Temperature dependence of Cu₂ZnSn(SexS_{1-x})₄ monograin solar cells, *Sol. Energy* 84 (2010) 379–383, <https://doi.org/10.1016/j.solener.2009.09.011>.
- [57] T.K. Todorov, S. Singh, D.M. Bishop, O. Gunawan, Y.S. Lee, T.S. Gershon, K. W. Brew, P.D. Antunez, R. Haight, Ultrathin high band gap solar cells with improved efficiencies from the world's oldest photovoltaic material, *Nat. Commun.* 8 (2017) 1–8, <https://doi.org/10.1038/s41467-017-00582-9>.
- [58] O. Gunawan, T. Gokmen, D.B. Mitzi, Suns- VOC characteristics of high performance kesterite solar cells, *J. Appl. Phys.* 116 (2014) 84504, <https://doi.org/10.1063/1.4893315>.
- [59] S.S. Hegedus, W.N. Shafarman, Thin-film solar cells: device measurements and analysis, *Prog. Photovoltaics Res. Appl.* 12 (2004) 155–176, <https://doi.org/10.1002/pip.518>.
- [60] B.E. McCandless, J.R. Sites, Cadmium telluride solar cells, in: *Handb. Photovolt. Sci. Eng.* John Wiley & Sons, Ltd, Chichester, 2005, pp. 617–662, <https://doi.org/10.1002/0470014008.ch14>.
- [61] T. Walter, R. Herberholz, C. Müller, H.W. Schock, Determination of defect distributions from admittance measurements and application to Cu(In,Ga)Se₂ based heterojunctions Determination of defect distributions from admittance measurements and application to Cu(In,Ga)Se₂ based heterojunctions, *Science* (1996) 4411–4420, <https://doi.org/10.1063/1.363401>, 80.
- [62] M. Huang, P. Xu, D. Han, J. Tang, S. Chen, Complicated and unconventional defect properties of the quasi-one-dimensional photovoltaic semiconductor Sb₂Se₃, *ACS Appl. Mater. Interfaces* 11 (2019) 15564–15572, <https://doi.org/10.1021/acsami.9b01220>.
- [63] C.N. Savory, D.O. Scanlon, The complex defect chemistry of antimony selenide †, <https://doi.org/10.1039/c9ta02022e>, 2019.
- [64] P. Handler, Physics and chemistry of II-VI compounds, in: M. Aven, J.S. Prener (Eds.), *North-Holland, Amsterdam; Interscience, Wiley, New York*, 1967, <https://doi.org/10.1126/science.159.3811.185>, 862 pp., illus. \$30, *Science* (80-.). 159 (1968) 185.

Update

Solar Energy Materials and Solar Cells

Volume 228, Issue , 15 August 2021, Page

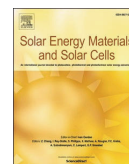
DOI: <https://doi.org/10.1016/j.solmat.2021.111098>



Contents lists available at ScienceDirect

Solar Energy Materials and Solar Cells

journal homepage: <http://www.elsevier.com/locate/solmat>



Corrigendum



Corrigendum to “Screening and optimization of processing temperature for Sb_2Se_3 thin film growth protocol: Interrelation between grain structure, interface intermixing and solar cell performance” [Solar Energy Mater. Solar Cell. 225 (2021) 1–13 111045]

Nicolae Spalatu^{a,*}, Robert Krautmann^a, Atanas Katerski^a, Erki Kärber^a, Raavo Josepson^b, Jaan Hiie^a, Ilona Oja Acik^a, Malle Krunks^a

^a Department of Materials and Environmental Technology, Tallinn University of Technology, Ehitajate Tee 5, 19086, Tallinn, Estonia

^b Division of Physics, Tallinn University of Technology, Ehitajate Tee 5, 19086, Tallinn, Estonia

The authors regret the miss-spelled name of a co-author. In the published version it is written “Erki Karber”, the correct version is “Erki

Kärber”. Please type correct name “Erki Kärber”.

The authors would like to apologise for any inconvenience caused.

DOI of original article: <https://doi.org/10.1016/j.solmat.2021.111045>.

* Corresponding author.

E-mail address: nicolae.spalatu@taltech.ee (N. Spalatu).

<https://doi.org/10.1016/j.solmat.2021.111098>

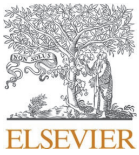
Available online 12 April 2021

0927-0248/© 2021 The Author(s). Published by Elsevier B.V. All rights reserved.

Appendix 2

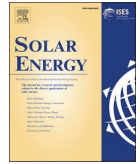
PUBLICATION II

R. Krautmann, N. Spalatu, R. Gunder, D. Abou-Ras, T. Unold, S. Schorr, M. Krunks, I. Oja Acik, "Analysis of grain orientation and defects in Sb_2Se_3 solar cells fabricated by close-spaced sublimation", *Solar Energy*, vol. 225, pp. 494–500, 2021, DOI: 10.1016/j.solener.2021.07.022.



Contents lists available at ScienceDirect

Solar Energy

journal homepage: www.elsevier.com/locate/solener

Analysis of grain orientation and defects in Sb₂Se₃ solar cells fabricated by close-spaced sublimation

R. Krautmann^{a,*}, N. Spalatu^{a,*}, R. Gunder^b, D. Abou-Ras^b, T. Unold^b, S. Schorr^{b,c}, M. Krunks^a, I. Oja Acik^a

^a Tallinn University of Technology, Department of Materials and Environmental Technology, Laboratory of Thin Film Chemical Technologies, Ehitajate tee 5, 19086 Tallinn, Estonia

^b Helmholtz-Zentrum Berlin für Materialien und Energie GmbH, Department Structure and Dynamics of Energy Materials, Hahn-Meitner Platz 1, 14109 Berlin, Germany

^c Freie University Berlin, Institute of Geological Sciences, Malteserstr. 74-100, 12249 Berlin, Germany

ARTICLE INFO

Keywords:

Antimony selenide
Close-spaced sublimation
Grain orientation
Pole figures
Deep defects
Admittance spectroscopy

ABSTRACT

The performance of a superstrate TiO₂/Sb₂Se₃ solar cell, fabricated by close-spaced sublimation technique (CSS), was improved after the deployment of a seed layer. The seed layer caused columnar Sb₂Se₃ film growth with texture coefficient analysis (TC) showing increased presence of crystal planes, which are inclined towards the [001] crystal direction. Given the highly anisotropic properties of Sb₂Se₃, preferential growth of (Sb₄Se₆)_n ribbons along the [001] direction is best suited for effective charge collection. Hence, grain orientation of Sb₂Se₃ films was studied more closely via measurement of pole figures by XRD and orientation distribution maps by electron backscatter diffraction (EBSD). Although the measurements did not reveal strong preferred orientation, it was observed that the columnar Sb₂Se₃ growth enhanced texture along the [001] direction. Temperature-dependent admittance spectroscopy (TAS) and capacitance–voltage (CV) profiling were performed on the seed-assisted TiO₂/Sb₂Se₃ solar cell to evaluate carrier density and deep defects in the Sb₂Se₃ absorber. TAS study revealed a deep defect with activation energy of 0.39 eV. CV profiles indicated that the density of defects could be as high as 10¹⁷ cm⁻³, which needs to be addressed by post-deposition treatments.

1. Introduction

Antimony selenide (Sb₂Se₃) has emerged as a potential photovoltaic absorber. Sb₂Se₃ has excellent optoelectronic properties: a high absorption coefficient (>10⁵ cm⁻¹ at shorter wavelengths) (Zhou et al., 2014) and suitable band-gap of 1.1–1.3 eV (Li et al., 2019c; Wen et al., 2018). Single phase binary structure and low evaporation point have made Sb₂Se₃ compatible with CdTe solar cell fabrication processes (Spalatu et al., 2017), also partly explaining the rapid growth in Sb₂Se₃ solar cell efficiency. While deposition techniques, such as magnetron sputtering (Liang et al., 2020) and rapid thermal evaporation (RTE) (Chen et al., 2017b) have allowed fabrication of Sb₂Se₃ devices with >6% efficiency, close-spaced sublimation (CSS) and vapor transport deposition (VTD) techniques have enabled to produce champion Sb₂Se₃ solar cells with efficiencies 9.2% (Li et al., 2019c) and 7.6% (Wen et al., 2018), respectively. Recently, Spalatu et al., reported on the optimization of growth conditions for depositing Sb₂Se₃ absorber layers by CSS, in which the Sb₂Se₃ layers deposited at 450 °C onto the TiO₂ buffer layer

saw optimal performance (Spalatu et al., 2021). This involved use of a seed layer, which significantly improved the microstructure of the Sb₂Se₃ absorber. In order to better understand the current limitations of CSS-deposited Sb₂Se₃ devices, the microstructure and defect properties are investigated in more detail in this work. This paper aims to give a significantly more accurate account on the orientations of polycrystalline Sb₂Se₃ films and shed light on the physical origin and role of one of the deep defects prevalent in the Sb₂Se₃ absorber.

Lately, a lot of attention has turned to the crystal anisotropy. Sb₂Se₃ possesses orthorhombic crystal structure, where crystals form one-dimensional (1D) (Sb₄Se₆)_n ribbons, in which atoms are covalently bonded (Ghosh, 1993; Liu et al., 2014). At the same time, ribbons adjacent to each other only bond via weak van der Waals' forces. After proving that the carrier transport is more efficient along the covalently bonded (Sb₄Se₆)_n ribbons than between them (Chen et al., 2017a), it became clear that carrier collection could be significantly improved provided that Sb₂Se₃ grains are preferentially grown along the c-axis, [001] crystal direction. To illustrate this, record Sb₂Se₃ solar cell

* Corresponding authors.

E-mail addresses: robert.krautmann@taltech.ee (R. Krautmann), nicolae.spalatu@taltech.ee (N. Spalatu).

<https://doi.org/10.1016/j.solener.2021.07.022>

Received 28 April 2021; Received in revised form 28 June 2021; Accepted 12 July 2021

Available online 29 July 2021

0038-092X/© 2021 The Authors. Published by Elsevier Ltd on behalf of International Solar Energy Society. This is an open access article under the CC BY-NC-ND

license (<http://creativecommons.org/licenses/by-nc-nd/4.0/>).

performance ($\eta = 9.2\%$) was largely attributed to the nanoribbons exhibiting preferred orientation in the *c*-axis direction (Li et al., 2019c). Today, links between preferred orientation and device performance have been demonstrated in many studies, and are mainly proven through texture coefficient (TC) analysis derived from the XRD patterns (Li et al., 2019a, 2017; Liang et al., 2020; Wang et al., 2017; Zhang et al., 2020; Zhou et al., 2020). By definition, TC value that is larger than 1 indicates a preferred orientation of a *hkl* reflection compared with the random distribution of grains in a powder (Bérubé and L'Espérance, 1989). Previously, it has been argued that the TC analysis might not be best suited for measuring texture in polycrystalline films with highly anisotropic crystallites, because the grain morphology could contribute to the overestimation of the actual texture (Ariosa et al., 2011). More recently, however, TC analysis was argued to be a trustworthy tool for evaluating preferred orientation in Sb_2Se_3 films, because the outcome was consistent with what was observed from pole figures measured by XRD (Pattini et al., 2020). Considering the above, pole figure measurements by XRD and orientation distribution maps by electron-backscatter diffraction (EBSD) were performed in addition to the TC analysis with the aim to provide more clarity regarding the grain orientation of the Sb_2Se_3 films.

While favorable Sb_2Se_3 grain orientations enhance charge transport, numerous deep defects in Sb_2Se_3 trap and prevent carriers from being collected. A large $V_{\text{OC}} > 0.7$ V deficit poses one of the many bottlenecks, explaining why Sb_2Se_3 devices are still far from the theoretical efficiency limit (Savory and Scanlon, 2019). For bandgaps of 1.1–1.3 eV, studies have reported V_{OC} values between 0.36 and 0.43 V (Hobson et al., 2020; Li et al., 2019b, 2019c; Wang et al., 2017; Wen et al., 2018). Significant levels of recombination via deep traps can in large part explain the low V_{OC} (Savory and Scanlon, 2019). Wen et al., were first to demonstrate multiple trap states deep in the band gap using deep-level transient spectroscopy (DLTS) (Wen et al., 2018). First-principles calculations by Huang et al., and Liu et al., also suggested that Sb_2Se_3 has large concentrations of multiple defects, especially antisite defects, e.g. Sb_{Se} , Se_{Sb} and 2Se_{Sb} , that are located deep in the band gap (Huang et al., 2019; Liu et al., 2017). So far, there are only few admittance studies in the literature exploring deep defects in Sb_2Se_3 devices. Chen et al., used temperature-dependent admittance spectroscopy (TAS) together with temperature-dependent conductivity measurements and found activation energies of 96 meV and 111 meV, respectively (Chen et al., 2017a). These defect energy levels were ascribed to a Se_{Sb} antisite defect. Hu et al., has reported activation energies at 352 meV, 495 meV and 526 meV, only ascribing the highest obtained energy to an interface defect (Hu et al., 2019, 2018b). Wang et al., demonstrated two defects with activation energies of 356 meV and 423 meV (Wang et al., 2020). Tang et al., reported two activation energies of 456 meV and 495 meV assigning these to V_{Se} and Sb_{Se} , respectively (Tang et al., 2019). Comparison of these studies shows significant discrepancies between the reported activation energies and the assignments to certain types of defects. Thus, further work is needed to elucidate the defect structure of Sb_2Se_3 .

This study presents a close analysis of grain orientation and defects in Sb_2Se_3 solar cells fabricated by close-spaced sublimation. XRD measurements were combined with advanced pole figure and electron backscatter diffraction measurements to study the grain growth and orientation in the absorber. The role of seed layer on the Sb_2Se_3 film structure and orientation is also discussed. Furthermore, TAS and CV profiling are performed to estimate the carrier density and potential deep defects. Better understanding of the Sb_2Se_3 film growth and defects helps to refine processing steps for tackling the dominant recombination processes, which are vital for improving Sb_2Se_3 device performance.

2. Experimental

2.1. Fabrication of Sb_2Se_3 thin film and solar cell

Soda-lime glass substrates with a 200 nm thick $20 \Omega \text{ sq}^{-1}$ fluorine-doped tin oxide (FTO) were used. TiO_2 films with a thickness of 100 nm were deposited onto FTO by ultrasonic spray pyrolysis at 340°C (Eensalu et al., 2019). A precursor solution was used, where 0.1 M titanium isopropoxide (TTIP) and acetylacetone (1:4 M ratio) were dissolved in ethanol. Next, substrates were vacuum annealed at 120°C and air-annealed at 450°C for 30 min. Sb_2Se_3 absorber films were deposited from a Sb_2Se_3 powder (5 N, Sigma-Aldrich) using close-spaced sublimation (CSS) setup under vacuum level of 10^{-4} Pa. A 60 nm thick Sb_2Se_3 seed layer was first deposited at 300°C . Next, Sb_2Se_3 film with $\sim 1.8 \mu\text{m}$ thickness was deposited at 450°C . Au back contacts with square area of 25 mm^2 were vacuum evaporated through a Mica mask onto Sb_2Se_3 absorber films.

2.2. Sb_2Se_3 thin film characterization

Sb_2Se_3 absorber films were imaged by Zeiss EVO-MA15 scanning electron microscope (SEM) equipped with a Zeiss HR FESEM Ultra 55 system. X-ray diffraction (XRD) patterns were measured using a Rigaku Ultima IV diffractometer with $\text{Cu K}\alpha$ radiation ($\lambda = 1.54 \text{ \AA}$, 40 kV, 40 mA). Texture analysis was performed by PANalytical MRD X-ray diffractometer equipped with Eulerian cradle employing two-axis scans along φ and χ in increments of 5° each. The intensity distribution was recorded along full circles ($\varphi = 0^\circ$ to 360°) and at sample tilts χ ranging between 0° and 85° . Electron backscatter diffraction (EBSD) orientation maps were acquired using a Zeiss UltraPlus scanning electron microscope equipped with an Oxford Instruments Symmetry EBSD detector. The measurements were conducted at a beam energy of 20 keV and a beam current of about 6 nA, by use of the acquisition and evaluation software AZtec.

2.3. Device characterization

J-V curves were measured using an AUTOLAB PGSTAT 30 and an Oriel class A solar simulator 91159A (100 mW cm^{-2} , AM1.5) in ambient air at room temperature. The external quantum efficiency (EQE) spectra were measured using a monochromatized light source (Newport 300 W Xenon lamp, 69911 with a monochromator Newport Cornerstone 260), a Merlin digital lock-in detector and a factory-calibrated Si reference detector. Capacitance-voltage (CV) profiling was performed at room temperature with a HP 4284 LCR meter at frequencies ranging from 0.5 kHz to 20 kHz and 30 mV ac voltage. DC bias was scanned from -0.3 V to 0 V. Temperature dependent admittance measurements were made with a HP 4284 LCR meter in R-X (resistance-reactance) mode at 0 V bias and 30 mV ac voltage. Frequency was varied from 0.1 kHz to 1 MHz. Temperature was varied from 80 K to 320 K.

3. Results and discussion

3.1. Analysis of Sb_2Se_3 grain orientation

The film structure of Sb_2Se_3 films was characterized by scanning electron microscopy (SEM). Under investigation were two structures: (1) Sb_2Se_3 with a seed layer (labelled as ' $\text{Sb}_2\text{Se}_3 + \text{SL}$ '; see Experimental section) between TiO_2 buffer and Sb_2Se_3 absorber and (2) Sb_2Se_3 without seed layer. Cross-sectional SEM images of these two structures are shown in Fig. 1. $\text{Sb}_2\text{Se}_3 + \text{SL}$ film, as shown in Fig. 1b, possesses a more compact structure as compared to the Sb_2Se_3 without seed layer in Fig. 1a. When comparing the two absorber films, it is likely the seed layer laid the groundwork for producing columnar grains and increased compactness.

Improved growth of Sb_2Se_3 has been explained by seed layer creating

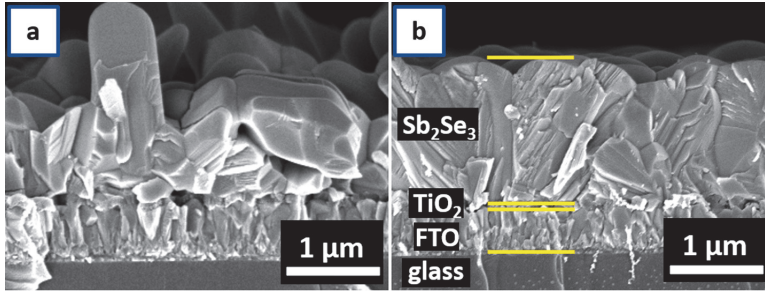


Fig. 1. Cross-sectional SEM image of $\text{Sb}_2\text{Se}_3/\text{TiO}_2/\text{FTO}/\text{glass}$ structures where in (a) Sb_2Se_3 absorber was grown without seed layer and in (b) Sb_2Se_3 absorber was grown onto seed layer.

ribbon-like seeds that start coalescing into columnar grains during the subsequent deposition process (Spalatu et al., 2021). Due to strong re-sublimation at 450 °C CSS processing, only a small number of seeds, from which grains evolve, remain active on the surface. This explains why the seed layer cannot be distinguished from Fig. 1b.

The two structures were then characterized by XRD to determine the crystal structure of Sb_2Se_3 films. As seen from Fig. 2a, Sb_2Se_3 films exhibit crystal structure with orthorhombic $Pbnm$ space group symmetry (JCPDS 15–0861); no secondary crystal phases were detected. To examine variation in crystal orientation, texture coefficient (TC) was calculated from Eq. (1):

$$TC(hkl) = \frac{I(hkl)}{I_0(hkl)} \times \left[\frac{1}{N} \sum_{i=0}^N \frac{I(h_i k_i l_i)}{I_0(h_i k_i l_i)} \right]^{-1} \quad (1)$$

where $I(hkl)$ is the intensity obtained experimentally for a given reflection with hkl indices, $I_0(hkl)$ is the reference intensity for the corresponding reflection acquired from the JCPDS Card No. 15–0861, and N is the number of reflections considered in the calculations (Bérubé and L'Espérance, 1989).

Calculated TC values are presented in Fig. 2b, revealing that both Sb_2Se_3 films with and without seed layer have lower TC values for $(hk0)$ planes than for $(hk1)$ planes. When comparing the two films, it can be noted that the TC values for $(hk0)$ planes are always lower in $\text{Sb}_2\text{Se}_3 + \text{SL}$. Given that the 221 and 231 planes show higher TC values, this could imply more Sb_2Se_3 crystals are orienting along the c -axis direction, which is reportedly beneficial for charge transport (Li et al., 2019c). Noteworthy is also the difference between TC values found for the 002 peak. While $\text{Sb}_2\text{Se}_3 + \text{SL}$ reaches TC of 1.2 for the (002) plane, the corresponding value for Sb_2Se_3 without seed layer stands low at 0.2. Knowing that the 002 peak refers to vertical Sb_2Se_3 crystals, high TC

values shared between the 221, 231, and 002 planes could indicate that the $\text{Sb}_2\text{Se}_3 + \text{SL}$ might grow preferentially along the [001] direction. To further study the grain orientation, advanced texture measurements were subsequently conducted.

Fig. 3 displays pole figures of the Sb_2Se_3 absorbers in 020 and 002 projections measured by XRD. Each pole figure is provided with an intensity scale, where the intensity correlates directly to the multiple of random distribution (MORD). Larger is the multiple of random distribution, stronger is the texture (strong texture translates into preferred orientation) (Abou-Ras et al., 2018). It was noted that Sb_2Se_3 without seed layer showed stronger intensity for the 020 peak, while $\text{Sb}_2\text{Se}_3 + \text{SL}$ recorded significantly stronger intensity for the 002 peak. The MORD of 002 peak at $\chi = 0^\circ$ for Sb_2Se_3 without seed is around 0.5, while it increased by a factor of 5 for the $\text{Sb}_2\text{Se}_3 + \text{SL}$. These results agree well with what was found from the TC analysis. Although pole figures showed a similar trend, the increase of intensity of the 002 plane was not as drastic for it to be considered a strongly preferred orientation. At this point, it is worth noting that pole figures for Sb_2Se_3 grown on TiO_2 have not yet been reported. In a recent study by Pattini et al., pole figures were measured for Sb_2Se_3 films grown onto glass, molybdenum, CdS, FTO and ZnO. Among the substrates, strongest texture along the [001] direction was found for the Sb_2Se_3 grown on FTO, proven by strong pole intensity of the 061 peak (Pattini et al., 2020). Considering that, the present study offers an additional view, by means of pole figures, into the grain orientation of the Sb_2Se_3 absorber deployed in the $\text{TiO}_2/\text{Sb}_2\text{Se}_3$ superstrate configuration.

Texture measurements were also made on individual grains of $\text{Sb}_2\text{Se}_3 + \text{SL}$ film via EBSD. The cross-sectional EBSD map shown in Fig. 4 illustrates that the Sb_2Se_3 layer does not exhibit any preferential growth direction. The average Sb_2Se_3 grain size was found to be around 300–400 nm. This means that not all grains start their growth from the

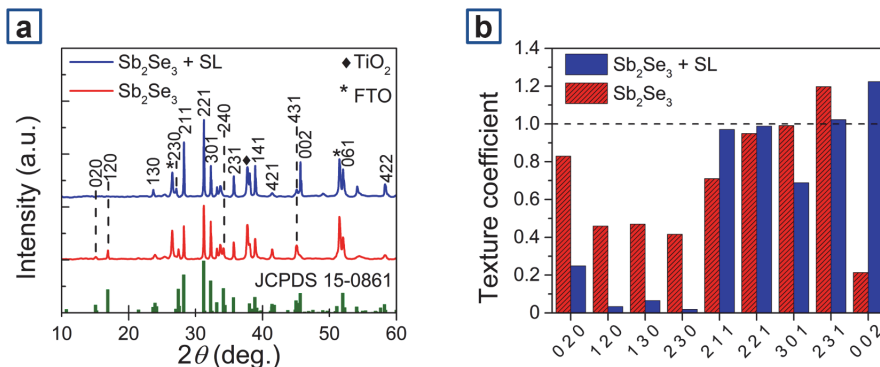


Fig. 2. (a) XRD patterns of $\text{FTO}/\text{TiO}_2/\text{Sb}_2\text{Se}_3$ structures. (b) Texture coefficient values for respective crystal planes in Sb_2Se_3 films.

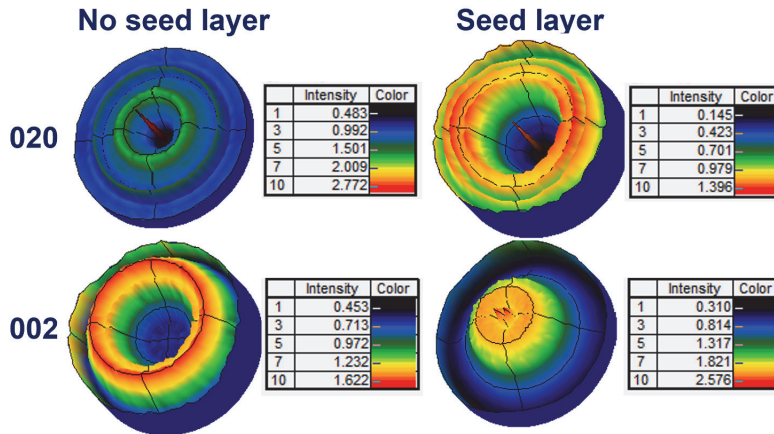


Fig. 3. Pole figures in 020 and 002 projections derived from the XRD measurements of Sb₂Se₃ films grown without and with seed layer onto TiO₂/FTO/glass substrates.

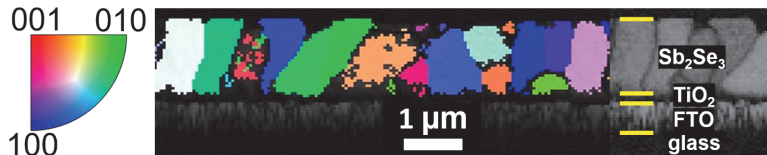


Fig. 4. EBSD map with orientation distribution of the Sb₂Se₃ + SL film (given by false colors, see legend) superimposed on the pattern-quality distribution of the FTO layer. The orientation distribution indicates no pronounced texture of the Sb₂Se₃ + SL layer.

seed layer up to the top and there is still room for improvement. This also relates to achieving favorable grain orientation. Although neither pole figures by XRD nor orientation distribution mapping by EBSD found proof for preferred orientation, clear increase of beneficial 002 peak in Sb₂Se₃ + SL was still detected, which could stem from the increased columnar growth. Hence, it can be argued that further enabling columnar growth would not only increase grain size, but would also enhance texture along the [001] direction. As to the grain orientation, it is now clear the TC analysis is not a trustworthy tool to determine preferred orientation in the orthorhombic Sb₂Se₃. Instead, careful texture analyses are required to draw strong conclusions on the preferred orientation.

3.2. Device performance and characterization

PV parameters of the solar cells employing Sb₂Se₃ + SL and Sb₂Se₃ without seed layer are listed in Table 1. The schematic of two solar cell configurations is presented in Fig. 5a. The dark and illuminated current density-voltage (*J-V*) curves are shown in Fig. 5b. The curves reveal that the Sb₂Se₃ + SL solar cell shows superior performance compared to the device without seed layer. Improved performance is also reflected from the increase in *J*_{SC}, *V*_{OC}, and FF parameters. As has been shown above, the seed layer helped to form columnar compact grains with (hk1) planes, which then seems to correlate with the improvement of PV

Table 1
Photovoltaic parameters of Sb₂Se₃ solar cells, where *V*_{OC} is open circuit voltage, *J*_{SC} is short circuit density, FF is field factor and η is the photoconversion efficiency. * Sb₂Se₃ + SL refers to device employing Sb₂Se₃ on seed layer.

Sample	<i>V</i> _{OC} (V)	<i>J</i> _{SC} (mA cm ⁻²)	FF (%)	η (%)
Sb ₂ Se ₃	0.24 ± 0.1	21.1 ± 0.5	35 ± 3	1.6 ± 0.3
Sb ₂ Se ₃ + SL *	0.35 ± 0.1	24.9 ± 0.4	43 ± 2	3.8 ± 0.1

parameters and device efficiency. In contrast, Sb₂Se₃ without seed layer had dispersed grains with increased presence of (hk0) planes and inferior device performance.

External quantum efficiency (EQE) curves, as shown in Fig. 6a, support the above findings. Throughout the wavelength region from 350 to 1050 nm, Sb₂Se₃ + SL device showed a higher spectral response. This suggests that the columnar microstructure allows more efficient collection of charge carriers, because the density of grain boundaries along the [001] direction is reduced. From the modified EQE plot, the value of the band-gap energy *E*_g was derived for the 3.7%-efficient Sb₂Se₃ device, shown in Fig. 6b. The band-gap of ~1.25 eV complies well with previous reports (Chen et al., 2015; Grossberg et al., 2020; Hobson et al., 2020).

Despite seed layer deployment allowing notable improvement of the PCE, the 3.7% efficiency is still low compared with the best reported TiO₂/Sb₂Se₃ solar cells (Chen et al., 2017b; Hobson et al., 2020). This means there are still several issues that need to be addressed. Low acceptor density and deep defects in the absorber may possibly limit performance (Chen et al., 2017a; Savory and Scanlon, 2019; Wen et al., 2018).

To gain insight into the carrier density and deep defects in the Sb₂Se₃ absorber, TAS measurement and CV profiling were conducted. As none of the Sb₂Se₃ solar cells grown without seed layer exhibited shunt resistances large enough to measure capacitance, *C*, the results below are presented only for the best seed-assisted device. Capacitance was measured using an equivalent circuit model that includes a capacitor, a series resistor *r* and a resistor in parallel. Series resistance *r* was first extracted from the real part of impedance *Z* (*f*, *T*) at high frequencies (Levchenko et al., 2016). This was used in the calculation of capacitance from the real and imaginary part of impedance *Z* (*f*, *T*) signal (Scofield, 1995). The capacitance response entails the response not only from free carriers, but also from bulk and possibly interface defects (Li et al.,

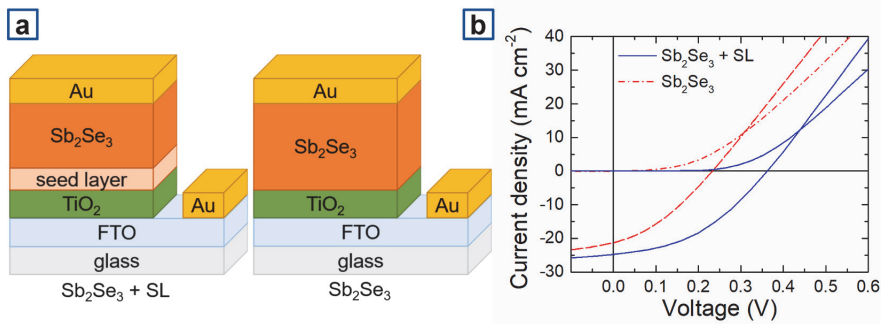


Fig. 5. (a) $\text{Sb}_2\text{Se}_3 + \text{SL}$ and Sb_2Se_3 device configurations and (b) current density–voltage (J–V) curves of the two respective devices.

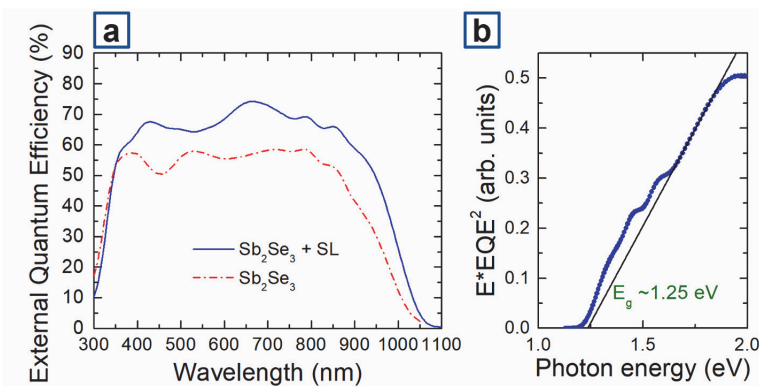


Fig. 6. (a) EQE curves of Sb_2Se_3 solar cells and (b) Band-gap energy of $\text{Sb}_2\text{Se}_3 + \text{SL}$ derived from the modified EQE plot in the long wavelength region.

2019c). Fig. 7a presents the C - f curves measured in the temperature range from 80 K to 320 K. The derivatives of the capacitance curves were then taken to determine the relaxation frequencies ω_0 , found from the maxima of the $-\omega dC(\omega)/d\omega$ plots, as shown in Fig. 7b. An Arrhenius plot of ω_0 frequencies allows to determine activation energy E_A and thermal emission prefactor ξ_0 of a defect state by using Eq. (2) (Walter et al., 1996):

$$\omega_0 = 2\pi f_0 = 2\xi_0 T^2 \exp(-E_A/kT) \quad (2)$$

where ξ_0 is the thermal emission prefactor, k is Boltzmann constant, T is temperature and E_A is activation energy. The Arrhenius plot in Fig. 8 gives a single activation energy of $E_A = 0.39$ eV with thermal emission

prefactor ξ_0 of $3 \times 10^6 \text{ s}^{-1} \text{ K}^{-2}$. Hu et al., has found activation energies at 0.3–0.4 eV and 0.2–0.6, assigning these to bulk defects (Hu et al., 2019, 2018a, 2018b). Activation energies of 0.39–0.40 eV were also found in both $\text{CdS}/\text{Sb}_2\text{Se}_3$ and $\text{TiO}_2/\text{Sb}_2\text{Se}_3$ solar cells (Spalatu et al., 2021). A defect level at 0.48 ± 0.07 eV has been reported in DLTS study, and attributed to a deep acceptor V_{Sb} (Wen et al., 2018). From first-principles calculations, transition energy levels were found for V_{Sb1} and V_{Sb2} acceptor defects, which lay close to 0.39 eV (Huang et al., 2019). DFT study calculated transition energy levels of 0.33 eV and 0.40 eV for Sb_{Se1} and Sb_{Se2} antisite defects, which are deep acceptor defects (Stoliaroff et al., 2020). Also, hybrid DFT study located Sb_{Se1} , Sb_{Se2} and Sb_{Se3} antisite defects close to the 0.39 eV energy (Savory and Scanlon,

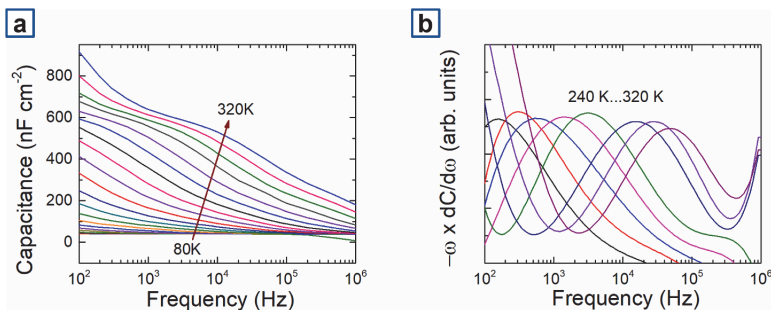


Fig. 7. (a) C - f - T curves measured from 80 K to 320 K and (b) $-\omega dC(\omega)/d\omega$ vs f curves of $\text{TiO}_2/\text{Sb}_2\text{Se}_3$ solar cell.

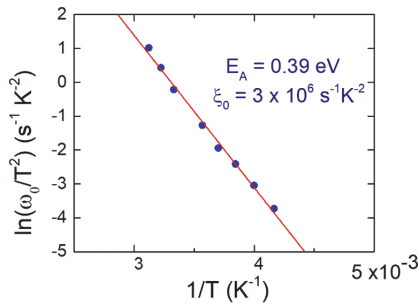


Fig. 8. Arrhenius plot of the inflection frequencies of TiO₂/Sb₂Se₃ device, from which activation energy and thermal emission prefactor were deduced.

2019). Given that the activation energies of 0.39–0.40 have been found in multiple devices, and the theoretical calculations predicted deep acceptor energy levels close to 0.39 eV, the activation energy obtained in the present study can be assigned to a deep acceptor defect.

To estimate the density of this defect, CV profiles were measured at room temperature. Since the defect band is centered at 10 kHz at room temperature, CV profiles were taken at similar modulation frequencies. Fig. 9 reveals the CV profiles take U-shaped curves, something that is commonly seen in polycrystalline thin film PV devices, and which could be indicative of either deep defect states, back contact barriers or full depletion of the absorber layer caused by large reverse bias (Cabas-Vidani et al., 2018; Eisenbarth et al., 2010; Hadke et al., 2019; Teymur et al., 2021). While the minima of the CV profiles are used to estimate the carrier density, the decrease in the minima values from 4.8×10^{17} to $2.0 \times 10^{17} \text{ cm}^{-3}$ also gives a rough estimate over the defect density that could be in the order of 10^{17} cm^{-3} . The free carrier density is estimated to be lower due to the lower values at higher frequencies, but cannot be reliably estimated from this experiment. High resistivities of Sb₂Se₃ absorber films that were determined to lie in the 10^5 – $10^6 \Omega \cdot \text{cm}$ range (Spalatu et al., 2021) indicate that the free carrier density might be substantially lower than the charge densities obtained from CV profiling, which also includes contributions from the deep defects.

From the fact that the admittance spectroscopy results are consistent with the results from CV profiling and that the hot-probe analysis has demonstrated poor, yet clear p-type conductivity for the Sb₂Se₃ absorber films on glass, it can be assumed that the free carrier density stems from this deep acceptor defect. Considering this, the free carrier density can be calculated by using Eq. (3) (Sze and Ng, 2006; Teymur et al., 2021):

$$p = 1/\sqrt{2} \times (N_V N_A)^{1/2} \exp(-E_A/2kT) \quad (3)$$

where N_V is the effective density of states of valence band, taken to be $1 \times 10^{19} \text{ cm}^{-3}$, N_A is $2.0 \times 10^{17} \text{ cm}^{-3}$, which is the carrier density taken from CV analysis and E_A is 0.39 eV, that was found in TAS analysis.

The free carrier density calculated at room temperature gives $\sim 5 \times 10^{14} \text{ cm}^{-3}$, which is significantly lower than the total charge densities estimated from the CV profiles. This is higher than the free carrier density of $1.8 \times 10^{13} \text{ cm}^{-3}$ reported for the intrinsic Sb₂Se₃ films (Chen et al., 2017a). Nevertheless, the carrier density below 10^{15} explains the large Sb₂Se₃ resistivity (Spalatu et al., 2021) and the fact Sb₂Se₃ cannot be measured with Hall measurement technique (Chen et al., 2017a; Hobson et al., 2020). Overall, this finding illustrates that in addition to further optimization of the Sb₂Se₃ microstructure, extrinsic doping steps, such as with copper, tin or halogenides, must be introduced to address low free carrier density and high density of defects.

4. Conclusion

In the present study, we performed careful analysis on the grain

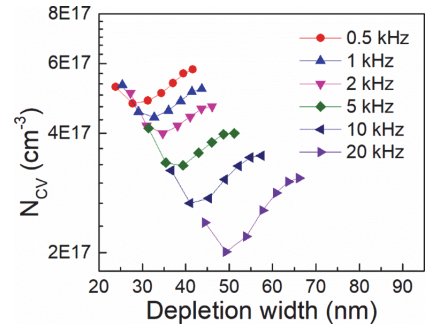


Fig. 9. CV profiles for TiO₂/Sb₂Se₃ solar cell showing carrier density decrease with increasing frequency.

orientation and deep defects in Sb₂Se₃ solar cells fabricated by close-spaced sublimation. Through the combination of pole figures measured by XRD and orientation distribution maps performed by EBSD, we refined the understanding of grain orientation in the emerging Sb₂Se₃ thin film solar cell absorber. The microstructures of two thin films were compared, i.e. Sb₂Se₃ grown on a TiO₂ seed layer and plain Sb₂Se₃ without any seed layer. The seed-assisted Sb₂Se₃ film exhibited more compact, columnar grains and significantly stronger texture along the [001] direction, as compared with the plain Sb₂Se₃, which had dispersed grain structure and a measurable texture along the [010] direction. The seed-assisted Sb₂Se₃ devices performed clearly better, which was attributed to the improved absorber microstructure, enhancing charge transport across the absorber layer. Our results indicate that the seed layer deployment serves as one of the processing routes for attaining preferential Sb₂Se₃ growth along the [001] direction. The present study also investigated the free carrier density and deep defects in the absorber by performing CV and TAS measurements on the seed-assisted Sb₂Se₃ device. TAS analysis revealed an activation energy of 0.39 eV that was assigned to a deep acceptor defect. From CV profiles, the sum of defect and the free carrier density were estimated to be at $\sim 10^{17} \text{ cm}^{-3}$. Free carrier density that was calculated from the deep defect band revealed a significantly lower value of $\sim 5 \times 10^{14} \text{ cm}^{-3}$. This value is consistent with large resistivities shown by intrinsic Sb₂Se₃ films. This in turn shows the defect density in the Sb₂Se₃ device could be in the order of 10^{17} cm^{-3} . Overall, the present study demonstrated that both, structural and optoelectronic properties, require additional processing routes, such as post deposition treatments and doping, to substantially boost the Sb₂Se₃ solar cell efficiency.

Declaration of Competing Interest

The authors declare that they have no known competing financial interests or personal relationships that could have appeared to influence the work reported in this paper.

Acknowledgements

This study was funded by the Estonian Research Council project PRG627 “Antimony chalcogenide thin films for next-generation semi-transparent solar cells applicable in electricity producing windows”, the Estonian Research Council project PSG689 “Bismuth Chalcogenide Thin-Film Disruptive Green Solar Technology for Next Generation Photovoltaics”, the Estonian Centre of Excellence project TK141 (TAR16016EK) “Advanced materials and high-technology devices for energy recuperation system”, and the EU H2020 program under the ERA Chair project 5GSOLAR grant agreement No 952509. R. Krautmann acknowledges Archimedes Foundation for financing the PhD student mobility through the Dora Plus program.

References

- Abou-Ras, D., Bär, M., Caballero, R., Gunder, R., Hages, C., Heinemann, M.D., Kaufmann, C.A., Krause, M., Levenco, S., Mainz, R., Márquez, J., Nikolaeva, A., Redinger, A., Schäfer, N., Schorr, S., Stange, H., Unold, T., Wilks, R.G., 2018. Advanced characterization and in-situ growth monitoring of Cu(In, Ga)Se₂ thin films and solar cells. *Sol. Energy* 170, 102–112. <https://doi.org/10.1016/j.solener.2018.04.032>.
- Ariosa, D., Elhordoy, F., Dalchiele, E.A., Marotti, R.E., Stari, C., 2011. Texture vs morphology in ZnO nano-rods: On the x-ray diffraction characterization of electrochemically grown samples. *J. Appl. Phys.* 110 (12), 124901. <https://doi.org/10.1063/1.3669026>.
- Bérubé, L.P., L'Espérance, G., 1989. A Quantitative Method of Determining the Degree of Texture of Zinc Electrodeposits. *J. Electrochem. Soc.* 136 (8), 2314–2315. <https://doi.org/10.1149/1.12097318>.
- Cabas-Vidani, A., Haass, S.G., Andres, C., Caballero, R., Figi, R., Schreiner, C., Márquez, J.A., Hages, C., Unold, T., Bleiner, D., Tiwari, A.N., Romanyuk, Y.E., 2018. High-Efficiency (χ_2 Cu_{1-x})₂ ZnSn(S, Se) 4 Kesterite Solar Cells with Lithium Alloying. *Adv. Energy Mater.* 8 (34), 1801191. <https://doi.org/10.1002/aenm.201801191>.
- Chen, C., Bobela, D.C., Yang, Y.e., Lu, S., Zeng, K., Ge, C., Yang, B.o., Gao, L., Zhao, Y., Beard, M.C., Tang, J., 2017a. Characterization of basic physical properties of Sb₂Se₃ and its relevance for photovoltaics. *Front. Optoelectron.* 10 (1), 18–30. <https://doi.org/10.1007/s12200-017-0702-z>.
- Chen, C., Zhao, Y., Lu, S., Li, K., Li, Y., Yang, B.o., Chen, W., Wang, L., Li, D., Deng, H., Yi, F., Tang, J., 2017b. Accelerated Optimization of TiO₂/Sb₂Se₃ Thin Film Solar Cells by High-Throughput Combinatorial Approach. *Adv. Energy Mater.* 7 (20), 1700866. <https://doi.org/10.1002/aenm.201700866>.
- Chen, C., Li, W., Zhou, Y., Chen, C., Luo, M., Liu, X., Zeng, K., Yang, B.o., Zhang, C., Han, J., Tang, J., 2015. Optical properties of amorphous and polycrystalline Sb₂Se₃ thin films prepared by thermal evaporation. *Appl. Phys. Lett.* 107 (4), 043905. <https://doi.org/10.1063/1.4927741>.
- Eensalu, J.S., Katerski, A., Kärber, E., Weinhardt, L., Blum, M., Heske, C., Yang, W., Oja Acik, I., Krunk, M., 2019. Semitransparent Sb₂S₃ thin film solar cells by ultrasonic spray pyrolysis for use in solar windows. *Beilstein J. Nanotechnol.* 10, 2396–2409. <https://doi.org/10.3762/bjnano.10.230>.
- Eisenbarth, T., Unold, T., Caballero, R., Kaufmann, C.A., Schock, H.-W., 2010. Interpretation of admittance, capacitance-voltage, and current-voltage signatures in Cu(In, Ga)Se₂ thin film solar cells. *J. Appl. Phys.* 107 (3), 034509. <https://doi.org/10.1063/1.3277043>.
- Ghosh, G., 1993. The sb-se (antimony-selenium) system. *J. Phase Equilibria* 14 (6), 753–763. <https://doi.org/10.1007/BF02667889>.
- Grossberg, M., Volobujeva, O., Penezko, A., Kaupmees, R., Raadik, T., Krustok, J., 2020. Origin of photoluminescence from antimony selenide. *J. Alloys Compd.* 817, 152716. <https://doi.org/10.1016/j.jallcom.2019.152716>.
- Hadke, S., Levenco, S., Sai Gautam, G., Hages, C.J., Márquez, J.A., Izquierdo-Roca, V., Carter, E.A., Unold, T., Wong, L.H., 2019. Suppressed Deep Traps and Bandgap Fluctuations in Cu₂CdSnS₄ Solar Cells with ≈8% Efficiency. *Adv. Energy Mater.* 9 (45), 1902509. <https://doi.org/10.1002/aenm.v9.4510.1002/aenm.201902509>.
- Hobson, T.D.C., Phillips, L.J., Hutter, O.S., Shiel, H., Swallow, J.E.N., Savory, C.N., Nayak, P.K., Mariotti, S., Das, B., Bowen, L., Jones, L.A.H., Featherstone, T.J., Smiles, M.J., Farnworth, M.A., Zoppi, K., Thakur, P.K., Lee, T.-L., Snaith, H.J., Leighton, C., Scanlon, D.O., Dhanak, V.R., Durose, K., Veal, T.D., Major, J.D., 2020. Isotope Heterojunction Solar Cells Using n-Type Sb₂Se₃ Thin Films. *Chem. Mater.* <https://doi.org/10.1021/acs.chemmater.0c00223>.
- Hu, X., Tao, J., Chen, S., Xue, J., Weng, G., Kaijiang, Hu, Z., Jiang, J., Chen, S., Zhu, Z., Chu, J., 2018a. Improving the efficiency of Sb₂Se₃ thin-film solar cells by post annealing treatment in vacuum condition. *Sol. Energy Mater. Sol. Cells* 187, 170–175. <https://doi.org/10.1016/j.solmat.2018.08.006>.
- Hu, X., Tao, J., Wang, Y., Xue, J., Weng, G., Zhang, C., Chen, S., Zhu, Z., Chu, J., 2019. 5.91%-efficient Sb₂Se₃ solar cells with a radio-frequency magnetron-sputtered CdS buffer layer. *Appl. Mater. Today* 16, 367–374. <https://doi.org/10.1016/j.apmt.2019.06.001>.
- Hu, X., Tao, J., Weng, G., Jiang, J., Chen, S., Zhu, Z., Chu, J., 2018b. Investigation of electrically-active defects in Sb₂Se₃ thin-film solar cells with up to 5.91% efficiency via admittance spectroscopy. *Sol. Energy Mater. Sol. Cells* 186, 324–329. <https://doi.org/10.1016/j.solmat.2018.07.004>.
- Huang, M., Xu, P., Han, D., Tang, J., Chen, S., 2019. Complicated and Unconventional Defect Properties of the Quasi-One-Dimensional Photovoltaic Semiconductor Sb₂Se₃. *ACS Appl. Mater. Interfaces* 11 (17), 15564–15572. <https://doi.org/10.1021/acsami.9b01220.1021/acsami.9b01220.s001>.
- Levenco, S., Just, J., Redinger, A., Larramona, G., Bourdais, S., Denner, G., Jacob, A., Unold, T., 2016. Deep Defects in Cu₂ZnSn(S, Se)₄ Solar Cells with Varying Se Content. *Phys. Rev. Appl.* 5, 024004. <https://doi.org/10.1103/PhysRevApplied.5.024004>.
- Li, G., Li, Z., Liang, X., Guo, C., Shen, K., Mai, Y., 2019a. Improvement in Sb₂Se₃ Solar Cell Efficiency through Band Alignment Engineering at the Buffer/Absorber Interface. *ACS Appl. Mater. Interfaces* 11 (1), 828–834. <https://doi.org/10.1021/acsami.8b17611.1021/acsami.8b17611.s001>.
- Li, K., Chen, C., Lu, S., Wang, C., Wang, S., Lu, Y., Tang, J., 2019b. Orientation Engineering in Low-Dimensional Crystal-Structural Materials via Seed Screening. *Adv. Mater.* 31 (44), 1903914. <https://doi.org/10.1002/adma.v31.4410.1002/adma.201903914>.
- Li, Z., Chen, X., Zhu, H., Chen, J., Guo, Y., Zhang, C., Zhang, W., Niu, X., Mai, Y., 2017. Sb₂Se₃ thin film solar cells in substrate configuration and the back contact selenization. *Sol. Energy Mater. Sol. Cells* 161, 190–196. <https://doi.org/10.1016/j.solmat.2016.11.033>.
- Li, Z., Liang, X., Li, G., Liu, H., Zhang, H., Guo, J., Chen, J., Shen, K., San, X., Yu, W., Schropp, R.E.I., Mai, Y., 2019c. 9.2%-efficient core-shell structured antimony selenide nanorod array solar cells. *Nat. Commun.* 10, 1–9. <https://doi.org/10.1038/s41467-018-07903-6>.
- Liang, X., Guo, C., Liu, T., Liu, Y., Yang, L., Song, D., Shen, K., Schropp, R.E.I., Li, Z., Mai, Y., 2020. Crystallographic Orientation Control of 1D Sb₂Se₃ Nanorod Arrays for Photovoltaic Application by In Situ Back-Contact Engineering. *Sol. RRL* 4 (10), 2000294. <https://doi.org/10.1002/solr.v4.1010.1002/solr.202000294>.
- Liu, X., Chen, J., Luo, M., Leng, M., Xia, Z., Zhou, Y., Qin, S., Xue, D.-J., Lv, L.u., Huang, H., Niu, D., Tang, J., 2014. Thermal evaporation and characterization of Sb₂Se₃ thin film for substrate Sb₂Se₃/CdS solar cells. *ACS Appl. Mater. Interfaces* 6 (13), 10687–10695. <https://doi.org/10.1021/am502427s>.
- Liu, X., Xiao, X., Yang, Y.e., Xue, D.-J., Li, D.-B., Chen, C., Lu, S., Gao, L., He, Y., Beard, M.C., Wang, G., Chen, S., Tang, J., 2017. Enhanced Sb₂Se₃ solar cell performance through theory-guided defect control. *Prog. Photovolt. Res. Appl.* 25 (10), 861–870. <https://doi.org/10.1002/pip.v25.1010.1002/pip.2900>.
- Pattini, F., Rampino, S., Mezzadri, F., Calestani, D., Spaggiari, G., Sidoli, M., Delmonte, D., Sala, A., Gilioli, E., Mazzer, M., 2020. Role of the substrates in the ribbon orientation of Sb₂Se₃ films grown by Low-Temperature Pulsed Electron Deposition. *Sol. Energy Mater. Sol. Cells* 218, 110724. <https://doi.org/10.1016/j.solmat.2020.110724>.
- Savory, C.N., Scanlon, D.O., 2019. The complex defect chemistry of antimony selenide. <https://doi.org/10.1039/c9ta02022e>.
- Scofield, J.H., 1995. Effects of series resistance and inductance on solar cell admittance measurements. *Sol. Energy Mater. Sol. Cells* 37 (2), 217–233. [https://doi.org/10.1016/0927-0248\(95\)0016-X](https://doi.org/10.1016/0927-0248(95)0016-X).
- Spalatu, N., Krautmann, R., Katerski, A., Karber, E., Josepov, R., Hiie, J., Acik, I.O., Krunk, M., 2021. Screening and optimization of processing temperature for Sb₂Se₃ thin film growth protocol: Interrelation between grain structure, interface intermixing and solar cell performance. *Sol. Energy Mater. Sol. Cells* 225, 111045. <https://doi.org/10.1016/j.solmat.2021.111045>.
- Spalatu, N., Krunk, M., Hiie, J., 2017. Structural and optoelectronic properties of CdCl₂ activated CdTe thin films modified by multiple thermal annealing. *Thin Solid Films* 633, 106–111. <https://doi.org/10.1016/j.tsf.2016.09.042>.
- Stoliaroff, A., Lecomte, A., Rubel, O., Jobic, S., Zhang, XiangHua, Latouche, C., Rocquefelte, X., 2020. Deciphering the Role of Key Defects in Sb₂Se₃: A Promising Candidate for Chalcogenide-Based Solar Cells. *ACS Appl. Energy Mater.* 3 (3), 2496–2509. <https://doi.org/10.1021/acsaem.9b02192.1021/acsaem.9b02192.s001>.
- Sze, S.M., Ng, K.K., 2006. *Physics of Semiconductor Devices*. John Wiley & Sons, Inc., Hoboken, NJ, USA.
- Zhang, R., Zheng, Z.-H., Su, Z.-H., Li, X.-J., Wei, Y.-D., Zhang, X.-H., Fu, Y.-Q., Luo, J.-T., Fan, P., Liang, G.-X., 2019. Highly efficient and stable planar heterojunction solar cell based on sputtered and post-selenized Sb₂Se₃ thin film. *Nano Energy* 64, 103929. <https://doi.org/10.1016/j.nanoen.2019.103929>.
- Teymur, B., Levenco, S., Hempel, H., Bergmann, E., Márquez, J.A., Choubrac, L., Hill, I. G., Unold, T., Mitzi, D.B., 2021. Optoelectronic and material properties of solution-processed Earth-abundant Cu₂BaSn(S, Se)₄ films for solar cell applications. *Nano Energy* 80, 105556. <https://doi.org/10.1016/j.nanoen.2020.105556>.
- Walter, T., Herberholz, R., Müller, C., Schock, H.W., 1996. Determination of defect distributions from admittance measurements and application to Cu(In,Ga)Se₂ based heterojunctions Determination of defect distributions from admittance measurements and application to Cu(In,Ga)Se₂ based heterojunctions. *J. Appl. Phys.* 80, 4411–4420. <https://doi.org/10.1063/1.363401>.
- Wang, L., Li, D.B., Li, K., Chen, C., Deng, H.X., Gao, L., Zhao, Y., Jiang, F., Li, L., Huang, F., He, Y., Song, H., Niu, G., Tang, J., 2017. Stable 6%-efficient Sb₂Se₃ solar cells with a ZnO buffer layer. *Nat. Energy* 2, 17046. <https://doi.org/10.1038/energy.2017.46>.
- Wang, Y., Li, J., Chen, Y., Zhou, J., Zhang, J., Mao, W., Zheng, S., Pan, Y., Liu, Y., Dai, K., Hu, X., Tao, J., Weng, G., Jiang, J., Chen, S., Chu, J., 2020. Effects of working pressure and power on photovoltaic and defect properties of magnetron sputtered Sb₂Se₃ thin-film solar cells. *Appl. Opt.* 59 (4), 948. <https://doi.org/10.1364/AO.382805>.
- Wen, X., Chen, C., Lu, S., Li, K., Kondrotas, R., Zhao, Y., Chen, W., Gao, L., Wang, C., Zhang, J., Niu, G., Tang, J., 2018. Vapor transport deposition of antimony selenide thin film solar cells with 7.6% efficiency. *Nat. Commun.* 9, 1–10. <https://doi.org/10.1038/s41467-018-04634-6>.
- Zhang, H., Yuan, S., Deng, H., Ishaq, M., Yang, X., Hou, T., Shah, U.A., Song, H., Tang, J., 2020. Controllable orientations for Sb₂Se₃ solar cells by vertical VTD method. *Prog. Photovolt. Res. Appl.* 28 (8), 823–832. <https://doi.org/10.1002/pip.v28.810.1002/pip.3278>.
- Zhou, H., Feng, M., Li, P., Gong, X., Zhang, D., Chen, S., 2020. Fabrication of a preferentially [001]-oriented Sb₂Se₃ thin film on diverse substrates and its application in photoelectrochemical water reduction. *Sustain. Energy Fuels* 4 (8), 3943–3950. <https://doi.org/10.1039/D0SE00646G>.
- Zhou, Y., Leng, M., Xia, Z., Zhong, J., Song, H., Liu, X., Yang, B.o., Zhang, J., Chen, J., Zhou, K., Han, J., Cheng, Y., Tang, J., 2014. Solution-processed antimony selenide heterojunction solar cells. *Adv. Energy Mater.* 4 (8), 1301846. <https://doi.org/10.1002/aenm.201301846>.

Appendix 3

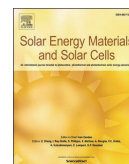
PUBLICATION III

R. Krautmann, N. Spalatu, R. Josepson, R. Nedzinskas, R. Kondrotas, R. Gržibovskis, A. Vembris, M. Krunks, I. Oja Acik, “Low processing temperatures explored in Sb_2S_3 solar cells by close-spaced sublimation and analysis of bulk and interface related defects”, *Solar Energy Materials and Solar Cells*, vol. 251, 2023, DOI: 10.1016/j.solmat.2022.112139.



Contents lists available at ScienceDirect

Solar Energy Materials and Solar Cells

journal homepage: www.elsevier.com/locate/solmat

Low processing temperatures explored in Sb₂S₃ solar cells by close-spaced sublimation and analysis of bulk and interface related defects

R. Krautmann^{a,**}, N. Spalatu^{a,*}, R. Josepson^b, R. Nedzinskas^c, R. Kondrotas^c, R. Gržibovskis^d, A. Vembris^d, M. Krunka^a, I. Oja Acik^a

^a Department of Materials and Environmental Technology, Tallinn University of Technology, Ehitajate tee 5, 19086, Tallinn, Estonia

^b Division of Physics, Tallinn University of Technology, Ehitajate tee 5, 19086, Tallinn, Estonia

^c State Research Institute Center for Physical Sciences and Technology, Saulėtekio Avenue 3, 10257, Vilnius, Lithuania

^d Institute of Solid State Physics, University of Latvia, Kengaraga iela 8, 1063, Riga, Latvia

ARTICLE INFO

Keywords:

Antimony sulfide
Close-spaced sublimation
Deep defects
Admittance spectroscopy
Photoluminescence

ABSTRACT

Antimony trisulfide (Sb₂S₃) is a promising photovoltaic absorber, which has so far been fabricated mainly by chemical deposition methods. Despite its aptness for congruent sublimation, less research efforts have been made on low-temperature Sb₂S₃ processing by physical methods. In this regard, recent studies show large variation in the processing temperature of Sb₂S₃ films, which overall brings into question the need for higher substrate temperatures (>350 °C). Furthermore, in-depth analysis of defect structure of Sb₂S₃ employing temperature-dependent admittance spectroscopy (TAS) and photoluminescence (PL) remains largely unexplored. In this work, we systematically study the effect of close-spaced sublimation (CSS) substrate temperature on Sb₂S₃ absorber growth, employing a wide temperature range of 240–400 °C. Temperatures above 320 °C caused cracking phenomena in the Sb₂S₃ absorber film, proving the unviability of higher processing temperatures. CSS processing temperature of 300 °C was found optimal, producing crack-free Sb₂S₃ films with increased presence of (hk1) planes, and achieving the best CdS/Sb₂S₃ device with photoconversion efficiency of 3.8%. TAS study revealed two deep defects with activation energies of 0.32 eV and 0.37 eV. Low-temperature PL measurement revealed a band-to-band emission at 1.72 eV and a broad band peaked at 1.40 eV, which was assigned to a donor-acceptor pair recombination. Temperature-dependent I-V analysis showed that recombination at CdS–Sb₂S₃ interface remains a large limitation for the device efficiency.

1. Introduction

Antimony trisulfide (Sb₂S₃) is a non-toxic and earth-abundant semiconductor material, which holds huge promise as a photovoltaic (PV) absorber for future thin film solar cell technologies. Sb₂S₃ has a suitable bandgap energy of 1.7–1.8 eV [1] and shows strong light absorption ($\alpha > 10^4 \text{ cm}^{-1}$) [2]. These impressive optoelectronic properties make Sb₂S₃ feasible for applications, such as tandem solar cells [3], solar windows [4], IoT sensors [5] and water splitting devices [6,7]. Sb₂S₃ also has an orthorhombic crystal structure, with crystals growing in quasi-one-dimensional (Q1D) ribbons [2]. While ribbons are formed from Sb-S covalent bonds, ribbons only have weak van der Waals' forces between them. This has been found to have drastic effect on the charge transport across the absorber layer, with quasi-vertical, (hk1)-oriented

ribbons having been deemed optimal [8,9]. Moreover, it has led to intensive research efforts to optimize Sb₂S₃ crystal growth toward the normal of the substrate (along the [001] crystal direction, or the c-axis) [10–13].

Although Sb₂S₃ is a single-phase binary compound with a relatively low melting point (550 °C) and high vapor pressure [14], chemical methods have been preferred for the synthesis of Sb₂S₃ absorber films [4,15,16], also leading to the current state-of-the-art device efficiency of 7.5% [17]. Despite this achievement, devices employing physically evaporated Sb₂S₃ absorbers have been recently gaining ground. Several recent studies have successfully deposited Sb₂S₃ by thermal evaporation (TE) [18,19], rapid thermal evaporation (RTE) [12,20], close-spaced sublimation (CSS) [21–23] and vapor transport deposition (VTD) [13, 24]. In these studies, a superstrate configuration was employed, with the

* Corresponding author.

** Corresponding author.

E-mail addresses: robert.krautmann@taltech.ee (R. Krautmann), nicolae.spalatu@taltech.ee (N. Spalatu).

<https://doi.org/10.1016/j.solmat.2022.112139>

Received 1 October 2022; Received in revised form 17 November 2022; Accepted 25 November 2022

Available online 10 December 2022

0927-0248/© 2022 The Authors. Published by Elsevier B.V. This is an open access article under the CC BY license (<http://creativecommons.org/licenses/by/4.0/>).

Sb₂S₃ absorber deposited onto a cadmium sulfide (CdS) buffer layer. CdS is an n-type semiconductor material that has been widely used as a heterojunction partner layer for p-type absorbers, such as CdTe, CZTS, Sb₂S₃, Sb₂Se₃ [25–28]. For instance, Lian et al. deposited Sb₂S₃ solar cells by TE and achieved photoconversion efficiency (PCE) of 6.2% [19]. Zeng et al. produced a 4.7%-efficient PV device with Sb₂S₃ absorber fabricated by VTD [24]. Xie et al. obtained PCE of 4.5% for a PV device employing a CSS-deposited Sb₂S₃ absorber [22]. A certain aspect in these studies is that rather high substrate temperatures from 350 °C to 500 °C have been used [13,22,24]. On one hand, this complies with growth conditions honed for Sb₂Se₃ solar cells, for which high processing temperatures between 450 °C and 500 °C for optimal grain growth have been reported [9,28–31]. On the other hand, lower melting point of Sb₂S₃ and higher partial pressure of sulfur (compared with selenium) indicate that high-quality material can be processed at significantly lower temperatures compared to Sb₂Se₃. Like with Sb₂Se₃, optimization of growth conditions is attributed to improved grain orientation along [001] crystal direction and increased compactness of adjacent Sb₂S₃ grains [21]. In that regard, a natural question arises whether higher processing temperatures (>350 °C) are necessary for obtaining high-quality Sb₂S₃ thin films by CSS and VTD deposition methods.

Aside from the optimization of growth conditions, another important aspect concerns the understanding of defect structure in Sb₂S₃ and recombination mechanisms at the CdS–Sb₂S₃ interface. Thus far, knowledge about the defect profile of Sb₂S₃ is often translated from works on Sb₂Se₃ devices, for which numerous deep-level transient spectroscopy (DLTS) and temperature-dependent admittance spectroscopy (TAS) studies have already been conducted [28,32,33]. However, only few studies related to deep defect analysis of Sb₂S₃ are currently available [34–36]. Moreover, low-temperature photoluminescence (PL) studies for getting a deeper insight into bulk defects in Sb₂S₃ absorber have not been successfully performed. Considering aforementioned aspects, the focus of present study is to identify suitable growth conditions for the Sb₂S₃ absorber as well as provide new insight into defects employing low-temperature PL on the Sb₂S₃ absorber and TAS on the Sb₂S₃ device.

2. Experimental

2.1. Sb₂S₃ thin-film and device fabrication

Sb₂S₃ thin film solar cells were fabricated in a superstrate configuration onto soda-lime glass substrates coated with CdS and fluorine-doped tin oxide (FTO) (20 Ω sq⁻¹) (glass/FTO/CdS/Sb₂S₃/Au). A custom-made close-spaced sublimation reactor was used to deposit CdS buffer and Sb₂S₃ absorber layers under vacuum of 10⁻⁴ Pa. CdS buffer layers were deposited from CdS powder (Sigma-Aldrich, 5 N) at substrate temperature of 350 °C and source temperature of 650 °C. Sb₂S₃ absorber layers were deposited from a Sb₂S₃ powder (Sigma-Aldrich, 5 N) at constant source temperature of 450 °C, while the substrate temperature was varied between 260 and 400 °C. Gold back contacts (with area of 0.25 cm²) were evaporated on top of Sb₂S₃ absorber layers by vacuum evaporation.

2.2. Material and device characterization

X-ray diffraction (XRD) patterns were recorded using a Rigaku Ultima IV diffractometer with Cu Kα radiation (λ = 1.54 Å, 40 kV, 40 mA). Morphology and cross-sections of Sb₂S₃ films were analyzed by a Zeiss HR FESEM Ultra 55 scanning electron microscope (SEM). Raman measurements were performed with a Horiba Jobin Yvon Labram HR 800 spectrometer (λ = 532 nm). J-V curves were measured for Sb₂S₃ devices with a Wavelabs LS-2 LED solar simulator (100 mW cm⁻², AM1.5) in ambient air at room temperature. Temperature-dependent J-V curves were measured for the Sb₂S₃ device with a KEITHLEY 2400 SourceMeter

at temperatures 20 K–320 K with a temperature step of ΔT = 10 K. External quantum efficiency (EQE) spectra were measured with a monochromatized light source (Newport 300 W Xenon lamp, Newport Cornerstone 260 monochromator), a Merlin digital lock-in detector and a factory-calibrated Si reference detector. The ionization potential values of CdS and Sb₂S₃ layers were determined with photoelectron emission spectroscopy (PES), by using an ENERGETIQ Laser Driven Light Source (LDLS EQ-99) white light source, a Spectral Products DK240 1/4 m monochromator and a Keithley 617 electrometer. These values were later used to derive the band diagram for the whole device. For temperature-dependent admittance spectroscopy (TAS), Sb₂S₃ device was mounted on a cold finger in a closed cycle Janis helium cryostat. C-f-T curves were obtained using a Wayne Kerr 6500B impedance meter, where impedance, Z, and phase angle, θ, were measured at 0 V bias and 30 mV ac voltage [37]. Frequency was varied from 10 Hz to 10 MHz; temperature ranged from 20 K to 320 K. Low-temperature photoluminescence (PL) measurements were conducted using a diode-pumped Nd:YAG solid state laser with wavelength of 266 nm, pulse width of 0.6 ns, and repetition rate of 19 kHz [38]. The maximum average power was approximately 3 mW, maximum peak power density was approximately 276.5 kW cm⁻². PL signal was detected using a 0.5 m focal length Andor SR-500i monochromator and thermoelectrically cooled InGaAs detector IGA-030-TE2-H of Electro-Optical Systems Inc that is equipped with a Hamamatsu R632 photomultiplier tube.

3. Results and discussion

3.1. Structural properties of Sb₂S₃ films

Sb₂S₃ films deposited onto CdS/FTO/glass substrates by CSS at substrate temperatures ranging from 240 to 400 °C were first characterized by XRD. Fig. 1 displays XRD patterns of Sb₂S₃/CdS/FTO/glass structures (with diffractograms of CdS/FTO/glass shown separately in Fig. S1 of the Supplementary Material). Reflections at 17.5°, 22.3°, 25.0°, 28.6°, 32.6° can be assigned to orthorhombic Sb₂S₃ crystal structure with *Pbnm* space group symmetry (JCPDS 42–1393) [19]. No secondary phases were detected. The lattice parameters and crystallite size (D) were calculated for the Sb₂S₃ films and included in Table S1 of the Supplementary Material. While the lattice parameters did not show any changes related to the applied substrate temperature, the crystallite size of Sb₂S₃ grew with increasing substrate temperature. Phase composition of Sb₂S₃ films was further analyzed by Raman spectroscopy, with all spectra presented in the Supplementary Fig. S2. Regardless of the substrate temperature, Raman spectra showed identical vibrational modes corresponding to the pure Sb₂S₃ phase [39].

Sb₂S₃ crystal growth depending on the substrate temperature was investigated through texture coefficient (TC) analysis, as shown in Fig. 1b. TC values were calculated from Eq. (1):

$$TC(hkl) = \frac{I(hkl)}{I_0(hkl)} \times \left[\frac{1}{N} \sum_{i=0}^N \frac{I(hkl)}{I_0(hkl)} \right]^{-1} \quad (1)$$

where *I*(*hkl*) is the measured intensity for a given reflection with *hkl* indices, *I*₀(*hkl*) is a reference intensity for a given reflection acquired from the JCPDS Card No. 42–1393, and *N* is the number of reflections considered in the analysis [40].

What can be immediately noted from the calculated TC values is that Sb₂S₃ films deposited at 260 °C and 300 °C show gradually increasing TC values for 211, 221 and 501 planes, with largest TC values (exceeding 1) arising from the 501 planes. For Sb₂S₃ films deposited at 340 °C and 380 °C, the largest TC values correspond to 110 and 320 planes. It can be deduced that lower substrate temperatures help induce growth of (*hk*1) planes as compared to higher substrate temperatures. Previous reports on both Sb₂S₃ and Sb₂Se₃ absorbers have also deemed (*hk*1)-oriented crystal grains optimal for efficient charge transport across the Sb₂S₃ (Sb₂Se₃) film [12,24,41,42].

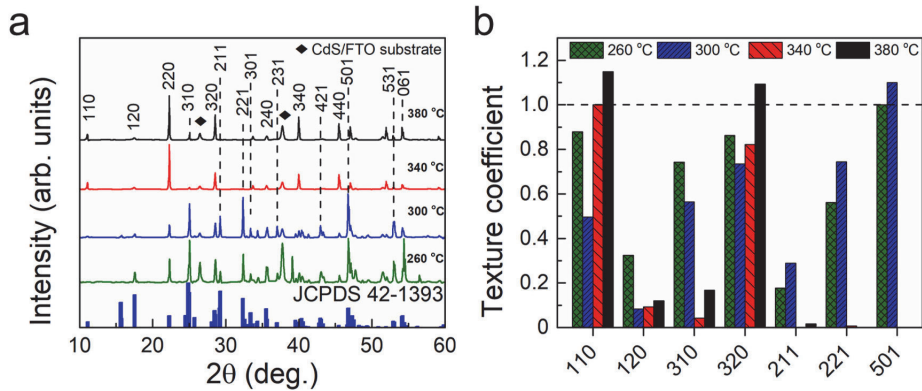


Fig. 1. (a) Sb₂S₃ absorber films deposited by CSS at substrate temperatures 260–380 °C onto CdS/FTO substrates. (b) TC values calculated from integrated intensity ratios for main crystal planes in Sb₂S₃ films.

The grain morphology in Sb₂S₃ films, deposited onto CdS/FTO/glass substrates, was analyzed by scanning electron microscopy (SEM). Top-down SEM images of Sb₂S₃ films, which were grown at substrate temperatures of 240–380 °C, as seen in Fig. 2a–d, illustrate well how the increase of substrate temperature converts to larger Sb₂S₃ grains. Ramp-up of substrate temperature caused Sb₂S₃ films to have bigger and denser plate-shaped grains as compared to smaller flakes at lower substrate temperatures (whole temperature range of 240–400 °C is shown in the Supplementary Fig. S3) – an observation that is consistent with previous CSS depositions of Sb₂Se₃ and SnS films [28,43]. Cross-sectional SEM images in Fig. 2e–h showed that Sb₂S₃ films also grow more compact with increasing substrate temperature.

While the Sb₂S₃ film fabricated at lower substrate temperature of 260 °C, as seen in Fig. 2a, shows relatively large voids between the grains, only a small number of pinholes in Fig. 2b–d are seen for Sb₂S₃ films at higher substrate temperatures. More intriguing, however, was the occurrence of microcracks, as can be clearly noted in Fig. 2d (and in Supplementary Figures S3e–h and S4a–c), which were found in Sb₂S₃ films grown at substrate temperatures of 320 °C and above. Interestingly, no cracks were noted in the previously grown Sb₂Se₃ films, also made by the CSS process [28]. It is likely that there are multiple plausible factors that altogether led to the crack formation. First, it can be argued that the cracking could be related to the difference in the thermal expansion coefficients (TECs) of orthorhombic Sb₂S₃ and Sb₂Se₃

crystals. Gan et al. reported that the TEC of Sb₂S₃ in the [010] crystal direction is two to seven times larger than the TECs in the [100] and [001] crystal direction [44]. At the same time, Herrmann et al. showed that Sb₂Se₃ has nearly identical TECs values in all three crystal directions [45]. This implies that Sb₂S₃ films could be subject to greater residual stress during the deposition process at higher temperatures. If there is either substantial tensile or compressive stress within the film, it could lead to crack formation [46,47]. Second, since Sb₂S₃ has a lower melting point (550 °C) compared with Sb₂Se₃ (611 °C) [9], it exhibits higher vapor pressure and sublimation is expected at lower temperatures. Therefore, substrate temperatures from 320 °C onwards could have induced such an intense re-sublimation of the already deposited Sb₂S₃ film, which eventually led to the crack formation in the Sb₂S₃ films.

3.2. Sb₂S₃ device properties depending on the CSS substrate temperature

Having noted systematic structural changes in the Sb₂S₃ film growth, the impact of CSS deposition temperature on the performance of superstrate glass/FTO/CdS/Sb₂S₃/Au solar cells was subsequently investigated. Fig. 3a–d shows main photovoltaic parameters with average values for devices with Sb₂S₃ deposited at substrate temperatures of 240–400 °C. Illuminated current density–voltage (J–V) curves are shown in Fig. 4a for the best devices. As seen in Fig. 3a–d, two

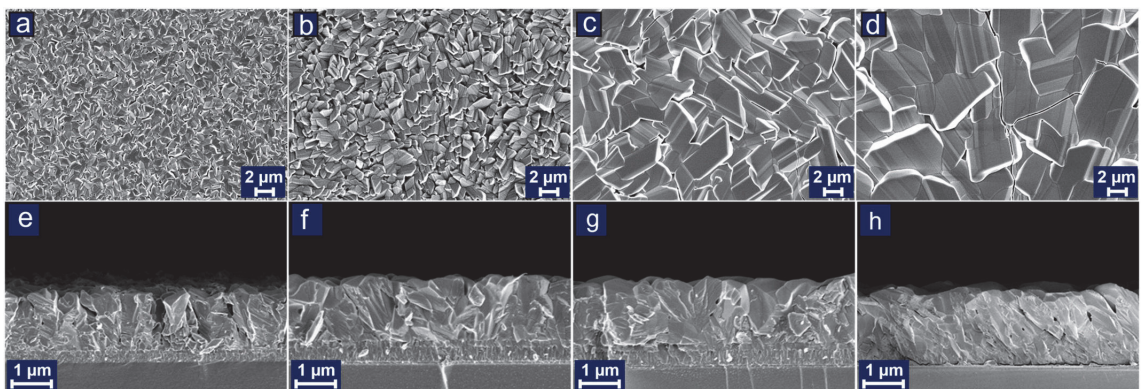


Fig. 2. Top-down (a–d) and cross-sectional (e–h) SEM images of Sb₂S₃ absorber films, which are deposited at varying substrate temperatures of 260 °C (a, e), 300 °C (b, f), 340 °C (c, g), and 380 °C (d, h) onto CdS/FTO/glass substrates.

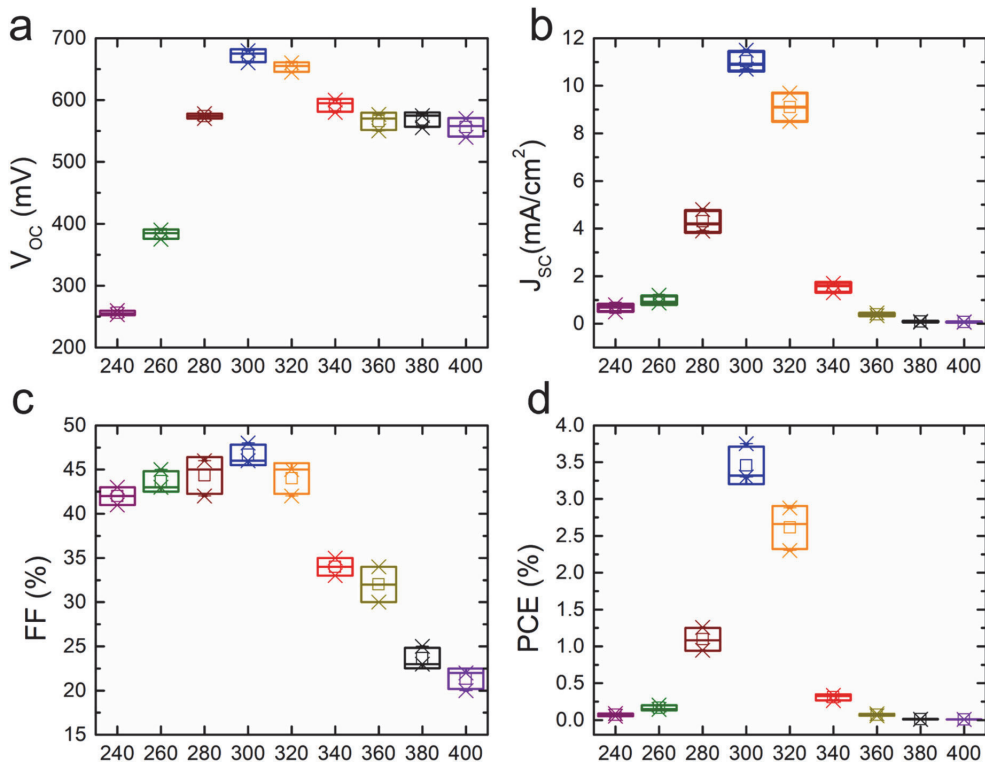


Fig. 3. Main photovoltaic parameters including (a) open circuit voltage (V_{OC}), (b) short circuit current density (J_{SC}), (c) fill factor (FF) and (d) photoconversion efficiency (PCE) with average values (marked as hollow squares) measured for Sb_2S_3 devices with Sb_2S_3 absorber deposited at substrate temperatures in the range of 240–400 °C.

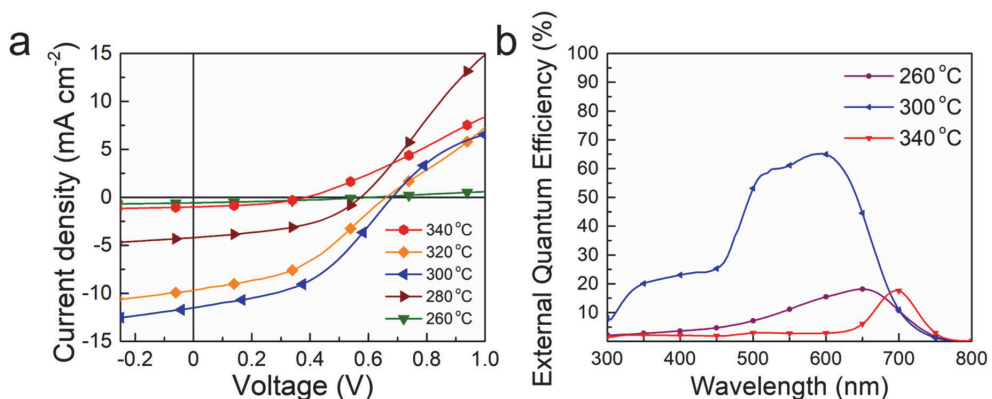


Fig. 4. (a) Illuminated J-V curves of best Sb_2S_3 devices and (b) external quantum efficiency (EQE) plots of Sb_2S_3 devices with Sb_2S_3 absorber layer deposited at substrate temperatures of 260–340 °C.

distinct regions can be noted. In the first region, from 240 °C to 300 °C, there is a gradual increase of all PV parameters, including open-circuit voltage (V_{OC}), current density (J_{SC}), fill factor (FF), and PCE. The maximum PV parameters, namely J_{SC} of 11.5 mA cm⁻², V_{OC} of 680 mV, FF of 48%, and PCE of 3.8% were obtained for the substrate temperature of 300 °C. In the second region, starting from substrate temperature of 320 °C, all the PV parameters start to decline. Interestingly, while the

V_{OC} shows only a slight decrease before plateauing at 550 mV, both J_{SC} and FF undergo a significant drop, with J_{SC} reducing to microamperes.

External quantum efficiency (EQE) measurements, as seen in Fig. 4b, support the trend observed during the J-V measurements, with the best device showing highest EQE response for the whole wavelength region. The band gap energy of ~1.8 eV was determined for the best Sb_2S_3 device (Supplementary Fig. S5). Nevertheless, the best device suffers a

significant EQE response drop in the short wavelength region, which is associated with parasitic absorption in the CdS buffer layer [28]. Such absorption has been widely reported also in CdTe and Sb_2S_3 cells, where a CdS buffer was employed [48,49]. For all the devices obtained with Sb_2S_3 deposited at temperatures higher than 340 °C, there was a futile EQE response throughout the whole wavelength region. This can be attributed to the detected microcracks, which were seen in the top-down and cross-sectional SEM images (Supplementary Figs. S4a–c), and which inherently lead to the current leakage, further evidenced by low FF values shown in Fig. 3c.

Based on the cumulative structural analysis of Sb_2S_3 absorber films and device characterization of respective Sb_2S_3 solar cells, it was demonstrated that the optimal CSS deposition of Sb_2S_3 films takes place at a substrate temperature of 300 °C, where a compact Sb_2S_3 grain growth is achieved together with increased presence of favorable (hk1) planes. When compared with recent reports on the Sb_2S_3 fabrication with CSS and VTD techniques, the optimal processing temperature found in the current work is clearly lower than the deposition temperature interval of 350–450 °C reported elsewhere [13,22,24]. For instance, Hiu et al., reported a VTD deposition temperature of 495 °C for depositing Sb_2S_3 films, and achieved a PCE of 4.7% for the superstrate glass/ITO/CdS/ Sb_2S_3 /Au device [24]. Zeng et al., reported a 1.4%-efficient CdS/ Sb_2S_3 device, where a higher CSS processing temperature (no exact values were given) was found optimal for high-quality Sb_2S_3 absorber [23]. Employing a similar CSS deposition technique, although with an additional selenization process, Xie et al., produced a device with PCE of 4.5% [13]. In this work, the optimal source and substrate temperatures in the CSS reactor were 450 °C and 370 °C, respectively [13]. Guo et al., used an identical CSS technique and obtained a device efficiency of 3.8% after screening substrate temperatures of 300–400 °C [21]. However, for the best Sb_2S_3 device, optimal substrate temperature was not provided. When looking at

studies where TE method was used, e.g., Chen et al., similarly found optimal substrate temperatures being in the 300–320 °C range, with the device achieving PCE of 3.0% [18]. Lian et al., followed a similar approach, employing a substrate temperature of 300 °C, yet also including a selenization step for the Sb_2S_3 absorber and a spiro-OMeTAD hole transport material (HTM) atop the absorber, which yielded a device with PCE of 6.2% [19]. As can be seen, the latter findings reported substrate temperatures that match well with the results obtained in this study. In addition, we revealed a physical phenomenon that had not been reported before. It is important to emphasize that the cracking phenomenon of Sb_2S_3 films, observed during the CSS deposition at temperatures 340–400 °C, had a clear impact on the eventual solar cell performance. Had the cracking phenomena not occurred, then inferring from previous experience with the CSS deposition of CdTe and Sb_2S_3 [28,50], e.g., Sb_2S_3 films grown at higher substrate temperatures, such as seen in Fig. 2c and d, would have probably performed better, given that the films have larger grains and higher level of compactness. Although cracking might be an expected occurrence at elevated temperatures in thin film technologies, it was still unusual for an antimony chalcogenide material, and it could have direct implications for some of the proposed applications. For instance, such physical phenomena could mean Sb_2S_3 is not compatible as a bottom cell for the recently proposed Sb_2Se_3 - Sb_2S_3 monolithic tandem solar cell [3].

3.3. Factors limiting the Sb_2S_3 device performance

Temperature-dependent J–V (J–V–T) curves, as shown in Fig. 5a, were measured to acquire better understanding of potential recombination processes for the best CdS/ Sb_2S_3 device (PCE = 3.8%). Fig. 5b shows a derived plot of logarithm of series resistance, R_s , vs. $1000/T$, where R_s increases with decreasing temperatures. Such behavior can be attributed to trapping of free carriers in the Sb_2S_3 bulk, which

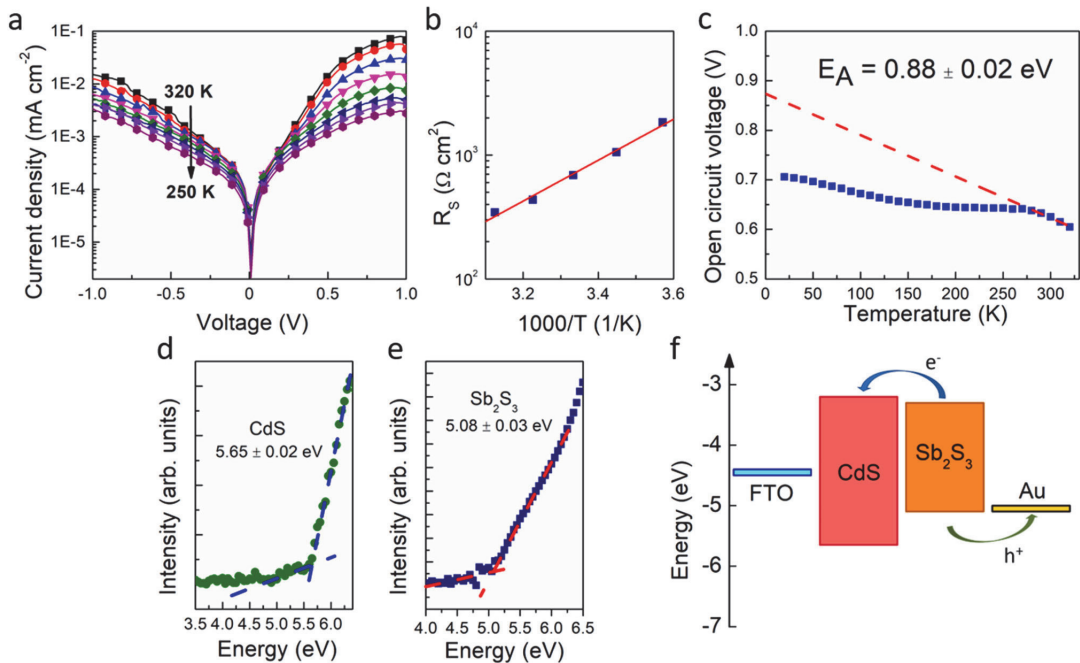


Fig. 5. (a) Semi-log plot of dark J–V curves, (b) series resistance derived from dark J–V curves plotted against $1000/T$, (c) activation energy calculated from the open-circuit voltage vs. T (V_{oc} - T) plot, photoelectron emission spectroscopy (PES) spectra of (d) CdS on FTO/glass substrate and (e) Sb_2S_3 on CdS/FTO/glass substrates, (f) derived band diagram for the FTO/CdS/ Sb_2S_3 /Au solar cell structure (CdS band gap value taken from [53]).

contributes to a significant R_s increase at lower temperatures [51]. The dominant recombination process in the CdS-Sb₂S₃ heterojunction was determined from the plot of temperature dependence of open-circuit voltage (V_{OC} -T), as shown in Fig. 5c. Activation energy, E_A , for the recombination process was found according to Eq. (2)

$$V_{OC} = \frac{E_A}{q} - \frac{Ak_B T}{q} \ln\left(\frac{J_{00}}{J_L}\right) \quad (2)$$

where E_A is the activation energy of the predominant recombination process, q is the elementary charge, A is the ideality factor, k_B is the Boltzmann constant, T is temperature, J_{00} is the reference current density and J_L is the photocurrent density [51].

Linear extrapolation from higher temperatures to 0 K in the V_{OC} -T plot gave the activation energy of 0.88 ± 0.02 eV, which is much lower than the Sb₂S₃ band gap energy of 1.8 eV. This implies that interface recombination is the dominant recombination process in the CdS/Sb₂S₃ device. In addition, photoelectron emission spectroscopy (PES) was performed on CdS and Sb₂Se₃ films, as shown in Fig. 5d and e, respectively, to elucidate band alignment for the FTO/CdS/Sb₂S₃/Au device structure. Ionization potential (I_p) was found through extrapolation of the linear fit from valence band edge photoemission to 0 eV, giving ionization potentials of 5.65 ± 0.02 eV and 5.08 ± 0.03 eV for CdS and Sb₂S₃, respectively. Considering the band gap values of CdS and Sb₂S₃, a band diagram of the device was subsequently drawn, as shown in Fig. 5f, which revealed a small positive conduction band offset (CBO) of ≈ 0.1 eV between the CdS buffer and Sb₂S₃ absorber. Although it implies a formation of a spike, an electrostatic barrier to electrons moving to the front electrode, it has been argued that for such a small CBO, thermionic emission across the junction would still allow unimpeded charge transport [52,53].

Deep defects could also explain substantial V_{OC} losses in the CdS/Sb₂S₃ devices. TAS enables characterization of deep defects in the Sb₂S₃ absorber, where the overall capacitance response has contribution from free carriers, bulk defects, and interface defects [41]. Impedance, $Z(\omega, T)$, and phase angle, $\theta(\omega, T)$, were measured to calculate capacitance, C , using an equivalent circuit model, which includes a capacitor, a series resistor, and a parallel resistor [10,37]. In the case of a capacitance step, its relaxation frequency, ω_0 , was found from the maxima of a derivative capacitance ($-\omega dC/d\omega$) plot. In the Arrhenius plot, natural logarithms of relaxation frequencies were plotted against inverse temperature to calculate the activation energy, E_A , and thermal emission prefactor, ξ_0 , according to Eq. (2) [37,54]:

$$\omega_0 = 2\pi f_0 = 2\xi_0 T^2 \exp(-E_A / k_B T) \quad (3)$$

where ξ_0 is the thermal emission prefactor, k_B is Boltzmann constant, T is temperature and E_A is the activation energy of defect level.

Temperature-dependent capacitance-frequency (C-f-T) curves of a Sb₂S₃ device are shown in Fig. 6a. From the derivative capacitance plot,

as shown in Fig. 6b, two distinct maxima could be discerned. Fig. 6c shows the Arrhenius plot with two activation energies: E_{A1} of 0.32 eV (ξ_0 of $4.2 \times 10^6 \text{ s}^{-1} \text{ K}^{-2}$) and E_{A2} of 0.37 eV (ξ_0 of $5.2 \times 10^6 \text{ s}^{-1} \text{ K}^{-2}$). The activation energy of 0.32 eV has also been reported in a DLTS study on a TiO₂/Sb₂S₃ solar cell and was assigned to an Sb vacancy (V_{Sb}) [55]. A first-principles calculations study assigned comparable activation energies to a S antisite (S_{Sb}) defect and an Sb vacancy, respectively, and where both were reported to exist in high concentration due to low formation energy [56]. Furthermore, a DFT study on intrinsic Sb₂S₃ found that V_{Sb} defects have two ionization energies between 0.3 and 0.4 eV, although these defects show relatively high defect formation energies [21]. Based on these reports and prior admittance measurements on the Sb₂Se₃ counterpart [10], at least one of the activation energies could be ascribed to the Sb vacancy.

Fig. 7 shows PL spectra measured at 3–70 K for the Sb₂S₃ deposited at substrate temperature of 300 °C onto the CdS/FTO/glass substrate. It is important to mention that initial PL measurements were performed using a continuous wave He-Cd gas laser and an InGaAs detector [43, 57]. Since the continuous wave laser led to localized heating of the sample and given that a half-band was detected at around 1.35 eV, which was at the detection limit of the working range of the InGaAs photomultiplier tube (0.77–1.35 eV), a pulsed laser with a detection limit greater than 1.35 eV was opted. Fig. 7a shows PL spectra that revealed two PL bands: a narrow emission band peaked at 1.72 eV and a very broad asymmetric emission band peaked at around 1.40 eV.

The band D1 peaked at 1.72 eV was fitted by assuming there is a single peak and is related to a band-to-band transition. The broad band D2 was fitted by a single asymmetric sigmoidal function for the deconvolution of asymmetric band, as presented in Fig. 7b [38,57]. Thereby, we obtained temperature-dependent PL spectra of band D2, as shown in Fig. 7c, which peak at approximately 1.40 eV. It is worth mentioning that while D1 band-to-band transition has been reported by a recent study employing room-temperature PL, to the best of our knowledge, the D2 band-related emission has not been reported thus far. To gain better understanding of the peculiarity of this band, the Arrhenius plot, as shown in Fig. 7d, was derived to calculate thermal activation energy, E_A , of the D2 band. Activation energy of 10 ± 2 meV was obtained, indicating that at least one shallow defect is involved in that recombination. In a classical approach, laser power dependence can provide supporting evidence if this D2 band originates from a donor-acceptor-pair (DAP) recombination. However, since at higher laser power (≥ 10 mW) sample degradation was observed, and at lower laser power (< 3 mW) intensity of the signal was lost, we were not able to conduct laser power dependence measurements. Nevertheless, a subtle blue shift of the D2 band was observed with increasing temperature. Such a phenomenon, where a band is shifted toward higher energies with increasing temperature, has been related to a DAP recombination at low temperatures [43]. To satisfy this DAP mechanism, we should assume contribution from a certain deep donor defect, such as the S

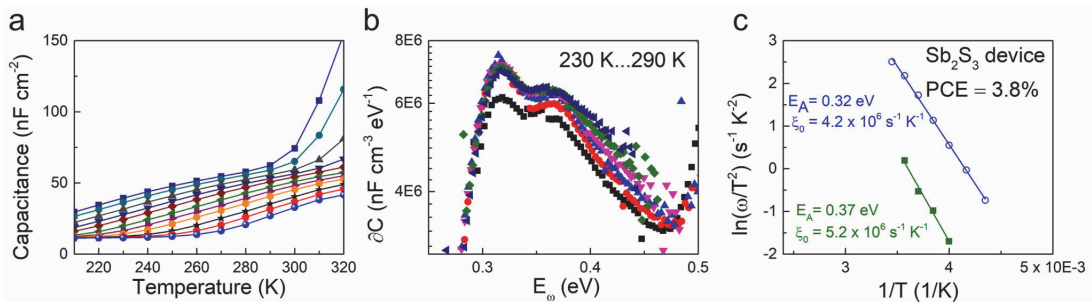


Fig. 6. (a) C-f-T curves of CdS/Sb₂S₃ solar cell (PCE = 3.8%) measured from 80 to 320 K, (b) $-\omega dC(\omega)/d\omega$ vs E_0 plots that show two distinct peaks, (c) Arrhenius plot of $\ln(\omega/T^2)$ vs $1/T$ used to calculate activation energies and thermal emission prefactors.

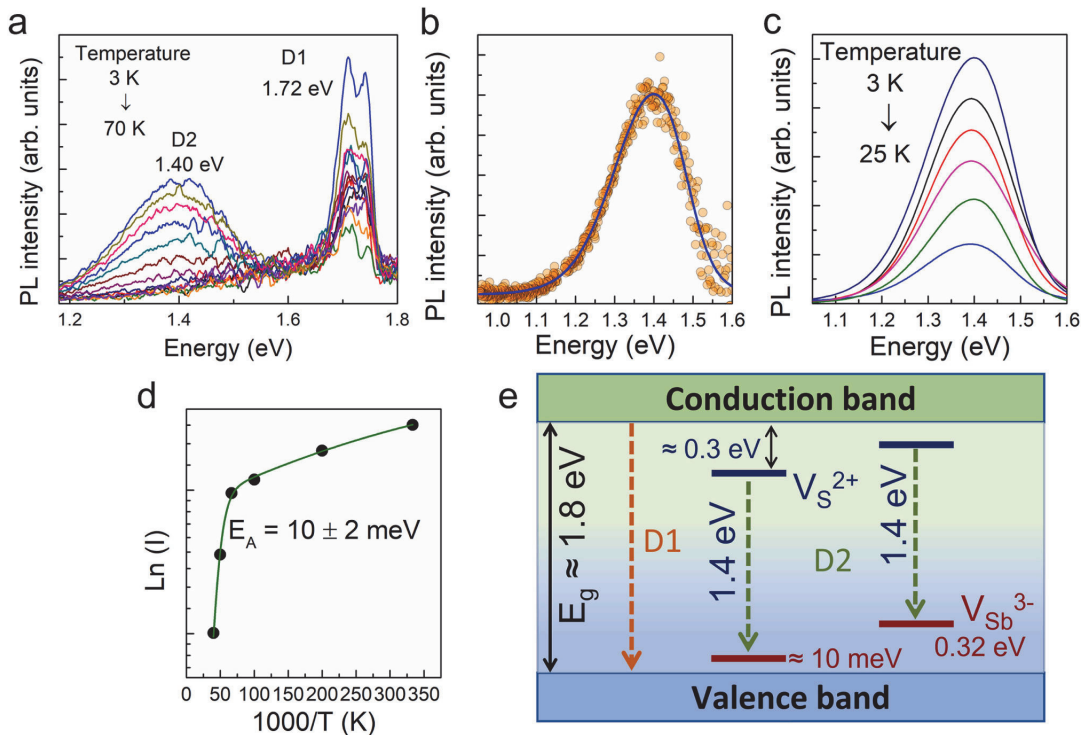


Fig. 7. (a) Low-temperature PL spectra of Sb_2S_3 films deposited at substrate temperature of 300°C onto a $\text{CdS}/\text{FTO}/\text{glass}$ substrate. For the given sample, (b) fitting of an asymmetric D2 band by using a single asymmetric sigmoidal function, and (c) temperature-dependent fitted PL spectra of D2 band measured in the temperature range of 3–25 K (d) Arrhenius plot giving thermal activation energy of the D2 band in Sb_2S_3 , which was obtained from fitted PL spectra, (e) model visualizing D1 band-to-band emission and D2 emission originating from a deep donor to shallow acceptor transition and/or from a deep donor to deep acceptor (V_{Sb}) transition.

vacancy (V_{S}) (0.3–0.6 eV) [55,56]. According to this scenario, the donor level will be occupied provided the temperature is increased, and recombination occurs between the conduction band and a deep acceptor. According to TAS results, this deep acceptor can be assigned to the Sb vacancy (V_{Sb}). As a rule of thumb, there is always one type of disorder, which prevails over others in the crystal lattice. Given that the theoretical studies have provided low formation energies for vacancy defects (V_{Sb} , V_{S}) [55,56], we consider these Schottky defects to be predominant and provide their formation mechanism in the Supplementary Material. Based on the above discussion and existence of possible defect levels, a DAP model is proposed in Fig. 7e. For the given model, it can be assumed the DAP transition could be related to either the transition between deep donor (DD) to shallow acceptor transition and/or between deep donor (V_{S}) and deep acceptor (V_{Sb}), as determined from TAS measurements). For better clarification, laser power dependence measurements would be needed to ascertain the shift of the band peak position per decade. Nevertheless, the presence of such complex defects is detrimental to the performance of Sb_2S_3 device, potentially limiting the built-in voltage and photocurrent collection.

4. Conclusions

In conclusion, we systematically studied the effect of substrate temperature on the Sb_2S_3 absorber growth with the CSS method, employing a wide substrate temperature range of $240\text{--}400^\circ\text{C}$. It was found that CSS processing temperature of 300°C is optimal, resulting in compact crack-free films with increased presence of favorable (hk1) planes. Higher substrate temperatures ($340\text{--}380^\circ\text{C}$) caused Sb_2S_3 films

to have bigger, more dense plate-shaped grains as compared to smaller flakes at lower substrate temperatures ($240\text{--}280^\circ\text{C}$). However, micro-cracks were detected in Sb_2S_3 films starting from substrate temperature of 320°C . The maximum PV parameters, namely J_{SC} of 11.5 mA cm^{-2} , V_{OC} of 680 mV, FF of 48%, and PCE of 3.8% were obtained for the substrate temperature of 300°C . For the same device the EQE showed the best response over the entire 300–800 nm wavelength range. For the best device, extraction of activation energy from the $V_{\text{OC}}\text{--}T$ plot indicated that interface recombination is the dominant recombination mechanism in these devices. Based on the determined ionization potentials, a band diagram was derived, which showed favorable band alignment between the CdS buffer and Sb_2S_3 absorber. TAS study showed two deep defects with activation energies of 0.32 eV and 0.37 eV, while low-temperature PL measurement revealed a band-to-band emission at 1.72 eV and a broad band peaked at 1.40 eV, which was assigned to a donor-acceptor pair recombination. Although the device efficiency of 3.8% is a promising achievement and well-placed result within reported Sb_2S_3 based devices processed by physical deposition methods, the limitation factors like absorber-buffer interface recombination and existence of deep defects in the absorber remain the key issues for this device structure. Further technological steps, such as post-deposition treatments and doping, combined with in-depth advanced characterization, need to be implemented to progress the development of emerging cost-efficient and environmentally friendly Sb_2S_3 thin-film solar cells.

CRedit authorship contribution statement

R. Krautmann: Writing – original draft, Visualization, Validation, Methodology, Investigation, Formal analysis, Data curation, Conceptualization. **N. Spalatu:** Writing – review & editing, Visualization, Validation, Supervision, Methodology, Investigation, Funding acquisition, Formal analysis, Conceptualization. **R. Josepson:** Visualization, Formal analysis. **R. Nedzinskas:** Visualization, Validation, Formal analysis. **R. Kondrotas:** Visualization, Validation, Formal analysis. **R. Grzibovskis:** Visualization, Validation, Formal analysis. **A. Vembris:** Visualization, Validation, Formal analysis. **M. Krunks:** Visualization, Validation, Project administration, Funding acquisition, Formal analysis. **I. Oja Acik:** Validation, Supervision, Project administration, Funding acquisition, Formal analysis.

Declaration of competing interest

The authors declare that they have no known competing financial interests or personal relationships that could have appeared to influence the work reported in this paper.

Data availability

No data was used for the research described in the article.

Acknowledgments

This study was funded by the Estonian Research Council project PRG627 “Antimony chalcogenide thin films for next-generation semi-transparent solar cells applicable in electricity producing windows”, the Estonian Research Council project PSG689 “Bismuth Chalcogenide Thin-Film Disruptive Green Solar Technology for Next Generation Photovoltaics”, the Estonian Centre of Excellence project TK141 (TAR16016EK) “Advanced materials and high-technology devices for energy recuperation systems”, and the European Union’s Horizon 2020 ERA Chair project 5GSOLAR (grant agreement No. 952509). The article is based upon work from COST Action Research and International Networking project “Emerging Inorganic Chalcogenides for Photovoltaics (RENEW-PV),” CA21148, supported by COST (European Cooperation in Science and Technology).

Appendix B. Supplementary data

Supplementary data to this article can be found online at <https://doi.org/10.1016/j.solmat.2022.112139>.

References

- M.Y. Versavel, J.A. Haber, Structural and optical properties of amorphous and crystalline antimony sulfide thin-films, *Thin Solid Films* 515 (2007) 7171–7176, <https://doi.org/10.1016/j.tsf.2007.03.043>.
- R. Kondrotas, C. Chen, J. Tang, Sb₂S₃ solar cells, *Joule* 2 (2018) 857–878, <https://doi.org/10.1016/j.joule.2018.04.003>.
- Y. Cao, X. Zhu, J. Jiang, C. Liu, J. Zhou, J. Ni, J. Zhang, J. Pang, Rotational design of charge carrier transport layers for optimal antimony trisulfide solar cells and its integration in tandem devices, *Sol. Energy Mater. Sol. Cell.* 206 (2020), 110279, <https://doi.org/10.1016/j.solmat.2019.110279>.
- J.S. Eensalu, A. Katerski, E. Kärber, L. Weinhardt, M. Blum, C. Heske, W. Yang, I. O. Acik, M. Krunks, Semitransparent Sb₂S₃ thin film solar cells by ultrasonic spray pyrolysis for use in solar windows, *Beilstein J. Nanotechnol.* 10 (2019) 2396–2409, <https://doi.org/10.3762/bjnano.10.230>, 230. 10.
- K. Li, F. Li, C. Chen, P. Jiang, S. Lu, S. Wang, Y. Lu, G. Tu, J. Guo, L. Shui, Z. Liu, B. Song, J. Tang, One-dimensional Sb₂Se₃ enabling ultra-flexible solar cells and mini-modules for IoT applications, *Nano Energy* 86 (2021), 106101, <https://doi.org/10.1016/j.nanoen.2021.106101>.
- L. Wang, W. Lian, B. Liu, H. Lv, Y. Zhang, X. Wu, T. Wang, J. Gong, T. Chen, H. Xu, L. Wang, Y. Zhang, H. Xu, W. Lian, H. Lv, X. Wu, T. Chen, B. Liu, T. Wang, J. Gong, A transparent, high-performance, and stable Sb₂S₃ photoanode enabled by heterojunction engineering with conjugated polycarbazole frameworks for unbiased photoelectrochemical overall water splitting devices, *Adv. Mater.* 34 (2022), 2200723, <https://doi.org/10.1002/adma.202200723>.
- Z. Zafar, S. Yi, J. Li, C. Li, Y. Zhu, A. Zada, W. Yao, Z. Liu, X. Yue, Recent development in defects engineered photocatalysts: an overview of the experimental and theoretical strategies, *Energy & Environmental Materials* 5 (2022) 68–114, <https://doi.org/10.1002/eeem2.12171>.
- L. Wang, D.B. Li, K. Li, C. Chen, H.X. Deng, L. Gao, Y. Zhao, F. Jiang, L. Li, F. Huang, Y. He, H. Song, G. Niu, J. Tang, Stable 6%-efficient Sb₂Se₃ solar cells with a ZnO buffer layer, *Nat. Energy* 2 (2017), 17046, <https://doi.org/10.1038/energy.2017.46>.
- T.D.C. Hobson, L.J. Phillips, O.S. Hutter, H. Shiel, J.E.N. Swallow, C.N. Savory, P. K. Nayak, S. Mariotti, B. Das, L. Bowen, L.A.H. Jones, T.J. Featherstone, M. J. Smiles, M.A. Farnworth, G. Zoppi, P.K. Thakur, T.-L. Lee, H.J. Snaith, C. Leighton, D.O. Scanlon, V.R. Dhanak, K. Durose, T.D. Veal, J.D. Major, Isotype heterojunction solar cells using n-type Sb₂Se₃ thin films, *Chem. Mater.* (2020), <https://doi.org/10.1021/acs.chemmater.0c00223>.
- R. Krautmann, N. Spalatu, R. Gunder, D. Abou-Ras, T. Unold, S. Schorr, M. Krunks, I. Oja Acik, Analysis of grain orientation and defects in Sb₂Se₃ solar cells fabricated by close-space sublimation, *Sol. Energy* 225 (2021) 494–500, <https://doi.org/10.1016/j.solener.2021.07.022>.
- X. Jin, Y. Fang, T. Salim, M. Feng, S. Hadke, S. Woei Leow, T. Chien Sum, L. H. Wong, X. Jin, Y. Fang, T. Salim, S. Hadke, S.W. Leow, L.H. Wong, M. Feng, T. C. Sum, In situ growth of [hk1]-Oriented Sb₂S₃ for solution-processed planar heterojunction solar cell with 6.4% efficiency, *Adv. Funct. Mater.* 30 (2020), 2002887, <https://doi.org/10.1002/adfm.202002887>.
- S. Yuan, H. Deng, D. Dong, X. Yang, K. Qiao, C. Hu, H. Song, H. Song, Z. He, J. Tang, Efficient planar antimony sulfide thin film photovoltaics with large grain and preferential growth, *Sol. Energy Mater. Sol. Cell.* 157 (2016) 887–893, <https://doi.org/10.1016/j.solmat.2016.07.050>.
- H. Zhang, S. Yuan, H. Deng, M. Ishaq, X. Yang, T. Hou, U.A. Shah, H. Song, J. Tang, Controllable orientations for Sb₂S₃ solar cells by vertical VTD method, *Prog. Photovoltaics Res. Appl.* 28 (2020) 823–832, <https://doi.org/10.1002/ppa.3278>.
- K. Wang, J. Cheng, X. Yang, R. Hu, L. Fu, J. Huang, J. Yu, L. Li, Enhanced photovoltaic properties in Sb₂S₃ planar heterojunction solar cell with a fast selenylation approach, *Nanoscale Res. Lett.* 13 (2018) 1–7, <https://doi.org/10.1186/s11671-018-2651-x/tables/3>.
- N. Juneja, S. Mandati, A. Katerski, N. Spalatu, S. Daskeviciute-Geguziene, A. Vembris, S. Karazhanov, V. Getautis, M. Krunks, I. Oja Acik, Sb₂S₃ solar cells with a cost-effective and dopant-free fluorene-based enamine as a hole transport material, *Sustain. Energy Fuels* 6 (2022) 3220–3229, <https://doi.org/10.1039/d2se00356b>.
- P. Büttner, F. Scheler, D. Döhler, M.K.S. Barr, M. Bosch, M. Rey, T. Yokosawa, S. Hinz, J. Maultzsch, E. Spieker, N. Vogel, I. Minguez-Bacho, J. Bachmann, Continuous, crystalline Sb₂S₃ ultrathin light absorber coatings in solar cells based on photonic concentric p-n heterojunctions, *Nano Energy* 103 (2022), 107820, <https://doi.org/10.1016/j.nanoen.2022.107820>.
- Y.C. Choi, D.U. Lee, J.H. Noh, E.K. Kim, S. il Seok, Highly improved Sb₂S₃ sensitized inorganic-organic heterojunction solar cells and quantification of traps by deep-level transient spectroscopy, *Adv. Funct. Mater.* 24 (2014) 3587–3592, <https://doi.org/10.1002/adfm.201304238>.
- X. Chen, Z. Li, H. Zhu, Y. Wang, B. Liang, J. Chen, Y. Xu, Y. Mai, CdS/Sb₂S₃ heterojunction thin film solar cells with a thermally evaporated absorber, *J Mater Chem C Mater* 5 (2017) 9421–9428, <https://doi.org/10.1039/c7tc02460f>.
- W. Lian, C. Jiang, Y. Yin, R. Tang, G. Li, L. Zhang, B. Che, T. Chen, Revealing composition and structure dependent deep-level defect in antimony trisulfide photovoltaics, *Nature Communications* 2021 12 (2021) 1–7, <https://doi.org/10.1038/s41467-021-23592-0>, 1. 12.
- S. Yuan, H. Deng, X. Yang, C. Hu, J. Khan, W. Ye, J. Tang, H. Song, Postsurface selenization for high performance Sb₂S₃ planar thin film solar cells, *ACS Photonics* 4 (2017) 2862–2870, [https://doi.org/10.1021/acsp Photonics.7b00858/ASSET/IMAGES/LARGE/PH-2017-008588_0008 \(JPEG\)](https://doi.org/10.1021/acsp Photonics.7b00858/ASSET/IMAGES/LARGE/PH-2017-008588_0008 (JPEG)).
- L. Guo, B. Zhang, S. Li, Q. Zhang, M. Buettner, L. Li, X. Qian, F. Yan, Scalable and efficient Sb₂S₃ thin-film solar cells fabricated by close space sublimation, *Appl. Mater.* 7 (2019), 041105, <https://doi.org/10.1063/1.5090773>.
- Y. Xie, K. Li, X. Li, F. Gao, X. Xiong, G. Zeng, B. Li, Fabrication of Sb₂S₃ solar cells by close space sublimation and enhancing the efficiency via co-selenization, *Mater. Sci. Semicond. Process.* 142 (2022), 106451, <https://doi.org/10.1016/j.mssp.2022.106451>.
- Y. Zeng, F. Liu, X. Hao, Fabrication of Sb₂S₃ planar thin film solar cells with closed-space sublimation method, 2018 IEEE 7th World Conference on Photovoltaic Energy Conversion, in: WCPEC 2018 - A Joint Conference of 45th IEEE PVSC, 28th PVSEC and 34th EU PVSEC, 2018, pp. 870–872, <https://doi.org/10.1109/PVSC.2018.8547305>.
- Y. Zeng, K. Sun, J. Huang, M.P. Nielsen, F. Ji, C. Sha, S. Yuan, X. Zhang, C. Yan, X. Liu, H. Deng, Y. Lai, J. Seidel, N. Ekins-Daukes, F. Liu, H. Song, M. Green, X. Hao, Quasi-vertically-orientated antimony sulfide inorganic thin-film solar cells achieved by vapor transport deposition, *ACS Appl. Mater. Interfaces* 12 (2020) 22825–22834, [https://doi.org/10.1021/acsaami.0c02697/ASSET/IMAGES/LARGE/AM0C02697_0006 \(JPEG\)](https://doi.org/10.1021/acsaami.0c02697/ASSET/IMAGES/LARGE/AM0C02697_0006 (JPEG)).
- T.P. Shalvey, H. Shiel, O.S. Hutter, G. Zoppi, L. Bowen, V.R. Dhanak, J.D. Major, Sodium fluoride doping approach to CdTe solar cells, *ACS Appl. Energy Mater.* 5 (2022) 3888–3897, [https://doi.org/10.1021/acsaem.1c03351/ASSET/IMAGES/LARGE/AE1C03351_0007 \(JPEG\)](https://doi.org/10.1021/acsaem.1c03351/ASSET/IMAGES/LARGE/AE1C03351_0007 (JPEG)).
- M. Valdes, A. Hernandez, Y. Sánchez, R. Fonoll, M. Placidi, V. Izquierdo, A. Cabas-Vidani, M. Valentini, A. Mittiga, P. Pistor, C. Malerba, E. Saucedo, A new approach for alkali incorporation in Cu₂ZnSnS₄ solar cells, *J. Phys.: Energy* 4 (2022), 044008, <https://doi.org/10.1088/2515-7655/AC96A4>.

- [27] T.P. Weiss, I. Mínguez-Bacho, E. Zuccalá, M. Melchiorre, N. Valle, E. Adib Brahime, Yokosawa Tadahiro, Erdmann Spiecker, J. Bachmann, P.J. Dale, S. Siebentritt, Post-deposition annealing and interfacial atomic layer deposition buffer layers of Sb₂Se₃/CdS stacks for reduced interface recombination and increased open-circuit voltages, *Prog. Photovoltaics Res. Appl.* (2022), <https://doi.org/10.1002/PIP.3625>.
- [28] N. Spalatu, R. Krautmann, A. Katerski, E. Karber, R. Josepson, J. Hiie, I.O. Acik, M. Krunk, Screening and optimization of processing temperature for Sb₂Se₃ thin film growth protocol: interrelation between grain structure, interface intermixing and solar cell performance, *Sol. Energy Mater. Sol. Cell.* 225 (2021), 111045, <https://doi.org/10.1016/j.solmat.2021.111045>.
- [29] V. Kumar, E. Artegiani, A. Kumar, G. Mariotto, F. Piccinelli, A. Romeo, Effects of post-deposition annealing and copper inclusion in superstrate Sb₂Se₃ based solar cells by thermal evaporation, *Sol. Energy* 193 (2019) 452–457, <https://doi.org/10.1016/j.solener.2019.09.069>.
- [30] K.J. Tiwari, M. Neuschitzer, M. Espindola-Rodriguez, Y. Sánchez, Z. Jehl, P. Vidal-Fuentes, E. Saucedo, P. Malar, Efficient Sb₂Se₃/CdS planar heterojunction solar cells in substrate configuration with (hk0) oriented Sb₂Se₃ thin films, *Sol. Energy Mater. Sol. Cell.* 215 (2020), 110603, <https://doi.org/10.1016/j.solmat.2020.110603>.
- [31] I. Caño, P. Vidal-Fuentes, L. Calvo-Barrio, X. Alcobé, J.M. Asensi, S. Giraldo, Y. Sánchez, Z. Jehl, M. Placidi, J. Puigdollers, V. Izquierdo-Roca, E. Saucedo, Does Sb₂Se₃ admit nonstoichiometric conditions? How modifying the overall Se content affects the structural, optical, and optoelectronic properties of Sb₂Se₃ thin films, *ACS Appl. Mater. Interfaces* 14 (2022) 11222–11234, <https://doi.org/10.1021/ACSAMI.1C20764>.
- [32] X. Wen, C. Chen, S. Lu, K. Li, R. Kondrotas, Y. Zhao, W. Chen, L. Gao, C. Wang, J. Zhang, G. Niu, J. Tang, Vapor transport deposition of antimony selenide thin film solar cells with 7.6% efficiency, *Nat. Commun.* 9 (2018) 1–10, <https://doi.org/10.1038/s41467-018-04634-6>.
- [33] X. Hu, J. Tao, G. Weng, J. Jiang, S. Chen, Z. Zhu, J. Chu, Investigation of electrically-active defects in Sb₂Se₃ thin-film solar cells with up to 5.91% efficiency via admittance spectroscopy, *Sol. Energy Mater. Sol. Cell.* 186 (2018) 324–329, <https://doi.org/10.1016/j.solmat.2018.07.004>.
- [34] C. Gao, J. Huang, H. Li, K. Sun, Y. Lai, M. Jia, L. Jiang, F. Liu, Fabrication of Sb₂S₃ thin films by sputtering and post-annealing for solar cells, *Ceram. Int.* 45 (2019) 3044–3051, <https://doi.org/10.1016/j.ceramint.2018.10.155>.
- [35] M.I. Medina-Montes, Z. Montiel-González, N.R. Mathews, X. Mathew, The influence of film deposition temperature on the subsequent post-annealing and crystallization of sputtered Sb₂S₃ thin films, *J. Phys. Chem. Solid.* 111 (2017) 182–189, <https://doi.org/10.1016/j.jpcs.2017.07.035>.
- [36] J. Han, S. Wang, X. Li, H. Tang, Q. Cao, J. Yang, J. Zhu, X. Liu, Z. Li, W. Liu, Alcohol vapor post-annealing for highly efficient Sb₂S₃ planar heterojunction solar cells, *Solar RRL* 3 (2019), 1900133, <https://doi.org/10.1002/SOLR.201900133>.
- [37] E. Kask, J. Krustok, S. Giraldo, M. Neuschitzer, S. López-Marino, E. Saucedo, Temperature dependent electrical characterization of thin film Cu₂ZnSnSe₄ solar cells, *J. Phys. D Appl. Phys.* 49 (2016), 085101, <https://doi.org/10.1088/0022-3727/49/8/085101>.
- [38] M.E. Uslu, R. Kondrotas, R. Nedzinskas, O. Volobujeva, K. Timmo, M. Kauk-Kuusik, J. Krustok, M. Grossberg, Study of the optical properties of Sb₂(Se_{1-x}S_x)₃ (x = 0–1) solid solutions, *Mater. Sci. Semicond. Process.* 144 (2022), 106571, <https://doi.org/10.1016/j.mssp.2022.106571>.
- [39] J.S. Eensalu, A. Katerski, E. Kärber, I.O. Acik, A. Mere, M. Krunk, Jako S. Eensalu, Atanas Katerski, Erki Kärber, Ilona Oja Acik, Arvo Mere, Malle Krunk, Uniform Sb₂S₃ optical coatings by chemical spray method, *Beilstein J. Nanotechnol.* 10 (2019) 198–210, <https://doi.org/10.3762/bjnano.10.18>.
- [40] L.Ph Bérubé, G. L'Espérance, A quantitative method of determining the degree of texture of zinc electrodeposits, *J. Electrochem. Soc.* 136 (1989) 2314–2315, <https://doi.org/10.1149/1.2097318>.
- [41] Z. Li, X. Liang, G. Li, H. Liu, H. Zhang, J. Guo, J. Chen, K. Shen, X. San, W. Yu, R.E. I. Schropp, Y. Mai, 9.2%-efficient core-shell structured antimony selenide nanorod array solar cells, *Nat. Commun.* 10 (2019) 1–9, <https://doi.org/10.1038/s41467-018-07903-6>.
- [42] Y. Zhou, L. Wang, S. Chen, S. Qin, X. Liu, J. Chen, D.J. Xue, M. Luo, Y. Cao, Y. Cheng, E.H. Sargent, J. Tang, Thin-film Sb₂Se₃ photovoltaics with oriented one-dimensional ribbons and benign grain boundaries, *Nat. Photonics* 9 (2015) 409–415, <https://doi.org/10.1038/nphoton.2015.78>.
- [43] N. Spalatu, J. Hiie, R. Kaupmees, O. Volobujeva, J. Krustok, I.O. Acik, M. Krunk, Postdeposition processing of SnS thin films and solar cells: prospective strategy to obtain large, sintered, and doped SnS grains by recrystallization in the presence of a metal halide flux, *ACS Appl. Mater. Interfaces* 11 (2019) 17539–17554, <https://doi.org/10.1021/acsami.9b03213>.
- [44] C.K. Gan, J.R. Soh, Y. Liu, Large anharmonic effect and thermal expansion anisotropy of metal chalcogenides: the case of antimony sulfide, *Phys. Rev. B Condens. Matter* 92 (2015), <https://doi.org/10.1103/PhysRevB.92.235202>.
- [45] M.G. Herrmann, R.P. Stoffel, I. Sergueev, H.C. Wille, O. Leupold, M. Ait Haddouch, G. Sala, D.L. Abernathy, J. Voigt, R.P. Herrmann, R. Dronskowski, K. Friese, Lattice dynamics of Sb₂Se₃ from inelastic neutron and X-ray scattering, *Phys. Status Solidi* 257 (2020), 2000063, <https://doi.org/10.1002/PSSB.202000063>.
- [46] Z.B. Zhao, S.M. Yalisoev, Z.U. Rek, J.C. Billelo, Evolution of anisotropic microstructure and residual stress in sputtered Cr films, *J. Appl. Phys.* 92 (2002) 7183, <https://doi.org/10.1063/1.1521791>.
- [47] S. Mani, T.M. Saif, Mechanism of controlled crack formation in thin-film dielectrics, *Appl. Phys. Lett.* 86 (2005), 201903, <https://doi.org/10.1063/1.1927267>.
- [48] N. Spalatu, J. Hiie, V. Valdna, M. Caraman, N. Maticiu, V. Mikli, T. Potlog, M. Krunk, V. Lugh, Properties of the CdCl₂ air-annealed CSS CdTe thin films, in: *Energy Procedia*, Elsevier, 2014, pp. 85–95, <https://doi.org/10.1016/j.egypro.2013.12.013>.
- [49] A. Graf, N. Maticiu, N. Spalatu, V. Mikli, A. Mere, A. Gavrilo, J. Hiie, Electrical characterization of annealed chemical-bath-deposited CdS films and their application in superstrate configuration CdTe/CdS solar cells, in: *Thin Solid Films*, Elsevier, 2015, pp. 351–355, <https://doi.org/10.1016/j.tsf.2014.11.003>.
- [50] N. Spalatu, M. Krunk, J. Hiie, Structural and optoelectronic properties of CdCl₂ activated CdTe thin films modified by multiple thermal annealing, *Thin Solid Films* 633 (2017) 106–111, <https://doi.org/10.1016/j.tsf.2016.09.042>.
- [51] R. Scheer, H.-W. Schock, Chalcogenide Photovoltaics, Wiley-VCH Verlag GmbH & Co. KGaA, Weinheim, Germany, 2011, <https://doi.org/10.1002/9783527633708>.
- [52] A. Niemegeers, M. Burgelman, A. de Vos, On the CdS/CuInSe₂ conduction band discontinuity, *Appl. Phys. Lett.* 67 (1998) 843, <https://doi.org/10.1063/1.115523>.
- [53] H. Shiel, O.S. Hutter, L.J. Phillips, J.E.N. Swallow, L.A.H. Jones, T.J. Featherstone, M.J. Smiles, P.K. Thakur, T.L. Lee, V.R. Dhanak, J.D. Major, T.D. Veal, Natural band alignments and band offsets of Sb₂Se₃Solar cells, *ACS Appl. Energy Mater.* 3 (2020) 11617–11626, [https://doi.org/10.1021/ACSAPM.0C01477/ASSET/IMAGES/LARGE/AE0C01477_0010 \(JPEG\)](https://doi.org/10.1021/ACSAPM.0C01477/ASSET/IMAGES/LARGE/AE0C01477_0010 (JPEG)).
- [54] T. Walter, R. Herberholz, C. Müller, H.W. Schock, Determination of defect distributions from admittance measurements and application to Cu(In,Ga)Se₂ based heterojunctions 80 (1996) 4411–4420, <https://doi.org/10.1063/1.363401>.
- [55] L. Zhang, W. Lian, X. Zhao, Y. Yin, T. Chen, C. Zhu, Sb₂S₃Seed-Mediated growth of low-defect Sb₂S₃ on a TiO₂Substrate for efficient solar cells, *ACS Appl. Energy Mater.* 3 (2020) 12417–12422, [https://doi.org/10.1021/ACSAPM.0C02400/ASSET/IMAGES/LARGE/AE0C02400_0006 \(JPEG\)](https://doi.org/10.1021/ACSAPM.0C02400/ASSET/IMAGES/LARGE/AE0C02400_0006 (JPEG)).
- [56] Z. Cai, C.M. Dai, S. Chen, Intrinsic defect limit to the electrical conductivity and a two-step p-type doping strategy for overcoming the efficiency bottleneck of Sb₂S₃-based solar cells, *Solar RRL* 4 (2020), 1900503, <https://doi.org/10.1002/SOLR.201900503>.
- [57] M. Grossberg, O. Volobujeva, A. Penezko, R. Kaupmees, T. Raadik, J. Krustok, Origin of photoluminescence from antimony selenide, *J. Alloys Compd.* 817 (2020), 152716, <https://doi.org/10.1016/j.jallcom.2019.152716>.

Curriculum vitae

Personal data

Name Robert Krautmann
Date of birth: 18.06.1994
Place of birth: Tallinn, Estonia
Nationality: Estonian

Contact data

E-mail: Robert.krautmann@taltech.ee

Education

2019–2023 Tallinn University of Technology, Chemical and Materials Technology, PhD
2017–2019 Tallinn University of Technology/University of Tartu, MEng in Materials and Processes for Sustainable Energetics, *cum laude*
2013–2016 University of Tartu, BSc in Materials Science
2011–2013 Tallinn English College, International Baccalaureate Diploma programme

Languages

Estonian native
English proficient
German basic
French basic

Conference participations

2019–2023 Graduate School of Functional Materials and Technologies (GSFMT), Tallinn University of Technology and Tartu University, Estonia. Oral and poster presentations
2022 12th Hybrid European Kesterite+ Workshop, Technical University of Denmark, Copenhagen, Denmark. Oral presentation
2021 Online European Materials Research Society (E-MRS) 2021 Spring Meeting. Three minute poster presentation
2019 10th European Kesterite+ Workshop, Uppsala University, Uppsala, Sweden. Poster presentation

Professional employment

2019–... Laboratory for Thin Film Energy materials, Tallinn University of Technology, Early Stage Researcher

Defended dissertations

2019 Master's degree, Development of Sb₂Se₃ thin film solar cells by close-spaced sublimation, supervisors: Dr. Nicolae Spalatu, Dr. Ilona Oja Acik

Study mobilities

8.–10.2020 Visiting researcher at Helmholtz-Zentrum Berlin for Materials and Energy research institute in Berlin, Germany

Research projects

PRG627	“Antimony chalcogenide thin films for next-generation semi-transparent solar cells applicable in electricity producing windows”
TAR16016EK	“Advanced materials and high-technology devices for energy recuperation systems”
PSG689	“Bismuth Chalcogenide Thin-Film Disruptive Green Solar Technology for Next Generation Photovoltaics”
VFP20035	„ERA chair of emerging next-generation photovoltaics“
CA21148	“Emerging Inorganic Chalcogenides for Photovoltaics (RENEW-PV)“

Supervised dissertations

2023	Anam Quddus Qureshi, master’s degree, Development of Sb_2Se_3 thin film solar cells by vapor transport deposition, Tallinn University of Technology, School of Engineering, Department of Materials and Environmental Technology. Supervisors: Robert Krautmann, Sajeesh Vadakkedath Gopi.
2020	Sepideh Safdari, master’s degree, Development of Sb_2S_3 thin film absorber by close-spaced sublimation for thin film solar cells applications, Tallinn University of Technology, School of Engineering, Department of Materials and Environmental Technology. Supervisors: Robert Krautmann, Dr. Nicolae Spalatu

List of publications

1. Spalatu, N.; **Krautmann, R.**; Katerski, A.; Karber, E.; Josepson, R.; Hiie, J.; Acik, I. O.; Krunks, M. (2021). Screening and optimization of processing temperature for Sb_2Se_3 thin film growth protocol: Interrelation between grain structure, interface intermixing and solar cell performance. *Solar Energy Materials and Solar Cells*, 225, 111045. DOI: 10.1016/j.solmat.2021.111045.
2. **Krautmann, R.**; Spalatu, N.; Gunder, R.; Abou-Ras, D.; Unold, T.; Schorr, S.; Krunks, M.; Oja Acik, I. (2021). Analysis of grain orientation and defects in Sb_2Se_3 solar cells fabricated by close-spaced sublimation. *Solar Energy*, 225, 494–500. DOI: 10.1016/j.solener.2021.07.022.
3. Koltsov, M.; **Krautmann, R.**; Katerski, A.; Maticiuc, N.; Krunks, M.; Oja Acik, I.; Spalatu, N. (2022). A Post-deposition annealing approach for organic residues control in TiO_2 and its impact on Sb_2Se_3/TiO_2 device performance. *Faraday Discussions*, 239, 273–286. DOI: /10.1039/D2FD00064D.
4. **Krautmann, R.**; Spalatu, N.; Josepson, R.; Nedzinskas, R. S.; Kondrotas, R.; Grzibovskis, R.; Vembris, A.; Krunks, M.; Oja Acik, I. (2023). Low processing temperatures explored in Sb_2S_3 solar cells by close-spaced sublimation and analysis of bulk and interface related defects. *Solar Energy Materials and Solar Cells*, 251, 112139. DOI: 10.1016/j.solmat.2022.112139.

Awards

- 2022 Laureate of “Science in 3 minutes” competition at the Estonian Academy of Sciences
- 2021 Three minute poster presentation award, Thin Film Chalcogenide Photovoltaic Materials symposium, Online European Materials Research Society (E-MRS) 2021 Spring Meeting

Popular science publications

- 2022 “Värkvõrgule võivad tulevikus vunki anda päikesepatareid”, Estonian Public Broadcasting (ERR) science news portal Novaator. URL: <https://novaator.err.ee/1608486575/varkvorgule-voivad-tulevikus-vunki-anda-paikesepatareid>
- 2022 Solar cells can galvanize IoT devices, laureate video, “Science in 3 minutes” competition, the Estonian Academy of Sciences. URL: <https://www.youtube.com/watch?v=Oa9s16MTrqs>

Elulookirjeldus

Isikuandmed

Nimi Robert Krautmann
Sünniaeg 18.06.1994
Sünniaeg Tallinn, Eesti

Kontaktandmed

E-post: Robert.krautmann@taltech.ee

Hariduskäik

2019–2023 Tallinna Tehnikaülikool, keemia- ja materjalitehnoloogia, PhD
2017–2019 Tallinna Tehnikaülikool/Tartu Ülikool, materjalid ja protsessid jätkusuutlikus energeetikas, MEng, *cum laude*
2013–2016 Tartu Ülikool, materjaliteadus, BSc
2011–2013 Tallinna Inglise Kolledž, Rahvusvahelise Bakalaureuse Diplomiprogramm (IBDP)

Keelteoskus

eesti emakeel
inglise kõrgtase
saksa algtase
prantsuse algtase

Osalemine teaduskonverentsidel

2019–2023 Graduate School of Functional Materials and Technologies (GSFMT), Tallinn University of Technology and Tartu University, Estonia. Suulised ja plakatettekanded.
2022 12th Hybrid European Kesterite+ Workshop, Technical University of Denmark, Copenhagen, Denmark. Suuline ettekanne.
2021 Online European Materials Research Society (E-MRS) 2021 Spring Meeting. Kolme minuti plakatettekanne.
2019 10th European Kesterite+ Workshop, Uppsala University, Uppsala, Sweden. Plakatettekanne

Teenistuskäik

2019–... Õhukestekileliste energiamaterjalide teaduslabor, Tallinn University of Technology, nooremteadur

Kaitstud väitekirjad

2019 Master's degree, Development of Sb₂Se₃ thin film solar cells by close-spaced sublimation, juhendajad: Dr. Nicolae Spalatu, Dr. Ilona Oja Acik

Õpiränded

8.–10.2020 Külalisteadur Helmholtz-Zentrum Berlin for Materials and Energy teadusinstituudis, Berliin, Saksamaa

Teadusprojektid

PRG627	“Antimon-kalkogeniid õhukesed kiled järgmise põlvkonna pool-läbipaistvatele päikeseelementidele kasutamiseks elektrit tootvates akendes”
TAR16016EK	“Advanced materials and high-technology devices for energy recuperation systems”
PSG689	“Õhukesekilelised vismutkalkogeniidid murrangulisele tulevase põlvkonna päikeseenergiatehnoloogiale”
VFP20035	“ERA chair of emerging next-generation photovoltaics”
CA21148	“Uudsetel anorgaanilistel kalkogeniididel põhinevad päikeseplatereid – rahvusvaheline koostöövõrgustik teadus- ja arendustöö läbiviimiseks”

Juhendatud väitekirjad

2023	Anam Quddus Qureshi, magistrikraad, Õhukesekileliste Sb_2Se_3 päikeseplatereide arendamine aurtransportsadestamise meetodil, Tallinna Tehnikaülikool, Inseneriteaduskond, Materjali- ja keskkonnatehnoloogia instituut. Juhendajad: Robert Krautmann, Sajeesh Vadakkedath Gopi.
2020	Sepideh Safdari, magistrikraad, Sb_2S_3 absorberkilede arendamine lähidistantssublatsioonil õhukesekilelistele päikeseplatereidele, Tallinna Tehnikaülikool, Inseneriteaduskond, Materjali- ja keskkonnatehnoloogia instituut. Juhendajad: Robert Krautmann, Dr. Nicolae Spalatu.

Publikatsioonid

1. Spalatu, N.; **Krautmann, R.**; Katerski, A.; Karber, E.; Josepson, R.; Hiie, J.; Acik, I. O.; Krunks, M. (2021). Screening and optimization of processing temperature for Sb_2Se_3 thin film growth protocol: Interrelation between grain structure, interface intermixing and solar cell performance. *Solar Energy Materials and Solar Cells*, 225, 111045. DOI: 10.1016/j.solmat.2021.111045.
2. **Krautmann, R.**; Spalatu, N.; Gunder, R.; Abou-Ras, D.; Unold, T.; Schorr, S.; Krunks, M.; Oja Acik, I. (2021). Analysis of grain orientation and defects in Sb_2Se_3 solar cells fabricated by close-spaced sublimation. *Solar Energy*, 225, 494–500. DOI: 10.1016/j.solener.2021.07.022.
3. Koltsov, M.; **Krautmann, R.**; Katerski, A.; Maticiuc, N.; Krunks, M.; Oja Acik, I.; Spalatu, N. (2022). A Post-deposition annealing approach for organic residues control in TiO_2 and its impact on Sb_2Se_3/TiO_2 device performance. *Faraday Discussions*, 239, 273–286. DOI: /10.1039/D2FD00064D.
4. **Krautmann, R.**; Spalatu, N.; Josepson, R.; Nedzinskas, R. S.; Kondrotas, R.; Grzibovskis, R.; Vembris, A.; Krunks, M.; Oja Acik, I. (2023). Low processing temperatures explored in Sb_2S_3 solar cells by close-spaced sublimation and analysis of bulk and interface related defects. *Solar Energy Materials and Solar Cells*, 251, 112139. DOI: 10.1016/j.solmat.2022.112139.

Preemiad

- 2022 Teaduste Akadeemia "Teadus 3 minutiga" konkursi laureaat
- 2021 Kolme minuti plakaettekande auhind, Õhukesekilelistel kalkogeniidmaterjalidel põhinevate päikesepatareide sümposium, Euroopa Materjaliuuringute Selts (E-MRS) 2021 kevadine konverents

Populaarteaduslikud artiklid

- 2022 "Värkvõrgule võivad tulevikus vunki anda päikesepatareid", Eesti rahvusringhäälingu (ERR) teadusportaal Novaator. <https://novaator.err.ee/1608486575/varkvorgule-voivad-tulevikus-vunki-anda-paikesepatareid>
- 2022 Päikesepatareid annavad vunki värkvõrguseadmetele. Võiduvideo, "Teadus 3 minutiga" konkurss, Eesti Teaduste Akadeemia. <https://www.youtube.com/watch?v=Oa9s16MTrqs>

ISSN 2585-6901 (PDF)
ISBN 978-9916-80-038-6 (PDF)